Genetic screens identify novel liabilities of senescent cells

Domhnall Seamus McHugh

A thesis submitted to Imperial College London
for the degree of Doctor of Philosophy

MRC London Institute of Medical Sciences
Faculty of Medicine
Imperial College London

December 2020

Statement of originality

Experiments included in this thesis are my own unless otherwise stated. RNA-seq sample collection (Figure 5.7a & b) was performed by Dr. Verena Wagner under Prof Jesus Gil, library preparation performed by MRC-LMS genomics core and bioinformatic analysis performed by Sanjay Khadyate of MRC-LMS bioinformatics core. Proteomics sample collection (Figure 5.7c) was performed by Dr. Pia Soogard under Prof Jesus Gil and sample preparation performed by proteomics core of Dundee University. Senescent tumour growth model experiment (Figure 5.15a-c) animal handling and measurements were performed by Dr Massimiliano Mellone under Prof Gareth J Thomas (University of Southampton). Animal handling, histological and transcriptional analysis for mouse lung fibrosis model (Figure 5.15d-j) were performed by Dr Fernanda Hernández-González under Prof Manuel Serrano (IRB Barcelona). N-myristoylation proteomics analysis (Figure 5.17a-c) was performed by Dr Wouter Kallemeijn under Prof Edward W. Tate (Imperial College London). *Ex vivo* Adamantinomatous craniopharyngioma experiments (Figure 5.21) were performed by Romain Guiho under Prof Juan Pedro Martínez-Barbera (Great Ormond Street Institute of Child Health, UCL).

Abstract

Drugs that selectively kill senescent cells, senolytics, can improve the outcomes of cancer, fibrosis and age-related diseases. Despite their potential, our knowledge of the molecular pathways that affect the survival of senescent cells is limited. To identify novel senolytic targets, we performed RNAi and CRISPR screens and identified COPI (Coatomer Complex I) vesicle formation as a liability of senescent cells. Genetic or pharmacological inhibition of COPI results in Golgi dispersal, intracellular accumulation of secreted factors, and unfolded protein response-dependent cell death of senescent cells. Knockdown of COPI subunits improves the outcomes of cancer and fibrosis in mouse models. Drugs targeting COPI have poor pharmacological properties, but N-myristoyltransferase inhibitors (NMTi) phenocopy COPI inhibition and are potent senolytics. NMTi eliminate senescent cells, ameliorating lung fibrosis and liver steatosis in aged mice. Our results suggest that senescent cells rely on a hyperactive secretory apparatus, and that inhibiting trafficking kills senescent cells in various senescence-associated diseases and during ageing.

Acknowledgements

This work in this thesis would not have been possible without a great number of people. Firstly, I would like to thank my supervisor and mentor over these last 4 years, Jesús. Without your patience, guidance and support I would not have made it to the first screen, let alone lasted through it. You have provided me many opportunities that others might not have to expand my experience in research and have been a great mentor, thank you.

This thesis is also owed though to all the members of the cell proliferation group past and present. I first joined the lab during my masters with next to no clue what I was doing; Athena and Marieke, I have to say a special thanks for, in these first few months, taking me under your wings and being so incredibly patient. I sincerely apologize and thank you for answering, the hundreds of questions I asked about one particular step or another in a protocol. Athena and Andrew (and for that matter all of the Cell proliferation group), I'd also like to say a special thanks for being inspirations with your unfaltering work ethic, it helped me through a lot of long nights. Thanks as well to Ana and Jodie, you were/are unifying personalities in the group, always listened attentively to any question I had, and I'll sincerely miss the conversations about politics and life when in tissue culture or at the desk. Bin - not only would a lot of the work in this thesis had not been possible without your help, you've been a great friend and have made the long lab hours fun. Sharon, thank you also for your cool headedness throughout the years, it saved me a few times from my own stress. Within the PhD cohort I'd like to thank Chiara, you've been a great friend over the course of the PhD, always providing level-headed rationale and grounding me in reality. Finally, I would like to thank my family, you have always been there for me when I needed to talk or an escape from work.

Table of contents

List of Figures

List of Tables

Abbreviations

°C	degrees centigrade
4EBP1	EIF4E-Binding Protein 1
4OHT	4-Hydroxytamoxifen
53BP1	p53-binding Protein 1
ACLT	anterior cruciate ligament transection
ACP	Adamantinomatous craniopharyngiomas
AD	Alzheimer's Disease
ADP	adenosine diphosphate
ALDOA	Aldolase, Fructose-Bisphosphate A
ALT	alternative lengthening of telomeres
AMPK	Protein Kinase AMP-Activated Catalytic Subunit Alpha 1
AMP	Adenosine Monophosphate
ANRIL	CDKN2B Antisense RNA 1
APP	Amyloid Beta Precursor Protein
APOE/C2	Apolipoprotein E/C2
ARCN1 /COPD	Archain 1 / Coatomer Protein Complex Subunit Delta
ARF	Alternative reading fram
ARF	ADP Ribosylation Factor
ARFGAP	ADP Ribosylation Factor GTPase Activating Protein
ARFGEF1/2	ADP Ribosylation Factor Guanine Nucleotide Exchange Factor 1
ARFRP1	ADP Ribosylation Factor Related Protein 1
ARID1A	AT-Rich Interaction Domain 1A
ARL1	ADP Ribosylation Factor Like GTPase 1
ARNO1	ARF Nucleotide-Binding Site Opener
ASF1a	Anti-Silencing Function 1A Histone Chaperone
ATCC	American Type Culture Collection
ATF4/6	Activating Transcription Factor 4/6
ATG	Autophagy Related
ATM	Ataxia Telangiectasia Mutated
ATP	Adenosine Triphosphate
ATR	Ataxia Telangiectasia and Rad3 related
AUC	Area under the curve
AzTB	azido-TAMRA-PEG-Biotin
BCA	bicinchoninic acid
BCL2	B-Cell CLL/Lymphoma 2
BCL2L1 /BCLxL	BCL2-Like-1 /B-cell Lymphoma xL
BCL2L2 /BCLw	BCL2-Like-2/B-cell Lymphoma w
BET	Bromodomain and Extra-Terminal motif
BFA	Brefeldin A
BH3	BCL2 homology domain 3
BMI1	BMI1 Proto-Oncogene, Polycomb Ring Finger
BRAF	B-Raf Proto-Oncogene, Serine/Threonine Kinase
BRD4	Bromodomain Containing 4
BrdU	5-Bromo-2'-deoxyuridine

BRG1	SWI/SNF Related, Matrix Associated, Actin Dependent Regulator Of Chromatin, Subfamily A, Member 4
BubR1	Budding Uninhibited By Benzimidazoles 1 Mitotic Checkpoint Serine/Threonine Kinase B
CAR	Chimeric antigen receptor
Cas9	CRISPR associated protein 9
C/EBPβ	CCAAT/enhancer binding protein beta
CBX7	Chromobox 7
CC3	Cleaved caspase 3
CCF	cytoplasmic chromatin fragment
CCL	C-C Motif Chemokine Ligand
CCL_4	Carbon tetrachloride
CCN1	Cellular Communication Network Factor 1
CDC6	Cell Division Cycle 6
CDK	Cyclin-Dependent Kinase
CDKI	CDK Inhibitor
CDKN1A	Cyclin Dependent Kinase Inhibitor 1A
CDKN2A	Cyclin Dependent Kinase Inhibitor 2A
cDNA	complementary DNA
cGAS	Cyclic GMP-AMP Synthase
CHK	Checkpoint Kinase
CHOP	CCAAT/Enhancer-Binding Protein Homologous Protein
CLTA4	Cytotoxic T-Lymphocyte Associated Protein 4
CM	Conditioned Media
COG	Component Of Oligomeric Golgi Complex
COL3A1	Collagen Type III Alpha 1 Chain
COPI /II	Coatomer Complex 1 /2
COPB1/2	COPI Coat Complex Subunit Beta 1 /2
COPG1/2	COPI Coat Complex Subunit Gamma 1/2
COPA	COPI Coat Complex Subunit Alpha
COPE	COPI Coat Complex Subunit Epsilon
COPZ1/2	COPI Coat Complex Subunit Zeta
COX	Cytochrome C Oxidase
CpG	5'-C-phosphate-G-3'
CpGI	CpG-island
CRISPR	clustered regularly interspaced short palindromic repeats
CTCs	Circulating tumor cells
CuAAC	Copper-catalysed azide-alkyne cycloaddition
CV	coefficient of variance
CXCL	chemokine (C-X-C motif) ligand
CXCR	C-X-C Motif Chemokine Receptor
DAB	3,3'-diaminobenzidine
DAMP	damage-associated molecular pattern
DAPI	4',6-diamidino-2-phenylindole
DDR	DNA Damage Response
DMEM	Dulbecco’s modified Eagle’s Medium
DMSO	Dimethyl sulfoxide

DNA	Deoxyribonucleic acid
DNA-SCARS	DNA-Segments with Chromatin Alterations Reinforcing Senescence
dNTP	deoxynucleoside triphosphate
DSB	Double-Strand Break
dsDNA	double stranded DNA
DTT	Dithiothreitol
ECM	Extracellular Matrix
EDTA	Ethylenediaminetetraacetic acid
EEA1	Early endosome antigen 1
EIF4E	Eukaryotic Translation Initiation Factor 4E
ELISA	Enzyme-linked immunosorbent assay
EMT	Epithelial to Mesenchymal Transition
ENTPD7	Ectonucleoside Triphosphate Diphosphohydrolase 7
ER	Endoplasmic Reticulum
ER	Eostrogen Receptor
ERGIC	ER-Golgi intermediate compartment
EVs	extracellular vesicles
EXOC7	Exocyst Complex Component 7
EZH2	Enhancer of Zeste 2 Polycomb Repressive Complex 2 Subunit
FASP	Filter-aided sample preparation
FBS	Fetal Bovine Serum
FDR	False discovery rate
FOXO4	Forkhead Box O4
g/ RCF	Relative centrifugal force
G3BP1	Ras GTPase-activating protein-binding protein 1
GAPDH	Glyceraldehyde 3-phosphate dehydrogenase
GATA4	GATA Binding Protein 4
GBF1	Golgi Brefeldin A Resistant Guanine Nucleotide Exchange Factor 1
GCA	Golgicide A
G-CSF	Granulocyte-colony stimulating factor
GDP	Guanosine diphosphate
gDNA	Genomic DNA
GECKOv2	Genome-scale CRISPR Knock-Out v2.0
GFP	Green Fluorescent Protein
GLB1	Galactosidase Beta 1
GM130	130 KDa Cis-Golgi Matrix Protein
GNAO1	G Protein Subunit Alpha O1
GNG8	G Protein Subunit Gamma 8
GO	Gene Ontology
GPCR	G-protein coupled receptor
GRO1	melanoma growth stimulating activity, alpha; C-X-C Motif Chemokine Ligand 1
GSEA	Gene set enrichment analysis
GSNOR	Alcohol Dehydrogenase 5 (Class III), Chi Polypeptide
GTP	Guanosine triphosphate
GWAS	Genome wide association study
Gy	Gray

H2BK119Ub	Histone 2B Lysine 119 ubiquitination
H3K27ac	Histone 3 lysine 27 acetylation
H3K9me3	Histone 3 lysine 9 tri-methylation
HBP1	HMG-Box Transcription Factor 1
HCA	High Content Analysis
HCC	Hepatocellular carcinoma
HDTVI	Hydrodynamic tail vein injection
HFFF2	Human Foetal Foreskin Fibroblast 2
HGPS	Hutchinson-Gilford progeria syndrome
HIER	Heat induced epitope retrieval
HIRA	Histone Cell Cycle Regulator
HMGA2	High Mobility Group AT-Hook 2
HMGB1	High Mobility Group Box 1
HMGCoA	3-hydroxy-3-methyl-glutaryl-coenzyme A reductase
HP1	Heterochromatin Protein 1
HPCA	Hippocalcin
HRAS	Harvey Rat Sarcoma Viral Oncogene Homolog
HRP	Horse radish peroxidase
HS	High sensitivity
HSP90	Heat shock protein 90
HP	High purity
HsC	Hepatic Stellate Cell
HSC	Hematopoietic stem cell
HTM	High-Throughput Microscopy
IDT	Integrated DNA Technologies
IF	Immunofluorescence
IFN	Interferon
IGF	Insulin Growth Factor
IGFBP7	Insulin Like Growth Factor Binding Protein 7
IgG	Immunoglobulin G
IL	Interleukin
IL6R	Interleukin 6 Receptor
IPF	Idiopathic Pulmonary Fibrosis
IRE1	Inositol-Requiring Protein 1
JAK	Janus Kinase
JMJD3	Jumonji domain containing-3, Lysine Demethylase 6B
KDELR	(Lys-Asp-Glu-Leu) endoplasmic reticulum protein retention receptor 1
KRAS	Kirsten Rat Sarcoma Viral Oncogene Homolog
Ku80	86 KDa Subunit Of Ku Antigen
LADs	lamin-associated heterochromatin domains
LAMP1/2	Lysosomal Associated Membrane Protein 1/2
LB	Lysogeny broth
LDLR	Low Density Lipoprotein Receptor
LESCs	liver sinusoidal vascular endothelial cells
LINE1	Long interspersed nuclear elements Type Transposase Domain Containing 1
LUC	Luciferase

macroH2A	MacroH2A.1 Histone
MAGeCK	Model-based Analysis of Genome-wide CRISPR-Cas9 Knockout
MAPK	Mitogen-Activated Protein Kinase
MAPKAPK2	Mitogen-Activated Protein Kinase-Activated Protein Kinase 2
MDM2	MDM2 Proto-Oncogene, E3 Ubiquitin Protein Ligase
MED1	Mediator Complex Subunit 1
MEF	Mouse Embryonic Fibroblast
MEK	Mitogen-Activated Protein Kinase Kinase
METAP2	Methionyl Aminopeptidase 2
mg/ml/mM	milligram/millilitre/millimolar
MiDAS	mitochondrial dysfunction-associated senescence
min	minute
MKK3/6	Mitogen-Activated Protein Kinase Kinase 3/6
MLL1	Lysine Methyltransferase 2A
MMP	Matrix Metallopeptidase
MOI	Multiplicity of infection
MRC	Medical Research Council
mRNA	messenger RNA
MSCs	mesenchymal stem cells
mtDNA	mitochondrial DNA
mTR	Methionine Synthase
MuSCs	Muscle stem cells
mTOR	Mechanistic Target Of Rapamycin
MVBs	multi vesicular bodies
Myc	V-Myc Avian Myelocytomatosis Viral Oncogene Homolog
N1ICD	Notch Receptor 1
NaAc	Sodium Acetate
NAC	N-acetylcysteine
NAD	Nicotinamide Adenine Dinucleotide
NADPH	NAD Phosphate Oxidase
NAFLD	Non-alcoholic fatty liver disease
NASH	Nonalcoholic steatohepatitis
NHLF	Normal human lung fibroblasts
NSCs	Neural stem cells
NSG	NOD scid gamma
NEB	New England Biolabs
NF-κB	Nuclear Factor-Kappa B
NGS	Next generation sequencing
NK	Natural killer
NMT	N-myristoyltransferase
NOXA	Phorbol-12-Myristate-13-Acetate-Induced Protein 1
NRAS	Neuroblastoma RAS viral oncogene homolog
NSCLC	Non-small cell lung carcinoma
nt	nucleotide
OCT	Optimal cutting temperature
OIS	Oncogene-induced senescence
p300	E1A-Binding Protein, 300kD

p400	P400 KDa SWI2/SNF2-Related Protein
PBEC	Primary Bronchial epithelial cells
PBS	Phosphate buffered saline
PCR	Polymerase chain reaction
PD	Parkinson's disease
PD-1	Programmed Cell Death 1
PDAC	Pancreatic ductal adenocarcinoma
PDGF-AA	Platelet Derived Growth Factor Subunit A
PDK1	Pyruvate Dehydrogenase Kinase 1
PDP2	Pyruvate Dehyrogenase Phosphatase Catalytic Subunit 2
PEG	Poly(ethylene glycol)
PERK	Pancreatic EIF2-Alpha Kinase
PFA	Paraformaldehyde
PGC-1β	Peroxisome Proliferator-Activated Receptor Gamma, Coactivator 1 Beta
PI3K	Phosphatidylinositol-4,5-Bisphosphate 3-Kinase
PLC	Phospholipase C
PML	PML Nuclear Body Scaffold
POT1	Protection of Telomeres 1
PRC	Polycomb repressive complex
PS1	Presenilin 1
PTBP1	Polypyrimidine tract binding protein 1
PTEN	Phosphatase and Tensin Homolog
pTEFb	positive transcription elongation factor
PTK2	Protein Tyrosine Kinase 2
qPCR	Quantitative PCR
RAD51	BRCA1/BRCA2-Containing Complex, Subunit 5
Rb	Retinoblastoma
RIPA	Radioimmunoprecipitation assay
RNA	Ribonucleic acid
RNA-seq	Next generation sequencing of RNA
ROS	Reactive oxygen species
RPKM	Read per kilobase per Million mapped reads
RPA	Replication Protein A1
RPS14	Ribosomal Protein S14
RRA	Robust ranking aggregation
RT	Reverse transcriptase
Rt	Room temperature
S6K1	Ribosomal Protein S6 Kinase B1
SA-β-Gal	Senescence-associated β-Galactosidase
SADS	senescence-associated distention of satellites
SAHF	Senescence-associated heterochromatic foci
SAPD	Senescence-associated protein degradation
SASP	Senescence-associated secretory phenotype
SB13	Sleeping beauty transposase system
scRNA-seq	single cel RNA-seq
SD	standard deviation
SDS	Sodium Dodecyl Sulphate

SDS-PAGE	SDS-Polyacrylamide Eel Electrophoresis
SE	Super enhancer
SEM	Standard error of the mean
SERP1	Stress Associated Endoplasmic Reticulum Protein 1
sgRNA	short guide RNA
shRNA	short hairpin RNA
SILAC	Stable Isotope Labeling by/with Amino acids
siRNA	small interfering RNA
SIRT	Sirtuin
SNARE	Soluble NSF attachment proteins receptor
SNX14	Sorting Nexin 14
SQSTM1/p62	Sequestosome 1
STAT3	Signal Transducer And Activator Of Transcription 3
STING	Stimulator Of Interferon Response CGAMP Interactor 1
TAE	Tris-acetate-EDTA
TAMRA	Tetramethylrhodamine
TASCC	TOR-autophagy spatial coupling compartment
TBS	Tris-buffered saline
TBTA	Tris((1-benzyl-4-triazolyl)methyl)amine
TCEP	(tris(2-carboxyethyl)phosphine)
TE	Tris-EDTA
TEAB	triethylammonium bicarbonate
TERT	Telomerase reverse transcriptase
TGs	Triglycerides
TGF	Transforming Growth Factor
TGFBR1	TGF-beta receptor 1
TGN	Trans-golgi network
TIDE	Tracking of Indels by Decomposition
TIF	Telomere induced foci
TIS	Therapy induced senescence
TMEM106B	Transmembrane Protein 106B
TNFα	Tumour necrosis factor alpha
TRAPPII	oligomeric complex transport protein particle 2
TREM2	Triggering Receptor Expressed On Myeloid Cells 2
TRF2	Telomeric Repeat Binding Factor 2
TWIST1/2	Twist Basic Helix-Loop-Helix Transcription Factor 1/2
TYRO	Tyrosine-protein kinase receptor
UBB/C	Ubiquitin B/C
ULK	Unc-51 Like Autophagy Activating Kinase
uPAR	Urokinase-type plasminogen activator receptor
UPR	Unfolded protein response
UV	ultraviolet
v/v	Volume per volume
VEGF	Vascular Endothelial growth factor
WB	Western Blot
WBCs	White blood cells
w/v	weight per volume

XBP1	X-Box Binding Protein 1
γH2AX	Phosphorylation of Histone A2 Variant X
ZER1	Zyg-11 Related Cell Cycle Regulator
ZFP36L1	Zinc Finger Protein, C3H Type, 36-Like 1
ZMPSTE24	Zinc Metallopeptidase STE24
ZYG11B	Zyg-11 Family Member B, Cell Cycle Regulator
µg/µl/µM	microgram/microlitre/micromolar

CHAPTER 1 - INTRODUCTION

1.1 What is Cellular Senescence?

Cellular senescence is, first and foremost, a mechanism through which an organism can suppress cells disruptive to tissue homeostasis. First identified as a cessation of cell division in serially passaged human fibroblasts (Hayflick and Moorhead, 1961), stable growth arrest is one of the hallmark features of the senescence program. The senescence program which has since been explored in great-detail both in vitro and in vivo in the context of cancer (Collado et al., 2007; Pérez-Mancera et al., 2014) and more recently aging (Muñoz-Espín and Serrano, 2014). These studies have highlighted that different senescence contexts share characteristic features, such as cell cycle arrest, altered cellular function and an inflammatory phenotype (Muñoz-Espín and Serrano, 2014; Salama et al., 2014). Further underscoring the complexity of the senescence program and its regulation, senescent cells also adopt increased levels of autophagy (Gewirtz, 2013), metabolic reprogramming (Kaplon et al., 2013; Wiley and Campisi, 2016) and global chromatin reorganization (Chandra et al., 2012; Narita et al., 2003; Sadaie et al., 2013).

1.2.1 Relationship between cellular senescence and aging

A relationship between senescence and aging was posited from early research on how it was induced (Campisi, 1997; Smith and Pereira-Smith, 1996). Later the discovery that senescent cells and their biomarkers are increasingly prevalent in aged tissues (Herbig et al., 2006; Krishnamurthy et al., 2004; Ressler et al., 2006; Wang et al., 2009), led to the hypothesis that senescence was driving aging. What however was driving senescence cell accumulation and were these drivers age-related?

Whilst senescence is not exclusively a damage response mechanism - given its reported roll in development in the embryo (Muñoz-Espín et al., 2013; Storer et al., 2013) – senescence

in adult tissues are primarily induced in response to damage – one of which is damage to telomeres. DNA polymerases require a template to synthesize DNA, resulting in progressive shortening of chromosomal ends with each cycle of DNA replication during cell division. As replication progressively shortens the ends of chromosomes, the risk of catastrophic end-to-end chromosomal fusions increases (O'Sullivan and Karlseder, 2010). To circumvent this "end-replication" problem, chromosomal ends are buffered by highly repetitive DNA structures called telomeres. These structures are formed by way of a ribonucleoprotein complex - telomerase - that serves to concatenate DNA to the ends of chromosomes thereby providing a template for DNA synthesis (Nandakumar and Cech, 2013). Telomerase expression however is seldom found outside of embryonic tissue. Repeated cell division in adult tissues that lack telomerase therefore results in progressive erosion of DNA. Mutations in genes involved in telomere lengthening or reduced telomere length induced senescence (Allsopp and Harley, 1995; Greidert et al., 1990; Lundblad and Szostak, 1989; Yu et al., 1990), providing evidence that the Hayflick's limit was a form of senescence induced by replicative shortening of telomeres.

Induction of senescence in response to telomeric shortening was later identified to be supressed by a telomere bound protein complex called Shelterin (reviewed in (de Lange, 2018; Palm and de Lange, 2008) This DNA damage response (DDR) suppressing protein complex, bound at telomeres, serves to protect the cell from potential telomere crisis and end-to-end fusions that would result from aberrant DNA repair processes on the exposed DNA ends (Karlseder et al., 2002; De Lange, 2005; Van Steensel et al., 1998). Its function is antagonistic however, as shortening of telomeres results in removal of Shelterin and allows for engagement of the very DDR it is meant to suppress (Sfeir and de Lange, 2012). This engagement of DDR then results in senescence induction and protection of the telomeres from further replicative shortening and potential fusion events (Sfeir and de Lange, 2012). In

accordance with this, disruption of several components of Shelterin, namely TRF2 and POT1, result in aberrant DDR and pre-mature induction of senescence *in vitro* (Denchi and de Lange, 2007; Konishi and De Lange, 2008). The senescence inducing effect of shelterin removal is further enhanced by small amounts of Shelterin still bound at shortened telomeres suppressing DNA repair (de Lange, 2018). Inability to repair allows for accumulation DNA damage markers and formation DNA damage foci, called telomere induced foci (TIFs). These TIFs are heavily demarcated for γH2Ax & 53BP1 (Takai et al., 2003) and result in engagement of the DDR and induction of senescence (Konishi and De Lange, 2008; Lenain et al., 2006). Interestingly, whilst other forms of senescence inducing damage such as irradiation don't necessarily have a propensity for damaging telomeres, the DNA repair resistant nature of telomeres means that they are often the source of sustained DNA damage signaling that induces senescence (Fumagalli et al., 2012). As an organism ages, the number of divisions a cell have undergone increases, resulting in more telomere erosion and senescence. Could this process be potentially driving aging?

One line of evidence, supporting a causative role for telomere erosion in aging, is that deletion of telomerase RNA component (mTR) in mice causes an accelerated aging phenotype after successive generations of progeny (Blasco et al., 1997, 1998). Conversely TERT-ER knock-in mice, which recapitulate the effects of $mTR^{-/-}$, can be rescued by pulsing mice with telomerase reverse transcriptase (TERT) expression - to re-lengthen telomeres (Jaskelioff et al., 2011). Cells from these telomere rescued mice have sustained proliferative ability correlating with reduced tissue deterioration. This corroborates findings in human centenary Hematopoietic Stem Cells (HSCs) that can be rejuvenated by telomerase expression (Lapasset et al., 2011). In addition, shortened telomeres are associated with liver cirrhosis (Rudolph, 2000), a decline in peripheral blood leukocytes (Anderlini et al., 1997) and higher mortality in those over 60 (Cawthon et al., 2003).

Primarily correlative evidence supports telomere shortening as being the main driver of the age dependent accumulation of senescent cells. This hypothesis is challenged by the presence of phenotypic aging decline in *Mus musculus* irrespective of telomeric length (Rudolph et al., 1999), highlighting the possibility of other driving factors. Our emerging understanding of the aging process now points to complex amalgamation of damages, including metabolic and proteostatic dysfunction (López-Otín et al., 2013). The involvement of metabolism in aging for example can be found at both an organismal and molecular level. At the former, caloric restriction retards the aging decline (Mitchell et al., 2016). On the latter, mutations in insulin receptor (Selman et al., 2008), S6K1 (Selman et al., 2009) and rapamycin treatment have been shown to increased healthspan (Harrison et al., 2010; Miller et al., 2011), reinforcing the hypothesis of metabolic dysfunction contributer to aging**.**

Linking metabolic dysfunction, senescence and aging - oxidative stress has been shown to induce senescence (Chen et al., 1995)**.** Oxidative stress is characterized by production of oxygen free radicals, primarily due to defective mitochondrial metabolism. These free radicals, also known as Reactive Oxygen Species (ROS) can induce DNA damage and have been hypothesized as a driver of aging (Pérez et al., 2009). ROS contributes to multiple senescence phenotypes (Kaplon et al., 2013; Macip et al., 2002; Moiseeva et al., 2009). Concordantly, treatment of cells with a ROS scavenger NAC, can bypass senescence growth arrest, supporting the link between oxidative stress and senescence (Macip et al., 2002). In the context of oncogene induced senescence (OIS), upregulation of pyruvate dehydrogenase upregulation that elevates oxygen consumption, contributes to ROS production (Kaplon et al., 2013); thereby suggesting that metabolic reprogramming results in ROS production during senescence (Wiley and Campisi, 2016). ROS induces senescence by forming single stranded DNA breaks (Lindahl, 1993) that will upregulate DDR pathways, as occurs with telomere erosion induced senescence. The production of ROS and mtDNA mutations that

further exacerbate its production have been found to increase in multiple tissues with age (Finkel and Holbrook, 2000; Krishnan et al., 2007). Moreover, caloric restriction - known to extend healthspan - suppresses ROS production (Gredilla et al., 2001). As with the hypothesis of telomeric shortening, certain *in vivo* models challenge the hypothesis of ROS driven aging however, with superoxide dismutase mutant mice having increased DNA damage but not having reduced healthspan (Melov et al., 1999). These results have led to the hypothesis that ROS production, whilst being an essential component of aging, is not the only driver (Sun et al., 2016).

Further linking metabolism with senescence are the metabolic pathways of mTOR, Sirtuins and autophagy. mTOR signaling has been shown to be differentially regulated during senescence (Herranz et al., 2015; Laberge et al., 2015). mTOR regulates cell growth, autophagy and protein/lipid synthesis through interacting with multiple pathways, such as the insulin signaling & AMPK, and is therefore intrinsically linked with the metabolic status of the cell (reviewed in (Zoncu et al., 2011). mTOR is typically upregulated during metabolic stress and it contributes to multiple senescence phenotypes including the a complex secretome called the senescence associated secretory phenotype (SASP) and autophagy (Herranz et al., 2015; Laberge et al., 2015; Walters et al., 2016). The sirtuin family of ribosyltransferases, have roles in regulating metabolism and DNA repair (Houtkooper et al., 2012). Their upregulation can be a result of oxidative stress in addition to telomere shortening. Different sirtuins however may have counteracting roles in senescence. For example, SIRT1 is downregulated during senescence by autophagic processes (Xu et al., 2020) and it can de-acetylate p53, promoting its degradation and senescence bypass (Solomon et al., 2006). Conversely, SIRT6 de-acetylates lysine 18 of histone H3 to prevent mitotic errors and suppresses senescence (Tasselli et al., 2016), demonstrating the often bidirectional interplay of senescence and metabolism. This dual nature of some metabolic processes is further

demonstrated by autophagy - another major metabolic pathway in the cell for recycling cellular components (Gewirtz, 2013). Autophagy has a complex relationship with senescence with its increase during senescence being shown to regulate production of the SASP (Narita et al., 2011) and its inhibition triggering metabolic dysfunction and therein senescence (García-Prat et al., 2016). There is also evidence to suggest that autophagy and other metabolic processes mediate senescent cell survival (Dörr et al., 2013).

DNA damage appears to be a key driver of senescence in aging through ROS production or sustained DNA damage from telomeres. This is further evidenced by the multitude of progeroid syndromes resulting from DNA repair deficiencies (Kudlow et al., 2007). However, senescence is also induced via upregulation of general stress sensing that converges on the MAPK p38 - $p16^{INK4a}$ signaling axis. Its upregulation can be triggered by oxidative stress, DNA damage, telomere attrition and oncogenic stress. Substantiating their role in aging, activation of MAPK p38 and $p16^{INK4a}$ limits the proliferative potential of HSCs and yields pro-aging phenotypes (Baker et al., 2016; Ito et al., 2006).

Recent strides have been made in identifying senescence *in vivo* using different biomarkers (Sharpless and Sherr, 2015). Biomarkers including increased levels of senescence associated-β gal staining (SA-B-gal), senescence associated heterochromatic foci (SAHF), increased expression of $p16^{INK4A}$ and presence of the SASP. This has led to renewed interest in understanding senescence and its role in aging**.** Mouse models of senescence caused by irradiation (Richardson, 2009; Wang et al., 2015a), telomere shortening (Blasco et al., 1998; Rudolph et al., 1999) and chemotherapy (Demaria et al., 2017), all display progeroid phenotypes with increased levels of senescence markers. Despite these stresses being able to drive accumulation of senescent cells *in vivo*, they fail to fully recapitulate the natural aging phenotype and its stochastic appearance. Therefore, senescent cell accumulation during aging might reflect a gradual accumulation of different damages in tissues and a

compromised clearance of senescent cells that leads to their accumulation and tissue dysfunction.

1.2.2 Oncogene-induced senescence

Alongside induction of senescence due to accumulated damage across an organism's life span, such as with telomeric shortening and oxidative stress; expression of oncogenes can activate an acute senescence response. The phenomenon of oncogene induced senescence (OIS) was first examined in fibroblasts overexpressing HRAS (Serrano et al., 1997) with the G12V mutation, a mutation found in a high percentage of lung, pancreatic and colorectal cancers (Bos, 1989; Prior et al., 2012). This mutation's potency lies within its ability to constitutively active RAS - MAP kinase pathway and proliferation, it does this by altering the Mg^{2+} binding domain of RAS and inhibits its ability to hydrolyze GTP to GDP (Prior et al., 2012). Ostensibly, constitutive MAP kinase signaling should result in hyper-proliferation. Indeed, cells overexpressing this mutant do undergo an initial phase of exponential cell division. Ultimately though, an opposing effect of stable cell cycle arrest results (Serrano et al., 1997). This *in vitro* biphasic proliferative profile is not only observed with overexpression of other members of the MAP kinase pathway but also with oncogenic events such as loss of the tumor suppressor PTEN and overexpression of Myc (Campaner et al., 2009; Chen et al., 2005; Lin et al., 1998; Zhu et al., 1998). In each instance, overexpression of oncogenes led to stable growth arrest and upregulation of classical senescence markers, such as senescence associated β-galactosidase activity and upregulation of the cyclin dependent kinase inhibitors, $p16^{INK4a}$ and $p21^{CIP1}$ (Collado et al., 2005; Lin et al., 1998; Serrano et al., 1997; Zhu et al., 1998).These results could also be translated to various *in vivo* models of the same oncogenic events (Campisi, 2005; Chen et al., 2005; Collado et al., 2005; Dankort et al., 2009; Michaloglou et al., 2005). Importantly it was later revealed that oncogenes cause senescence by activating DNA damage response, as seen through formation of γH2Ax and

53BP1 foci (Bartkova et al., 2006; Di Micco et al., 2006). During RAS induced OIS, CDC6 was found to be upregulated leading to formation of DNA replication origins and stalled replication forks during the hyper-replicative phase, both able to induce DDR and senescence (Di Micco et al., 2006). These stalled replication forks and resulting DNA damage from their processing was shown to be due to nucleotide depletion (Mannava et al., 2013), with overexpression of thymidylate synthase and ribonucleotide reductases partially rescuing senescence induction. Nucleotide depletion driven DNA damage is also supported by the upregulation of the chromatin remodeler ARID1B during OIS, resulting in expression of a nucleotide hydrolyzing enzyme ENTPD7 (Tordella et al., 2016).

The formation of stalled replication forks during OIS can explain the initial induction of DDR and cell cycle arrest. However, most DNA damage foci in OIS cells are resolved due to DNA repair (Suram et al., 2012) – raising the question, how do OIS cells sustain DDR to enable stable cell cycle arrest? Suram et al. identified that during OIS, despite widespread repair, stalled replication forks remain at telomeres, which as discussed before are DNA repair resistant due to the activity of the Shelterin complex. This discovery, along with the presence of DDR foci at telomeres and that expression of TERT destabilizes OIS (Patel et al., 2016), suggest that like telomere attrition, sustained DDR signaling originates from telomeric regions and other DNA repair resistant regions in the genome.

1.3.1 Regulation of the senescence cell cycle arrest

Aberrant proliferation can be highly disruptive to tissue function, as is seen with neoplastic disorders. To protect against such disruption, senescence causes cell cycle arrest. Over the past 20 years, usage of *in vitro* models of senescence, such as oncogene induced senescence (OIS), have greatly improved our understanding of the pathways regulating

senescence. Most inducers of senescence activate at least one of two downstream pathways: the p53/p21^{CIP1} and p16^{INK4a}/Rb tumor suppressor pathways.

p53/p21^{CIP1} regulation in senescence - In the context of telomeric shortening - uncapping of telomeres and the resulting sensing of DNA breaks upregulates p53 and p21^{CIP1} leading to a senescence growth arrest (Chin et al., 1999; di Fagagna et al., 2003; Takai et al., 2003)**.** This is also complemented by observations in other forms of senescence such as irradiation and OIS (d'Adda di Fagagna, 2008). In each case, double or single stranded DNA breaks results in increased deposition of γH2Ax, RPA and 53BP1 that in turn activate ATM/ATR kinases to phosphorylate p53 via CHK1/2 kinases, thereby preventing its degradation by MDM2 and resulting in p21^{CIP1} expression (d'Adda di Fagagna, 2008; Fumagalli et al., 2012). The cyclin dependent kinase inhibitor (CDKI) p21^{CIP1} will then subsequently block the activity of CDK4/6, leading to hypophosphorylated Rb and blocking G1 progression in the cell cycle (d'Adda di Fagagna, 2008). Elevated p53 levels can also enact a quiescent state and activate DNA repair processes if its upregulation is transient (Kruiswijk et al., 2015; Salama et al., 2014). During senescence however, cells have sustained elevation of p53 expression due to sustained DDR. This is a result of repair resistant regions of the genome known such as DNA-SCARS (DNA-Segments with Chromatin Alterations Reinforcing Senescence) which are enriched for γH2Ax, p53, CHK2 and ATM/ATR but are depleted of DDR proteins associated with repair such as RPA and RAD51. DNA-SCARS can be found at telomere induced foci (TIFs) in cells that have undergone telomere attrition and associated with PML nuclear bodies in pericentromeric regions during non-telomere induced DNA damage (Fumagalli et al., 2012; Rodier et al., 2009, 2011). Their DNA repair inhibitory nature, alongside the effects of Shelterin complex at telomeres, allow for a stable arrest of cell cycle by continual induction of the CDKI p21^{cip1} via the p53 signaling axis. Paradoxically, single cell tracking of cancer cells treated with chemotherapeutic agents, demonstrate that initial

elevated $p21^{CIP1}$ expression need not correlate with senescence induction (Hsu et al., 2019). As cells undergoing senescence were found to either have an early rapid upregulation or delayed induction of $p21^{CIP1}$, with the intermediary cells continuing to proliferate.

The importance of p53 in senescence induction and thereby prevention aberrant proliferation necessitates additional post-transcriptional and translational mechanisms that can fine tune the senescence response. For example, p53 is post-translationally regulated via acetylation and phosphorylation, events essential for p53 activity and senescence induction (Banin et al., 1998; Pearson et al., 2000). Phosphorylated p53 is also regulated through its FOXO4 mediated localization to DNA-SCARS and the promoter of $p21^{CIP1}$. Inhibition of this interaction excludes p53 from the nucleus and allows for engagement of pro-apoptotic pathways in senescent cells (Baar et al., 2017). This corroborates with the role of FOXO transcription factors in aging. For example dFOXO activity in *Drosophila* muscle delays protein homeostasis and oxidative stress induced aging as well as regulates lifespan (Demontis and Perrimon, 2010; Hwangbo et al., 2004).The above are only some examples of the regulatory pathways that have been shown to regulate p53 in senescence (reviewed in (Kruse and Gu, 2009; Salama et al., 2014))

INK4/ARF locus in senescence - Alongside the discovery of $p53/p21^{CIP1}$ and its involvement in regulating senescence growth arrest, de-repression of the *INK4/ARF* locus was found to play a similar role. Mice or cells lacking genes within this locus fail to undergo senescence (Kamijo et al., 1997; Serrano et al., 1997). This locus expresses two genes *CDKN2A* and *CDKN2B*, the former of which has two alternatively spliced transcripts producing the $p16^{INK4a}$ and $p19^{ARF}$ proteins and the latter $p15^{INK4b}$. $p16^{INK4a}$ and $p21^{CiP1}$ can inhibit the activity of CDK4/6 and G1 progression. $p19^{ARF}$ on the other hand inhibits the activity of MDM2, thereby facilitating crosstalk between the INK4/ARF locus and the $p53/p21^{CIP1}$ pathways. p53 in turn can regulate expression of $p19^{ARF}$ through a negative feedback loop, as is displayed by $p53^{-}$

$^{/-}$ MEFs having elevated p19^{ARF} expression (Harris and Levine, 2005; Leong et al., 2009). The activity of *INK4/ARF* produced proteins, provide a potent tumor suppressive mechanism and as such the *INK4/ARF* locus is one of the most frequently mutated in cancer alongside p53 (Gil and Peters, 2006; Kim and Sharpless, 2006).

In healthy growing cells the *INK4/ARF* locus is epigenetically silenced through deposition of repression histone and DNA marks such as H3K27me3 and DNA methylation (Bracken et al., 2007). Methylation of Lysine 27 on histone H3 (H3K27me3) is regulated by the Polycomb repressive complexes (PRCs), comprising of PRC1 and PRC2. PCR2, containing the H3K27 methyl transferase, EZH2, is a common epigenetic alteration in cancer (Hock, 2012; Kim and Roberts, 2016). PRC1 complex functions to enact compaction of chromatin and silencing through recruitment to H3K27me3 and deposition of H2BK119Ub. In support of the role of Polycomb in *INK4/ARF* regulation, disruption of the PRC2-recruited PRC1, by knockdown of methylation mark reading CBX7 or assembly ring finger protein BMI1 can induce senescence via p16^{INK4A} expression (Bracken et al., 2007; Gil et al., 2004; Jacobs et al., 1999). While there is still debate over how, mechanistically, PRCs are recruited to specific loci (Blackledge et al., 2015), in senescence, recruitment may be facilitated by a long non-coding RNA *ANRIL* which is divergently transcribed from the INK4/ARF locus (Pasmant et al., 2011). It is important also to understand how this repressive barrier to senescence is lifted. Studies have shown that disruption of the histone demethylase, JMJ3D, prevents the removal of H3K27me3 during senescence induction and suppresses induction of p16^{INK4a} and p19^{ARF} (Barradas et al., 2009). These epigenetic regulators, both repressive and activating, convene on the *INK4/ARF* locus to provide stringent control over its expression ensuring a robust senescence induction.

Upregulation of the p16^{INK4a} is observed in tissues during natural aging (Burd et al., 2012; Herbig et al., 2006; Krishnamurthy et al., 2004; Ressler et al., 2006). As discussed previously,

no single stimulus appears to be responsible for senescence induction in aging, however various acute damage stimuli have been found to upregulate the *INK4/ARF* locus. These include oncogene overexpression, irradiation, telomere damage or oxidative stress (reviewed in (Gil and Peters, 2006; Kim and Sharpless, 2006)). In the case of OIS and Telomere-damage, p38 MAPK pathway has been shown to be essential for upregulation of the *INK4/ARF* locus (Bulavin et al., 2004; Deng et al., 2004; Iwasa et al., 2003; Kwong et al., 2009). Corroborating this, p38 inhibition bypasses senescence during ROS-mediated HSC decline and extends lifespan of HSCs in $ATM^{-/-}$ mice models of ataxia telangiectasia and in Werner syndrome fibroblasts (Ito et al., 2006). In addition, p38 MAPK has also been found to regulate the senescence secretome upstream of p53 and NF-κB (Freund et al., 2011). How though does p38 MAPK activity activate *INK4/ARF*? Whilst there is still debate on specific mediators of p38 MAPK downstream signaling, HBP1 is indicated as a potential candidate. HBP1 is a transcription factor known to be upregulated during OIS (Zhang et al., 2006), with its knockdown or overexpression able to bypass or induce senescence respectively, via regulation of $p16^{INK4a}$ expression (Li et al., 2010). Serine 401 on HBP1 is phosphorylated by p38 MAPK, capable of stabilizing the protein, providing a potential link between HBP1 and $p16^{INK4a}$ expression (Xiu et al., 2003). While specific isoforms of p38 can be activated irrespective of DNA damage status of the cell, downstream these same isoforms can also induce CHK1/2 and subsequently DDR pathways (Xu et al., 2014). In addition, MKK3/6, an upstream activator of p38 can also induce DDR through p38 mediated activation of PRAK and p53 (Xu et al., 2014).

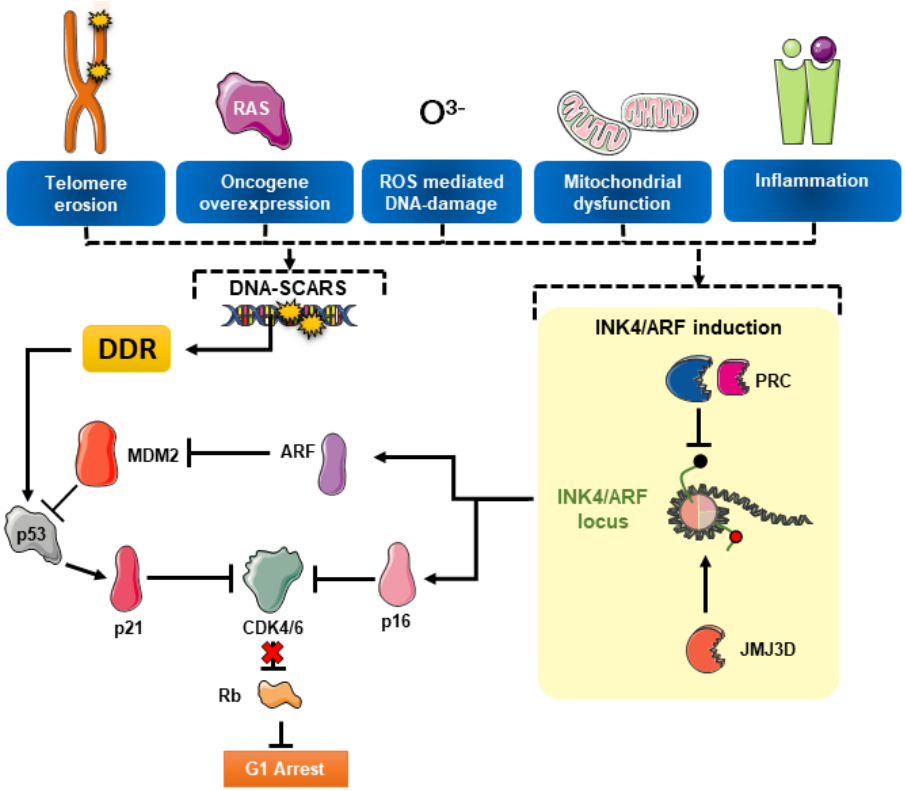

Figure 1.1. Regulatory pathways of senescence growth arrest.

Senescence enacts growth arrest through two signalling axis, p16^{INK4a}-Rb and p53-p21^{CIP1}, which in-turn inhibit CDK4/6. Both p16^{INK4a} – transcribed through derepression of the INK4/ARF locus - and p21^{CIP1} – transcribed by p53 - are activated in response to either constitutive DNA damage response (DDR) from DNA-SCARS or in response to cellular stress. (Adapted from McHugh et al., 2017)

1.3.2.1 Regulation of the senescence associated secretory phenotype (SASP)

The senescence program serves two major purposes. The first, discussed above is to enact a cell cycle arrest that limits the proliferation of potentially damaged cells. The second is to facilitate clearance of aforementioned cells and to contain potential dysfunction from damage. For the later, senescent cells secrete a complex milieu of factors referred to as the SASP. This phenomenon was first identified in oncogene induced senescence (Coppé et al., 2008) and is regulated by factors including G3BP1, p38, GATA4-NF-κB signaling, MLL1, C/EBPβ (Acosta et al., 2008; Capell et al., 2016; Chien et al., 2011; Freund et al., 2011; Kang et al.,

2015; Kuilman et al., 2008; Omer et al., 2020) and induction of DNA damage (Rodier et al., 2009) (see figure 1.2). Over 200 pro-inflammatory cytokines, chemokines, growth factors and proteases have been identified as components of the SASP (Coppé et al., 2010; Kuilman and Peeper, 2009).

The SASP has both beneficial and detrimental roles in human physiology (reviewed in (Coppé et al., 2010; Kuilman and Peeper, 2009). Senescent fibroblasts, for example can remodel the tumor microenvironment by secreting angiogenesis promoting VEGF and CCL5 (Coppe et al., 2006; Eyman et al., 2009), growth promoting GROα and Osteopontin (Haghnegahdar et al., 2000; Krtolica et al., 2001; Pazolli et al., 2009), as well as enhancing cancer cell motility via the secretion of Metalloproteinases (Liu and Hornsby, 2007) - all potentially pro-tumorigenic events. On the other hand, the SASP can potentially mediate fibrotic resolution, wound healing and embryonic patterning (Demaria et al., 2014; Krizhanovsky et al., 2008; Muñoz-Espín et al., 2013). SASP also facilitates tumor suppressive immunosurveillance through recruitment of macrophages, NK cells and CD4+ T cells (Xue et al., 2007). Recently, CCL2 secretion from senescent cells has been shown to play a role in immature myeloid cell recruitment and macrophage differentiation in hepatocellular carcinoma, essential for early immunosurveillance. Underscoring the dualistic nature of the SASP in cancer, this same recruitment can suppress the activity of NK cells and promotes tumor growth in established tumors (Eggert et al., 2016).

Fibrosis occurs, much like senescence, as a response to damage. Otherwise known as scarring, likelihood of pathological fibrosis accumulates with age. SASP components such as matrix metalloproteinases (MMPs) are key component of remodeling fibrotic plaques that may be beneficial in wound healing and liver fibrosis (Demaria et al., 2014; Krizhanovsky et al., 2008). Prevention of senescence has also been demonstrated to exacerbate liver fibrosis and as a result liver cirrhosis (Krizhanovsky et al., 2008), displaying how the SASP could be

beneficial in the context of fibrotic damage. Whilst the SASP itself may be anti-fibrotic, the presence of senescent cells in the context of lung and liver damage has been shown to be pro-fibrotic in some contexts (Ogrodnik et al., 2017; Schafer et al., 2017), obfuscating their relationship to one another.

The SASP can also reinforce senescence in an autocrine manner. CXCR2, the receptor of IL-8, GROα and other CXCL chemokines upregulated in senescence, enable p53 and C/EBPβ dependent feedback loops to reinforce senescence and the SASP in an autocrine manner (Acosta et al., 2008). Perhaps more interesting, senescent cells can spread their phenotype to surrounding cells via paracrine senescence. During OIS, several SASP components such as TGF-β, VEGF, CCL2, IL-1 and CCL20 are secreted and are capable of inducing senescence in co-cultured cells (Acosta et al., 2013; Coppé et al., 2008). Furthermore, factors such as TGF-β and IL-1 induce paracrine senescence partially through induction of oxidative stress and DNA damage (Hubackova et al., 2012). Paracrine senescence can also be observed in preneoplastic models *in vivo* (Acosta et al., 2013). The actual biological purpose of paracrine senescence is unknown, but it has been hypothesized as a form of tissue 'bet-hedging'. Where bet-hedging refers to tolerance of a detrimental cellular state for the purposes of enhancing or modifying responses to stress or damage. For example, tissues attempting to contain any potentially damaged or tumorigenic cells that may also be near the site of damage by inducing paracrine senescence.

The SASP is comprised of different modules. For example, overexpressing N1ICD increases juxtracrine Notch signaling and switches senescent cells to secreting a TGF-β enriched secretome (Hoare et al., 2016). This secretome is a result of N1ICD inhibition of C/EBPβ with N1ICD deletion enhancing paracrine senescence while inhibiting senescence surveillance *in vivo* (Hoare et al., 2016).. Notch signaling in senescence has also been shown also to mediate a pro-fibrotic phenotype in paracrine senescent cells (Teo et al., 2019). Inverse to

the TGFβ secretome, the pro-inflammatory arm of the SASP appears to be regulated by IL-1 signaling (Acosta et al., 2013). Here, IL-1α is sufficient to partially recapitulate the pro-inflammatory arm of the SASP *in vitro* (Acosta et al., 2013; Laberge et al., 2015). Moreover, inhibition of the NLRP3 inflammasome - that processes IL-1β, as well as knockdown of IL-1 receptor is able to blunt the SASP and its senescence transmitting ability (Acosta et al., 2013). IL-1α can also rescue suppression of the SASP that occurs with mTOR inhibition (Laberge et al., 2015).

In line with the potential roles of mTOR signaling, the detrimental inflammatory nature of the SASP and aging, mTOR inhibition downregulates the SASP via two mechanisms. The first is by reducing IL-1α translation (Laberge et al., 2015) and the second is by blocking phosphorylation and inhibition 4EBP1, an inhibitor of EIF4E translation initiation factor (Herranz et al., 2015). This latter reduces translation of MAPKAPK2 and subsequently reduces inhibition of ZFP36L1. This Zinc finger RNA-binding protein binds AU-rich elements found in the 3'-untranslated regions of mRNA transcripts such as IL-8, IL-1β and other SASP transcripts (Herranz et al., 2015).

Another post-transcriptional regulator of the SASP, identified through screening for genes suppressing OIS induction of IL6 and IL8 is the alternative splicing factor PTBP1 (Georgilis et al., 2018). Depletion of PTBP1 splicing factor resulted in increased exon inclusion and alternative splicing of several targets, among these, EXOC7 and SNX14 alternative splicing was found to mediate SASP production. EXOC7 is a core subunit of the exocyst complex involved in secretory vesicle trafficking, specifically in the tethering and fusion of vesicles to the plasma membrane (Wu and Guo, 2015). Less is known about the general function of SNX14, it is however a member of the sorting nexin family. Other members of this protein family are involved in intracellular trafficking (Lunn et al., 2007). The function of different isoforms of EXOC7 and SNX14 with respect to the SASP however remains to be understood.

SASP production therefore also appears to be dependent on alterations to splicing that occurs in senescent cells.

The SASP is also regulated at the epigenetic level. Inhibition of the chromatin remodeling proteins BRD4 and MLL1 prevents SASP induction (Capell et al., 2016; Tasdemir et al., 2016). In the case of BRD4, binding to acetylated H3K27 at enhancers and super-enhancers was shown to be essential for SASP induction (Tasdemir et al., 2016). With regards to MLL1, its inhibition blunts the SASP response. Surprisingly, this effect is mediated through a decrease in γH2Ax levels at SASP genes rather than deposition activating H3K4me3 as is reported for MLL in cancer (Capell et al., 2016). The effects of MLL1 were found to be due to decreased DDR and NF-κB induction through ATM signaling, suggesting MLL1 was important in mediating DDR in senescent cells (Capell et al., 2016). In addition to chromatin remodeling - formation of chromatin fragments in the cytoplasm of senescent cells is a key SASP inducer via the cGAS/STING pathway (Dou et al., 2017; Glück et al., 2017)

In addition, the SASP may be directly regulated through morphological changes in the Golgi apparatus (Narita et al., 2011). Here, expansion of the trans-Golgi facilitates the creation of the TOR-autophagy spatial cellular component or TASCC, facilitating production of SASP components such as IL6 and IL8 (Narita et al., 2011). The trans-Golgi has also been hypothesised to facilitate high SASP production indirectly through formation of the early endosome and lysosome biogenesis, both essential steps in the autophagic pathway (Razi et al., 2009). Macroautophagic processes provide a key way of recycling cellular components and sustaining the metabolic functions of a cell (Ravikumar et al., 2009). It has been hypothesised that the upregulation of autophagy during senescence is to facilitate production of the SASP (Gewirtz, 2013). In proliferating cells, autophagy – in opposition to its potential role in SASP production - supresses the upregulation of GATA4, a key SASP transcription factor, through SQSTM1/p62 mediated degradation (Kang et al., 2015). This interaction

between GATA4 and SQSTM1/p62 appears to be absent during senescence despite the latter's increased levels. It has been hypothesised this is due to ATM/ATR mediated phosphorylation of SQSTM1 or that GATA4 is simply outcompeted for binding by the milieu of other proteins. in the cell.

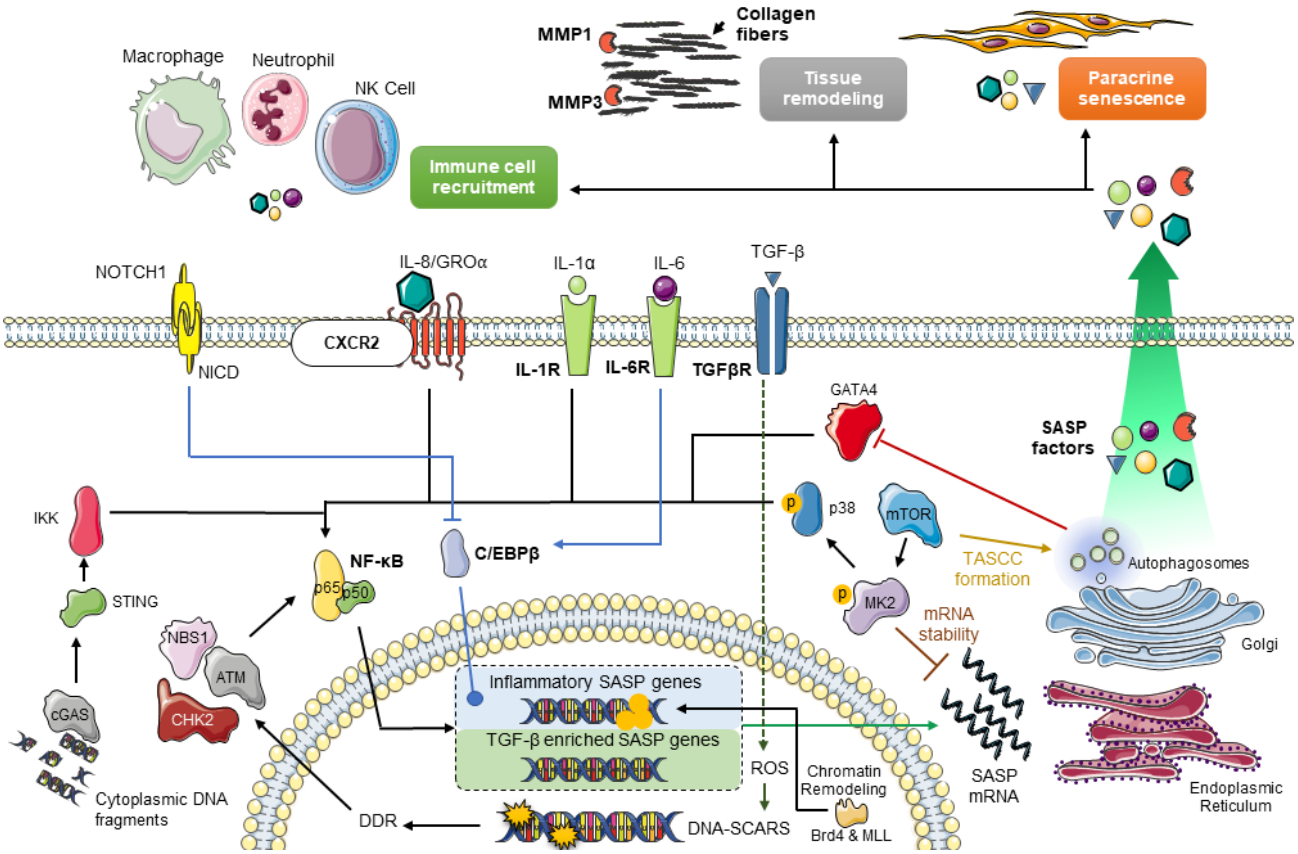

Figure 1.2. SASP regulatory pathways

Summary of major regulatory pathways of the SASP. Unresolved DNA damage response facilitates SASP production intrinsically through activation of cGAS-STING and DNA damage response proteins mediated activity of NF-κB. The Senescence phenotype - including the SASP - is reinforced by a multitude of autocrine signalling pathways. Secretion of the SASP into extracellular matrix is capable of inducing paracrine senescence, immune cell recruitment and tissue remodelling.

1.3.3 Epigenetic alteration of senescent cells

Senescent cells require extensive changes to the transcriptome and proteome to support cell cycle arrest and extracellular signaling. For this new state to be sustained there must be drastic changes in gene regulation at the epigenetic level. The first evidence to support this

came from observations of senescence associated heterochromatic foci (SAHFs) – tightly packed DNA visible in the nuclei of DAPI stained senescent cells (Narita et al., 2003). They are hypoacetylated, have a H3K9me3 core, surrounded by H3K27me3 histone modifications and are enriched for macroH2A and heterochromatin protein 1 (HP1) (Narita et al., 2003; Zhang et al., 2005). The function of SAHF formation in senescence appears to be the repression of genes related to proliferation, such as the MDM2 and CDK4 (Narita et al., 2003, 2006; Zhang et al., 2005) mediated through the High mobility group (HMG) A proteins – key mediators of SAHF formation (Narita et al., 2006). SASP gene expression due to exclusion from heterochromatic regions also occurs during SAHF formation and is mediated by HMG group B proteins (Aird et al., 2016) - highlighting that SAHF formation does not only coincide with repression. SAHF also depends on the histone chaperones HIRA and ASF1a (Zhang et al., 2005) as well as the chromatin remodelers BRG1 and p400 (Chan et al., 2005; Tu et al., 2013).

SAHFs can be found in oncogene, replicative and chemotherapy induced senescence (Kosar et al., 2011; Kovatcheva et al., 2017; Narita et al., 2003) with evidence extending to *in vivo* aging and senescence (Denchi et al., 2005; Herbig et al., 2006; Jeyapalan et al., 2007; Kreiling et al., 2011; Webster et al., 2015). However, they are seldom found in fibroblasts isolated from patients with Hutchinson-Gilford progeria syndrome (HGPS) and select senescence modalities do not display strong SAHF formation (Chandra and Kirschner, 2016; Kosar et al., 2011). Chromatin conformation capture studies show weaker SAHF compaction in cells undergoing replicative senescence when compared with oncogene-induced senescence (Chandra et al., 2012; Sati et al., 2020), further highlighting the heterogeneity of SAHFs and raising questions as to the nature and necessity of the SAHF in senescence.

As discussed earlier, the *INK4/ARF* locus is subjected to epigenetic regulation with demarcation by PRC complexes in healthy cells for repression (Bracken et al., 2007). Whilst

formation of the SAHF does lead to enrichment of H3K27me3 within SAHFs and depletion of H3K27me3 at some genes and enhancers (Narita et al., 2003; Sadaie et al., 2013; Shah et al., 2013), it does not appear to be the result of *de novo* heterochromatin demarcation. Rather SAHF results from redistribution of heterochromatin (Chandra et al., 2012). Through study of the chromatin spatial organization of senescent cells, it has been suggested that SAHFs are instead generated through reorganization of local lamin-associated heterochromatin domains (LADs) located at the nuclear membrane (Sadaie et al., 2013). Loss of nuclear lamin B1 is considered a marker of senescence (Dreesen et al., 2013; Freund et al., 2012; Shimi et al., 2011) and may explain the release of heterochromatin domains from the periphery of the nucleus to form SAHFs. Lamin B1 loss can pre-mature senescence (Dreesen et al., 2013; Shimi et al., 2011). Further complicating the attribution of a causal role of lamin B1 in inducing senescence, it's overexpression only delays senescence rather than prevents it (Dreesen et al., 2013). Lamin B1 loss and the formation of SAHF does however result in modification of the senescence phenotype (Aird et al., 2016; Dreesen et al., 2013; Sati et al., 2020), indicating that nuclear reorganization during senescence may be primarily a senescence reinforcement event.

Sati et al. examined the differences in chromatin spatial organization across different senescent modalities that potentially explain the lack of ubiquity in SAHF appearance (Sati et al., 2020). It was found that the strong compartmentalization and decompaction of heterochromatin within the SAHFs of cells undergoing OIS was dependent on demethylation mediated expression of HMGA2. This decompaction resulted in enhanced inter-heterochromatin domain interactions and compartmentalization. It is not known however what functional relevance this differential organization in OIS has compared to the weak compartmentalization and compaction of heterochromatin domains observed during

replicative senescence. These observations however may explain the absence of strong SAHF formation in HGPS fibroblasts.

Pericentromeric chromatin decondensation has been shown to also occur during senescence (De Cecco et al., 2013; Zhang et al., 2007b). These regions are rich in DNA satellite repeats and their decompaction is termed senescence-associated distention of satellites (SADS). SADS formation occurs prior to SAHF formation and is driven by hypomethylation and expression of satellite repeats that occurs during senescence (Cruickshanks et al., 2013; Swanson et al., 2013). Recently, expression of satellite DNA and its decompaction, specifically of L1 retrotransposable elements, has been shown to drive interferon signaling and the SASP via the generation of cytoplasmic DNA (De Cecco et al., 2019). SADS therefore appear to have a functional role in reinforcing the SASP. Loss of LADs also is able to contribute to SASP induction via a similar mechanism in which compromised nuclear membrane integrity results in cytoplasmic chromatin fragments (CCFs) (Dou et al., 2017; Glück et al., 2017; Takahashi et al., 2018). Intracellular DNA sensing pathways such as cGAS-STING can detect these chromatin fragments to induce the SASP.

Superenhancers (SE) are key regulators of the senescence transcriptome (Sen et al., 2019; Tasdemir et al., 2016). Super enhancers are large regions of H3K27ac, H3K4me1 and Mediator complex (Med1) enrichment, that can regulate many genes either proximal or distal to the position of the SE (Pott and Lieb, 2015). The presence of the BET protein, BRD4, at a subset of senescence-associated SEs regulates the expression of many SASP genes including IL6 & IL-1α (Tasdemir et al., 2016). BRD4 is known to bind NF-κB binding sites at SEs and mediate long range interactions with promoters, Med1 and transcription elongation factors complexes such as p-TEFb, to enhance gene expression (Brown et al., 2014), providing a possible mechanism for BRD4 regulation of the SASP. The accumulation &

relocalization of macroH2A1 deposition (Zhang et al., 2007b) and accumulation of histone variant H2A.J (Contrepois et al., 2017), are also key to induction of the SASP.

The establishment of the senescence associated super enhancers is primarily driven through the binding of the histone acetyltransferase p300 (Sen et al., 2019). Knockdown of p300 delays onset of oncogene induced senescence and replicative senescence. Interestingly, super enhancers appear modality specific, with OIS SEs proximal to SASP genes and replicative senescence SE proximal to genes involved in metabolic dysfunction (Sen et al., 2019). Potentially this highlights that different epigenetic reprogramming during senescent programs are specialized to the risk they pose with oncogene overexpressing cells needing to be rapidly targeted for immune cell clearance.

The modification of the chromatin landscape is not the only epigenetic modification in senescent cells. A global loss in methylation and hypermethylation promoter CpG islands is a hallmark epigenetic characteristic of cancer with tumor suppressor genes falling victim to these modifications (Michalak et al., 2019). Similar methylation characteristics were also observed in senescent cells and might precede the methylation status of cancers (Cruickshanks et al., 2013). Unlike cancer hypermethylation, which largely occurs stochastically at the promoters of genes involved in development, senescent cells have programmed changes in their methylome at the CpGIs of metabolic and biosynthesis genes (Xie et al., 2018). It remains unclear whether re-distribution of methylation is required for tumorigenesis and through what mechanism is it enacted in cell escaping senescence.

1.3.4 Metabolic reprogramming of senescent cells

Senescent cells undergo extensive metabolic changes, with alterations to mitochondria and autophagy machinery being chief among them. While senescence was initially thought of as

a ‘dead state’ of the cell, senescent cells are remarkably metabolically active, with the SASP placing unique metabolic requirements on the cell. One of the first signs of this metabolic nature of senescent cells was the discovery of the now considered universal senescent marker - increased activity of β-galactosidase (Dimri et al., 1995; Sharpless and Sherr, 2015). This senescent associated β-Galactosidase activity, detectable in low pH environments, reflects its increased expression of the lysosomal enzyme GLB1 (Lee et al., 2006). Despite its increased expression, GLB1 is not required for induction of replicative senescence (Lee et al., 2006) raising questions as to its function during senescence. The increased activity of this enzyme correlates with increased autophagic flux of senescent cells (Gerland et al., 2003; Lee et al., 2006). Autophagy is a mechanism through which organelles, protein and cellular debris are broken down through a stepwise process (Glick et al., 2010). This involves the recognition of cargo to be degraded followed by envelopment by a membrane called the phagophore – bound by class III PI3K - in a process called nucleation (Glick et al., 2010). When a phagophore membrane envelops its cargo, this new vesicle – termed the autophagosome undergoes fusion with low pH, proteolytic enzyme containing vesicles called lysosomes. From here the protein is broken down and its contents either repurposed for other metabolic processes in the cell or excreted. Increased levels of autophagy have been observed in senescent cells (Gerland et al., 2003; Gewirtz, 2013; Young et al., 2009), with increased expression of autophagy genes such as the ATG and ULK families alongside increased lysosome acidification and formation (Kurz et al., 2000; Lee et al., 2006). The interplay of senescence and autophagy is complex. As discussed previously, SASP production is dependent on increased autophagy (Narita et al., 2011), conversely however inhibition of autophagy can induce senescence (García-Prat et al., 2016).

Another key metabolic alteration of senescent cells closely linked to autophagic pathways is the increased production of extracellular vesicles (EVs) observed during senescence

(Borghesan et al., 2019; Fafián-Labora et al., 2020; Lehmann et al., 2008; Takasugi et al., 2017). EVs are categorized based on their size and origin. Exosomes are small vesicles generated from endosome budding and are released from the cell through fusion with multi vesicular bodies (MVBs) at the plasma membrane (Colombo et al., 2014). Microvesicles on the other hand, are larger and produced by budding of the plasma membrane. EVs are of particular interest due to their contents. This includes protein, lipids and even nucleic acids such as mtDNA, miRNA and mRNA (Colombo et al., 2014; Korkut et al., 2009; Valadi et al., 2007) potentially providing another mode of intracellular communication in senescence independent of the SASP. In the context of senescence, small extracellular vesicles have been shown to mediate paracrine senescence (Borghesan et al., 2019) and through loss glutathione-S-transferase activity, to mediate systemic aging in mice (Fafián-Labora et al., 2020).

Further underscoring the importance of metabolic processes in senescence, mitochondrial dysfunction is able to induce a unique form of senescence called MiDAS (mitochondrial dysfunction-associated senescence), complete with its own SASP (Wiley et al., 2016). Disruption of mitochondria in the context of replicative senescence delays onset of senescence phenotypes, further illustrating the interconnectedness of the two (Correia-Melo et al., 2016). Replicative senescent cells undergo a metabolic shift to a more glycolytic state resembling that of the Warburg effect in cancer (Hsu and Sabatini, 2008). Both metabolic profiling and measurements of ADP/AMP : ATP ratios showing this shift to a less energetic state (Wiley and Campisi, 2016; Zwerschke et al., 2003). This also extends to senescence conditioned media (James et al., 2015). A number of genes related to metabolism are altered during p53 expression, such as glucose transporters (Kaplon et al., 2013; Schwartzenberg-Bar-Yoseph et al., 2004; Wiley and Campisi, 2016) and could partially explain the increase of glycolysis during senescence. Oncogene induced senescence displays key alterations in

pyruvate metabolism. Pyruvate dehydrogenase (PDH) has been shown to be a key mediator of oncogene induced senescence and metabolic changes therein (Kaplon et al., 2013). Upregulation of PDH occurs via both downregulation of PDK1 - a PDH inhibitor – and upregulation of PDH-activating enzyme PDP2. This results in enhanced linkage between glycolysis and the TCA cycle resulting in increased oxygen consumption and ROS production. There is also the possibility that the effects of pyruvate metabolism are supraphysiological due to atmospheric oxygen levels being significantly higher than those found in tissues and has been found to alter senescence induction (Parrinello et al., 2003). The coupling of increased glycolysis with increased oxidative phosphorylation in OIS stands juxtaposition to replicative senescence highlighting senescence modality specific alterations to metabolism. Senescence is also marked by significant changes fatty acid metabolism (Quijano et al., 2012) and nucleotide synthesis (Aird et al., 2013, 2015).

In addition to alterations of metabolic pathways, the mitochondrial network itself appears to be altered in senescence (Chapman et al., 2019). These networks become hyperfused in senescent cells (Correia-Melo et al., 2016) in a manner dependent on mitochondrial biogenesis. Knockout of the mitochondrial biogenesis regulator PGC-1β rescues this phenotype. Removal of defective mitochondria through mitophagy is essential to maintaining normal metabolic homeostasis. Several pathways regulating mitophagy are downregulated in a p53-dependent manner (Ahmad et al., 2015) and senescent cells additionally downregulate mitophagy regulators such as GSNOR (Rizza et al., 2018). This enhanced mitochondrial biogenesis and impaired mitophagy may explain the accumulation of defective mitochondria in senescence. These changes to mitochondria during senescence appear to directly contribute to the two primary senescence phenotypes via oxidative stress; the growth arrest and the SASP (Correia-Melo et al., 2016; Moiseeva et al., 2009; Wiley et al., 2016).

1.4 Senescence and cancer

1.4.1 Paradoxical roles of senescence in cancer

Standing juxtaposition to the characteristic stable growth arrest during senescence, cancer is earmarked by its absence of proliferative limits. Being first noted as an “insensitivity to anti-growth signals”, the evasion of the senescence growth arrest is a hallmark feature of cancer (Hanahan and Weinberg, 2011). Our understanding of the role for senescence in cancer has evolved, with increasing evidence suggesting a complex interplay with other cancer hallmarks such as immune evasion (Eggert et al., 2016), tumor promoting inflammation (Coppé et al., 2010), genome instability (De Cecco et al., 2019) and invasion and metastasis (Demaria et al., 2017; Luo et al., 2016; Szczerba et al., 2019). This has originated from an increased understanding of the non-autonomous aspects of senescent cells where senescence can play paradoxical roles in promoting and suppressing tumor growth.

With Hayflick’s replicative limit discovery, it didn’t take long for a hypothesis to emerge that this limit could play a key role in limiting tumorigenesis. The subsequent demonstration that Hayflick’s limit was a result of critical shortening of telomeres (Allsopp and Harley, 1995) and that further shortening results in chromosomal instability suggested that cancer cells must have some way of bypassing telomere shortening (Kim et al., 1994; Shay and Bacchetti, 1997). Supporting this, mice that are deficient in telomere lengthening machinery have reduced spontaneous tumorigenesis (Blasco et al., 1997). In addition, a majority of cancers display telomerase activity, normally switched off in non-embryonic tissues (Shay, 2016; Shay and Bacchetti, 1997). In those 15% of tumors that do not express telomerase, alterative lengthening of telomeres (ALT) mechanisms were identified (Reviewed in (Cesare and

Reddel, 2010) suggesting that bypass of telomere lengthening and thereby senescence was a prerequisite for tumor growth.

Whilst lengthening of telomeres is required for tumor proliferation - to both evade senescence and prevent chromosomal fusion - the senescence program provides additional barriers to transformation. This most notable example - induction of senescence through oncogene activation. OIS was first identified in vitro with constitutive overexpression of HRAS (Serrano et al., 1997) and subsequently validated with other oncogenes (see *'1.2.2 Oncogene-induced senescence'*). Initially it appeared paradoxical that mitogenic signals trigger an opposing effect in the form of senescence. Further confounding this, the absence of senescent cells in single-copy mutant KRAS mouse tumors and MEFs (Tuveson et al., 2004), raised the possibility that the in vitro models of OIS were supraphysiological – requiring excessive expression of oncogenes.

Melanocytic nevi are benign tumors often positive for mutations in BRAF that result in hyperactivity of the MAP kinase protein, most notably the V600E mutation (Pollock and Meltzer, 2002). These nevi are positive for classical senescence markers and do not have significant telomere attrition (Michaloglou et al., 2005). Subsequent demonstration of senescence markers in pre-neoplastic lesions and their ability to limit tumorigenesis in the context of lung adenocarcinomas, prostate tumors and lymphomas (Dankort et al., 2007)(Collado et al., 2005; Dankort et al., 2009), proved that oncogene-induced senescence was physiologically relevant to cancer. Furthermore, work by (Dankort et al., 2007) and (Collado et al., 2005) showed that malignant but not benign transformations involving oncogenes, lose expression of key senescence markers - further supporting OIS as a barrier to tumor formation. This evidence also extends to human pre-neoplastic lesions such as prostate neoplasia's (Gray-Schopfer et al., 2006) and colon adenomas (Bartkova et al., 2006).

Oncogene induced senescence is now understood as barrier in tumorigenesis (Hanahan and Weinberg, 2011), with many pre-neoplastic lesions undergoing transformation through mutation of senescence mediators such as $p16^{INK4a}$ and p53 (Dankort et al., 2007). Further supporting this, monitoring expression of $p16^{INK4a}$ using a luciferase reporter highlights focal upregulation of $p16^{INK4a}$ in early stages of tumorigenesis (Burd et al., 2012). Additionally, removal of $p16^{INK4a}$-positive cells using a genetic ablation systems does decrease tumorigenesis in mice (Baker et al., 2016).

The inflammatory nature of tumor stroma can have significant implications for prognosis – with it in some contexts fueling tumor growth and in others suppressing it (reviewed in (Coppé et al., 2010; Kuilman and Peeper, 2009)). The effect of the senescence program on tumors extends beyond the initial stages of transformation, with the SASP modulating tumorigenesis at multiple stages. Immune surveillance is a key mechanism used in the body to suppress tumor growth and something that cancer must evade to proliferate & metastasize. This is supported by the numerous tumor susceptible immunodeficient mouse models (Billiau et al., 1988; Takeda et al., 2002)(reviewed in (Zitvogel et al., 2006)), the observation of tumor infiltrating lymphocytes (TILs) and that inhibition of immune checkpoint proteins in these tumors is an efficacious cancer therapy (reviewed in (Waldman et al., 2020). One of the first demonstrations that the SASP may facilitate immunosurveillance of tumors was in models of HCC, where reactivation of p53 led to senescence induction and tumor regression through recruitment of the innate immune system (Xue et al., 2007). Subsequently, pre-neoplastic cells in the liver undergoing OIS were shown to be suppressed through the SASP mediated recruitment of adaptive CD4+ T cells and macrophages (Kang et al., 2011). Despite the tumor immunosuppressive nature of the SASP's interaction with immune cell recruitment this can also be detrimental in established tumors. Liver OIS results in recruitment of CCR2+ myeloid cells which then undergo maturation and facilitate suppression of HCC development (Eggert

et al., 2016). However, in livers that have formed HCC that suppress myeloid cell maturation, the immature myeloid derived suppressor cells (iMDSCs) recruited by senescent HsCs instead promote tumor growth. In this context iMDSCs suppress the activity of natural killer cells and fail to activate macrophages required for immune clearance (Eggert et al., 2016). SASP mediated immune cell recruitment may also help drive metastases formation, as circulating tumor cells (CTCs) retain their proliferative capacity through their interaction with white blood cells (WBCs) and neutrophils (Szczerba et al., 2019). This interaction between WBC-CTCs depends on G-CSF and VCAM1 secretion, as well as WBC presence in primary tumor site – both events that can be triggered by the presence of senescent cells. Further evidence of the pro-metastatic nature of senescent cells was highlighted from studies of chemotherapy treated mice (Demaria et al., 2017). Here, senescence increased the incidence of metastases in mice. It was hypothesized that the pro-inflammatory SASP could enhance tumor seeding by creating a pro-tumorigenic niche with secretion of factors such as VEGF (Demaria et al., 2017). Conversely however, pro-metastatic processes such as endothelial to mesenchymal transition counteracts senescence (EMT) are suppressed in senescent cells (Ansieau et al., 2008). Increased expression of Twist1 and Twist2 was shown not only induce EMT but bypasses OIS through suppression of p53 and Rb pathways, showing that senescence can both enhance and suppress metastases.

The SASPs ability to trigger immune clearance of tumors is not limited to the early stages of tumorigenesis. Although PD-1 and CTLA inhibitor immunotherapies have proved efficacious in treatment of some cancers, they have limited effect in tumors that do not have high levels of TILs (Pardoll, 2012) and have minimal effect when used with cell cycle inhibitors such as Palbociclib (Ruscetti et al., 2018). The inability of CDK4/6 inhibitors to trigger immune cell clearance, is thought to be due to the largely absent pro-inflammatory SASP in this senescence modality. Induction of the SASP in palbociclib treated cells with the MEK inhibitor

Trametinib, enhanced the efficacy of immune checkpoint blockade and increase NK cell activity in lung adenocarcinomas models (Ruscetti et al., 2018). Additionally, induction of the SASP in pancreatic ductal adenocarcinoma (PDAC) mouse models again improved the efficacy of immune checkpoint blockade but also demonstrated enhanced T-cell infiltration mediated through vascular remodeling (Ruscetti et al., 2020). These studies highlight how the SASP induces immunosurveillance of established tumors.

Different SASP components can have either proliferative and anti-proliferative effects (Coppé et al., 2010). The ability of SASP factors such as IL6 & IL8 as well as IGFBP7 to not only reinforce senescence in an autocrine manner but induce paracrine senescence in surrounding cells extends to suppressing tumorigenesis (Acosta et al., 2013; Wajapeyee et al., 2008). Models where KRAS driven pancreatic cancers induce OIS display accelerated growth when TGFBR1 or CXCR2 signaling is blocked (Acosta et al., 2013). Similarly, suppression of IL-1α signaling, in the context of PTEN mutant prostate cancer, not only prevents induction of senescence in surrounding epithelial stroma but accelerates tumor growth (Laberge et al., 2015).

On the one hand, it has been clearly demonstrated that SASP can be tumor-suppressive through induction of paracrine senescence and immunosurveillance. However, conversely, proliferative SASP factors can fuel tumor growth. Pro-inflammatory tumor microenvironments are also known to be poor prognostic markers in various cancers. This raises the question; can the senescence program be targeted in treatment of cancers and does its dual roles necessitate a more nuanced approach?

1.4.2 Targeting senescence in cancer

The current first line of treatment for most patients with cancer is treatment with high doses of chemotherapy (Chabner and Roberts, 2005). Chemotherapy induces the DDR in tumours resulting in the engagement of pro-apoptotic or senescence pathways, to cause tumour regression. Therefore, it could be argued that pro-senescence therapies have been a mainstay of cancer therapy for decades. The induction of senescence in surrounding tumour stroma when using chemotherapy however, as discussed above, may have drawbacks in already established tumours (Coppé et al., 2010; Eggert et al., 2016; Kuilman and Peeper, 2009). In addition the off-target effects on healthy cells of chemotherapy leave much to be desired (Demaria et al., 2017). Given that senescence can both have pro and anti-tumorigenic properties, could re-engagement of senescence mediators or modulation of its phenotypes be a more nuanced and viable approach for cancer therapy?

One such approach is the engagement of senescence using drug inhibitors of cyclin dependent kinase (reviewed in (Asghar et al., 2015)). Targeting downstream of the p53 and $p16^{INK4a}$, these drugs negate the issue of resistance due to mutations in these genes that frequently occur in cancer. CDK4/6 inhibitors (CDK4/6i) such as palbociclib have proven highly efficacious in clinic (Flaherty et al., 2012; Goldman et al., 2014; Slamon et al., 2010). Moreover, CDK4/6i confer a permanent arrest in some cancers, with induction of oxidative stress mediating upregulation of DDR (Klein et al., 2018). Senescence caused by CDK4/6 inhibition, has a minimal pro-inflammatory secretome, limiting its efficacy due to reduced immunosurveillance (Ruscetti et al., 2018). Combination of CDK4/6i with MEK inhibitors such as Trametinib (Ruscetti et al., 2018), greatly increases its inflammatory secretome and tumour reduction, opening the possibility of further combinatorial therapies to enhance SASP.

CDK4/6 inhibitors may require a more nuanced approach when used in a combinatorial manner in clinic. Application of CDK4/6i after treatment with chemotherapies such as Taxol

enhances of tumour regression (Salvador-Barbero et al., 2020), due to inhibition of DNA repair. Given that many cancers rely on DNA repair machinery for recovery from chemotherapy this suggests combining chemotherapy with CDK4/6 inhibitors. One potential drawback of combinatorial therapy with CDK4/6i is that many chemotherapies result in DNA damage as due to cell cycle progression in the presence of mitotic poisons. Concordantly, it was found that in some instances if CDK4/6i treatment proceeded chemotherapy, response was impaired (Salvador-Barbero et al., 2020). Therefore, whilst combination with CDK4/6i could improve the effectiveness of chemotherapy, careful consideration must be taken in understanding the effects of each treatment.

Another senescence targeted cancer therapy approach that has been hypothesised is the 'senomorphic' approach (Myrianthopoulos et al., 2019). This is the idea that by modulating specific phenotypes of senescence you may negate some of their negative effects in cancers. Targeting the alternative splicing factor PTBP1 results in suppression of the pro-inflammatory SASP but maintenance of the senescence growth arrest (Georgilis et al., 2018). In the context of liver cancer this resulted in decreased tumour growth, thereby providing validation of a senomorphic therapy approach. Targeting of the senescence program in the context of cancer is in its relative infancy with only a handful of drugs currently in clinical use. The robust understanding of senescence regulation could provide opportunity for further development of this approach in cancer therapy.

1.5 Beneficial aspects of senescence

In addition to its tumour suppressive effect, senescence induction has benefits beneficial in wound healing and embryogenesis (Demaria et al., 2014; Muñoz-Espín et al., 2013; Storer et al., 2013).

Apoptosis, another programmed cellular response to stress, has been shown to be essential in mediating morphological changes during embryogenesis and limb bud formation (Suzanne and Steller, 2013). However, whilst the removal of cells via programmed cell death would be an obvious function required for segmentation of developing limbs, a potential role for senescence in embryogenesis is not as apparent. Despite this, studies have shown that defects in senescence pathways can induce developmental defects in embryos (Muñoz-Espín et al., 2013; Storer et al., 2013). In this context, programmed developmental senescence appears to serve two functions, protection of cells from apoptosis and through production of a SASP-like secretome developmental pattering, akin to the function of a developmental organizer (Storer et al., 2013). Unlike ageing or cancer related senescence, developmental senescence is not triggered by DNA damage. Induction, of $p21^{CIP1}$, during developmental senescence is the result of paracrine signalling from surrounding stroma.

The process of wound healing progresses sequentially through a series of steps that involve inflammation and tissue remodelling (Telgenhoff and Shroot, 2005). Should this process not proceed in a timely manner or be interrupted, scarification of the wound can result. Removal of senescent cells from wounds using a genetic ablation system significantly impairs wound healing (Demaria et al., 2014). Senescent cells are present in wounds and were associated with wound closure and limit fibrosis (Kim et al., 2013b). The beneficial effect of senescence on wound healing was due, in part, due to secretion of PDGF-AA, that induces myofibroblast differentiation (Demaria et al., 2014). There may also be effects on remodelling of tissue due to secretion of other SASP factors such as MMPs. These beneficial aspects of senescence potentially explain the strong evolutionary conservation of the senescence secretome.

1.6 Senescence in aging and disease

1.6.1 The Aging phenotype and senescence

Aging is a process of functional decline. In mammals, aging emerges heterogeneously across multiple organ systems - eventually leading to an inability to respond appropriately to stress and maintain a physiological baseline due to tissue dysfunction. Whilst both environmental and genetic variation between individuals makes aging difficult to examine, there are several traits of aging that have emerged. These attributes of aging mediate their effects on multiple molecular pathways ranging from nutrient to inflammatory signaling that eventually disrupt the activity of a cell (reviewed in (López-Otín et al., 2013)) (see Figure 1.3). In several instances of this theatre of decline senescence can be found.

Somatic stem cells, such as hematopoietic stem cells (HSCs), facilitate the renewal of some tissues throughout the body. With aging, the functionality of these stem cells declines. This is demonstrated as HSCs have decreased success rate of transplantation when isolated from elderly patients (Anderlini et al., 1997; Kollman et al., 2001). HSC decline correlates with increased numbers of senescent cells in the HSC niche and results in a functional decline in immunity (Geiger and Van Zant, 2002; Sudo et al., 2000), with depletion of naïve B and T cells (Linton and Dorshkind, 2004; Miller and Allman, 2003; Min et al., 2005) and impaired NK cell activity (Mocchegiani and Malavolta, 2004). Ageing stem cell decline is not only limited to high turnover tissues. Neural stem cells (NSCs) experience a reduction in neurogenic capacity with age also (Kuhn et al., 1996; Maslov et al., 2004). Complementing this, aged mice display a reduction in NSC numbers (Maslov et al., 2004), coinciding with an increase in senescence markers (Molofsky et al., 2006). Age is also associated with increased frailty as exemplified by increased sarcopenia, cachexia, osteoporosis and osteoarthritis (Fried et al., 2001). In accordance with these phenotypes, satellite cells (Lavasani et al., 2012; Shefer et al., 2006), chondrocytes (Loeser, 2009; Price et al., 2002),

adipocytes (Graja and Schulz, 2015; Tchkonia et al., 2010), osteoclasts (Chung et al., 2014) along with their parent mesenchymal stem cells (MSCs) (Raggi and Berardi, 2012), have reduced self-renewal capacity and senescence markers resulting in a reduced ability to withstand damage. Stem cell exhaustion provides one of the more material links between senescence and the aging process, but senescence is a complex phenotype interacting with aging at multiple levels.

Chronic low-level inflammation complicates factor the pathology of several diseases where risk increases with age (Franceschi and Campisi, 2014; López-Otín et al., 2013). Such that inflammatory markers such as IL-1 and IL-6 can act as prognostic markers for diseases such as type II diabetes (Dandona et al., 2004), atherosclerosis (Libby, 2002) and declining stem cell functionality (Doles et al., 2012; Pietras et al., 2016). One of the major extrinsic effects of senescent cells is inflammation (Coppé et al., 2010), As senescent cells accumulate with age and their clearance can reduce inflammation, suggesting an association between the two (Baker et al., 2016).

Aged individuals display multiple defects in metabolic function that can be observed through both systemic changes with altered insulin signaling (Fink et al., 1983) and through mitochondria with increased oxidative stress and reduced mitochondrial biogenesis (reviewed in (Sun et al., 2016)). Pancreatic islet cells that produce insulin show increased numbers of cells with defective insulin response during age (De Tata, 2014) and show accumulation of senescence cells (Krishnamurthy et al., 2006), a possible major contributor to diabetes risk in over 60s. As for Oxidative stress - a marker of breakdown in the respiratory chain and mitochondrial dysfunction is a major inducer of senescence (Chen et al., 1995; Salama et al., 2014). Senescent cells may also have decreased levels of mitophagy (Ahmad et al., 2015; Correia-Melo et al., 2016; Manzella et al., 2018), resulting in an ‘old’ defective mitochondrial network that may cause metabolic dysfunction. It remains unclear however,

whether some of the alterations to mitochondria during senescence is due to alterations in mitophagy, biogenesis or senescence specific metabolites.

Age is one of the largest risk factors for diseases (Niccoli and Partridge, 2012) such as cardiovascular disease (North and Sinclair, 2012), dementia (Querfurth and LaFerla, 2010), osteoporosis and osteoarthritis (Raisz, 1988), cancer (de Magalhães, 2013), type II diabetes (Gunasekaran and Gannon, 2011) and idiopathic pulmonary fibrosis (Nalysnyk et al., 2012) and glaucoma (McMonnies, 2017). Therefore, understanding the etiology of aging and how it links with its correlate, senescence, will hopefully open a window into these complex diseases that have remained resistant to therapeutic advancement.

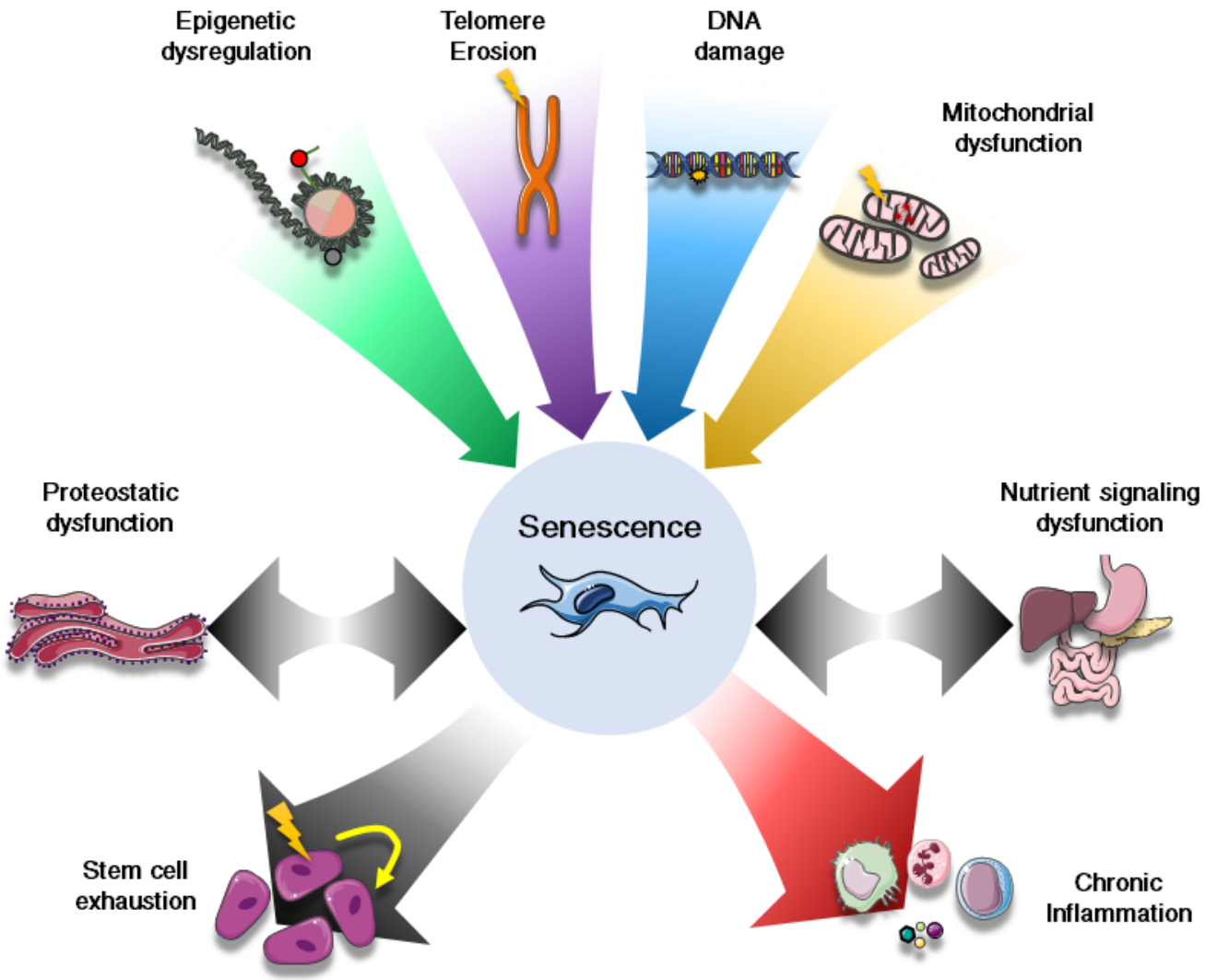

Figure 1.3. Senescence and the aging phenotype.

Aging is driven by several damage stimuli which are primarily telomere shortening, DNA damage, oxidative stress and aberrant epigenetic regulation all of which have been found to induce senescence. The senescence phenotype itself mediates and interacts with several hallmarks of aging including metabolic/proteostatic dysfunction, stem cell exhaustion and chronic inflammation. Adapted from (McHugh et al. 2017 & López-Otín et al. 2013)

1.6.2 Linking senescence with aging pathologies

Multiple lines of evidence now show that expression of the *INK4/ARF* locus correlates with aging in tissues and high levels of $p16^{INK4a}$ (Hudgins et al., 2018; Krishnamurthy et al., 2004) and can act as a prognostic marker for some age-related diseases such as idiopathic pulmonary fibrosis and glomerulosclerosis (Lomas et al., 2012; Melk et al., 2004). Genomic variants at this locus identified in GWAS studies have also been shown to be major risk factors for atherosclerosis, stroke and diabetes (Jeck et al., 2012). In addition, disruption of

p16^{INK4a}, which is increased in hematopoietic stem cells of aged individuals age, mitigates functional decline and loss of proliferation in a transplant setting (Janzen et al., 2006). p16^{INK4a} expression is also increased in aged tissues such as in fat tissue (Baker et al., 2016; Xu et al., 2015a), the islet of Langerhans (Helman et al., 2016) and the renal cortex (Melk et al., 2004) among others (Krishnamurthy et al., 2004). One could surmise from these studies that *INK4/ARF* derepression is only detrimental in aging. However increased gene dosage of *INK4/ARF* in mice does not result in a reduced lifespan (Matheu et al., 2009). The life shortening aspects of p16^{INK4a} overexpression may be outweighed by the clear tumor suppressive benefits (Sharpless et al., 2001), with 3-fold reduction in tumor incidence (Matheu et al., 2009). *In vivo,* knockout of Ku80$^{-/-}$, mTR$^{-/-}$ and Zmpste24$^{-/-}$ produce a progeria phenotype, some of these can be abrogated through knockout of p53$^{-/-}$ (Chin et al., 1999; Lim et al., 2000; Varela et al., 2005). This rescue however is limited as longevity is prevented due to significantly increased tumorigenesis, thereby obscuring our understanding of p53 in aging. p53's contribution to aging is further obfuscated by the fact that upregulation of p53/p21^{CIP1} pathway is observed in senescent cells, but transgenic overexpressing p53 or p19^{ARF} in mice results not only increases tumor resistance but delays aging (García-Cao et al., 2002; Matheu et al., 2007). Indicating that there may be an age protective role of p53 counteracting its role in senescence.

Until recently tools to visualize senescence *in vivo* and expression of biomarkers such as p16^{INK4a} in a whole-body context were lacking, meaning our *in vivo* understanding of senescence dynamics in aging across tissues was severely hindered. Most senescence studies in aging relied on surrogate markers of senescence (Hudgins et al., 2018), such as SA-β-gal activity which strongly stains some non-senescent tissues such as immune cells (Hall et al., 2017). With the advent of the p16^{INK4a}-LUC mice that have a p16^{INK4a} luciferase reporter, there is now confirmation that multiple tissues show an exponential age-related

increase in p16^{INK4a} expression, correlating with higher levels of pro-inflammatory factors or SASP components (Burd et al., 2012). The premise of senescent cell reporters *in vivo* has been further expanded upon in recent years to track individual p16^{INK4a} positive cells coupled to single cell transcriptomics (Omori et al., 2020). Disassociation and scRNA-seq of lung, liver, kidney, heart and brain tissues revealed the presence of a population of cells that were senescent and were enriched with age. Interestingly, senescent cell populations in different tissues had differing transcriptomic phenotypes and half-life in tissues, with senescent cell turnover in kidney and lung being longer than in liver.

Determining whether a gene is causal in diseases such as cancer is usually a matter of either knockout or overexpression, acting as a form of Koch's postulate. With senescence in aging however that same approach has been complicated by tumor suppressive roles of the *INK4/ARF* locus and p53, as illustrated by the paradoxical lengthening of lifespan in mice with hyperactivation to these pathways. Seminal studies by Baker et al. first in progeroid BubR1 mice (Baker et al., 2011) and later in naturally aged mice (Baker et al., 2016) showed that expression of a transgene containing a small molecule inducible caspase-8 under the control of a *Cdkn2a* minimal promoter to ablate p16^{INK4a} positive senescent cells drastically improved healthspan of aged mice. The healthspan reducing aspects of p16^{INK4a} senescent cells in aging is further supported by a lieu of studies using other p16^{INK4a} reporter ablation systems such as the p16-3MR and INK-NTR systems (Childs et al., 2016; Demaria et al., 2014). For the first time in the senescence field, there is a clear causal link between it and aging. The next important step is to determine the mechanisms through which presence of these cells in tissues causes decline.

The SASP in cancer has been shown to be important in both clearance of pre-malignant cells and establishing a tumor microenvironment (Coppé et al., 2010; Eggert et al., 2016; Kang et al., 2011). Much less is known about its role in aging, but it has been hypothesized

to be a mediator of dysfunction in the tissues where senescent cells reside (Luo et al., 2016; Muñoz-Espín and Serrano, 2014). p16^{INK4a} expression across multiple tissues can act as a biomarker of aging. Similarly, IL-1α, IL-6, TNFα, NF-κB alongside a multitude of inflammatory factors have been found to increase in tissues with age (Bruunsgaard et al., 2000; Dinarello, 2006; Kiecolt-Glaser et al., 2003; Kirwan et al., 2001; Liao et al., 1993). With inhibition of NF-κB conferring resistance to progeroid conditions in mice (Tilstra et al., 2012), inflammation has been hypothesized to contribute to tissue dysfunction during aging. This is supported epidemiologically with age-related disease severity (Balestro et al., 2016; Brunt et al., 2009; Dinarello et al., 2010; Libby et al., 2002) and physical frailty (Soysal et al., 2016) correlating with levels of chronic inflammation. This age-related chronic inflammation has become collectively termed as 'inflammaging' (reviewed in (Salminen et al., 2012). The causative element in this chronic inflammation has yet to be fully elucidated. Lifelong antigenic load and chronic exposure to damaging stimuli are undoubtedly contributors to this, senescence is also promising candidate for a mediator of inflammaging, that may result in their detrimental effects during age.

Accumulation of damage in a tissue will result in an ever-increasing proportion of cells becoming senescent and increased SASP production. SASP induced immunosurveillance in healthy organisms results in clearance of these senescent cells and therefore SASP driven inflammation is resolved (Acosta et al., 2013; Kang et al., 2011; Tasdemir et al., 2016). During aging however, the immune system is in decline due in part to the senescence program itself (Chang et al., 2016; Desdín-Micó et al., 2020). Immune system senescence, termed 'immunosenescence', thereby compromises the senescent cell clearance capacity further exacerbating any inflammatory phenotype by their accumulation in tissues. Studies using senolytic systems and drugs, show that elimination of senescent cells reduces inflammatory load in multiple tissues (Jeon et al., 2017; Baker et al., 2016). Moreover,

generating defects in the metabolic pathways that recapitulate aging effects on T-cells result in a reduced functionality and a premature aging phenotype (Desdín-Micó et al., 2020) that correlates with the accumulation of senescent cells and increased inflammation. Several groups have now observed infiltrating immune cells, high in $p16^{INK4a}$, are present in aged tissues (Childs et al., 2016; Liu et al., 2019), raising the question, are they contributing to chronic inflammation also? Senolytic and T-cell dysfunction studies unfortunately have yet to truly verify the inflammatory cell-of-origin and determine if increased inflammation is due to presence of senescent cells in aged tissues or intrinsic alterations to immune cells. Future studies will need to establish the causal link between the SASP, chronic inflammation and tissue dysfunction. Leveraging knowledge of how the SASP is regulated may be helpful in unraveling these questions. Disruption of BRD4, ZFP36L1 or PTBP1 can abrogate the SASP and inhibition of NOTCH1 can alter the effects of the SASP, thereby potentially allowing delineation of its effects in aging.

As discussed previously, with the advent of Senolytic systems a causal link between $p16^{INK4a}$ positive senescent cells and the aging health decline has been established. What is not known however is whether these senescence cells mediate their effects systemically, potentially in an endocrine manner or is each tissue its own example of 'seno-dysfunction'. Senescent cell engraftment in young mice resulting in systemic aging would seem to suggest that the former is possible (Xu et al., 2018). Senolytics has established of a causal link between senescent cells and the etiology of specific tissue dysfunctions that had previously shown to correlate with senescence markers (see Figure 1.4).

1.6.3 Senescence in the musculoskeletal system.

Physical frailty during aging, involves a decline in multiple systems involved in mobility, such as the muscle, joints and bone. This involves failures in the joint, muscle, bone and fat – resulting in predisposition to osteoarthritis, sarcopenia, osteoporosis and weight loss.

Degradation of joints and ligaments provides a significant risk factor for the development of arthritis and overall frailty in aged individuals. Cartilage production from mesenchymal stem cell derived chondrocytes is essential in maintaining joint mobility and several lines of evidence point to senescence driven decline in this function. In individuals with osteoarthritis, chondrocytes have elevated $p16^{INK4a}$ expression and fail to produce sufficient cartilage to sustain joint function (Price et al., 2002). Anterior cruciate ligament transection (ACLT) surgery in mice can be used to model osteoarthritis and leads also to an accumulation of senescent cells in the ligament (Kuyinu et al., 2016). Senolytic elimination of senescent cells rejuvenates the remaining chondrocytes resulting in proliferating and upregulated expression of cartilage components. Moreover, this revival of chondrocyte function resulted in cartilage replenishment and partially restored physical function (Jeon et al., 2017).

Another significant contributor to physical frailty in aging is skeletal muscle weakness. Normal skeletal muscle function requires an ability to repair and rejuvenate myocytes in order to maintain and develop strength. Muscle stem cells (MuSCs) or 'satellite cells' provide skeletal muscle with this ability through the generation of myoblast precursor cells (Ten Broek et al., 2010; Gopinath and Rando, 2008). The breakdown in this process is hypothesized to be driven by senescence and is the underlying cause of age dependent muscle wasting or sarcopenia. MuSCs during age become marked by $p16^{INK4a}$ expression and are senescent (Sousa-Victor et al., 2014). They therefore cannot make the transition out of their normally quiescent state to generate myoblasts and repair muscle. Senescent MuSCs when cleared from irradiated mice using senolytics were found to increase the ability of remaining MuSCs to form muscle cell colonies (Chang et al., 2016). This observation that senescence induction is responsible for MuSC decline is supported by experiments where bypass of MuSC senescence by inhibition of p38 or $p16^{INK4a}$ strengthens muscle in geriatric mice (Cosgrove et al., 2014; Sousa-Victor et al., 2014).

Finally, a decrease in bone mineralization, as well as decreased proliferation of osteoblasts and osteoclasts derived from Mesenchymal Stem Cells, results in loss of bone density known as osteoporosis. Osteoporosis is a significant contributor to age related frailty, increasing the risk of bone fractures and spinal curvature. Senescent cells are often found in the aged bone microenvironment and the MSC lineage that produce osteoblasts and osteoclasts (Farr et al., 2016). Recently, evidence of senescence in this tissue's dysfunction has been developed upon to provide a causal link between the presence of senescent cells and bone loss. With INK-ATTC transgenic mice and senolytics in aging reducing loss of femur cortical bone and enhanced bone strength (Farr et al., 2017). The elimination of senescent cells increases osteoclastogenesis, with increased differentiation of bone marrow derived stem cells to form osteoclasts. Moreover, treatment with JAK inhibitors to suppress the SASP (Xu et al., 2015b) mimicked this effect, demonstrating that senescence and specifically the SASP may drive age-related osteoporosis.

Another marker of physical frailty in aged individuals is their reduced adiposity associated with reduced thermogenic capacity with age, fatigue and anemia. This wastage of fat tissue alongside the reduction in muscle mass is termed cachexia. Aged mice have increased markers of senescence in their white adipose tissue (Baker et al., 2016). Alongside this, removal of these cells restores adiposity and mass of aging mice (Baker et al., 2016). Adipocyte differentiation underlies the beiging of white adipose tissue and serves an important function in off-setting the effects of age-related cachexia. Disruption of senescent pathways such as $p16^{INK4a}$, p38 and removal of senescent cells restore this process in mice and improve metabolic function (Berry et al., 2016; Xu et al., 2015a). This suggests that not only can senescent cells contribute to a decline in adiposity with age through inhibition of adipocyte differentiation, but they may have wider systemic impacts on metabolism. These effects could also manifest themselves as increased diabetes mellites risk, as altered tissue

metabolism forms part of the dysfunction of that disease. The combined evidence of senolytics and presence of senescence markers in aging models of sarcopenia, osteoarthritis, osteoporosis and cachexia demonstrates that senescent cells are a primary driver or age-related physical frailty.

1.6.4. Senescence in the aging endocrine system

The endocrine system comprises multiple organ systems across the body, such as brain (hypothalamus & pituitary), kidney (adrenal gland) and pancreas. During age, hormonal insensitivity due to a declining endocrine system can have drastic outcomes, manifesting as increased risk of diseases such as diabetes mellites and osteoporosis.

Evidence of the link between diabetes and senescence initially came from the observations that β-cells isolated from the pancreas of diabetic mouse models have an increase in senescence markers alongside production of SASP factors such as IL-1β (Chen et al., 2009; Dinarello et al., 2010; Ehses et al., 2009; Sone and Kagawa, 2005). Correlation of *INK4/ARF* SNPs with incidence of diabetes in patients also suggests this correlation may translate into humans (Jeck et al., 2012; Zeggini et al., 2007). Following, overexpression of $p16^{INK4a}$ in pancreatic islets (Krishnamurthy et al., 2006) or derepression of the *INK4/ARF* locus via EZH2 knockout in β-cells (Chen et al., 2009) resulted in a decline in β-cell regenerative capacity, predisposing mice to development of diabetes. Additionally, clearance of senescent cells in mouse models of type 1 and 2 diabetes resulted in restoration of insulin secretion (Aguayo-Mazzucato et al., 2019; Thompson et al., 2019). Despite the predisposition that presence of senescent cells poses, senescent β-cells paradoxically appear to have higher insulin secretion (Helman et al., 2016). This may be due to the supraphysiological nature of the promoters $p16^{INK4a}$ was linked to in these mice (Aguayo-Mazzucato et al., 2019). Another possibility is that whilst senescent beta cells do secrete more insulin, the paracrine SASP signaling within the islet is sufficient to induce further senescence and tissue dysfunction –

with insulin production merely providing a stop-gap to diabetes onset. This may explain the phenomenon of prediabetes observed in patients (Palmer et al., 2015). Other effects of senescent cells in the pancreas are only beginning to be understood. Recently induction of senescence in the context of pancreatic ductal adenocarcinomas was shown to promote vascular remodeling to enhance sensitivity of PDACs to chemo and immunotherapies (Ruscetti et al., 2020). Does the presence of senescent cells potentially alter function of pancreas through the same mechanism during aging?

Decline in the endocrine system with age is not just found in the pancreas, hypothalamic dysfunction is also associated with age and is linked with onset of osteoporosis. In agreement with this, mice with a defective hypothalamic neural stem cells produce a neuroendocrine progeroid phenotype (Zhang et al., 2017) and during normal aging become senescent due to the lost expression of a $p16^{INK4a}$ suppressing lncRNA, *HNSCR* (Xiao et al., 2020). These studies demonstrate the modulatory nature of senescence in the neuroendocrine system with age, modulations that can result in severe clinic repercussions like type 1 and 2 diabetes mellites or even systemic aging effects like those observed with changes in the hypothalamus.

1.6.5 Senescence effects in the cardiovascular system

Cardiovascular disease in an aging population presents a major challenge for healthcare providers and is one of the leading causes of death. Age is amongst the most significant risk factors for development of atherosclerosis, cardiomyopathy and occurrence of serious cardiovascular events (North and Sinclair, 2012). In line with a potential role of senescence in mediating this risk, senescent markers were found at vascular smooth muscle cells (VSMCs) at atherosclerotic plaques (Uryga and Bennett, 2016). Senescence was also found to be induced in instances of mouse and rat cardiomyopathy models (Anderson et al., 2019; Boon et al., 2013), one of the causes of myocardial infarction with age. Further supportive of

the role of senescence in cardiovascular decline with age, senolytic treatment both protected mice form cardiac stress and cardiomyocyte hypertrophy but also reduced formation of atherosclerotic plaques in LDLR$^{-/-}$ mice under high fat diet (Baker et al., 2016; Childs et al., 2016). Interestingly, senescent macrophages were found to be present in atherosclerotic plaques, where they contribute significantly to production of the SASP (Childs et al., 2016), underscoring the importance of infiltrating senescent immune cells in underlying disease etiologies.

1.6.6 Senescence effects in the nervous system

Alzheimer's (AD) and Parkinson's disease (PD) are progressive and terminal with clinical interventions being largely palliative with lifestyle changes suggested to delay the course of the diseases. Risk of developing these disorders increases with age as does general cognitive decline. What role does senescence play in the decline in neurological function and homeostasis? Senescent markers can be found in the astrocytes and glial cells of patients with AD (Bhat et al., 2012) and PD (Chinta et al., 2013). Specific isoforms of p53 are associated with lower neurotoxic effects of astrocyte SASP and were seldom found in patients with AD and other neurodegenerative diseases such as amyotrophic lateral sclerosis (Turnquist et al., 2016). In mice treated with paraquat to model PD development showed higher levels of senescence markers. Importantly, clearance of senescent cells reduced neuropathies, restored neurogenesis and motor function in these mice (Chinta et al., 2018). This same approach also alleviated cognitive deficits and restored proliferative capacity of oligodendrocyte progenitor cells in mice with APP/PS1 mutations that model early onset AD (Zhang et al., 2019). Senescence is also detrimental to the sensory nervous system with senescence markers being identified in cells of trabecular meshwork of patients with glaucoma (Liton et al., 2005). Moreover removal of prevents loss or retinal ganglia and relieves inter-ocular pressure in mouse models of glaucoma (Rocha et al., 2020).

1.6.7 Senescence and the hematopoietic lineage

Infection is one of the highest risk factors for end-of life complications resulting in fatality. As individuals age, the ability of their immune system to respond effectively declines. This decline is linked not only to a decline in differentiation ability of hematopoietic stem cells that supply the immune cell lineage but an decline in the functionality of the immune cells themselves (Chang et al., 2016; Desdín-Micó et al., 2020). Senescent cells expressing $p16^{INK4a}$ and staining for SA-β-gal activity accumulate within the HSC niche during aging (Chang et al., 2016). Additionally, T-cells with defects in mitochondria that occur during ageing, adopt a senescence like phenotype with compromised ability to respond to infection and production of pro-inflammatory cytokines disrupting multiple tissues (Desdín-Micó et al., 2020). Further supporting the detrimental nature of senescence in HSC and immune system decline, Senolysis has both been shown to rejuvenate the HSC niche when mice are irradiated (Chang et al., 2016). In these experiments removing senescent cells increased HSC differentiation and numbers of B and T cells post-bone marrow transplantation. These highlight that senescence appears to be a cause of ageing decline of the immune system with age.

1.6.8 Senescence and fibrosis

Senescence appears to both drive establishment of fibrosis and at the same time assist in its resolution. Wound healing processes lead to accumulation of ECM proteins such as collagen around the site of damage, resulting in thickening and scarification of the tissue. Unwanted deposition of ECM proteins in tissues such as the lung, liver and heart result in a pathological condition known as the fibrosis. Fibrosis, if left unresolved can eventually lead to tissue dysfunction and diseases such as idiopathic pulmonary fibrosis (IPF) and liver cirrhosis. The induction of IPF and liver cirrhosis are complex processes, both of which are associated with age (Dai et al., 2015; Frith et al., 2009). One of the leading causes of liver cirrhosis that is

associated with senescence is development of non-alcoholic fatty liver disease (NAFLD). The etiology of liver cirrhosis induced by NAFLD involves both abnormal accumulation of lipids and subsequently hepatic steatosis and liver fibrosis (Hardy et al., 2016; Pellicoro et al., 2014). In both NAFLD and IPF, the presence of senescent cell markers such as $p21^{CIP1}$ and SA-β-gal correlate with fibrotic disease progression (Krizhanovsky et al., 2008; Schafer et al., 2017; Yanai et al., 2015) suggesting that there is a link between the two.

The secretion of MMPs by senescent cells suggest that senescence could drive resolution as fibrosis through remodeling of the ECM (Giannandrea and Parks, 2014). Indeed, early evidence in mice with p53 or $p16^{Ink4a}$ knockout show an increase in fibrotic tissue area with CCL_4 induced liver damage (Krizhanovsky et al., 2008). In this model, hepatic stellate cells (HsCs) that become senescent had lower expression of collagen - increased MMP expression that could assist in fibrosis resolution (Krizhanovsky et al., 2008). Other studies of liver fibrosis highlighted that induction of HsC senescence with CCN1, a protein found in the ECM of cirrhotic livers, accelerated resolution of liver fibrosis (Kim et al., 2013b). Here, CCN1 knockout or overexpression resulted in lower or higher levels of senescence respectively and acceleration or resolution of cirrhosis development. Senescent cells however accumulate in mouse models of primary biliary cholangitis, another leading cause of liver cirrhosis (Ferreira-Gonzalez et al., 2018). Here suppression of paracrine senescence using TGFβ inhibitors resulted in reduced collagen deposition and recruitment of macrophages – also shown to potentially be detrimental in liver fibrosis (Hardy et al., 2016).

Further confounding the hypothesis of senescence as a fibrotic disorder resolving process are experiments using senolytic mouse models. Removal of senescent cells in bleomycin-induced lung fibrosis mouse models of IPF resulted in reduction in pro-fibrotic SASP production and improving of pulmonary function (Schafer et al., 2017). Similarly, clearance of senescent cells reduces lipid burden in the liver and therein age related hepatic steatosis

(Ogrodnik et al., 2017). In this study, senescent cells were found to contribute to hepatic steatosis due to their altered lipid metabolism. Senolysis in the context of fibrotic disorders however is not always beneficial. Subsets of senescent cells in liver, specifically liver sinusoidal vascular endothelial cells (LESCs) with high levels of $p16^{INK4a}$, were found to limit development of liver fibrosis (Grosse et al., 2020). Removal of senescent LESCs resulted in breakdown of blood-tissue barriers in the liver, disrupting flux of macromolecular waste from the blood.

The seemingly incongruous nature of senescence as both a mediator and resolver of fibrotic dysfunction, seem to indicate that whilst targeting senescent cells may be beneficial in aged individuals further research needs to be done to understand the effects of targeting all versus subsets of senescent cells.

1.6.9 Senescence in renal dysfunction

Renal tissue declines with age, with a reduction in cortical volume and glomerular filtration rate. This decrease can manifest in the pathological conditions of chronic kidney disease such as nephropathy, glomerulosclerosis and tubulointerstitial fibrosis. Onset of these pathologies and renal disease in general correlates with increased p53 / $p16^{INK4a}$ levels and an increase in senescence suggesting a detrimental link between the two (Melk et al., 2003, 2004; Sturmlechner et al., 2017). Senolysis in middle aged 1 year old mice was found to improve kidney function and protect against glomerulosclerosis with lower blood urea nitrogen concentration and a lower percentage of sclerotic glomeruli (Baker et al., 2016). Together, these lines of evidence would suggest that senescent cells in the kidney post a risk for renal dysfunction during ageing.

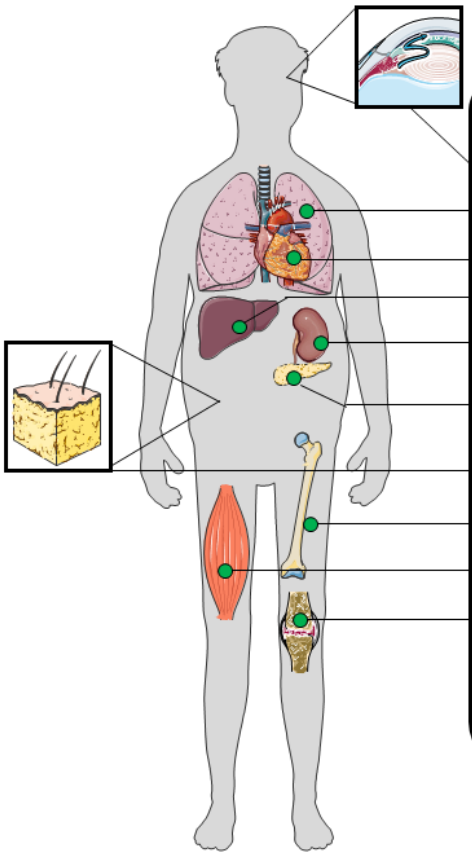

Diseases	Senescence Markers	p16$^{-/-}$ or p53$^{-/-}$ mice	Senolytic	Reference
Glaucoma	✓		✓	Liton et al. 2005 Rocha et al. 2020
Idiopathic pulmonary fibrosis (IPF)	✓		✓	Yanai et al. 2015 Schafer et al. 2017
Atherosclerosis	✓		✓	Uryga and Bennett, 2015 Childs et al., 2016
Liver cirrhosis / NAFLD	✓	✓	✓	Krizhanovsky et al. 2008 Kim et al., 2013 Ogrodnik et al., 2017 Wiemann et al., 2002 Grosse et al. 2020
Glomerulosclerosis	✓		✓	Melk et al. 2003, 2004 Baker et al. 2016
Type I / II Diabetes	✓	✓	✓	Chen et al. 2016 Helman et al. 2016 Aguayo-Mazzucato et al. 2019 Thompson et al. 2019
Cachexia	✓	✓	✓	Berry et al., 2016 Xu et al., 2015 Baker et al., 2016
Sarcopenia	✓	✓	✓	Sousa-Victor et al., 2014 Cosgrove et al., 2014 Chang et al., 2016
Osteoarthritis	✓		✓	Price et al. 2002 Jeon et al., 2017

Figure 1.4. Evidence of senescence in disease processes.

The detection of senescence markers and senescent cell ablation models (senolytics) has provided an ever-expanding list of diseases in which senescent cells play a causative role. (Adapted from McHugh et al. 2017)

1.5.3 The potential for senolytics

The evidence linking senescence to different age-related pathologies is compelling and makes therapeutic targeting of senescence an attractive approach for treating these thus far largely immedicable diseases. However, bypassing of senescence carries significant risk of tumour development as evidenced by the effects of inhibition of p38, p53, p16^{INK4a} and telomeric re-lengthening (Ito et al., 2006; Janzen et al., 2006; Sharpless et al., 2001; Shay, 2016) due to inability of supressing pre-neoplastic cells and tissues. Elimination of senescent cells however appears not to carry these same risks (Baker et al., 2016), with mice cleared of senescent cells having reduced incidence of tumours. This opens the possibility of using

Senolysis as a therapeutic avenue for the multitude of diseases that senescence is found to correlate with or be causative in.

Usage of genetic ablation systems such as those found in the INK-ATTC and p16-3MR mice allow for near ubiquitous elimination of senescent cells in a controlled manner (Baker et al., 2011; Demaria et al., 2014). Attempting a similar approach in clinic would only be possible through the use of gene therapies or the novel but rapidly developing use of nanoparticles (Petros and Desimone, 2010). Without these approaches the use of other drugs and approaches to target senescent cells must be relied upon. One of the first senolytic agents discovered was the BH3 mimetic ABT-263, also known as Navitoclax. Treating senescent cells with ABT-263 preferentially eliminates senescent cells by inhibiting the activity of anti-apoptotic BCL-2 family proteins (Chang et al., 2016). In senescence, this sensitivity is dependent on the increased translation and protein levels of BCL2L1 (BCL-XL) and BCL2L2 (BCL-W) observed during senescence (Yosef et al., 2016). With the understanding that senescence induction across an individual's lifespan manifests in age-related pathologies, senolytic therapies could be utilized in a prophylactic manner to prevent disease onset. Unfortunately, due to its ability to cause severe neutropenia and thrombocytopenia ABT-263 would be unsuitable for this approach (Rudin et al., 2012). As a result, many groups are now attempting to identify novel ways of eliminating senescent cells.

One such approach is the re-localization of p53 to the cytoplasm causing engagement of the p53-mitocondrial apoptotic pathway. During senescence upregulation of FOXO4 facilitates trafficking of p53 to the nucleus and DNA-SCARS (Baar et al., 2017). Interruption of this event using FOXO4 inhibiting peptides was found to not only display enhanced specificity for elimination of senescent cells, but it alleviated some aging phenotypes (Baar et al., 2017). One potential caveat with FOXO4 inhibition was the suppression of $p21^{CIP1}$ expression observed in treated senescent cells. This carries the potential risk of senescence bypass and

increased tumorigenesis, similar to what was observed in p53 and p16^{INK4a} depleted mice. Several other drugs that can selectively kill senescent cells have been identified. These include dasatinib and quercetin (referred as D+Q) (Zhu et al., 2015), ABT-737 (Yosef et al., 2016), HSP90 inhibitors (Fuhrmann-Stroissnigg et al., 2017), cardiac glycosides (Guerrero et al., 2019; Triana-Martínez et al., 2019) and β-galactosidase activated nanoparticles and pro-drugs (González-Gualda et al., 2020; Guerrero et al., 2019; Muñoz-Espín et al., 2018).

Another senolytic approach that has been investigated is the CAR T-cell therapy. Generation of T-cells recognizing soluble uPAR, found to be secreted from senescent cells, were able to eliminate senescent cells (Amor et al., 2020). This resulted in protection of mice from CCl_4 and NASH induced liver fibrosis but did result in some off-target effects due to CAR T-cell recognition of uPAR from non-senescent tissues.

First-in-human studies have validated the potential of senolytics to decrease senescence burden in human patients (Ellison-Hughes, 2020; Hickson et al., 2019; Justice et al., 2019). However, the failure of a recent Phase 2 clinical trial of a senolytic mdm2 inhibitor against osteoarthritis (Roy et al., 2020) highlights the need to identify more effective senolytics. Senolytics as a therapeutic approach whilst promising carry significant questions that remain to be answered. In a study of osteoarthritis using senolytics, senescent cells were observed to re-appear after treatment, thought to be due to the surgical injury still being present (Jeon et al., 2017). It could be indicative however of the limited benefit senolytics might have when the damage that induced them remains unresolved. As the inducing stimuli of senescence during age is complex, research into senolytics has sought to identify targets that confer a broad effect on multiple senescence modalities and cell types. A potential caveat of this however is that senescent cells appear to be clearly beneficial in some contexts, such as is the case with LESCs (Grosse et al., 2020), elimination of these may have the opposite desired effect. Most senolytic research has also not thoroughly investigated whether

senescent cell elimination is sustained with short term treatment. The ability of senolytics to rejuvenate stem cell niches, causing increased differentiation and proliferation of stem cells raises another potential issue. Sustained proliferation of these cells and their elimination once senescent in multiple senolytic treatments could ultimately deplete the reservoir of cells tissues for the sake of increased functionality with age.

The aim of many senolytics is to induce apoptosis and through removal of these cells decrease inflammatory burden on a tissue. In a competent immune system, apoptotic cells are phagocytosed through recruitment of immune cells (Poon et al., 2014) in a largely anti-inflammatory process. However without clearance, apoptotic bodies undergo secondary necrosis, releasing pro-inflammatory danger associated molecular patterns or DAMPs such as ATP, IL-1α and mtDNA. Therefore, the effects of Senolysis with compromised immune clearance, such as occurs with age, should be investigated as it may further exacerbate chronic inflammation. This may suggest that there is a therapeutic window for senolytics, where patients need to have a functional immune system to handle the apoptotic burden that senolytics may cause.

1.8 Project Aims

Multiple lines of evidence suggest that targeted elimination of senescent cells may be beneficial in treating many age-related diseases. Despite surging interest in therapeutically targeting survival pathways in senescent cells our mechanistic understanding of these pathways remains limited, with only a handful of pathways being implicated. This highlights the need for a more thorough exploration of pathways mediating senescent cell survival. Here, we aimed to perform unbiased genetic screens to discover targetable vulnerabilities of senescent cells that could be exploited to treat senescence-associated pathologies.

Chapter 2 - Materials and Methods

2.1 Tissue culture

2.1.1 Culturing mammalian cell lines

IMR90 human diploid fibroblasts (ATCC CCL-186), HEK293T (ATCC, CRL-3216), SK-HEP-1 hepatic adenocarcinoma (ATCC HTB-52), A549 lung adenocarcinoma (ATCC CCL-185), HCT-116 colorectal carcinoma (ATCC CCL-247) and Primary bronchial airway epithelial cells (PBECs) cell lines were obtained from American Type Culture Collection (ATCC®). Adult normal human lung fibroblasts (NHLFs) were obtained from Lonza®. Primary bronchial airway epithelial cells (PBECs) were cultured in Airway Epithelial Cell Basal Medium (ATCC-PCS-300-030; ATCC) supplemented with Bronchial Epithelial Cell Growth Kit supplements (ATCC-PCS-300-040; ATCC) and 0.1% antibiotic–antimycotic solution (Gibco®) with media replenished every 48 hours. Adult normal human lung fibroblasts (NHLFs) were cultured in Fibroblast Basal Medium (CC-3131; Lonza) supplemented with SingleQuot Kit of supplements and growth factors (CC-4126; Lonza), with media replenished every 3-4 days as required. All other cell lines under normal culture conditions were maintained on Dulbecco's modified eagle medium (DMEM) (Gibco®) supplemented 1% 100X Gibco® Antimycotic-antibiotic and 10% (v/v) Foetal bovine serum (FBS) (Labtech – Batch 41213, South American Origin) hereinafter referred to as DM10 media. Media was replenished on cells every 3-4 days as required.

Passaging of cells was performed by enzymatic detachment using 0.05% Trypsin-EDTA (Gibco®) on cells for 5 minutes followed by inactivation in DM10 media and centrifugation at 180g for 5 min. Supernatant was aspirated to remove dead cells/debris and cell pellet resuspended in fresh DM10. Cell viability and counts were determined by flow cytometry on a Guava EasyCyte platform (Millipore®) using Guava ViaCount Reagent to provide stains of

dying and nucleated cells. In-built GauvaSoft software was used to gate live cells and remove cell debris/ dead cells from final cell count. Experiments using IMR90 cells or cell lines generated from them were carried out using cells between passage 10 to 14 with viability above 90%.

Primary cells and cell lines underwent cryopreservation for long term storage. To cryopreserve - cells were detached, pelleted and resuspended in DM10 media supplemented with 10% DMSO as a cryoprotectant and immediately transferred to cryovials placed in a Nalgene® MrFrosty™ freezing container at -80°C. Freezing container would then provide cooling at 1°C / min allowing for gradual temperature reduction of the cells. After 24 hours, cryovials were transferred to liquid nitrogen tanks for long term storage. Revival of cells from -80°C or liquid nitrogen was performed by thawing in a 37°C water bath and diluting in DM10 media, followed by centrifugation and resuspension again in fresh DM10 media to remove DMSO. After 24 hours, media was replaced, and cells allowed to rest an additional 48-72h before plating experiments.

2.1.2 Generation of cell stocks and senescence induction.

Lentivirus and retrovirus infection – Lentivirus and retrovirus were generated using HEK293T cells. The day prior to transfection HEK293T cells were split to ensure between 60-70% confluency for retrovirus production and 80-90% for lentivirus production - on a 10cm plate. On day of transfection, a transfection mix containing either - 15-20µg of retroviral plasmid combined with 8µg of pGAG-pol (Clonetech) and 2.5µg pVSV-G (Clontech), or 10µg of lentiviral plasmid with 8µg of psPAX2 (Addgene) and 2µg pVSV-G - was supplemented with 80µl of linear 25kDa linear polyethyleneimine (PEI, 1mg/ml (w/v), Polysciences) and made up to a final volume of 1mL with DMEM, before vortexing and incubation for 30min. Transfection mix was then added to cells in a dropwise manner as to not disturb layer of 293T cells. Cells were then cultured for 24h and media replaced with 6ml of fresh DM10 media.

The reduction in volume served to concentrate virus in culture supernatant. In parallel, target cells were seeded for infection ($1x10^6$ per 10cm plate). On the following day, supernatant from transfected 293T plates was collected and filtered using 0.45µm acetate filters (VWR International). For large scale lentivirus preparation for screening libraries low-protein binding PVDF Millex Durapore™ filters (Millipore®) were used. For lentiviral infections, supernatant was diluted depending on viral titre determined prior using functional titration with antibiotic selection, typically this was a 1:4 to 1:8 dilution. Polybrene was then added to diluted lentivirus for a final concentration 4µg/ml. This was then added to target cells and incubated between 2-8h before washing with PBS and replacement of media with fresh DM10. For retroviral infection, undiluted viral supernatant with 4µg/ml of polybrene was added to target cells and incubated for 3hr. Infection round was repeated for a total of 3 rounds by adding freshly conditioned viral supernatant from original plate of transfected 293T cells. Media was then removed, target cells washed with PBS and media replaced with fresh DM10. Both retrovirally and lentiviral infected cells were left to rest for 72h before being passaged 1:3 into antibiotic selection. Cells were further passaged - if necessary - to maintain 60-70% confluency during selection process. (see Table A2 for antibiotic concentrations and selection time)

Overview of senescence induction - IMR90 cells were used to generate inducible ER: RAS cells to model Oncogene induced senescence (OIS), through retroviral infection of pLNC-ER:RAS-neo into IMR90 cells followed by selection with Neomycin. IMR90 cells containing the pLNC-ER:RAS plasmid backbone pLXSN were infected in parallel to assess leakiness in the pLNC-ER:RAS system. Treatment with 100nM 4-OHT (Sigma, in DMSO) was used to induce IMR90 ER:RAS cells to undergo oncogene induced senescence (OIS). Therapy induced senescence (TIS) was induced in IMR90 cells by treatment with 33µM (50ug/ml) Bleomycin sulfate (Generon, A10152) for 24 hours, 20µM Palbociclib (Selleckchem, S1116) for 7 days, 100nM Doxorubicin (Cayman chemical, #15007) for 7 days or exposure to 20Gy

of γ-irradiation. Senescence was induced in A549 & SK-HEP-1 cells by treatment with 2μM Etoposide (Sigma-Aldrich, E1383) for 7 days. (See Table A1. for an overview of drugs used in this project.)

2.2 Assays for cell growth and sruvival

Colony formation assays - to assess senescence induction, colony formation assays were performed by seeding 0.08-0.12 $x10^6$ IMR90 or IMR90 ER:RAS cells in 10cm dishes. Cells were then induced to senesce and cultured for 10-14 days or until DMSO treated – proliferating cells had reached 80-90% confluency. To assess senolysis, cells were seeded in 10cm plates at high density; 0.5-0.8$x10^6$ for IMR90 or ER:RAS, 0.015$x10^6$ for DMSO treated or 0.08$x10^6$ for Etoposide treated A549 and SK-HEP-1 cell lines and 0.0075$x10^6$ for DMSO. Plates were cultured for 7 days and then media changed to low serum media with 0.5% FBS (hereinafter low serum media) to induce quiescence in DMSO treated cells and to not underestimate potential non-senescent cell toxicity. Senolytic drugs were added at their indicated concentration in DMSO (< 0.2% v/v final concentration) and cultured for a further 3 days. If longer drug treatment was required fresh drug and media was added on day 3 and cultured for a further 4 days. Upon experiment endpoint plates were then fixed with 0.5% (w/v, PBS) glutaraldehyde (Sigma) for 1 hour, washed twice with dH_2O and left to dry overnight. Dried plates were then stained with a 0.2% (w/v, PBS) solution of crystal violet (Sigma, C6158) for 1 hour, washed 3 times with dH_2O and left to air dry overnight. Plates were then imaged using HP Scanjet4850 photo scanner.

BrdU Incorporation - Cell proliferation was assessed through incorporation of nucleotide analogue 5-Bromo-2'-deoxyuridine (BrdU) into cells. $2x10^3$ or $8x10^3$ IMR90 cells were seeded into 96-well plates in duplicate for DMSO/Palbociclib treated and Bleomycin/Doxorubicin treated cells respectively. 10μM BrdU was added to cells 18h before desired time point and wells were then washed in PBS and fixed using 4% Paraformaldehyde (w/v, PBS) for 45

minutes to 1 hour before removal and washing 3 times with PBS. BrdU incorporation was assessed via immunofluorescence and high-content analysis (see section 'Immunofluorescence & High throughput microscopy').

High-throughput microscopy survival assay - To assess senolytic effect of drugs, cells were cultured for 7 days, culture media was changed to DM0.5 media and drugs in DMSO were added (<0.2% v/v final concentration), drugs were replenished after 3 days if assay length was longer than 72h. At experiment endpoint, wells were fixed in 4% PFA for 1 hour at day 10 to 14, washed 3 times with PBS and then stained with 1μg/mL DAPI (w/v, PBS) for 10 minutes. Wells were then washed 3 times with PBS. Optionally plates could be stored at 4ºC for up to 2 weeks and DAPI stained. Image acquisition of DAPI stained cells was performed on an automated InCell Analyser 2000 (GE Healthcare®) and high-content analysis on the InCell Investigator 2.7.3 software used to quantify number of DAPI positive cells per well. A 'top-hat' method was used to segment cell-nuclei based on DAPI stained area and a minimum nuclear area threshold of 80μm used to exclude debris. For cancer cell lines, nuclear area threshold was reduced to 40μm. Survival was measured as cell counts relative to DMSO/non-targeting control treated quiescent or senescent cells unless otherwise stated.

2.3 Protein analysis

2.3.1 Immunofluorescence and High throughput microscopy

Immunofluorescence staining was carried out by first fixing wells of 96 well plate at desired timepoint for 1 hour using 4% PFA (w/v, in PBS) followed by washing 3 times with PBS. For staining of COPI proteins plates were washed after 20-30 minutes' fixation with 4% PFA. Wells were then permeabilized using 0.2% Triton® X-100 (v/v, PBS) for 10 min or with 0.5% Triton® X-100 (v/v, PBS) for COPI staining. Wells were then washed twice with PBS to halt permeabilization and then non-specific antibody binding blocked by incubation with a blocking

solution for 1 hour at RT. Blocking solution contained 1% BSA (w/v, PBS) supplemented with 0.4% Fish Skin Gelatin (v/v, PBS) or for COPI staining protocol a solution of 5% BSA (w/v, PBS) and 0.3% Saponin (w/v, PBS). Primary antibodies were diluted in respective blocking solution (see Table A3. for Antibodies used and their dilutions), blocking solution removed from well and incubated with primary antibody solution for 1 hour at RT. For BrdU staining primary antibody solution was supplemented with 0.5U/ul DNase (Sigma) and 1mM $MgCl_2$ and incubation times reduced to 30 minutes. Following incubation, primary antibody was then removed by washing 3 times with PBS. Secondary antibodies conjugated to Alexa-594 or Alexa-488 fluorophores were then diluted in blocking solution added to wells to be incubated in dark for 1 hour. Secondary antibody was then removed by washing 3 times with PBS and nuclei counterstaining with 1μg/mL DAPI (w/v, PBS) for 10 minutes. Wells were then washed with PBS three times.

Immunofluorescence image acquisition was performed using an automated InCell Analyzer 2000 high-throughput microscope. Multiple 96-well plates were placed into stacks from which a KiNEDx Robotic arm (PAA) running Overlord™ software so that plates could be sequentially loaded, imaged and removed with the InCell microscope. Wells were imaged using a 20x objective except for wells stained only with DAPI or Golgi-related staining, which were performed at 10x and 40x respectively. 2x2 binning of images were used to reduce image file sizes. Fluorophores were imaged using pre-set 'DAPI', 'Texas Red' & 'FITC' wavelengths on microscope for DAPI stain, AlexaFluor® 594 and AlexaFluor® 488 respectively. 8, 24 & 18 fields per well were captured for 10x, 20x and 40x objectives respectively.

High content image analysis was carried out using the InCell Investigator 2.7.3 software (GE Healthcare®). DAPI nuclear counterstain was used to segment cells using a Top-hat method and used to provide a mask for nuclear localized stains. For cytoplasmic stains a 6μm collar

was applied around the cell and for detection of cytoplasmic organelles such as golgi, a 'region growing' collar was used. Quantification for nuclear staining was measured as average pixel intensity (grey scale) for the wavelength of fluorophore across the area of the nuclear mask. Cytoplasmic staining quantification was of either the average pixel intensity or the coefficient of variance of pixel intensities within collar area. Golgi structural analysis utilized a multiscale top-hat segmentation method to detect organelle structures between 1 and 3 pixels in size within a region growing collar.

2.3.2 Live-cell microscopy

To analyse live-cell induction of apoptosis, cells were incubated with IncuCyte caspase-3/7 reagent (1:500, Essen Bioscience) following reverse transfection with senolytic siRNAs or drug treatment. Four images per well of a 96-well plate were collected every 2h for 3-4 days using a 10x objective on IncuCyte microscope (Essen Bioscience) and fluorescence images analysed in IncuCyte Zoom software (Essen Bioscience). Cleaved-caspase 3/7 activity analysis was performed by segmentation of green fluorescing dots above a size and fluorescence intensity threshold.

2.3.3 Flow cytometry

Flow cytometry was carried out on a Guava EasyCyte platform (Millipore®). Cells were disassociated via trypsinization and pelleted before resuspension and dilution 1:8 in PBS before running on flow cytometer. Gating of cells was first performed on forward scatter and side scatter cell measurements to determine shape of cell as to exclude debris. Analysis of GFP or mCherry fluorescing populations was performed by gating measures of intensity at 525nm (GFP) and 610nm (mCherry) wavelength excitation. Gating criteria were determined using cells without fluorescence markers and cells constitutively expressing either GFP or mCherry. Measurements for >5000 live-cell events were obtained for each sample.

2.3.4 Immunoblotting

Cells were collected for protein extraction by first washing twice with ice-cold PBS, scraping and centrifugation performed at 180g for 5 min at 4°C. Cell pellets were then resuspended in RIPA lysis buffer (Thermo Scientific™, 89900) supplemented with one tablet of PhosSTOP® (Roche) and one tablet of cOmplete™, Mini, EDTA-free Protease inhibitor (Roche). Lysis was performed on ice for 30 min with periodic vortexing. After lysis samples were centrifuged at 13,000g for 20min at 4°C and protein containing supernatant transferred to fresh tube. RIPA lysed sample quantification was then performed using the Pierce BCA assay (Thermo Scientific™) and equal amounts of sample resuspended in required volumes of 4x Laemili sample Buffer (Bio-Rad, #1610747) and boiled at 95°C for 10 min. To immunoblot proteins, samples were separated by size on pre-cast polyacrylamide gradient gels (Bio-Rad, #4561084) and transferred onto 0.2µm nitrocellulose membranes (Bio-Rad). Efficient transfer and correct gel loading was verified by Ponceau S staining prior to 1hr blocking of membranes with 5% milk (w/v) diluted in TBS supplemented with 0.1% Tween-20 (v/v) (TBST). Primary antibodies were diluted in 5% milk (w/v, TBST) and incubated with membranes overnight at 4°C (see Table A3. for Antibodies used and their dilutions). This was then followed by three washes with TBST followed by 1hr incubation with horseradish peroxidase conjugated secondary antibody. Secondary antibody binding was visualized using Amersham ECL Prime Western Blotting Detection Reagent (Cytiva) and imaged on Amersham Imager 680 blot and gel imager (Cytiva).

2.3.5 ELISA

For detection of secreted IL-1β in conditioned media of IMR90 ER:RAS cells, 100µL of media (DMEM supplemented with 0.5% (w/v) FBS and 1% antibiotic-antimycotic solution) incubated with cells and inhibitors for 48-72h was collected and filtered using a 0.2µm cellulose acetate membrane (Gilson). Filtered samples were then subject to ELISA kit according to

manufacturer's instructions (Human IL-1β, DY201, R&D Systems). To detect suPAR, 50μL of serum was isolated from whole blood collected from tail-vein of mice and ELISA performed according to manufacturer's instructions (Mouse suPAR, DY531, R&D Systems).

2.3.6 Metabolic tagging of N-myristoylated proteins

To label N-myristoylated proteins cells were incubated in tissue culture with 20μM of YnMyr. For short-term YnMyr labelling and proteomics cells were collected after 18 hours, for longer-term analysis samples were collected after 72 hours. In parallel cells were also treated with either N-myristoyltransferase inhibitors, IMP1088 (300nM) or of DDD86481 (1.5μM) for the duration of the experiment. Cell collection was performed by washing plates twice with ice-cold PBS and scraping before centrifugation for 5min at 200g at 4°C. Pelleted cells were lysed in lysis buffer (0.1% SDS, 1% Triton X-100, PBS) supplemented with 1 tablet of cOmplete™, EDTA-free protease inhibitor cocktail (Roche Diagnostics™) and incubated on ice for 20min with regular vortexing to assist lysis. Samples were then centrifuged for 20min at 17,000g and 4°C to pellet debris. Supernatant was then transferred to a fresh tube and protein concentration determined with DC Protein Assay (Bio-Rad™). Samples were then processed by Dr. Wouter Kallemeijn in the lab of Prof. Ed Tate, using the Copper-catalysed azide-alkyne cycloaddition (CuAAC) with azido-TAMRA-PEG-Biotin (AzTB) capture method as previously described. (Thinon et al., 2014). To summarize, CuAAC ligation reagent (100μM AzTB, 1mM $CuSO_4$, 1mM TCEP, 100μM TBTA) was added to lysates and incubated for 1h at RT. This method results in reaction of YnMyr analogue with AzTB which contains both a TAMRA fluorescent moiety and biotin for further analysis. For in-gel fluorescence precipitated protein sample pellets were resuspended in a of solution of 2% SDS, 10mM EDTA in PBS followed by addition of sample loading buffer (4x NuPAGE LDS sample buffer supplemented with 5:1 ratio of β-mercaptoethanol). Resuspended samples were boiled at 95°C for 5min and loaded onto SDS-polyacrylamide gels for electrophoresis. SDS-PAGE gels

were then washed 3 times with dH_2O and incubated with fixative (40% MeOH, 10% acetic acid, (v/v) in dH_2O) for 20min and again washed 3 times with dH_2O. Fluorescence was detected using Ettan DIGE imager. Loading was either checked by immunoblotting for α-Tubulin or staining gel with Coomassie. For proteomics-based analysis CuAAC w. AzTB processed samples were resuspended in a solution of 2% SDS, 10mM EDTA in PBS and diluted to a final concentration of 1mg ml^{-1} with PBS. Diluted samples were mixed with Pierce™ NeutrAvidin™ agarose resin (Thermo Scientific™) bead slurry (50µl mg^{-1}) and left to incubate for 2h to enrich for Biotin containing proteins. Enriched samples were then processed for Tandem-Mass tag MS analysis as described previously (Thinon et al., 2014). Proteomics data was processed using MaxQuant version 1.6.17.0 with peptide identification of spectra performed using Andromeda search engine against human Swissprot+Isoforms database (September 2020). Label-free quantification (LFQ) was performed using in-built tool in MaxQuant software. LFQ based on peak intensities and ion currents carried of proteins with >3 unique peptides. Sample analysis was performed by Dr. Wouter Kallemeijn in the lab of Prof. Ed Tate (Imperial College London)

2.3.7 Proteomics

Proteomics on IMR90 ER:RAS cells was performed in triplicate with control (DMSO) and senescent (4OHT) cells collected on day 8 after induction. Cells were collected for protein extraction by first washing twice with ice-cold PBS, scraping and centrifugation performed at 180g for 5 min at 4°C. Cell pellets were then resuspended in FASP buffer (1% SDS, 5 mM MgCl2, 10 mM CHAPS and 100 mM triethylammonium bicarbonate (TEAB)) to lyse. Sample preparation was performed previously by Dr. Pia Sogaard. Samples were analysed by Tandem mass tag MS performed and analysed by Proteomics core at Dundee University.

2.5 RNA processing and analysis

2.5.1 Total RNA extraction

Tissue Extraction - Total RNA from tissues was bulk extracted by way of bead disruption in 800µL of TRIzol® reagent (Invitrogen) using TissueLyser (Qiagen) followed by further homogenization using QIAshredder kit (Qiagen) according to manufacturer's instructions. Homogenized tissue in TRIzol® was then mixed with 160µL of Chloroform (Sigma) and vortexed for 15s, then centrifuged at 15,000rpm at 4°C for 30-45 min. Top aqueous phase containing RNA was then column purified using RNAeasy® Mini Kit (Qiagen) and subjected to DNase treatment as per manufacturer's instructions. RNA concentration was determined using NanoDrop® ND-1000 UV-Vis spectrophotometer at 260nm wavelength.

Cell extraction - For extraction of total RNA from cells, 6-well plates were scraped in 800µL of TRIzol® reagent (Invitrogen), mixed with 160µL of Chloroform (Sigma), vortexed and centrifuged as stated above. Aqueous phase was then transferred to a new tube and processed from step 2 onwards of manufacturer's instructions for RNAeasy® Mini Kit (Qiagen).

2.5.2 cDNA generation and qPCR

To generate cDNA, total RNA was diluted in nuclease-free water to the same concentration across samples of the same experiment and 1-5µg amplified using SuperScript® II Reverse Transcriptase kit (Invitrogen). Briefly, RNA was combined with 1µL of random hexamer primers (50ng/µL, Invitrogen), 1µL dNTP mix (10mM, Bioline®) and made up to a final volume of 11µL in nuclease-free water. 4µL of 5x First strand buffer, 1µL of 0.1M DTT and 200U of SSII reverse transcriptase was then added and ran on thermocycler (Bio-Rad Dyad Peiter Thermal Cycler) for one cycle of 10min at 25°C, 50min at 42°C and 15 min at 70°C. cDNA samples were then diluted to 10ng/µL based on input RNA concentration.

mRNA expression analysis was carried out using real-time quantitative PCR (RT-qPCR) by way of amplification of cDNA using SYBR® Green PCR Master Mix (Applied Biosystems) run on a CFX96™ Real-Time PCR Detection system (Bio-Rad). Reactions were performed by mixing 10µL of 2x SYBR Green mix and 5µL of cDNA with 0.5µL of each of the forward and reverse primers (10µM). Samples were loaded in duplicate into wells of an opaque 96-well plate (Hard-Shell® PCR 96-well thin-wall white plate, Bio-Rad). Thermal cycling conditions were as follows: (1.) 2 min at 52ºC (2.) 5 min at 95ºC (3.) 30s at 95ºC (4.) 30s at 60ºC (5.) 15s at 72ºC, 39 more cycles of steps 3-5 were performed with measurement of fluorescence after each step 5. RT-qPCR primers (see Table A4.) were selected from PrimerBank (Wang et al., 2012) spanning exon-exon junctions or flanking intronic region >1kb in size. These primers must also anneal to all transcript variants of gene and produce an amplicon <150bp. Relative gene-expression in human cell lines was determined using $2^{-\Delta\Delta Ct}$ method ($\Delta\Delta Ct = \Delta Ct_{treated} - \Delta Ct_{control}$ / $\Delta Ct = Ct_{target} - Ct_{housekeeping}$ by measuring RT-qPCR signal relative to signal of housekeeping gene RPS14 and normalization to control samples. For mouse mRNA expression, ΔΔCt method was again used but signal measured relative to GAPDH.

2.5.3 RNA-seq

Total RNA extracted and purified from tissues or from cell extraction was analysed on a 2100 Bioanalyzer (Agilent) using RNA 6000 Nano Kit (Agilent) to verify RNA purity and integrity prior to library preparation (Figure 2.1a). RNA extraction from cells was performed previously by Dr. Verena Wagner in lab group. RNA from tissue samples with an RNA integrity number (RIN) corresponding to the ratio of 18S to 28S rRNA peaks on bioanalyzer trace of less than 3 were not submitted for library processing. Library preparation to generate cDNA was performed by MRC – LMS genomics core facility with 200ng of starting RNA using the NEBNext® Poly(A) mRNA magnetic isolation kit (NEB, E7490) to isolate mRNA from total RNA sample. Purified samples were then processed using the NEBNext® Ultra™ II

Directional RNA Library Prep Kit for illumina (NEB, E7760). Libraries were then assessed on a 2100 Bioanalyzer and concentration determined using a Qubit® Fluorometer and the Qubit dsDNA HS Assay kit (Thermo Scientific™). Indexed libraries were then run on 4 lanes of a NextSeq 550 sequencer (Illumina) with > 11 million single end 75bp reads being generated per sample. Mouse RNA-seq reads were assessed for quality using FASTQC and then aligned to mouse genome mm9 by Tophat (v. 2.0.11) using '-library-type- fr-firststrand' parameters along with gene annotation from Ensembl (v.67). Expression levels were determined Gene set enrichment analysis (GSEA) was carried out on the differential expression between vehicle and drug treated aged tissues using "wald statistics" parameters in DESeq2 and all curated gene sets in MSigDB (https://www.gsea-msigdb.org/gsea/msigdb). RNA-seq data analysis was performed by Sanjay Khadayate of the MRC – LMS bioinformatics core.

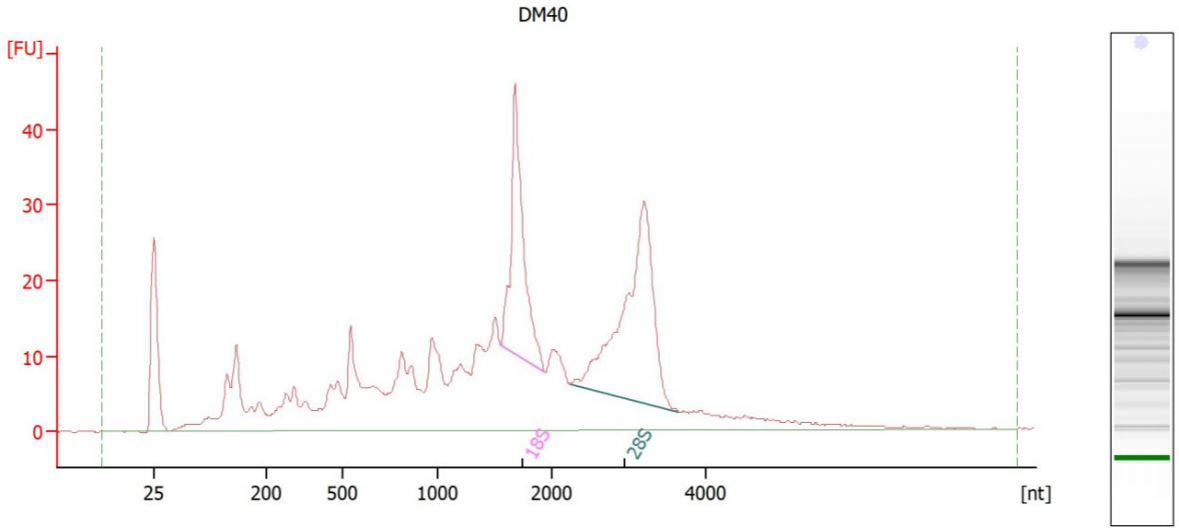

Overall Results for sample 4 : DM40

RNA Area:	622.1	RNA Integrity Number (RIN):	7 (B.02.10)
RNA Concentration:	220 ng/µl	Result Flagging Color:	
rRNA Ratio [28s / 18s]:	1.6	Result Flagging Label:	RIN:7

Fragment table for sample 4 : DM40

Name	Start Size [nt]	End Size [nt]	Area	% of total Area
18S	1,557	1,945	63.6	10.2
28S	2,253	3,642	100.6	16.2

Figure 2.1. Bioanalyzer trace of purified total RNA extracted from aged tissue.

Shown is a representative image of bioanalyzer trace of total RNA extracted from aged lung tissue with acceptable quality of RNA.

2.6 siRNA screening

2.6.1 Druggable-genome siRNA screening and siRNA transfection

Druggable genome-siRNA libraries were purchased from Qiagen (Human Druggable Genome siRNA Set V4.1, 2 siRNA per gene) and Dharmacon™ (siGenome human druggable genome). Individual siRNAs were purchased from the siGenome reagent family of Dharmacon™ (Horizon Discovery) and came lyophilised in tube format or coated onto 96-well plates. Prior to transfection, plates containing 0.1nM of lyophilised siRNA were resuspended in 100µL of nuclease-free water and 3.6µL of siRNA aliquoted into daughter plates. For large-scale libraries, daughter plates were aliquoted using Laboratory Automation Workstation Biomek® NX^P (Beckman Coulter). Transfection mix containing 0.2µL DharmaFECT™ 1 with 17.4µL of DMEM only or 0.4µL DharmaFECT™ 1 with 17.2µL of DMEM were added to daughter siRNA plates for IMR90 ER:RAS or IMR90 experiments respectively. To reverse transfect cells, 100µL suspensions of proliferating or senescent cells in media with DMEM supplemented with 10% FBS only were added to plates with combined transfection mix and siRNA (final siRNA concentration – 30nM). After 18 hours when cells had been allowed to adhere, media was replaced with DMEM supplemented with 0.5% (w/v) FBS and 1% antibiotic-antimycotic solution. Plates were then fixed in 4% PFA (w/v) 72 hours after media change, to then be processed for quantitative IF. For analysis of mRNA, protocol was scaled to a 6-well plate format and cells collected by addition of TRIzol ® RNA isolation reagent (Invitrogen) to well followed by scraping and collection. (see Table A5. for siRNA sequences)

2.6.2 B-score normalization analysis

To analyse siRNA screen, cell counts were normalized by B-score using R package, CellHTS2 (https://doi.org/doi:10.18129/B9.bioc.cellHTS2) (Boutros et al,. 2006). Cell count

normalization were performed using plate-averaging method on separate transfection batches for each control and senescent condition.

2.7 Plasmid generation and amplification

2.7.1 Vector construction

Inducible ER:RAS - Construction of pLNC-ER:RAS-neo has been previously described in work published by our lab (Acosta et al., 2008).

Golgicide A resistant GBF1 mutant - Mutant $GBF1_{M832L}$ construct was a gift from Prof van Kuppeveld (Utrecht University). Cloning was of $GBF1_{M832L}$ intro retroviral expression vector (pBabe-puro,) was performed by first PCR amplification using Human5SnaBIGBF1 and Human3SalIGBF1 primers (see Table A8. For cloning primers used) with Q5® High-Fidelity DNA Polymerase (New England Biosciences (NEB), #M0491) according to manufacturer's instructions. Amplified $GBF1_{M832L}$ was subcloned into pBabe-puro empty vector. Subcloning was carried out by way of purification of PCR product using QIAquick PCR Purification kit (Qiagen, #28104) followed by processing of sample with SnaBI (NEB, R0130) and SalI (NEB, R3138) restriction enzymes according to manufacturer's instructions. Briefly, 1.5µL each of SnaBI and SalI were combined with 15µL of purified PCR product along with 3.5µL of CutSmart® Buffer and made up to a final volume of 35µL in ddH_2O. Reaction was then incubated in a thermocycler at 37°C for 4h and then restriction enzymes inactivated by incubation at 65°C for 20min. Sample was then run on 1% agarose gel and gel purification of processed amplicon at the correct size was then performed using QIAquick gel extraction kit (Qiagen, #28115). Excised gel fragments were first solubilized in 3 volumes of Buffer QG to every 1 volume of gel (1 gel volume – 100mg - 100µl) by incubation at 50°C for 10min with periodic vortexing. If percentage agarose was >1.5%, 6 volumes of QG buffer. 1 volume of 100% isopropanol and 10µl of 3M NaAc (pH 5.0) was added to precipitate DNA and buffer

solution, respectively. Sample was then loaded onto QIAquick spin column and next steps in protocol carried out as per manufacturer's instructions.

Similarly, 5µg of target vector (pBabe-puro) was processed and purified using SnaBI and SalI. To prevent re-ligation of vector with excised fragment, vector sticky-ends were dephosphorylated using QuickCIP kit containing alkaline phosphatase (NEB, M0525). This was carried out by 1h prior to inactivation adding 1µl of QuickCIP phosphatase to reaction tube. If restriction enzyme buffer was not CutSmart®, a separate dephosphorylation would be performed after purification using QIAquick PCR purification kit (Qiagen). Following digestion and dephosphorylation vector was purified using QIAquick PCR purification kit (Qiagen) to remove any contaminants that could inhibit ligation reactions. Both purified/processed insert and vector concentrations were determined using a NanoDrop® ND-1000 UV-Vis spectrophotometer. Ligation of insert was carried in a thermocycler at 16°C for 18h using T4 DNA ligase (NEB, M0202). Ligase was inactivated at 65°C for 10min to minimize probability or vector re-ligation. In a molar ratio of 3:1 of insert:vector DNA was combined with 2µL of T4 DNA ligase buffer and 1µL of T4 DNA ligase and made up to a final volume of 20µL for ligation reaction. All subsequent subcloning detailed was performed in a similar manner as described above with their respective restriction enzymes. Full length GBF1 mutant was sanger sequenced using GBF1seq primers (Table A14.)

NRAS-Gaussia luciferase HDTVI construct - Gaussia luciferase (Gluc) containing plasmid was gifted from Prof Uta Griesenbach (Imperial College London). To generate Gluc expressing HDTVI construct (CaNiGluc), Gluc was PCR amplified using 5'-BmgBI-sogLUX and 3'sogLUX-Age1 primers and Q5® High-Fidelity DNA Polymerase (New England Biosciences) according to manufacturer's instructions. Amplified Gluc was subcloned into HDTVI construct (CaNiG). Gaussia luciferase in vector was subject to sanger sequencing with sogLux primers (Table A13.)

shRNA cloning - Tetracycline inducible (Tet-ON all-in-one) shRNA vector (LT3GEPIR) was gifted from Dr Johannes Zuber (IMP Vienna). Generation of miRE-based inducible shRNA vectors was performed using protocol provided by Dr. Johannes Zuber. Briefly 97-mer oligonucleotides selected from published shRNA datasets (Pelossof et al., 2017) were ordered (IDT ultramers™) (see Table A9. for shRNA sequences) and PCR amplified. PCR was performed using 2.5µL each primers miRE-Xho-Fw and miRE-EcoOligo-rev (10µM) using AccuPrime Pfx DNA Polymerase (Invitrogen) kit according to manufacturer's instructions. Amplicon was then processed with EcoRI and XhoI restriction enzymes and sub-cloned into LT3GEPIR vector. shRNA sequence was validated by sanger sequencing using miREseq primer (Table A13.)

sgRNA cloning – all-in-one Cas9/sgRNA vector (LentiCRISPRv2) or sgRNA only vector (pLentiGuide-puro) were purchased from addgene. sgRNA sequences were designed using the CHOPCHOP webtool (https://chopchop.cbu.uib.no/, v2.0, (Labun et al., 2016) and sense/anti-sense oligonucleotides ordered (IDT ultramers™), see Table A10. for sgRNA oligonucleotide sequences). These oligos were then phosphorylated and annealed using T4 Polynucleotide Kinase (PNK) (NEB, M0201) with 1µL of each oligonucleotide (100µM) and 0.5µL of T4 PNK made up to 10µl in ddH_2O. Reaction was carried out using two steps in a thermocycler (1.) 37°C for 30min (2.) 95°C for 5 min then decrease to 25°C at a rate of 5°C/min. These annealed oligos were then diluted 1:200 and 1µl subcloned into 50ng of BsmBI processed and dephosphorylated LentiCRISPRv2 or pLentiGuide-puro plasmid. Presence of sgRNA sequence was confirmed by sanger sequencing with LKO1.5 primer (Table A13.)

2.7.2 Bacterial transformation

Chemical transformation – Chemically competent bacteria were allowed to thaw on ice prior to the addition of plasmid DNA. For general transformation to amplify plasmids, chemically

competent *E.coli* DH5α were used. In instances were ligation reactions were being transformed, high-efficiency One Shot TOP10® *E. coli* was used. 50µl of bacteria were first mixed with either 5µl of ligation reaction or 50-100ng of plasmid DNA, on ice for 30 min to coat bacteria in DNA. Mixture was the subjected to heat shock by incubation at 42°C for 45s and recovery on ice for 2min. Heat-shocked bacteria were then resuspended in 150µl of pre-warmed LB broth or SOC medium and incubated at 37°C for 1h with horizontal shaking at 220rpm. 20µl of plasmid DNA transformations was diluted 1:2 and streaked-out on pre-warmed LB agar plates with ampicillin (100µg/ml) or other antibiotic depending on plasmid (Zeocin – 25µg/ml , Kanamycin sulfate - 50µg/ml). For ligation reactions 100µl of bacteria was spread over entire surface of LB agar plate with antibiotic. These plates were then incubated at 37°C for 18h and colonies picked for inoculation of 4ml of LB broth with antibiotic. Plasmid DNA was isolated from these cultures using Zymo plasmid miniprep™ kit (ZymoResearch™). Plasmid DNA isolated from ligation reactions was then submitted for sanger sequencing.

Electroporation – Transformation of electrocompetent cells (MegaX DH10B T1, Invitrogen, C6400-03) was carried out as per manufacturer's instructions. Briefly, 1mm of sterile electroporation cuvettes were chilled in a -20°C freezer prior to use. 30µl of electrocompetent bacteria was mixed with 2µl of phenol purified ligation reaction to coat bacteria and incubated on ice for 30min. Transformation mix was then added to bottom of chilled electroporation cuvette, ensuring no bubbles are present that may cause arcing of current. Cuvettes were then wiped dry and placed in Eppendorf Eporator® and -2.0kV applied with time constant of 4-5s. Transformation mix was immediately resuspended in 1ml of pre-warmed recovery medium and placed into a shaking incubator at 37°C for 1h with 220rpm shaking. Transformations were then plated on LB agar plates with antibiotic or flasks with LB broth with antibiotics for further culture.

2.7.3 Plasmid DNA purification

Normal plasmid DNA isolation – Bacteria cultured for 18h were centrifuged for 15 minutes at 6000xg. For standard plasmid isolation for cloning or sequencing the Zymo Plasmid Miniprep kit (Zymo Research™, D4054) was used. 3-4ml bacteria were pelleted and resuspended in P1 buffer (50nM Tris-HCL, pH 8.0, 10mM EDTA, 100µg/ml RNase A) and transferred to fresh Eppendorf. This was then followed by lysis buffer P2 (200nM NaOH, 1% SDS (w/v) and 3 min after P3 buffer (3.0M KAc, pH 5.5) to neutralize lysis reaction. Lysed samples were then centrifuged at 13,000g to pellet precipitate and supernatant transferred to Zymo-Spin IIN (Zymo Research™) plasmid DNA binding column and washed with included wash buffer. Plasmid DNA was eluted from filtration column through addition of TE Buffer.

Endotoxin-free plasmid DNA isolation - For endotoxin free plasmid isolation of midi (50mL) and maxi (200mL) size bacterial cultures, Qiagen Plasmid *plus* Midi (Qiagen) and GeneElute™ HP Endotoxin-Free Plasmid Kits (Sigma-Aldrich) were used respectively. Endotoxin free midipreps were typically performed for lentiviral libraries and plasmids to be used in tissue culture as to prevent endotoxin induced toxicity. Endotoxin free maxipreps were performed for constructs to be used *in vivo* such as in HDTVI. Qiagen Plasmid Midi purification was performed similarly to Zymo Plasmid Miniprep kit mentioned above with the addition of a endotoxin removal buffer (Buffer ETR) wash step. For GeneElute™ Maxipreps, plasmid isolation was performed according to manufacturer's instructions.

2.7.4 Agarose gel electrophoresis

To analyse/isolate fragments generated from cloning and PCR, samples were mixed with 6x DNA loading buffer containing 0.2% (w/v) Orange G and 3% glycerol (w/v) and loaded into wells of a cast agarose gel. Agarose gels were made up with 0.5-2% agarose, depending on fragment size and ethidium bromide (Sigma) added to a final concentration of 0.5µg/ml in

TAE buffer (40mM Tris, 1mM EDTA, 0.1% HAc (v/v), pH 8.0). DNA fragments were separated by application of 90-100V across gel in TAE buffer for 45-60min. This would separate fragments by size based on electrophoretic mobility of DNA. Visualization of DNA and imaging of gel was carried out under UV using the Gel Doc™ XR+ imager (BioRad). Fragments were isolated using clean scalpels before either being frozen or processed with QIAquick gel extraction kit (Qiagen).

2.7.5 DNA sequencing

Sanger sequencing – Standard sanger sequencing of DNA was performed at MRC LMS genomics core using a ABI3730xl DNA analyser (Applied Biosystems). Reactions were performed using 3.2 pmol of sequencing primer and 600ng of purified plasmid DNA or PCR product (TIDE sequencing) in a final volume of 10µl of nuclease-free dH_2O (see Table A13 for sequencing primers used). Sequence analysis was performed using SnapGene™ Viewer or using TIDE analysis software (https://tide.nki.nl/).

2.8 CRISPR and shRNA pooled screening

2.8.1 TIDE analysis

Tracking of Indels by DEcomposition or TIDE was used to analyse indels generated by CRISPR/Cas9 editing as described (Brinkman et al., 2014). Briefly, genomic DNA was isolated from cells using Quick-DNA microprep kit (Zymo, D3020) as per manufacturer's instructions. 50ng of genomic DNA for edited and non-edited samples were PCR amplified using MyTaq Red Mix (Bioline, BIO-25043) and primers flanking >500bp upstream and downstream from predicted sgRNA cut site (See Table A6. for TIDE PCR primers). Thermocycler program for TIDE amplification was as follows: (1.) 95ºC for 1min (2.) 95ºC for 15s (3.) 55ºC for 15s (4.) 72ºC for 1min. Steps 2-4 were repeated for an additional 25 cycles

and samples placed at 4°C. PCR products were purified using QIAquick PCR purification kit (Qiagen). Samples were then sanger sequenced using primers >200bp upstream from predicted cut-side inside amplicon to allow TIDE software to accurately convolute sample (see Table A7. for TIDE sequencing primers). Reference gDNA and edited gDNA sequences were uploaded to TIDE website (https://tide.nki.nl/) and percentage of nonsense or missense mutations determined for each sgRNA.

2.8.2 GECKOv2 library amplification

Pooled sgRNA library against human genome was purchased from Addgene™ (Addgene, # 1000000049) as two half pools at 50ng/µl concentration. Library amplification was performed as outlined in previous studies (Joung et al., 2017). Libraries were transformed into high efficiency TOP10® (Thermo Scientific™) chemically competent cells (see '2.7.2 Bacterial transformation'), with 1 transformation per 1,500 sgRNA in library. 24 transformation reactions for each half pool were plated and spread evenly on 24 large LB agar plates (245mm square bioassay dish) with 100µg/ml of Ampicillin and incubated at 37°C for 12h. In parallel, transformation reactions were diluted to generate 100, 1000 and 10,000-fold dilutions and each spread on 10cm LB agar plates with ampicillin. These would then be used to estimate transformation efficiency at >100 colonies per sgRNA in library. Large agar plates were then scraped in 50ml of LB broth w. Ampicillin and pooled into large bacterial culture flasks. These were then placed in a shaking incubator for 4h at 37°C with 180rpm shaking. Cultures were then collected into 50mL falcon tubes, centrifuged at 15,000g for 10min and bacterial pellets frozen until ready to be purified using Qiagen® Plasmid *Plus* Midiprep kit (*see '2.7.3 Plasmid DNA purification'*). Purified library plasmid DNA for separate pools was then PCR amplified (*see '2.8.5 Next Generation Sequencing (NGS) library generation'*) and submitted for next generation sequencing to verify if library had sufficient representation of sgRNAs.

2.8.3 Custom shRNA library generation

Pooled oligonucleotide amplification - Custom shRNA sequences for library were generated by the lab of Dr Johannes Zuber (IMP Vienna) based on previously published work (Fellmann et al., 2013), with 6 shRNA sequences being generated per target. Library generation protocol was provided by the lab of Dr Johannes Zuber. Pooled oligonucleotide libraries were ordered from Twist Bioscience®, diluted to working concentration of 20ng/µl and aliquoted. From aliquots a working stock solution of 2ng/µl was generated. All library preparation was performed in a shRNA-clean area with pipettes being sterilized beforehand to prevent cross contamination of libraries. Water controls were included at each step to ensure libraries did not become contaminated. 1µL of working stock amplified using Q5® High-Fidelity polymerase kit (NEB, M0491) according to manufacturer's instructions using 2.5µL each of miRE-Xho-Fw and miRE-EcoOligo-rev primers (10µM) (see Table A8.). Thermocycler conditions were as follows (1.) 98ºC for 30s (2.) 98ºC for 10s (3.) 72ºC for 30s (4.) 72ºC for 1 min, with 12 cycles between step 2 and 3. 40 PCR reactions were performed in parallel and pooled into a single tube to be purified using the QIAquick PCR purification kit (Qiagen). Parallel reactions were carried out to ensure enough coverage of shRNAs in library.

Insert & vector processing/ligation - Purified PCR product was then digested with EcoRI and XhoI restriction enzymes as per manufacturer's instructions and run on a 1.5% agarose gel. Lower band on gel (~135bp) was excised and purified using QIAquick gel extraction kit (Qiagen). In parallel, 5µg of Tetracycline inducible (Tet-ON all-in-one) shRNA vector (LT3GEPIR) was digested with EcoRI (NEB, R3101) and XhoI (NEB, R0146) and dephosphorylated using QuickCIP (NEB, M0525). Processed vector was then purified using QIAquick PCR purification kit (Qiagen). Up to six ligation reactions were performed in parallel using a molar ratio of vector:insert of 1:2, in order to minimize probability of concatemers in ligation reaction. Each 20µl ligation reaction used 500ng of processed vector alongside 1µl

of high concentration T4 DNA ligase (2,000,000 U/ml) (NEB, M0202M). Processed vector-only ligation reaction was set up in parallel as a control for re-ligation. Ligation reaction was performed in a thermocycler at 16°C for 18h, followed by heat inactivation at 65°C for 10min.

Phenol DNA extraction - Due to the sensitivity of electroporation to salt contamination ligation reactions were pooled and purified using phenol extraction/precipitation. Briefly, pooled oligonucleotides or processed vector were made up to 300µl in ddH_2O and mixed by vortexing with 300µl of cold equilibrated phenol (pH 8.0, wo. Chloroform, wo. Isoamyl alcohol. Sample was then added to pre-centrifuged 5PRIME Phase lock light gel tubes (QuantBio™, #10847). Sample was then added to phase lock gel tubes and centrifuged at 16,000g for 8min. 250µl of top, aqueous phase was then transferred to a new tube taking care not to disturb gel layer. 25µl of 3M NaAc (pH 5.2) and 1µl of pellet paint (Novagen™, #69049) were then added to buffer aqueous phase and assist in DNA precipitation respectively. DNA was precipitated by addition of 750µl of ice-cold 96% Ethanol, vortexing and incubation for 18h at -20°C. Precipitated DNA was then pelleted by centrifugation at 16,000g for 30min at 4°C. Supernatant was removed and pellet was washed with 70% Ethanol. This was then followed by a centrifugation at 16,000g for 5 min at 4°C, removal of supernatant and air drying of pellet to remove residual ethanol. Pellet was resuspended in 12.5µl of elution buffer (10 mM Tris-Cl, pH 8.5, ddH_2O) (Qiagen, #19086).

Library amplification – To amplify library generated, MegaX DH10B T1 bacteria (ThermoScientific™, C640003) were transformed by electroporation *(see '2.7.2 Bacterial transformation')*. Following electroporation, transformation reactions were pooled in 250ml of LB broth with Ampicillin (100µg/ml) and incubated for 14-16h in a 37°C shaking incubator set at 180rpm. In parallel a single transformation reaction was serially diluted 1:100, 1:1000, 1:10,000 and 1:100,000 and plated on 10cm LB agar plates with ampicillin (100µg/ml). Number of colonies per serially diluted plates was used to determine transformation

efficiency, ideally >5,000 colonies per shRNA in library is needed to maintain sufficient coverage. Large cultures of transformation reactions were aliquoted into 50ml tubes and centrifuged at 15,000g for 10min. Plasmid DNA was purified from pellets using Qiagen® Midiprep Plus Kit *(see '2.7.3 plasmid DNA purification')***.** Library quality was assessed by next generation sequencing prior to usage for screening (*see '2.8.5 Next Generation Sequencing (NGS) library generation'*)

2.8.4 Genomic DNA isolation

High-yield genomic DNA extraction – For isolation of genomic DNA for drop-out screens with large libraries (>10,000 sg/shRNAs), such as a genome-wide CRISPR screen, maximising recovery of gDNA is essential to maintaining high coverage. For this, cells were collected from large 245mm square tissue culture bioassay plates and by scrapping in PBS and pelleted by centrifugation at 180g for 5min. These cell pellets could then be frozen at -80°C for later processing. To extract genomic DNA from cell pellets containing $3x10^7$-$5x10^7$ cells, pellets were first resuspended in 6ml of NK Lysis Buffer (50mM Tris, 50mM EDTA, 1% SDS, pH 8.0) and 30µl of Proteinase K (Qiagen, #19101) at stock concentration 20mg/ml added to sample. Samples were then incubated in water bath for 18-24h at 55°C until homogenous. RNA was removed from sample by adding 30µl of RNase A at 10mg/ml (Qiagen, 19101) and mixing by inversion, samples were then incubated at 37°C for 30min. Proteins were then precipitated from solution by addition of 2ml chilled 7.5M ammonium acetate solution in dH_2O vortexing for 20s and centrifugation at 4000g for 10min. Supernatant was then transferred to a fresh tube containing 6ml of 100% Isopropanol, and inverted 50 times to precipitate DNA. Genomic DNA was then pelleted by centrifugation at 4,000g for 10min. Pellet was then washed twice with 6ml of 70% Ethanol after centrifugation for 1min. Remaining ethanol was removed and pellet left to air dry for 30min. Genomic DNA was then eluted by adding 500µl of TE Buffer (10 mM Tris-HCl, 1mM EDTA, pH 8.0) and incubating in a 65°C waterbath for

1hr and leaving at room temperature overnight. Genomic DNA sample concentration was then determined on a NanoDrop® ND-1000 UV-Vis spectrophotometer at 260nm wavelength.

High-purity genomic DNA recovery – Unless high yield is required to maintain coverage, genomic DNA isolation was typically performed via phenol extraction as performed for ligation reactions to be electroporated *(see '2.8..3 Custom shRNA library generation – phenol DNA extraction').* As with high-yield protocol cells were collected by scrapping in PBS, centrifugation at 180g for 5min and storage at -80°C. For phenol extraction, cell pellet was resuspended in 400µl of DNA extraction buffer (10mM Tris-HCl, 150mM NaCl, 10mM EDTA, pH 8.0) and 4µl each of a 10% solution of SDS and 20mg/ml stock of Proteinase K added to samples. These samples were then digested by incubation at 55°C for 18h. Sample was then resuspended in phenol and extracted as normal.

2.8.5 Next Generation Sequencing (NGS) library generation

GECKOv2 screen – Next generation sequencing library generation protocol was adapted from (Joung et al., 2017). After genomic DNA was isolated sgRNA cassette was amplified using NEBNext High Fidelity PCR kit (NEB). PCR was optimized for genomic DNA loaded (1-10µg). With 5µg being non-inferior to the recommended 2.5µg >700X coverage in genomic DNA was PCR amplified from screen per sample. (1 cell = ~6.6x10^{-12}g of DNA). Each reaction was carried out by combining 25µl of 2x NEBNext High Fidelity PCR Master Mix, with 5µg of genomic DNA and 1.25µl each of unique forward primers (see Table A11. for GECKOv2 NGS library primers) and reverse sequencing barcode primers (final concentration – 0.25µM). PCR mix was made to a final volume of 50µl. Usage of unique forward barcodes increases diversity in sequencing library and a barcode primer allows for pooling of libraries into the same lane of a NextSeq 550 flow cell. PCR reaction tubes were placed in a thermocycler with the following protocol: (1.) 98°C for 3min (2.) 98°C for 10s (3.) 63°C for 10s (4.) 72°C for 25s (5.)

72°C for 2 min, with 28 cycles repeated for steps 2-4. PCR reactions were then pooled together using the QIAquick PCR purification kit (Qiagen) and half was stored at -20°C for backup processing. The remaining half was loaded onto a 2% (w/v) Agarose gel and fragments of ~260-270bp excised (Figure 2.2a) and purified using the QIAquick gel extraction kit (Qiagen). Samples were then run on a 2100 Bioanalyzer (Agilent®) using a DNA high sensitivity 6000 Kit (Agilent) to confirm presence of a single peak (Figure 2.2b). Quantification of DNA was performed using the Qubit dsDNA HS Assay Kit as per manufacturer's instructions.

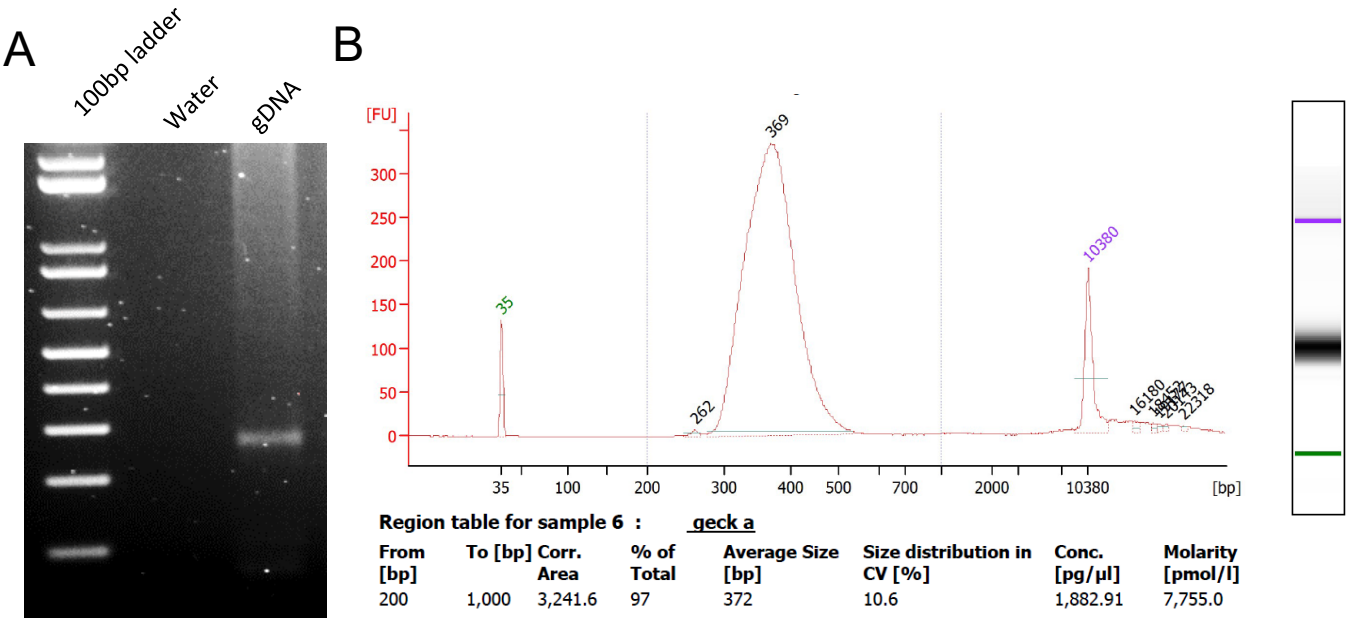

Figure 2.2. Quality control of GECKOv2 CRISPR libraries

(A) Representative gel electrophoresis showing PCR product of GECKOv2 library cassette from genomic DNA at predicted size of 270bp. Water control indicates no contamination of PCRs.

(B) Shown is a representative bioanalyzer trace of GECKOv2 cassette PCR product showing single peak indicating product successfully purified.

shRNA screen - Next generation sequencing library construction protocol was obtained from the lab of Johannes Zuber (IMP Vienna). After genomic DNA was isolated using *High purity genomic DNA recovery* method, shRNA cassette was amplified using a nested PCR. Briefly, 1µg of DNA was combined with Amplitaq Gold PCR kit containing 0.5µl Amplitaq gold

polymerase, 1µl of dNTPs (10mM), 5µl 10xPCR buffer. These were combined with 1.5µl of P5 and P7 primers (10µM each). P5 primer contained i5 adaptor sequence for illumina sequencing platform, P7 the i7 adaptor along with barcode sequence. (see Table A12. for list of library primers used). PCR sample was then made up to 50µl and placed in thermocycler using the following program: 1.) 95 ^{o}C for 10min (2.) 95 ^{o}C for 30s (3.) 55 ^{o}C for 45s (4.) 72 ^{o}C for 45s (5.) Cycle step 2-3 for 9 more cycles (6.) 95 ^{o}C for 30s (7.) 63 ^{o}C for 45s (8.) 72 ^{o}C for 45s (9.) Cycle step 6-8 22 more times (10.) 72 ^{o}C for 7 min. Number of PCR reactions was scaled up to generate sufficient coverage (>1000X) of genomic DNA samples. PCR samples were then pooled and purified using the QIAquick PCR purification kit (Qiagen) and half was stored at -20°C for backup processing. The remaining half was loaded onto a 1.5% (w/v) Agarose gel and fragments of ~370bp excised (Figure 2.3a) and purified using the QIAEX II gel extraction kit (Qiagen) as per manufacturer's instructions. Samples were then run on a 2100 Bioanalyzer (Agilent) using a DNA high sensitivity 6000 Kit (Agilent) to confirm presence of a single peak (Figure 2.3b). Quantification of DNA was performed using the Qubit dsDNA HS Assay Kit as per manufacturer's instructions.

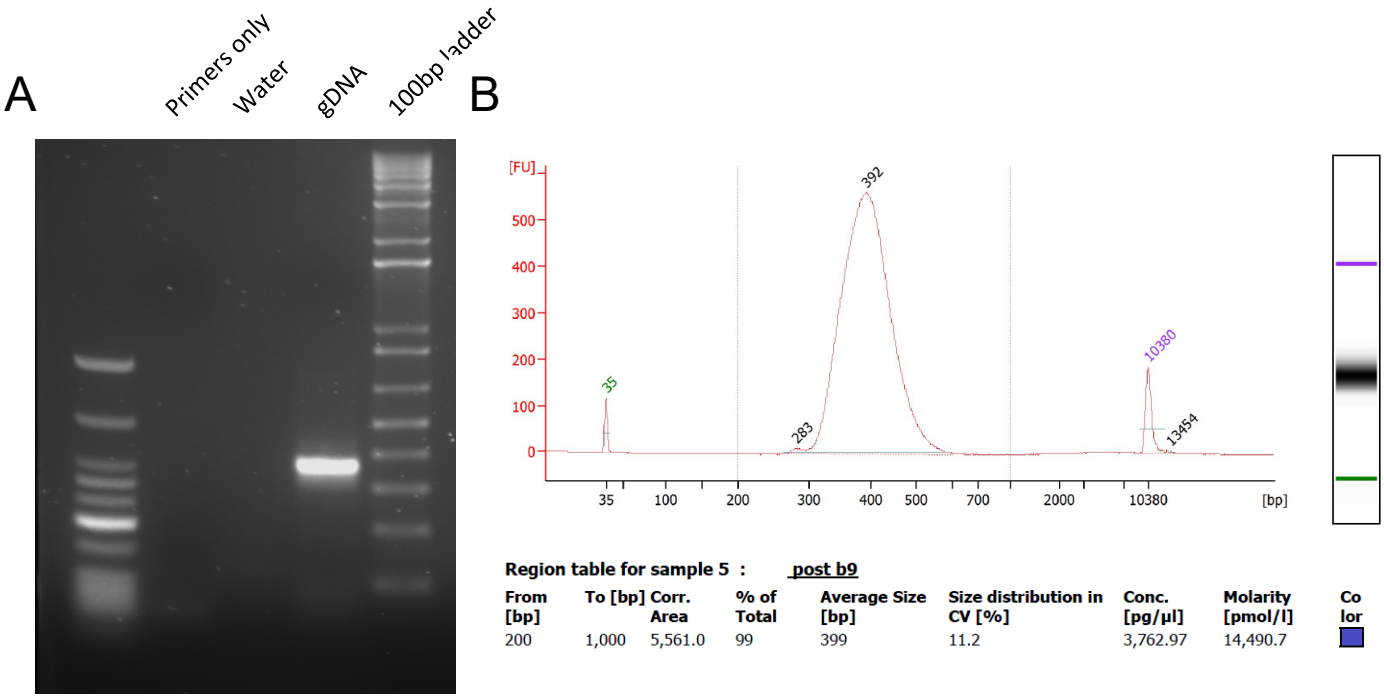

Figure 2.3. Quality control of custom shRNA libraries

(A) Representative gel electrophoresis showing PCR product of shRNA cassette from genomic DNA at predicted size of 370bp. Water control indicates no contamination of PCRs.

(B) Shown is a representative bioanalyzer trace of GECKOv2 cassette PCR product showing single peak indicating product successfully purified.

2.8.6 Next Generation Sequencing (NGS)

Deep sequencing of amplified library samples was performed on an Illumina NextSeq550. After quality control, barcoded library samples were pooled together in equal quantities and 6pM loaded across required number of lanes of flow cell. For GECKOv2 libraries paired-end 100bp runs were performed with sgRNA sequences being detectable on Read1 (Figure 2.4a). Custom shRNA libraries were sequenced using single-end 50bp run (Figure 2.4b). For primers used in NGS sequencing see (Table A12.). Bioinformatic analysis and alignment of reads was performed by Sanjay Khadayate of the MRC – LMS bioinformatics core.

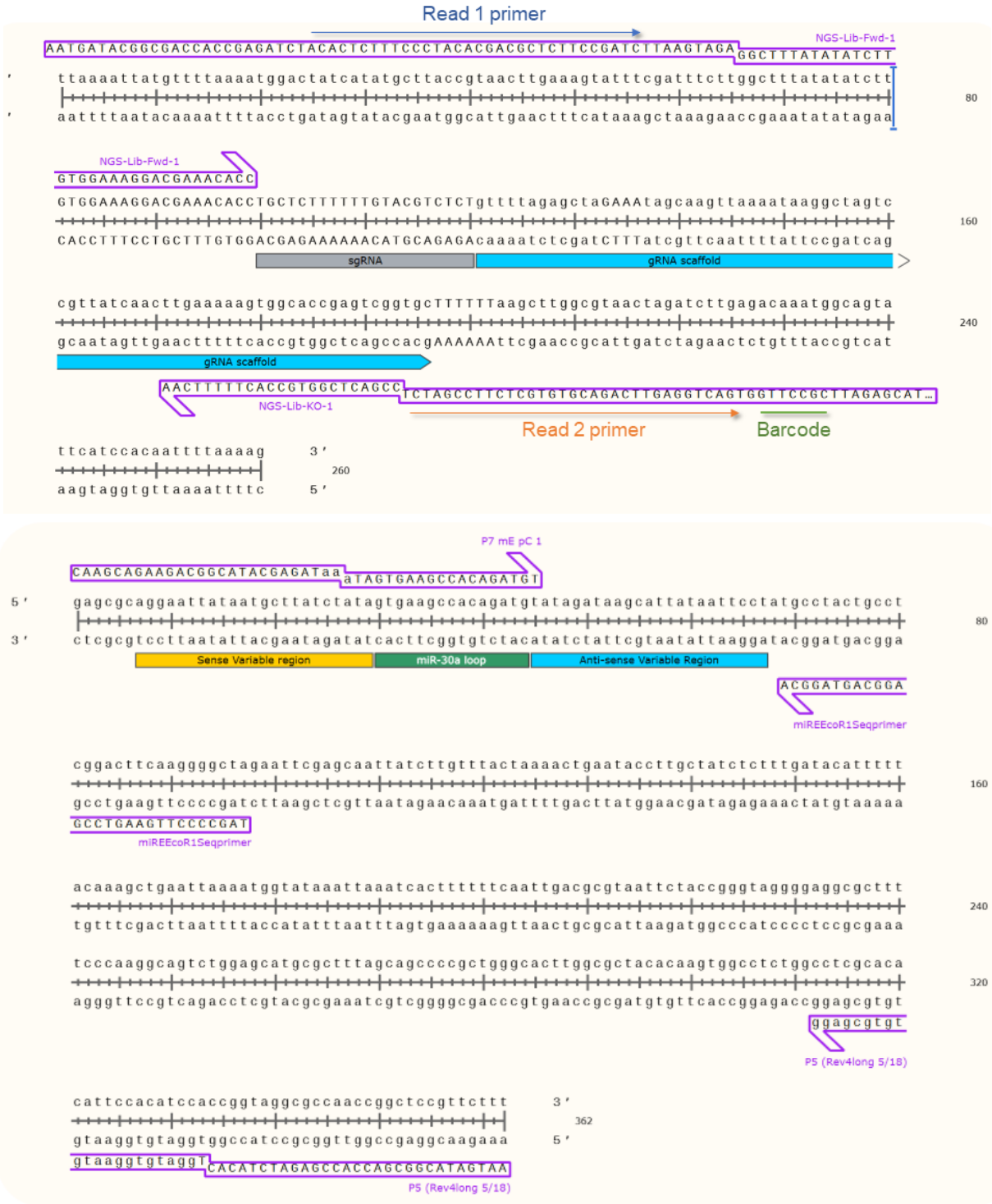

Figure 2.4. GECKOv2 & shRNA NGS sequencing strategy

(A) Shown is summary of GECKOv2 sgRNA cassette sequencing strategy. Forward primers containing illumina read 1 primer binding sites with adaptor sequences, and reverse containing read 2 primer binding sites with adaptor sequences were used to amplify sgRNA cassette from pLentiGuide-puro vector. Read 1 deconvolution was used to detect sgRNA sequence and Read 2 index barcode sequences.

(B) Shown is sequencing strategy used for custom shRNA library. Forward and reverse primers with illumina adaptor sequences were used to amplify anti-sense variable region of shRNA cassette in pRRL-Tet-on vector. Single-end reads were generated using miREEcoR1seqprimer.

2.9 Animal studies

2.9.1. Mouse models

All mice were purchased from Charles River UK, Ltd. Mouse handling and tissue sectioning performed by Dr Bin Sun and Joaquim Pombo in the lab. For Hydrodynamic tail vein injection (HDTVI) experiments female C57BL/6J mice aged 5-6 weeks were given 20μg of $Nras^{G12V}$ & *gaussia* luciferase (Gluc) expressing plasmid and 5μg of SB13 transposase-expressing plasmid. Plasmids were prepared using GeneElute HP Endotoxin-free Plasmid Maxiprep kit (Sigma). Purified plasmids were diluted in sterile-filtered PBS to a total volume of 10% mouse body weight and injected into mouse lateral tail vein within a 10s window. 4 days after HDTVI, mice were bled to assess presence of gaussia luciferase signal in the blood serum and used to randomize/equalize groupings for vehicle and drug treated groups. On day 5 mice were given 25 mg/kg of IMP1320 (n=9) or Vehicle (n=9) (10mM Na_2HPO_4-7H2O & NaH_2PO_4H2O buffer, 0.2% Tween-80, pH 7.4) intraperitoneally (i.p.) daily for 4 days and every 48 hours' blood collected for assessment of serum gaussia signal. 24 hours after last drug injection mice were culled and livers collected for paraffin embedding and frozen in Optimal cutting temperature (OCT) using liquid N_2.

For cancer xenograft experiments, $6.7x10^5$ 5PT cells ± $2x10^6$ HFFF2 cells were resuspended in 100μl PBS and injected subcutaneously (s.c.) in the flanks of immunocompromised, male NSG mice (3-5 months old). At least 7 biological replicates were used per group. Tumour size was measured over time using an electronic calliper and calculated using the formula 4π/3 x r3 [radius (r) calculated from the average diameter, measured as the tumour width and length]. The area under the curve (AUC) for each individual tumour within a treatment group for single experiments was analysed by homoscedastic two tailed Student's t-test. For multiple experiments it was analysed by ordinary Two Way Anova using as two independent variables 'the experiments' (factor 1) and 'the treatments (factor 2), and as dependent

variable ‘the AUC’ of each mouse; then, we looked at just factor 2. Cancer xenograft experiments were performed by Dr. Massimiliano Mellone in the lab of Gareth J Thomas (Cancer Sciences Unit, CRUK, University of Southampton)

For testing senolytics ex vivo in the ACP model of OIS, neoplastic pituitaries from 18.5dpc Hesx1Cre/+;Ctnnb1lox(ex3)/+ embryos were dissected. For the lung fibrosis experiments, we used a previously described mouse model of lung fibrosis induced by intratracheal administration of senescent human cells (Triana-Martínez et al., 2019). Normal proliferating (IMR90 vector) or gamma-irradiated senescent human fibroblasts IMR90 (IMR90 vector, IMR90 shCOPB2.1 or IMR90 shCOPB2.2) were delivered into the lungs of immunodeficient nude mice (Envigo Laboratory). Two days before intratracheal instillation, these animals started treatment with doxycycline (1mg/ml, per oral) until the end of the experiment. Three weeks after intratracheal instillation, their lungs were removed and analysed.

For aging experiments C57BL/6J mice aged 109-111 weeks were injected with 10 mg/kg of DDD86481 (n=6; 4 p16+/+ and 2 p16+/luc (Burd et al., 2013)), or vehicle (n=6; 4, p16+/+ and 2, p16+/luc) i.p. once a day as described in the timeline of Fig. 7A. DDD86481 was dissolved by cold water bath sonication in 5% DMSO, 20% PEG400, 10mM Na_2HPO_4-7H2O & NaH_2PO_4H2O buffer, 0.5% Tween-80, pH 7.3. At the end of the experiment, mice were culled, collecting organs for freezing in OCT, paraffin embedding and collecting blood for serum-isolation. Data for the full cohorts (n=6 for DDD86481 and vehicle) are presented, but similar results are observed considering only the wildtype (p16+/+) mice. All mouse procedures were performed under licence, according to UK Home Office Animals (Scientific Procedures) Act 1986 and local institutional guidelines (for University College London, Imperial College or Southampton University ethical review committees) or performed in compliance with guidelines established by the Barcelona Science Park's Committee on Animal Care (CEEA 10884).

2.9.2 Detection of Gaussia luciferase activity in blood

Gaussia luciferase detection in serum – Whole blood from tail-vein of mice was collected into heparinised tubes (Abraxis™) at least 4 days after they had received HDTVI treatment with gaussia luciferase expressing construct. Tubes were then centrifuged at 1000g for 10 min at 4°C to pellet cells and serum supernatant was then collected for storage at -80°C until use. Gaussia luciferase activity was measured using the FLUOstar omega microplate reader and the Pierce™ Gaussia Luciferase Glow Assay Kit (Thermo Scientific™, #16160). Briefly, 10μL of serum was combined with working solution containing 100X Coelenterazine substrate diluted in provided Glow assay buffer in an opaque white 96-well plate (Thermo Scientific™, # 236108). To minimize bias between signal measurement and pipetting order, in-built injector on the FLUOstar was used to deliver 50μL of working solution and immediately measure signal. Correction for time between each well measurement was also performed as to not skew measurement of later wells. Measurements for luminance were obtained every 2 minutes over a 30-minute time-course and corrected against a sample with serum from mice not having received HDTVI. Gaussia signal is shown as area under the curve (AUC) for luminance measurements from 0 min to 30 min.

2.9.3 Immunohistochemistry (IHC)

Tissue Processing - Organs/specimens were fixed in 4% PFA overnight before being transferred to 70% Ethanol. Tissue processing prior to paraffin-embedding was performed on a Sakura Tissue-Tek VIP® 6 automated tissue processor. Briefly, specimens in embedding cassettes were dehydrated by progressing through steps of 70% Ethanol for 45min at 37°C, 80% Ethanol for 45min at 37°C, 90% Ethanol for 30min at 37°C, 96% Ethanol for 45min at 37°C, 100% Ethanol for 30min at 37°C, 100% Ethanol for 1hr at 37°C, 100% Ethanol for 1hr at 37°C. Dehydrated samples are then cleared by three washes in Xylene for 30min, 45min and 1hr at 37°C. Finally, specimens are infiltrated by two immersions in 62°C paraffin wax for

45 min and 1hr, followed by two immersions in 62°C paraffin wax for 30min. Specimen was then embedded in paraffin-block on an embedding centre (Leica™ EG1160 Embedding Centre) and 4μm sections made using Thermo Scientific™ Microtome Microm HM355S and attached to slides.

Immunohistochemical staining - Slides were deparaffinised by washing slides twice in Histoclear™ for 5 min each, followed by 5min washes in decreasing concentrations of ethanol with 100%, 75%, 50% & 25% ethanol washes before a final wash 5 min in dH_2O. Heat induced epitope retrieval (HIER) was then performed in pressure cooker for 20 min using either antigen-unmasking solution, Citrate-based at pH 6.0 (VectorLab, H-3300-250) or antigen-unmasking solution, Tris-based at pH 9.0 (VectorLab, H-3301-250) depending on antibody manufacturer's instructions. Following HIER, slides were cooled on ice for 10min and then washed in PBS for 5 min. For intracellular stains, sections were permeabilized with 0.2% Triton X-100 in PBS for 10min and washed twice in PBS for 5 min. For NRAS staining in Liver slides were washed in 0.1% H_2O_2 in PBS for 15 min followed by washing twice in PBS to reduce endogenous peroxide activity. Sections were marked using hydrophobic pen and Non-specific antigen binding was blocked by incubating slides with CAS-Block™ Histochemical reagent (ThermoFisher, 008120) for 30-45 min in a humidified chamber. Slides were then incubated with primary antibody overnight in a humidified chamber at 4°C. Slides were washed twice in PBS for 5 min and incubated with secondary antibody SignalStain® Boost IHC detection reagent Mouse/ Rabbit, HRP (Cell Signalling Technology, 8125) for 30-45 min. Next, slides were washed twice in PBS for 5 min and incubated for 2-10min with SignalStain® DAB substrate kit (CST, 8059) to detect HRP signal. Signal development was stopped when visible positive cells could be detected on a microscope, by washing slides in dH_2O. To counterstain DAB signal, slides were incubated for 30s in Modified Mayer's Haematoxylin (Lillie's Modification) (DAKO™), washed in dH_2O, and incubated for 30s in

0.05% Ammonium solution (PBS) followed by washing in dH_2O. Prior to mounting coverslips with VectaMount aqueous mounting media (VectorLab, H-5501-60) slides were dehydrated by washing 1min in 75% Ethanol, 5 min in 100% Ethanol and 5 min in Histoclear®.

Slide image acquisition & analysis - Slides were acquired using a 20x brightfield objective on a Zeiss AxioScan Z.1 slide scanner and analysis performed using QuPath version 0.2.0-m9 using in built positive cell detection tool to segment Haematoxylin stained nuclei and quantify mean intensity of DAB.

2.9.4 Histologic analysis of the mouse fibrosis experiment.

Left lung tissue was fixed in 10% neutral buffered formalin solution for 24 hours and subsequently transferred into tissue cassettes and placed into PBS for a minimum of 24 hours. Tissues were then shipped to Institute for Research in Biomedicine (IRB, Barcelona) Histopathology Facility for paraffin embedding, sectioning, and Masson's Trichrome and Hematoxilin-Eosin stainings. Samples were examined first in blinded fashion and in a second round in an unblinded fashion. Semiquantitative histological scoring of fibrosis was scored at 20-40x magnification using the following scale: 1, x1; 2, x2; 3, x3 increase the thickening of alveolar walls; 4, >x3 thickening of alveolar walls and focal areas of single fibrotic masses. If there was difficulty in deciding between two scores, the intervening number was given. Mouse fibrosis experiments were performed Dr. Fernanda Hernández-González in the lab of Manuel Serrano (Institute for Research in Biomedicine (IRB Barcelona))

2.9.5 Hydroxyproline assay

Superior and middle lung lobes were surgically dissected, weighed, and placed into 1.5-mL sterile tubes and flash-frozen until all the samples were collected. Homogenates of the lung samples were performed grinding the frozen samples with liquid nitrogen using a mortar and pestle. On the day of the assay, tissues were thawed, and 1 mL of distilled water was added

to the tissues. Tissues were homogenized using a microsample homogenizer (Precellys). 200 µL of 12N hydrochloride was added to 200 µL of homogenized tissues. Samples were placed into a preheated oven set to 120ºC and incubated overnight. The next morning, samples were cooled and vortexed. Biochemical quantification of hydroxyproline was performed using a hydroxyproline assay kit (Amsbio). Mouse fibrosis experiments were performed Dr. Fernanda Hernández-González in the lab of Manuel Serrano (Institute for Research in Biomedicine (IRB Barcelona))

2.9.6. Cytochemical senescence associated-β-galactosidase assay

Tissue samples frozen in optimal cutting temperature (OCT) were cryosectioned (15µM) and frozen sections fixed in ice-cold 0.5% Glutaraldehyde (w/v, PBS) for 15 min and washed 1mM $MgCl_2$/PBS (pH 6.0) for 5 min. β-galactosidase activity was stained for with X-gal staining solution (1mg ml^{-1} X-gal, Thermo Scientific™, 5mM $K_3(Fe(CN)_6)$, 5mM $K_4(Fe(CN)_6)$) for 18h at 37ºC. Slides were dehydrated and coverslips mounted prior to being imaged using 20x brightfield objective on Zeiss AxioScan Z.1 slide scanner. ImageJ was used to quantify staining by measuring the β-gal stained area as a percentage of the total tissue area excluding luminal spaces.

For *in vitro* staining for Senescence Associated-β-galactosidase activity, 6-well plates were fixed with a solution of 0.5% glutaraldehyde (w/v, PBS) (Sigma) for 10 min and washed twice in solution of 1mM $MgCl_2$/PBS (pH 6.0). To stain plates were incubated with X-gal staining solution for 18h at 37ºC. Images were acquired by brightfield microscopy using an inverted microscope (Olympus CKX41) with attached digital camera (Olympus DP20). Cells were counted using ImageJ software to determine percentage positive cells.

2.9.7. Oil Red O staining

Oil Red O staining for lipids was carried out on liver tissue in OCT was snap-frozen in liquid N_2 and cryosectioned (15μM). Sections were equilibrated to RT for 10 min and then stained with 0.5% Oil Red O solution (w/v, in isopropanol, Sigma, O1391) for 5 min, rinsed in tap water and counterstained with Mayer's haematoxylin for 30s. Then sections were again rinsed in tap water for 30min and coverslips mounted. Images were acquired on Zeiss AxioScan Z.1 and ImageJ quantification of Oil-red stain area relative to background tissue area performed for 3 fields per section.

2.9.8. Sirius Red staining

Sirius red staining was carried out for collagen I / III fibre containing connective tissue on paraffin embedded sections using Pico-Sirius Red Stain Kit (Abcam, ab150681). Prior to staining, sections were deparaffinised in Histoclear and graded ethanol washes as described above (*see Immunohistochemical staining)* and hydrated in distilled water. Sections were then incubated with Pico-Sirius red solution for 60 min at Rt and then rinsed twice with 0.5% glacial acetic acid solution (in dH_2O). Excess water was then removed by shaking slides and then rinsing in 100% ethanol. Sections were then dehydrated by two washes 100% ethanol for 2 min each and two washes in Histoclear for 2 min each. Coverslips were mounted and slides imaged on Zeiss AxioScan Z.1. Staining was quantified by thresholding collagen stained area for detection of fibres (red) and measuring this area relative to the total cytoplasmic area (yellow).

2.9.9. Ex vivo pituitary culture

Neoplastic pituitaries from 18.5dpc Hesx1Cre/+;Ctnnb1lox(ex3)/+ embryos were dissected and placed on top of 5 μM Nuclepore membranes (VWR™) in 24 well plates containing 500 μl of media (DMEM-F12, Gibco, 1% Pen/Strep, Sigma and 1% FBS, Thermo Fisher

Scientific™) supplemented with either IMP1088 or vehicle (DMSO). Media was changed every 24h, pituitaries were processed for analysis after 72 hours. Immunofluorescence staining was performed as previously described (Mario Gonzalez-Meljem et al., 2017). The proportion of β-catenin-accumulating cells was calculated as an index out of the total DAPI-stained nuclei. Over 120,000 DAPI nuclei were counted from 15 to 22 histological sections per sample, in a total of eight neoplastic pituitaries. The proportion of cleaved-caspase-3 and synaptophysin positive cells was calculated as an index out of the total tissue area, from 6 to 12 histological sections per sample. All *ex vivo* pituitary culturing, treatment and section analysis was performed by Romain Guiho in the lab of Prof J.P. Martinez-Barbera (UCL Institute of Child Health)

2.10 Statistical analysis

Statistical analyses were performed and plotted using GraphPad Prism™ 9 software and Microsoft Excel. Details of test used are given in the corresponding figure legends. Corrections for multiple comparisons were performed using the Holm-Šídák method.

Chapter 3 – siRNA screenings for senolytic targets

3.1 Introduction

The promise of senolytics in their ability to act as a prophylactic therapy for many age-related diseases, necessitates the identification of wide range of robust targets that minimize toxicity to normal cells. As our group has demonstrated previously, senolytic targets can be specific to a particular mode of induction such as oncogene or therapy-induced senescence (Guerrero et al., 2019). Modality specific senolytics could allow for a more targeted elimination of senescent cells in a specific disease context. During aging however (*see 1.2.1 Senescence & aging stress triggers*), senescence does not appear to be mediated through a single specific damage stimulus. Senolytics that can kill many types of senescent cells could be therapeutically more efficacious in increasing healthspan of patients and targeting age-related diseases.

Genetic screens have proved invaluable in elucidating both regulators of senescence induction and the SASP phenotype (Georgilis et al., 2018; Gil et al., 2004; Tordella et al., 2016). Unbiased genetic screenings has led to the discovery of many novel liabilities of cancer cells (Moffat et al., 2014). However, no such unbiased genetic screenings for liabilities of senescence have been performed, with most genetic screening libraries being curated based on transcriptomic data or subsets of genes (Zhu et al., 2015). Screening a druggable siRNA library could provide the starting point for identifying new senolytic targets.

3.2 Cellular models of therapy and oncogene induced senescence

Senescence can be induced through a variety of stresses. Although most senescence responses share markers such as expression of p21, $p16^{INK4a}$ and induction of DDR, phenotypes such as the SASP production and the role of autophagy vary significantly between them (Roy et al., 2020). Given that several already known senolytic targets implicate the SASP and autophagy in senescent cell survival (Dörr et al., 2013; Fuhrmann-Stroissnigg et al., 2017), it is therefore important to perform parallel screens, to highlight senolytic targets with broad specificity. In the case of OIS, this has the added benefit of identifying targets that are not just toxic due to a synthetic lethal effect with the oncogene, RAS^{G12V} in our case. Screening for targets relevant to oncogene-induced senescence and chemotherapy-induced senescence could potentially yield a way to target both cancer and pre-neoplastic lesions (Guerrero et al., 2019) and alleviate post chemotherapeutic fatigue (Demaria et al., 2017). Additionally, using these senescence modalities provides a robust and rapid means of senescence induction, juxtaposed to replicative or metabolic-stress induced senescence which are more stochastic and emergent and could potentially reduce penetrance of hits.

The inducible expression of a chimeric form of the ligand-binding domain of estrogen receptor fused to oncogenic $HRAS^{G12V}$, termed ER:RAS, is a well-established model of senescence in our lab that has been previously used for large scale-screening (Georgilis et al., 2018; Tordella et al., 2016). Here, the treatment of cells with 100nM 4-OHT (4-Hydroxytamoxifen) for 6 days results in the induction of constructively signaling oncogenic $HRAS^{G12V}$ and senescence induction (Figure 3.1a). A stock of human IMR90 fibroblasts that could be induced to undergo oncogene-induced senescence were generated by retrovirally infecting them with ER:RAS construct (pLNC-ER:RAS) and vector control (pLXSN). Cells infected with ER:RAS undergo rapid growth arrest with incorporation of BrdU significantly reduced after 5 days post 4-OHT treatment relative to both, DMSO treated IMR90 ER:RAS

cells (Figure 3.1b). A reduction in colony formation was also observed over a 14-day culture (Figure 3.1c) indicating that cells that had expressed ER:RAS had undergone a stable growth arrest, characteristic of senescence. 4-OHT treated IMR90 ER:RAS cells also displayed significantly elevated expression of $p16^{INK4a}$ and $p21^{CIP1}$ (Figure 3.1d & e), key tumor suppressive pathways upregulated during senescence. These senescent cells also display high levels of senescence associated β-galactosidase activity (SA-β-gal) (Figure 3.1f) as well as IL-6 and IL-8 expression (Figure 3.1g & h). Importantly, IMR90 ER:RAS cells were amenable to screening, being highly enriched for senescence with upwards of 60% of cells being positive for senescence markers.

Drugs such as bleomycin, doxorubicin or etoposide are primarily used in the treatment of cancers (Chabner and Roberts, 2005). Doxorubicin intercalates into DNA during replication and inhibits the activity of topoisomerases thereby causing DNA damage and induction of apoptosis or senescence (Tacar et al., 2013). To assess whether therapy induced senescence was amenable to screening, IMR90 cells were treated with chronic dose of Doxorubicin (Figure 3.2a). Doxorubicin treatment resulted in rapid reduction in BrdU incorporation (Figure 3.2b) and a stable growth arrest (Figure 3.2c). Again, similar to IMR90 Doxorubicin treatment also resulted in increased expression of tumor suppression genes $p16^{Ink4a}$ and $p21^{Cip1}$ (Figure 3.2d & e). This was also coupled with increased levels SA-β-gal activity (Figure 3.2f). Chemotherapeutic treatment resulted in robust enrichment of the cell population for senescent cells, suggesting it too was amenable to screening.

To assess the senolytic effect of siRNAs, cells must be transfected after senescence is fully established - thereby minimizing the probability of detecting synthetic lethal effects related to senescence establishment. Screening for senolytics in early senescence may not yield hits that could eliminate resident fully established senescent cells in aged tissues. In addition, some senescence phenotypes such as the SASP, are late senescence phenotypes that early

timepoint screening may not necessarily leverage for toxicity. Given the potential toxicity of siRNA transfections (Breunig et al., 2007) it was therefore important to choose a chemotherapy treatment regime that had minimal induction of apoptosis as to minimize the probability of detecting hits due to general toxicity. We examined apoptosis induction with our chronic doxorubicin treatment strategy compared with two other chemotherapies with acute treatment windows. Chronic doxorubicin treatment displayed significantly lower levels of cleaved caspase-3 staining than treatment with other chemotherapies such as bleomycin and etoposide, indicating lower levels of apoptosis (Figure 3.2g).

The presence of senescence markers in both IMR90 ER:RAS cells and doxorubicin treated IMR90s alongside the reduced apoptosis of doxorubicin compared with other chemotherapeutic treatments highlighted these systems as preferable for large-scale screening for senolytics targets.

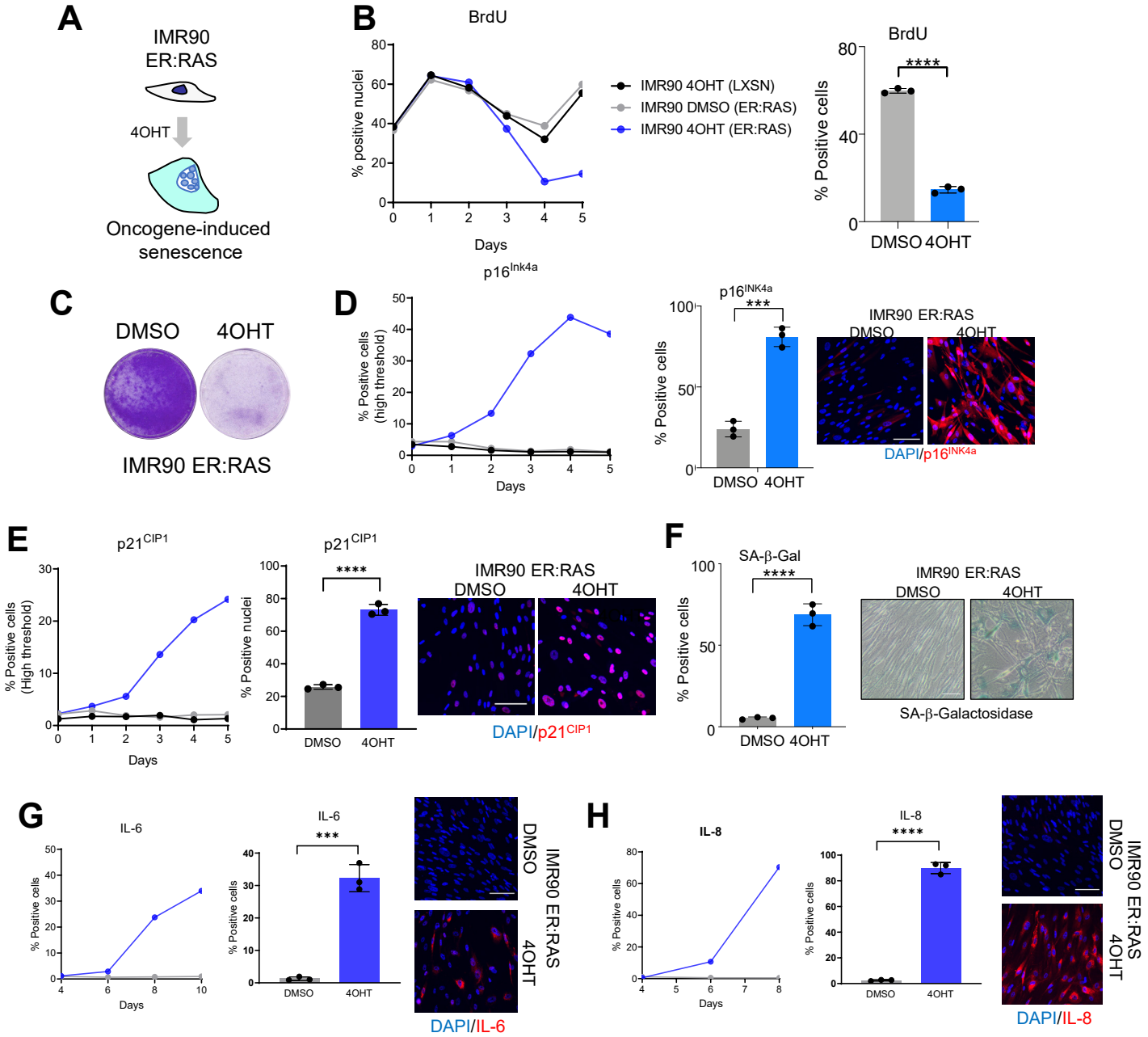

Figure 3.1 IMR90 ER:RAS as a model of oncogene-induced senescence

(A) Outline of IMR90 ER:RAS system for modelling oncogene-induced senescence (OIS). Treatment for 7 days with 100nM 4-OHT induces ER:RAS, triggering OIS.

(B) Quantification of IF staining for BrdU incorporation in IMR90 ER:RAS cells. (Left) timecourse of BrdU incorporation (n=2) (Right) 5 days after treatment with 4-OHT or DMSO (n = 3). Data represented as mean±SD, ****p < 0.0001. Unpaired, two-tailed, Student's t-test.

(C) Crystal violet staining of control (DMSO) or senescent (4OHT) IMR90 ER:RAS cells 14 days after induction. Shown is representative image of three independent experiments.

(D) Time course quantification (left, high threshold, n=2) of percentage of cells staining positive for p16INK4a in IMR90 ER:RAS cells, (Centre) 5 days after treatment with 4-OHT or DMSO (n = 3). (Right) panels show representative IF images for p16INK4a staining. Scale bar, 100µm. Data represented as mean±SD, ***p < 0.001. Unpaired, two-tailed, Student's t-test.

(E) Time course quantification (left, high threshold, n=2) of percentage of cells staining positive for p21CIP1 in IMR90 ER:RAS cells, (Centre) 5 days after treatment with 4-OHT or DMSO (n = 3). (Right) panels show representative IF images for p16INK4a staining. Scale bar, 100µm. Data represented as mean±SD, ****p < 0.0001. Unpaired, two-tailed, Student's t-test.

(F) Quantification (left) of percentage of cells staining positive for SA-β-galactosidase activity in IMR90 ER:RAS cells 5 days after treatment with 4-OHT or DMSO (n = 3). Right panels show representative brightfield images. Scale bar, 100µm. Data represented as mean±SD, ****p < 0.0001. Unpaired, two-tailed, Student's t-test.

(G & H) Time course quantification (left, n=2) of percentage of cells staining positive for IL6 (G) and IL8 (H) in IMR90 ER:RAS cells, (Centre) 8-10 days after treatment with 4-OHT or DMSO (n = 3). (Right) panels show representative IF images for staining. Scale bar, 100µm. Data represented as mean±SD, ***p < 0.001, ****p < 0.0001. Unpaired, two-tailed, Student's t-test.

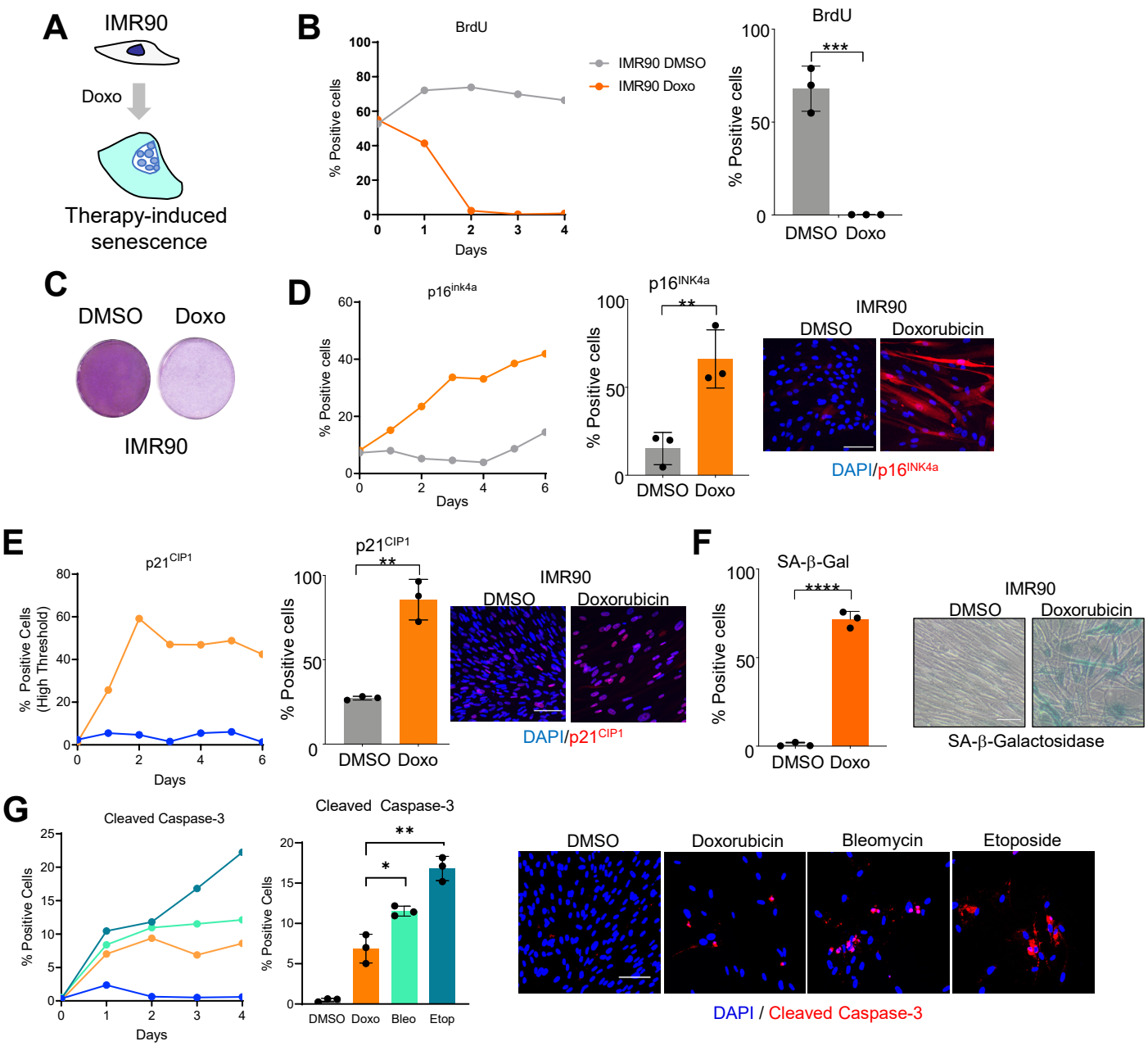

Figure 3.2 Treatment of IMR90 cells with doxorubicin as a model of therapy-induced senescence

(A) Model of therapy-induced senescence (TIS). Senescence was induced by 7 days of 100nM doxorubicin treatment in IMR90 cells.

(B) Quantification of IF staining for (Left) timecourse of BrdU incorporation in IMR90 cells, (Right) 2 days after treating with doxorubicin or DMSO (n = 3). Data represented as mean±SD, ***p < 0.001. Unpaired, two-tailed, Student's t-test.

(C) Crystal violet staining of control (DMSO) or senescent (Doxo) IMR90 cells 14 days after induction. Shown is representative image of three independent experiments.

(D) Time course quantification (left, high threshold, n=2) of percentage of cells staining positive for p16INK4a in IMR90 cells, (Centre) 3 days after treatment with Doxo or DMSO (n = 3). (Right) panels show representative IF images for p16INK4a staining. Scale bar, 100µm. Data represented as mean±SD, **p < 0.01. Unpaired, two-tailed, Student's t-test.

(E) Time course quantification (left, high threshold, n=2) of percentage of cells staining positive for p21CIP1 in IMR90 cells, (Centre) 6 days after treatment with Doxo or DMSO (n = 3). (Right) panels show representative IF images for p21CIP1 staining. Scale bar, 100µm. Data represented as mean±SD, **p < 0.01. Unpaired, two-tailed, Student's t-test.

(F) Quantification (left) of percentage of cells staining positive for SA-β-galactosidase activity in IMR90 cells 7 days after treatment with Doxo or DMSO (n = 3). Right panels show representative brightfield images. Scale bar, 100µm. Data represented as mean±SD, ****p < 0.0001. Unpaired, two-tailed, Student's t-test.

(G) Time course quantification (left) of percentage of cells staining positive for cleaved caspase-3 in IMR90 cells, (Centre) 3 days after treatment with 100nM Doxorubicin, 33µM Bleomycin, 1µM etoposide or DMSO (n = 3). (Right) panels show representative IF images for staining. Scale bar, 100µm. Data represented as mean±SD, *p < 0.05. Unpaired, two-tailed, Student's t-test.

3.3 Optimizing druggable siRNA screens for senolytics targets

For screening of potential senolytics targets, our lab had a 96-well formatted Qiagen™ siRNA library targeting Human Druggable genome, kinases and G-protein coupled receptors (GPCR) in limited quantity that would be used to screen OIS. Along with this we acquired a Dharmacon siGenome™ siRNA library targeting - druggable genome, kinase, phosphatases, GPCR, Ubiquitin conjugating enzymes, proteases and ion channels – for expanded screening in TIS. To increase the likelihood of detecting senolytics candidates, we sought to optimize siRNA transfection settings and control siRNAs in order to provide the largest dynamic range for effect (Figure 3.3a).

Firstly, multiple Dharmafect™ concentrations per well were tested by reverse transfection of a fluorescently tagged siRNA, siGlo™ (Dharmacon®), into both senescent and non-senescent IMR90 ER:RAS cells at day 6, when cells were fully senescent. 0.2µL of Dharmafect 1 provided a high percentage (>60%) of cells with detectable siGlo™, with higher concentrations being non-superior (Figure 3.3b). Importantly, senescent cells displayed comparable levels of transfection, indicating transfectability of senescent and non-senescent cells was not a potentially bias factor for siRNA screening.

As senescent cells were to be reverse transfected by re-seeding onto plates coated with siRNA when they had become senescent, it was pertinent to confirm that the differences in re-seeding numbers observed between senescent and non-senescent cells wasn't biasing transfection and knockdown efficiency. To this end, IMR90 ER:RAS cells were infected with vector containing GFP (pRLL-shRenilla) and subsequently transfected with siRNAs against GFP at a range of different seeding densities. No significance difference in GFP knockdown was detected between seeding densities when compared against scrambled non-targeting siRNA (Figure 3.3c).

Assessment of the dynamic range of the screen would require the use of a positive control to determine which timepoint gives the best differential toxicity between senescent and non-senescent cells. Previous screens in our lab for bypassers of senescence and regulators of the SASP have used canonical regulators of these processes, such as p53/p21 and NF-κB, as positive controls (Georgilis et al., 2018; Tordella et al., 2016). With regards to essential genes in senescent cells only a few candidates exist as a positive control and several of them are context specific (Baar et al., 2017; Yosef et al., 2016; Zhu et al., 2015). A small 96 well custom siRNA library plate containing both wells with 4 pooled siRNAs per gene and deconvoluted siRNAs against a range of potential positive control targets obtained from published literature and unpublished screens from the lab were tested for their senolytics effect. A senolytic drug or target should selectively kill senescent cells but have minimal effects on proliferating or quiescent cells. Therefore, for all experiments testing senolytic drugs or RNAi/CRISPR, cells are placed in low-serum conditions. This was done to induce quiescence and thereby not underestimate toxicity, as further cell division could replace cells that have died due to toxicity, underestimating off-target effects. Cell survival in our siRNA screen for positive controls was determined through high throughput microscopy and measured relative to dH_2O transfected cells. Survival was measured relative to dH_2O transfected control to observe if potential toxicities from non-targeting siRNAs were present. siTOX™ (Dharmacon) was included as a toxic RNA control. Senescent cells transfected with pooled siRNAs targeting both BCL2L1 and FOXO4 showed reduced survival matching observations of the effects of known senolytics ABT-737 and FOXO4-DRI (Baar et al., 2017; Yosef et al., 2016) (Figure 3.3d). When deconvoluted into individual siRNAs, only BCL2L1 siRNAs displayed a senolytic effect with multiple siRNAs, in contrast to 4 different non-targeting siRNAs with no significant reduction in survival in either growing or senescent cells (Figure 3.3e). The effect of BCL2L1 siRNAs was comparable to the effect of ABT-263, a BH3

mimetic and known senolytic that targets BCL2 family protein (Chang et al., 2016). The robust senolytic effect detected with multiple siRNAs against BCL2L1 was subsequently leveraged for further optimization in OIS and TIS.

Optimization of the transfection timings showed that for an siRNA against BCL2L1, the best senolytic index - or the largest difference between senescent and control cells - was produced between day 5-7 after senescence induction in both OIS and therapy induced senescence(Figure 3.3f). Day 7 siRNA transfections for IMR90 ER:RAS (Figure 3.3g) and day 6 for IMR90 cells treated with doxorubicin produced the highest senolytic effect (Figure 3.3h). These optimization experiments had provided us with a potent positive control target, timing for the maximum differential toxicity between control and senescent cells and transfection settings that maximize knockdown without biasing the screen.

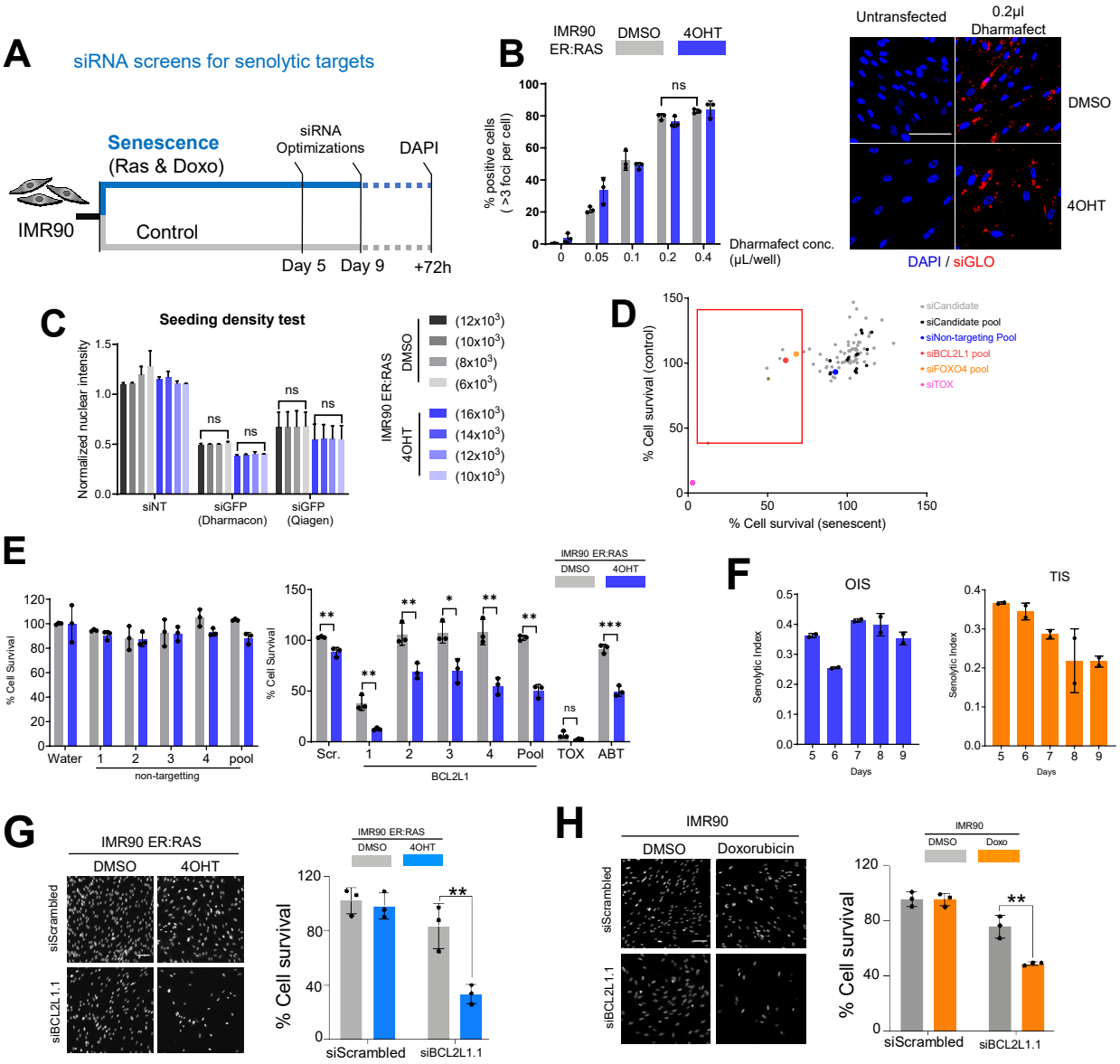

Figure 3.3 Optimization of the siRNA screen for senolytic targets

(A) siRNA optimization strategy. Senescent and control cells were transfected with siRNAs between Day 5 and Day 9

(B) Quantification of transfection efficiency (left) as percentage positive cells with >3 siGLO foci and representative IF images (right) of day 5 senescent (4OHT) and control (DMSO) IMR90 ER:RAS cells 72h post transfection with siGLO (n=3). Data represented as mean±SD. Scale bar, 100µm; ns, not significant. Unpaired, two-tailed student's t-test.

(C) (left) Quantification of GFP levels 72h after siRNA transfection with either control (DMSO) or day 5 oncogene-induced senescent (4OHT) cells seeded at densities ranging from 6-12x10^3 control or 10-16x10^3 senescent per well. (n=2). Data represented as mean±SD; ns, not significant. Ordinary Two-way ANOVA.

(D) Screening of potential positive control siRNAs. Data represented as percentage cell survival in control (DMSO) versus senescent (4OHT) cells. Each point represents mean of three replicates. Candidate considered hit if senescent cell survival was < 60% and difference between control and senescent survival > 20%.

(E) Percentage cell survival of cells transfected with deconvoluted siRNAs on day 6 from positive control siRNA screen in the context of OIS (4OHT) and control cells (DMSO) (n=3). Data represented as mean±SD. *p < 0.05, **p < 0.01, ***p < 0.001; ns, not significant. Unpaired, two-tailed student's t-test.

(F) Timepoint optimization experiments for senolytic positive control. Quantification senolytic index (difference in survival between control and senescent cells) shown for (left) oncogene-induced senescence and (right) therapy induced senescence transfected with BCL2L1.1 siRNA between day 5 and day 9 after senescence induction. (n=2). Data represented as mean±SD.

(G) Quantification of cell survival (right) and representative DAPI stained IF pictures (left) of senescent (4OHT) and control (DMSO) IMR90 ER:RAS cells 3 days post transfection with BCL2L1 siRNA (n=3). Data represented as mean±SD. **p < 0.01; ns, not significant. Unpaired, two-tailed, Student's t-test. Scale bar, 100 µm.

(H) Quantification of cell survival (right) and representative DAPI stained IF pictures (left) of doxorubicin-induced senescent (Doxo) and control (DMSO) IMR90 cells 3 days post transfection with BCL2L1 siRNA (n=3). Data represented as mean±SD. **p < 0.01; ns, not significant. Unpaired, two-tailed, Student's t-test. Left panel shows representative DAPI stained IF images. Scale bar, 100 µm.

3.4 siRNA screening for senolytic targets in a model of oncogene-induced senescence

To identify novel senolytic targets in cells that have undergone OIS, 4OHT treated IMR90 ER:RAS cells were plated in parallel to DMSO treated control cells. Parallel siRNA screenings were performed 7 days after cells had been induced to senesce (Figure 3.4a). This was done by reseeding the senescent and non-senescent cells into 96 well plates, in triplicate, transfecting and then imaging for DAPI cell counts using high throughput microscopy. Plates had been pre-coated with siRNAs aliquoted from the master plates of the Qiagen® Druggable genome siRNA library, with each well containing 2 pooled siRNAs for a single target. First and last columns of the plates were left empty so that positive (siBCL2L1) and negative control siRNAs along with dH_2O controls could be added. Due to the large number of plates, siRNA transfections were performed in batches over several days, with all replicate plates being performed on the same day to minimize freeze thawing of the library. Performing transfections in different batches, potential edge-plate effects and inter-plate variability on not only candidate siRNA wells but our positive controls could invariably lead to identification of false-positive hits. To account for these potential effects, B-score normalization was applied to each well's cell count (Figure 3.4b). B-score normalization compensates for changes in cell number due to the aforementioned batch and inter-plate effects by using a plate-median normalization method. This assumes that given the randomized nature of large libraries there should be similar numbers of cells between plates (Boutros et al., 2006). In addition, the location of a well within a plate is taken into account to reduce biases in cell number changes due to edge effects. Our external control siRNAs against BCL2L1 produced a significantly lower B score in senescent cells than compared to control cells, correlating to a lower level of survival (Figure 3.4c) indicating that the screen settings worked as intended.

Filtering was then applied to the initial list of 6,961 gene targets. A B score of less than -3 in 4OHT treated cells – correlating to three standard deviations (SD) lower than average plate

median - in at least two replicates was used first as criteria for filtering candidates. This highlighted 127 genes targeted that had toxicity towards senescent cells (Figure 3.4e & f). Of these, 62 genes targeted displayed preferential toxicity towards senescent over control cells, with B-scores 2 less than the growing B score used as a filter (Figure 3.4f).

Arrayed type screens often, as is the case here, rely on pooling of siRNAs as to not make screening prohibitively labor intensive. A drawback of this is identification of false-positives due to potential off-target effects. A secondary screen was therefore performed using 4 individual, deconvoluted siRNAs for each of the 127 siRNA gene pools with ability to kill senescent cells. Candidates that only produced an effect with 1 siRNA were filtered out in order to exclude targets were most likely off-targets. 6 genes had 2 or more siRNAs producing a senolytic effect with survival 20% less than the control cell survival (Figure 3.4g & h). Amongst these candidates identified, BCL2L1 - that we had used as an external positive control, re-tested, thereby providing additional validation of the screen as an internal positive control. Two of the candidates encoded for components of the Coatomer-complex I (COPB2 & COPG1) (Figure 3.4h), proteins involved in the formation of Golgi-budding vesicles with roles in maintaining intra-Golgi dynamics and retrograde ER-Golgi transport. Ubiquitin C (UBC) is another candidate, suggesting that OIS cells could be sensitive to inhibition of proteasome function. ALDOA, is a fructose-biphosphate aldolase, a key enzyme in the glycolysis metabolic pathway, a pathway altered during senescence. Finally, GNG8 a G-protein coupled receptor GTPase was also identified as a senolytic target.

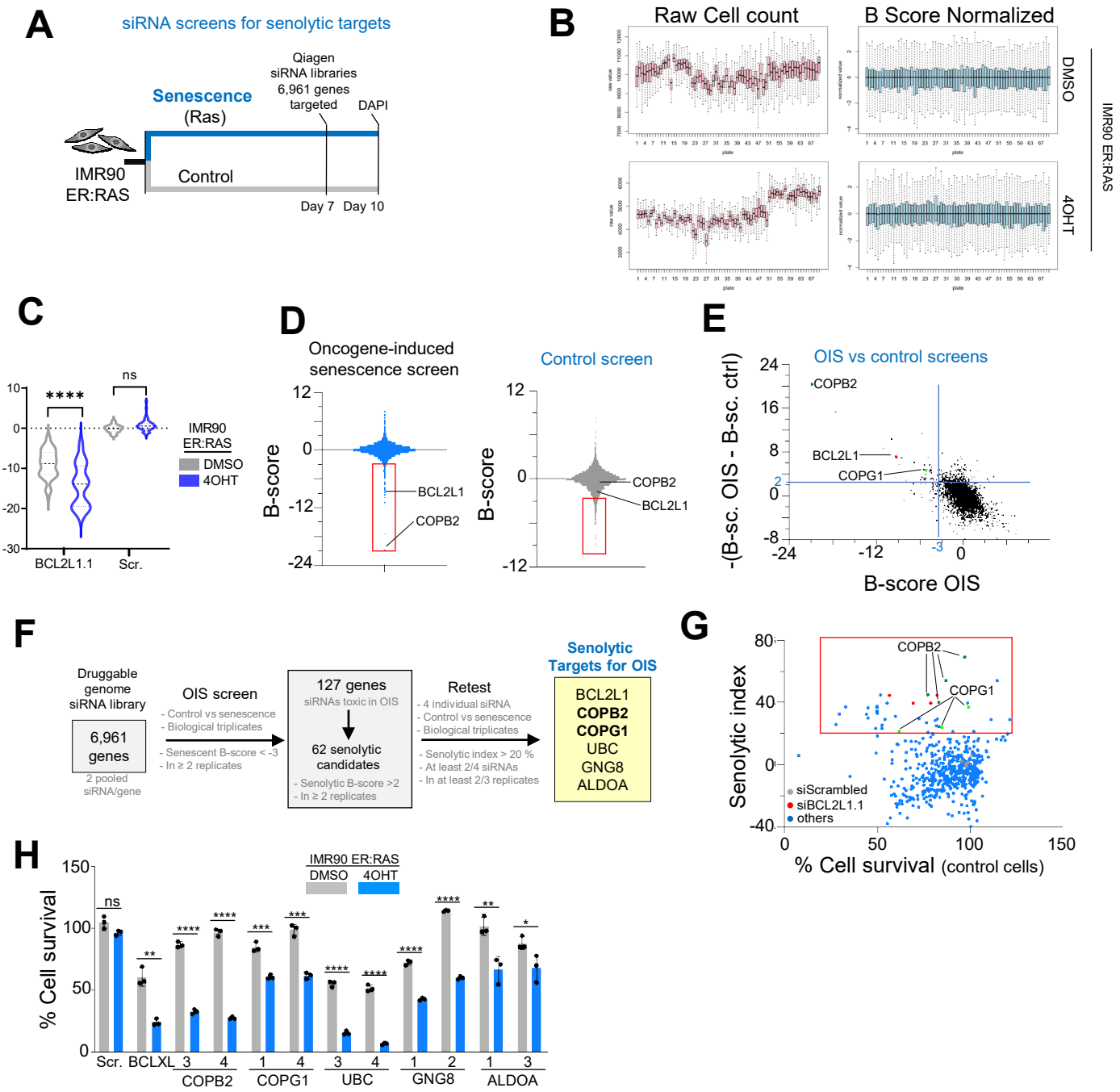

Figure 3.4 siRNA screening for novel senolytic targets in oncogene-induced senescence

(A) Experimental design for the RNAi screens to identify senolytic targets in model of oncogene induced senescence.

(B) B score normalization of screen cell counts. (Left) Panels show averaged raw cell counts for plates transfected on the same day for control (DMSO) and senescent (4OHT) cells. (Right) Panels show plate averages for normalized cell counts (B-score).

(C) Results of the primary siRNA screen for senolytic targets in OIS. Normalized cell counts shown as B-score. Candidate considered a hit if B-score in ≥2 replicates was <-3.

(D) B score normalization of cell numbers shown for the siRNA screen performed on (left) senescent (4OHT) and (right) control, non-senescent (DMSO treated) IMR90 ER:RAS cells. Points shown normalized values for 3 replicates.

(E) Screen results for control (DMSO-treated IMR90 ER:RAS) and OIS (4OHT-treated IMR90 ER:RAS). Graph displays B-score in OIS versus the negative of the difference in B score between OIS and control screens. Points show normalized values for 3 replicates with cut-offs shown for OIS B-score < -3 and a difference in B score of > 2 between control and OIS cells.

(F) Summary of the siRNA screen for senolytic targets in OIS.

(G) Re-test of OIS screen candidates. Data represented as percentage cell survival in control cells versus the difference in cell survival between control and senescent cells (senolytic index). Each point represents the mean of three replicates. Candidate was considered a hit if senolytic index >20% with siRNAs in ≥2 replicates.

(H) Percentage cell survival of best candidate senolytic siRNAs shown in the context of OIS (4OHT) and control cells (DMSO) (n=3) Data represented as mean±SD. *p < 0.05, **p < 0.01, ***p < 0.001, ****p<0.0001; ns, not significant. . Unpaired, two-tailed, Student's t-test.

3.5 siRNA screening for senolytic targets in a model of therapy-induced senescence

Screening for senolytic candidates for therapy-induced senescence was performed similarly to our screenings in IMR90 ER:RAS cells. Doxorubicin treated IMR90 cells were transfected with the Dharamcon™ druggable genome siRNA library set. This library contained 4 pooled siRNAs per well against a single gene target. As some of the candidates that re-tested from OIS screen, such as UBC, were toxic to the control screening samples but later displayed senolytic effect upon re-testing/deconvolution, we decided not to perform a parallel control in the primary screen. siRNA screening was therefore performed in triplicate for doxorubicin treated IMR90s, 6 days after treatment (Figure 3.5a). The same B-score normalization method was used to account for positional and batch effect biases in the screen data (Figure 3.5b). Reduced B scores of control siRNAs against BCL2L1 compared to non-targeting siRNA again validated this screen (Figure 3.5c). The same filtering criteria were applied to narrow the list of 7,582 genes to 121 gene targets (Figure 3.5d & e). A secondary screen was performed by deconvolution of the siRNAs present in the library pools (Figure 3.5f) and from these, 5 genes produced a senolytic effect of 15% lower survival in senescent compared to control cells, with at least 2 siRNAs. Amongst these again we identified siRNAs targeting BCL2L1, validating our screening approach. TREM2 a lipoprotein receptor involved in inflammatory signaling and APOC2 a lipoprotein was identified as senolytic targets. Of particular interest, two senolytic targets belonged to the pathways of candidates identified in the OIS screen. The first is the ubiquitin pathway, with UBB re-testing in doxorubicin induced senescence and UBC in oncogene-induced senescence. The other, being the coat proteins of the Coatomer complex I (COPI), COPB2 and COPG1 detected in OIS screens and ARF1, a GTPase that regulates assembly of the COPI coat.

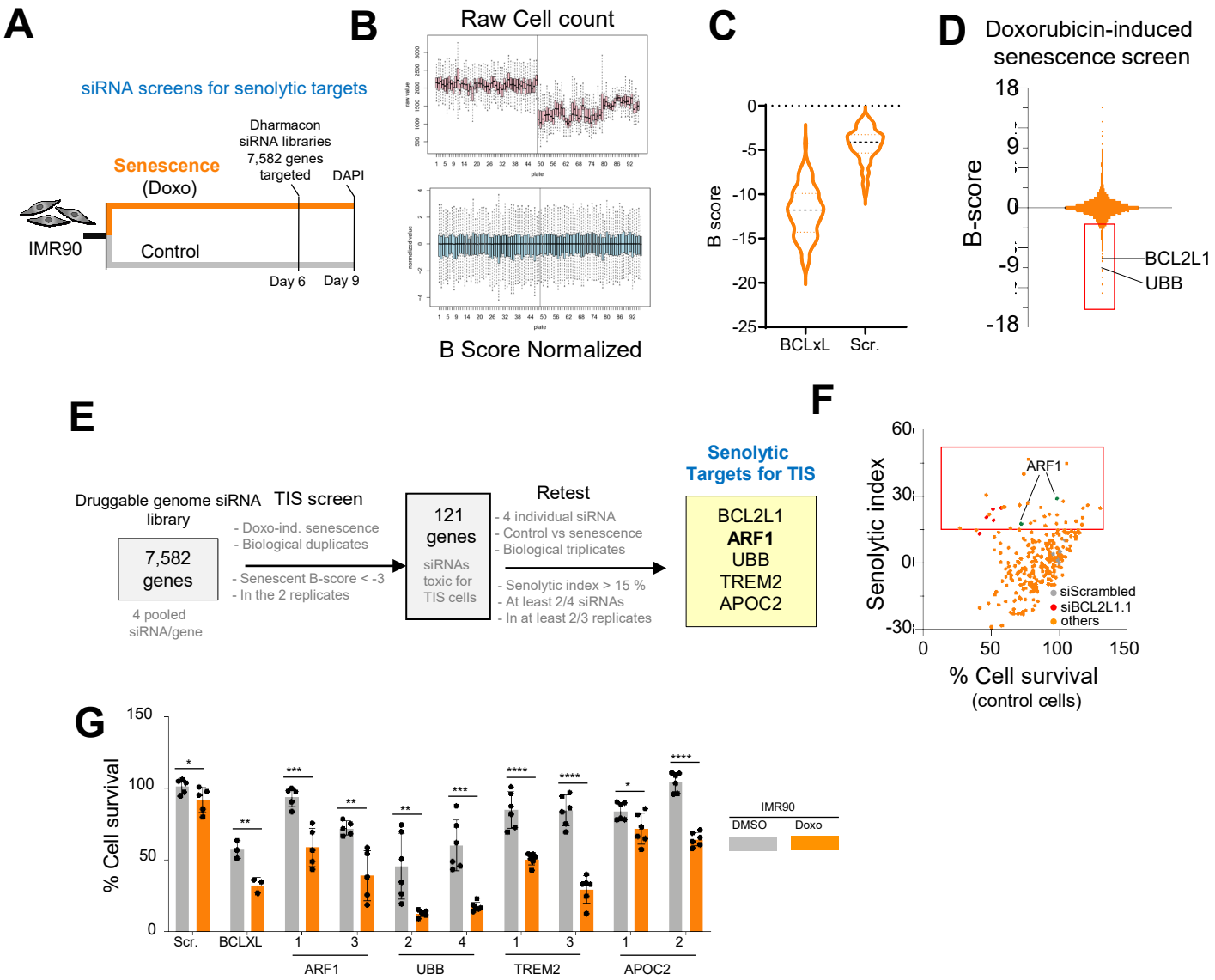

Figure 3.5 siRNA screening for novel senolytic targets in therapy-induced senescence

(A) Experimental design for the RNAi screens to identify senolytic targets in model of therapy induced senescence.

(B) B score normalization of screen cell counts. (Top) Panels show averaged raw cell counts for plates transfected on the same day for senescent (Doxo) cells. (Bottom) Panels show plate averages for normalized cell counts (B-score).

(C) Results of the primary siRNA screen for senolytic targets in doxorubicin-induced senescence. Normalized cell counts shown as B-score. Candidate considered a hit if B-score was <-3 in ≥2 replicates. **(D)** B score normalization of cell numbers shown for the siRNA screen performed on control, non-senescent (DMSO treated) IMR90 ER:RAS cells. Points shown normalized values for 3 replicates.

(D) Summary of the siRNA screen for senolytic targets in doxorubicin-induced senescence.

(E) Graph showing results of re-testing doxorubicin-induced senescence senolytic candidates with deconvoluted siRNAs. Data represented as percentage cell survival in control cells versus the difference in cell survival between control and senescent cells (senolytic index). Each point represents the mean of three replicates. Candidate was considered a hit if senolytic index >15% with siRNAs in ≥2 replicates.

(F) Percentage cell survival of best candidate senolytic siRNAs for doxorubicin-induced senescence (Doxo) and control cells (DMSO) (n=6, for DMSO and 4OHT treated cells, n=3 for BCLXL siRNA transfected cells). Data represented as mean±SD. *p < 0.05, **p < 0.01, ***p < 0.001, ****p<0.0001; ns, not significant. Unpaired, two-tailed, Student's t-test.

3.6 Summary & Discussion

Arrayed screening for senolytics has been performed previously both with drug libraries in our own lab (Guerrero et al., 2019), and with others using siRNA libraries curated based on transcriptomic data of senescent cells (Zhu et al., 2015). Our screening approach in this project however combines the unbiased approach of a genome-scale library with the precise gene-level targeting offered by siRNAs. The screening of the human druggable genome with siRNAs identified several novel senolytic targets for oncogene induced senescence and therapy induced senescence. Three pathways were common in both screening contexts.

When screening for liabilities in cells that overexpress RAS, as is the case with IMR90 ER:RAS cells, it is important to account for targets that are synthetic lethal with RAS expression, rather than those that are true liabilities of senescent cells. However, pathways being detected in both senolytic screens suggests an effect on senescent cells. This is the case for the BCL2 family, Ubiquitin proteins and COPI vesicle trafficking. BCL2 family proteins are already known to be robust, albeit a clinically limited senolytic target. COPI vesicle trafficking and Ubiquitin proteins are both essential parts of protein homeostatic machinery of the cell, with the former regulating secretion (Beck et al., 2009) and the latter essential for functional proteasomal function (Pickart and Eddins, 2004).

Chapter 4 – Genome wide CRISPR/Cas9 screens for senolytic targets.

4.1 Introduction

The ability of arrayed type screening to identify regulators of novel senolytics pathways has been demonstrated in this project and elsewhere (Guerrero et al., 2019; Wang et al., 2017a). The scale of these types of screens is limited due to their labor intensiveness. A solution to this issue is to perform pooled screenings. Here, infection of cells, *en masse,* with a single library of either shRNAs or sgRNAs is coupled with next generation deep sequencing to measure changes in cassette representation. This approach can screen many candidates in parallel, but drawbacks include the inability to do high-content analysis and reduced sensitivity for candidates with low representation in the library (Agrotis and Ketteler, 2015). Pooled loss-of-function type screens come in two varieties, enrichment or depletion screens – with the former seeking an increase in cassette representation in a population and the latter a decrease. Bypassers of senescence have successfully been screened for in our lab by detection of enrichment in a pooled shRNA screen (Tordella et al., 2016). Whilst the druggable genome siRNA screen for senolytic targets did produce several interesting candidates, due to only ~30% of human genes being targeted by this approach could potentially miss other valuable targets. Therefore, we decided to perform a genome-wide pooled screen looking for targets that could constitute liabilities of senescent cells.

Validation of pooled shRNA screening can often be complicated by off-targets associated with RNAi; with CRISPR/Cas9 however, off-target effects are less due to the high specificity that short guide RNAs (sgRNAs) bind to their target site with (Evers et al., 2016; Kim et al., 2015). Another drawback of shRNA screening, as it is with arrayed siRNA screening, is potentially poor phenotype penetrance due to insufficient levels of knockdown. CRISPR, theoretically should avoid this issue as sgRNAs in the selected libraries are designed to bind

to close to the start codon, could introduce indels that produce a nonsense or truncated transcript and therefore provide a knockout of the protein. Given the purported efficiency of CRISPR for screening when compared to RNAi (Evers et al., 2016; Morgens et al., 2016), we sought to use genome-wide CRISPR screening in parallel to our arrayed siRNA screens to enhance our detection of putative senolytic targets.

4.2 Derivation of a model of senescence expressing inducible Cas9

We reasoned that a tet-inducible Cas9 could allow us to begin editing once senescence had been established thereby maximizing the identification of senolytic targets. Constitutive CAS9 and tetracycline-inducible CAS9 IMR90 ER:RAS and IMR90 cell lines were generated by lentiviral infection and used to validate CRISPR induced senolysis during OIS and TIS. Both IMR90 and IMR90 ER:RAS inducible CAS9 cell lines expressed CAS9 when treated with doxycycline as detectable by IF and western blot for FLAG tag (Figure 4.1a - c). Senescence had no effect on CAS9 expression, however when doxycycline was added 6 days after senescence induction only 50-60% expressed CAS9. This could mean that there is toxicity expressing CAS9 at high levels or that cells are expressing CAS9 at a low level that cannot be detected by FLAG immunofluorescence and expression could be leaky. These issues could stem from the fact that as these cell lines are primary and CAS9 expressing clones cannot be derived. This issue was compounded by the fact that both vector carrying sgRNA library and inducible CAS9 construct, were selectable by puromycin. Therefore, selection of CAS9 could not be assured. With this potential issue in mind, we next validated the efficiency of sgRNAs against BCL2 family proteins as these could act as positive control sgRNAs to validate CAS9 systems. IMR90 cells were infected with all-in-one CRISPR/cas9 constructs containing sgRNAs against BCL2L1, BCL2L2 and BCL2 along with non-targeting sgRNA (3 sgRNAs per target). These cells were cultured for 7 days, genomic DNA collected, and PCR

amplified using primers flanking the predicted cut site. Sanger sequencing was carried out on amplicons and indels detected by using Tracking of Indels by Deconvolution (TIDE) analysis (Brinkman et al., 2014). Each target displayed at least one sgRNA with >37% knockout efficiency with a single sgRNA against BCL2L1 generating 53.8% cells with knockout (Figure 4.1d), in line with predicted editing efficiency of CRISPR systems (Evers et al., 2016). This effect of BCL2L1 sgRNAs in inducible CAS9 systems matches this observation, with immunofluorescence levels in senescent cells reducing by >40%, 48 hours after doxycycline induction when compared against non-targeting sgRNA (Figure 4.1e). These experiments show successful derivation of an inducible CAS9 system in senescent model systems. Additionally, the validation of sgRNA against the BCL2 family also can be used for optimization of screens for senolytic targets in these cell lines.

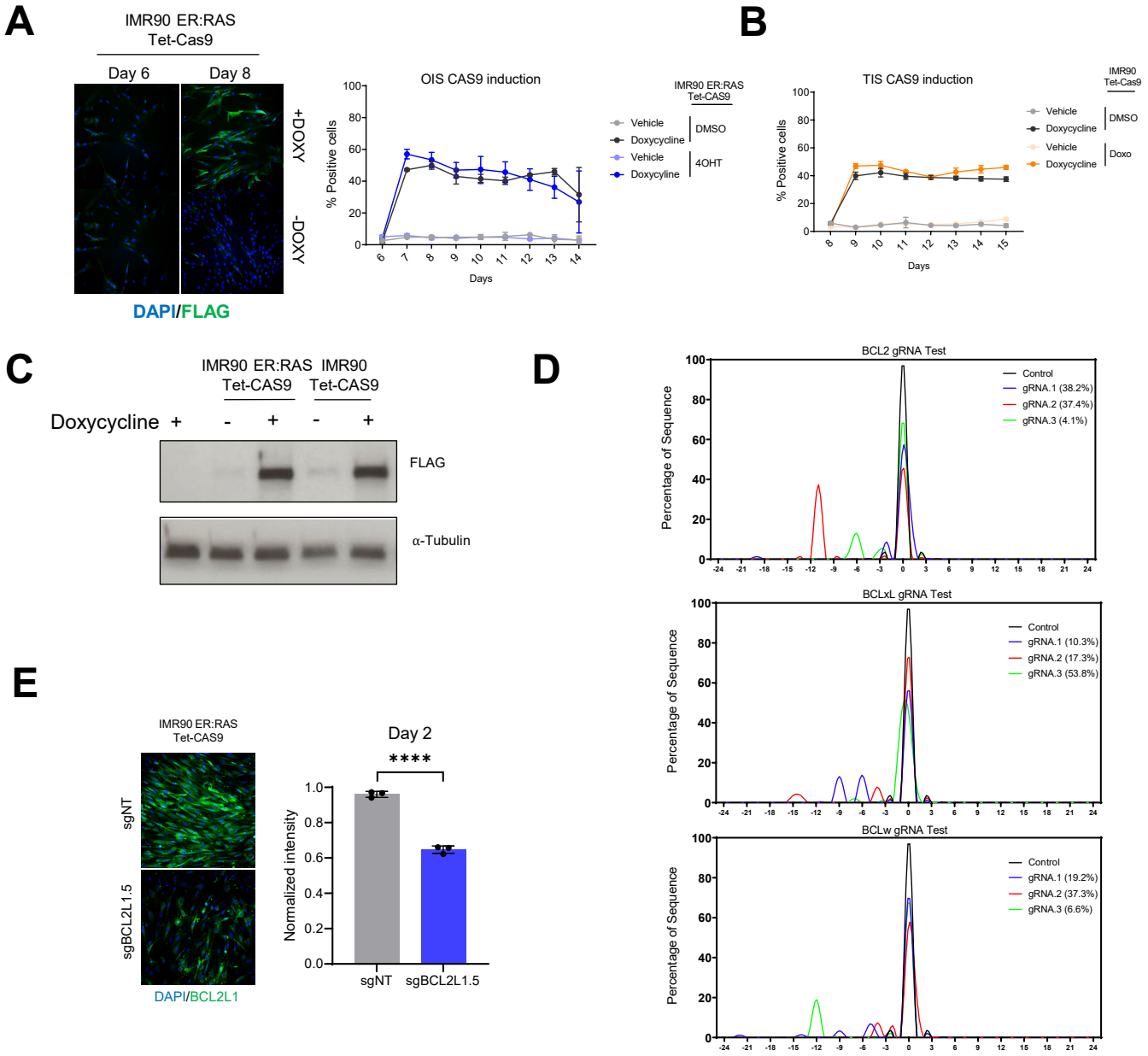

Figure 4.1 Derivation of CAS9 expressing cells

(A) (Right) Quantification of percentage positive cells for FLAG-CAS9 by IF following treatment of control (DMSO) or oncogene-induced senescent (4OHT) cell lines with 4µg/ml of doxycycline beginning 6 days after induction. (Left) Representative images for FLAG IF shown for day 6 and day 8 timepoints. (n=2, average of 3 wells). Data represented as mean±SD.

(B) Quantification of percentage positive cells for FLAG-CAS9 by IF following treatment of control (DMSO) or therapy-induced senescent (Doxo) cells with 4µg/ml of doxycycline beginning 8 days after induction. (n=2). Data represented as mean±SD.

(C) Treatment of Tet-CAS9 cell lines with doxycycline results in increased levels of FLAG tagged protein expression. IMR90 or IMR90 ER:RAS infected with Tet-CAS9 constructs were treated with 4µg/ml doxycycline and cultured for 3 days before protein extraction. Immunoblots of a single experiment are shown.

(D) Graph showing frequency of mutations introduced in target sites for BCL2 (top), BCL2L1 (middle) and BCL2L2 (bottom) sgRNAs in IMR90 cells 7 days after infection with all-in-one CRISPR/Cas9 constructs (LentiCRISPRv2) and analysed using TIDE. Frequency of 'knockout' mutations represented as percentage of deconvoluted sequence with frameshift mutations. Data represented as cublic spline analysis of TIDE data. (n=1).

(E) (Left) Representative image of BCL2L1 IF shown for day 2 timepoint. (Right) Quantification of normalized cellular intensity of BCL2L1 by IF in oncogene-induced senescent (4OHT) cells infected with BCL2L1 or non-targeting (NT) sgRNA and treated with doxycycline for 2 days. (n=3) Data represented as mean±SD. ****$p < 0.0001$; ns, not significant. Unpaired, two-tailed, Student's t-test.

4.3 Validation of CRISPR induced senolysis and editing kinetics

Pooled screening requires use of a robust positive controls. As we did with our druggable siRNA screen, different senolytic targets were tested based on known literature (Chang et al., 2016; Yosef et al., 2016). Given that siRNAs targeting BCL2L1 produced a good senolytic effect, we focused on testing sgRNAs against the BCL2 family proteins (Figure 4.2a). Testing first the most efficient sgRNAs against BCL2, BCL2L1 and BCL2L2 in an all-in one CRISPR vector (LentiCRISPRv2) we observed a senolytic effect in oncogene induced senescence with BCL2L1 sgRNAs (Figure 4.2b). This was next validated in both our constitutive CAS9 and inducible CAS9 cell lines in the context of OIS and therapy induced senescence (Figure 4.2c & d). In each instance BCL2L1 sgRNAs produced a senolytic effect, observable with the inducible systems when CAS9 was induced once senescence was established (Day 7) (Figure 4.2c & d).

However, sgRNAs targeting BCL2L1 caused a significant reduction in cell survival in senescent cells not treated with doxycycline (Figure 4.2d), raising questions about the suitability of an inducible CAS9 system for senolytic screening. It was believed that leaky expression of CAS9 could potentially be the cause. To examine further the editing kinetics of the inducible CAS9 lines, cells were infected with an editing reporter (Yamauchi et al., 2018). This reporter contained a sgRNA against GFP on one promoter and on a separate promoter, mCherry and GFP separated by T2A cleavage site (Figure 4.2e). If a cell is expressing CAS9 then GFP should be knocked out and cells will be $mCherry^{+}/GFP^{-}$ rather than $mCherry^{+}/GFP^{+}$. Normal and senescent, constitutive CAS9 or doxycycline treated inducible cells, displayed a significant increase in cells with GFP knockout (Figure 4.2f). Unfortunately, non-doxycycline treated inducible CAS9 cell lines already had a comparable level of GFP knockout. The process of CAS9 editing requires that a single CAS9 enzyme bind the target DNA site and introduce a cleavage. This raises the possibility that even a small amount of

leak could produce a knockout (Brinkman et al., 2018). Without the ability to select for clones it would be difficult to obtain cells without leakiness that would be suitable for the screen. Constitutively expressed CAS9 cell lines would also have the advantage of avoiding the variability of doxycycline-induction in the screening context and that selection for the CAS9 cassette could be maintained. However, they have the drawback that we would not - without secondary post-senescence screening - be able to exclude synthetic lethal hits for our oncogene-induced senescence screen. Editing reporters and senolytic experiments with positive control sgRNAs however indicate that inducible CAS9 cells would provide minimal additional benefit with regards to the latter issue. Therefore, constitutive CAS9 cells would be used to perform the screen.

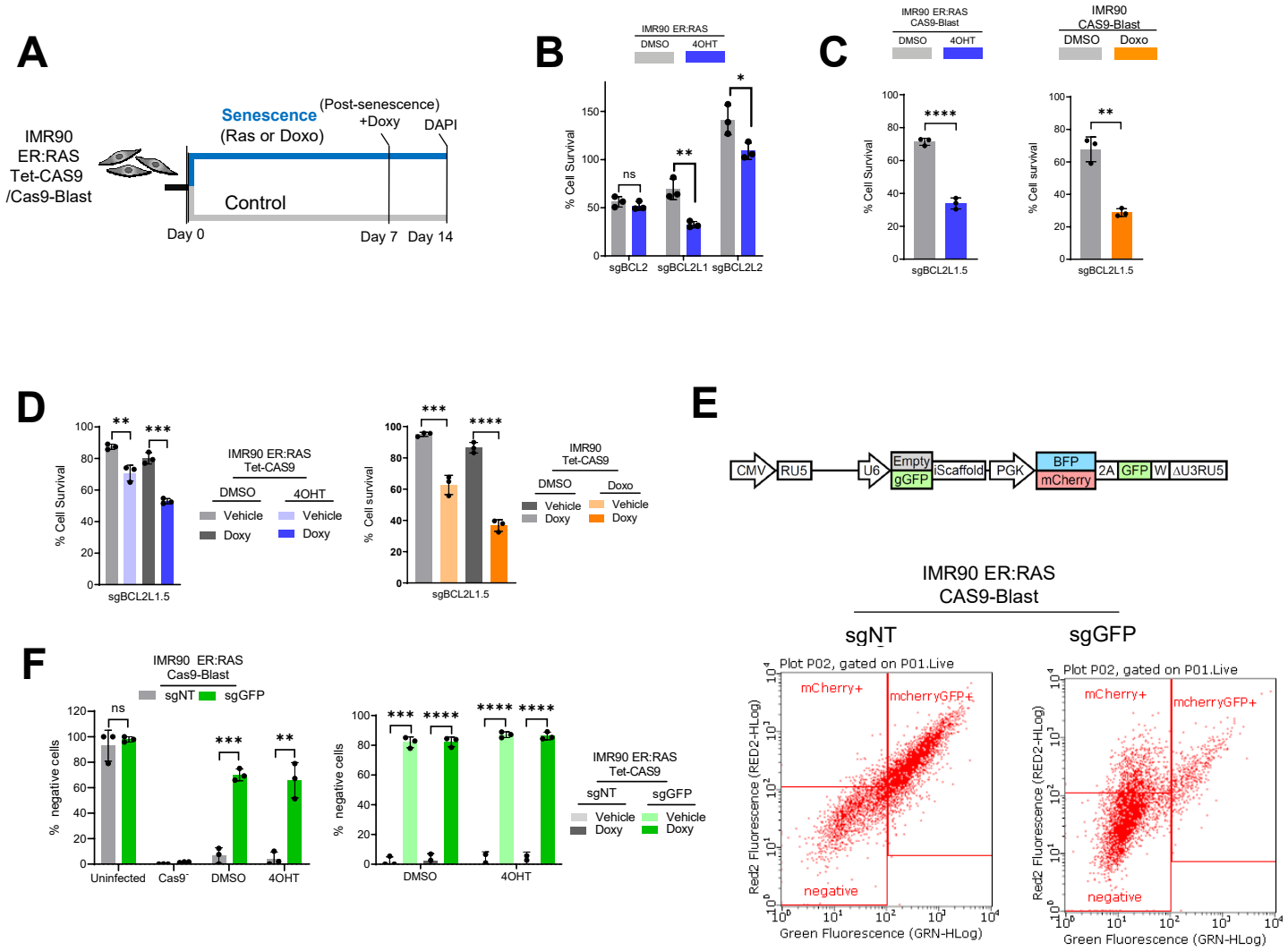

Figure 4.2 Validation of the CAS9 expressing cell lines and set up of the senolytic target screen

(A) Experimental design for validation of CRISPR induced Senolysis. Constitutive or Tet-inducible CAS9 cell lines were infected with sgRNA and cultured for 14 days. Inducible CAS9 system had 4µg/ml doxycycline added at day 7 after senescence is established.

(B) Quantification of cell survival of control (DMSO) or oncogene-induced senescent (4OHT) cells infected with all-in-one CRISPR vectors with sgRNAs against putative positive control targets. Survival measured relative to sgNT vector infected cells. (n=3). Data represented as mean±SD. *p < 0.05, **p < 0.01; ns, not significant. Unpaired, two-tailed, Student's t-test.

(C) Quantification of cell survival in constitutively CAS9 expressing control (DMSO), (Left) oncogene induced senescent (4OHT) and (Right) therapy induced senescent (Doxo) cells infected with BCL2L1 sgRNA. Survival measured relative to sgNT infected cells (n=3). Data represented as mean±SD. **p < 0.01, ****p < 0.0001; ns, not significant. Unpaired, two-tailed, Student's t-test.

(D) Quantification of cell survival in inducible CAS9 control (DMSO), (Left) oncogene induced senescent (4OHT) and (Right) therapy induced senescent (Doxo) cells infected with BCL2L1 sgRNA with or without doxycycline treatment. Survival measured relative to sgNT infected cells of the same condition. (n=3). Data represented as mean±SD. **p < 0.01, ***p < 0.001, ****p < 0.0001; ns, not significant. Unpaired, two-tailed, Student's t-test.

(E) Plasmid map of CRISPR reporter construct. sgNT or sgGFP expression located on separate promoter to mCherryt2aGFP expression.

(F) Quantification of percentage of cells negative for GFP in population of mCherry positive control (DMSO) or oncogene induced senescent (4OHT) cells with (Left) constitutive or (Centre) inducible CAS9 expression 9 days after infection with CRISPR reporter constructs containing sgNT or sgGFP. GFP and mCherry positive cells were detected by flow cytometry. (Right) Representative flow cytometry profiles for Red and Green fluorescence channels shown on live gated cells. (n=3). Data represented as mean±SD. **p < 0.01, ***p < 0.001, ****p < 0.0001; ns, not significant. Unpaired, two-tailed, Student's t-test.

4.4 Genome-wide CRISPR screens for senolytic targets

To perform the CRISPR screens, a genome-wide sgRNA library, GECKOv2, containing 123,411 sgRNAs against 19,050 protein coding genes and 1,185 non-coding genes with 6 sgRNAs per target was obtained from Addgene®. The library was amplified in bacteria and used to generate lentivirus, that could then be kept at -80°C to be tittered later. Normal screening protocols suggest that libraries should be infected into target cells with an MOI < 0.3 and selected to remove uninfected cells (Joung et al., 2017), this increases the likelihood that each cell has only 1 sgRNA. This is important in enrichment type screens as there is the possibility of propagation and expansion of sgRNAs with no effect alongside those that do. Multiple sgRNAs per cell could then ultimately at later timepoints result in increased noise and false positives in the screen. One drawback of this approach in a senolytic CRISPR screen using primary cells, is that cells must divide to provide sufficient coverage. Given that our screening cell lines have already been subjected to multiple passages for introduction of ER:RAS and CAS9 - both with low infection efficiency - further expansion could cause replicative senescence controls. Another issue is cells undergoing TIS, immediately arrest upon treatment with some loss of cells across the course of the experiment (Figure 3.2b & g). This means a high number of cells would need to be plated at day 0 to maintain coverage of the screen. With these two issues in mind we opted not to select for the library, instead tittering our library virus to infect 50-60% of cells thereby generating a MOI=0.8-1 and avoiding additional passages of cells. This also has the added benefit of reducing divergence of reference samples for each replicate and thereby reducing noise in the screen. As we are performing a drop-out screen and thereby loosing representation of sgRNAs, the likelihood of the same sgRNA dropping out with the same toxic sgRNA multiple times is very low meaning this is not as significant of an issue as with enrichment type screens.

Screening was performed using the IMR90 CAS9-blast and IMR90 ER:RAS CAS9-blast cells over the course of 14 days. As previous CRISPR screens in the lab had observed (Unpublished) use of independent infections as a reference sample drastically increased statistical noise in the screen as libraries quickly diverged from one another whilst proliferating, possibly due to sgRNA editing as CAS9 is constitutively expressed. Therefore a single reference timepoint sample for each cell line was collected at day 0 and then duplicates plated for growing (IMR90 CAS9 + DMSO), therapy induced senescent (IMR90 CAS9 + doxorubicin) and oncogene induced senescent (IMR90 ER:RAS CAS9 + 4OHT) samples (Figure 4.3a). 14 days after plating, genomic DNA was isolated and sequencing libraries generated.

Each sample was barcode PCR amplified as to maintain 700x coverage, ensuring enough representation of each sgRNAs to observe a dropout event. Coverage was estimated based on functional titer of infected cells and quantity of genomic DNA isolated. Samples were then sequenced at a depth of >400 reads per sgRNA per sample. These reads were then aligned and processed using the MaGeCK CRISPR screen analysis pipeline (Li et al., 2014). Briefly, this pipeline applies read count normalization for each sample, followed by fitting of a negative binomial model to identify sgRNAs that have significantly different abundances between reference and sample timepoint. The combined sgRNA p values are then used to rank genes using a robust ranking aggregation (RRA) algorithm (Kolde et al., 2012) allowing for genes to be ranked based on essentiality. Applying pre-filtering for individual sgRNAs that have an FDR <0.1 and a gene level filter for genes with an FDR <0.05 in any senescent condition narrows the list of 19,050 genes to 574 gene targets that were depleted in senescent cells (Figure 4.3b). Of these, 59 genes were commonly identified in the therapy induced and oncogene induced senescence contexts (Figure 4.3b). Unsurprisingly, BCL2L1 was amongst the most depleted genes in both contexts (Figure 4.3c), validating the screenings, as an

internal control was detected. The COPI component, COPA, was also depleted, providing further support of its role in senescent cell survival after being detected as a hit in our siRNA screen.

To gain more insight into the functional processes underlying senescent cell survival and whether there are drugs that could mimic the effect of CRISPR knockout gene ontology analysis and drug expression analysis was carried out on our candidate list using the EnrichR package (Figure 4.3d & e) (Chen et al., 2013). GO terms for cellular response to DNA damage, Notch signaling, and mitotic cell cycle progression were all enriched in our candidate list. The presence of DNA damage and mitotic cell cycle GO terms are not unsurprising as it has been demonstrated that further enhancement of DDR can induce senolysis (Wakita et al., 2020). These GO terms therefore provided confidence that our screening approach and filtering of candidates was enough. In addition, drug expression analysis highlighted Dasatinib, used in concert with quercetin, is a widely used senolytic agent in literature (Hickson et al., 2019; Justice et al., 2019; Zhu et al., 2015) further supporting our screening approach.

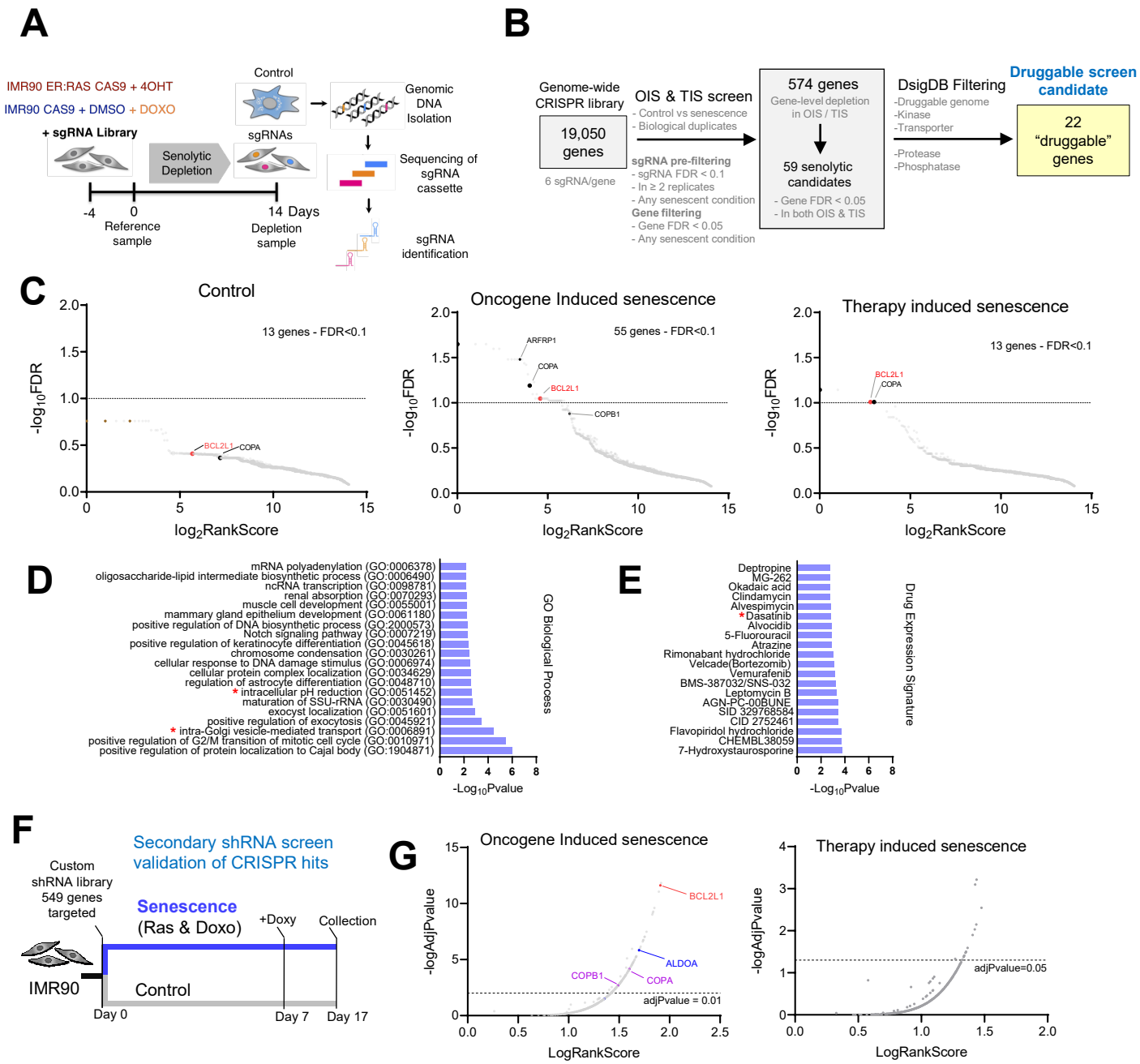

Figure 4.3 Genome wide CRISPR screen for novel senolytic targets.

(A) Experimental design of pooled genome wide CRISPR screen experiments to identify novel senolytics. Cells were collected 3 days after infection for reference sample and then plated in duplicate for control (IMR90 +DMSO) therapy-induced senescent (IMR90 +Doxo) and oncogene-induced senescent (IMR90 ER:RAS +4OHT) conditions. sgRNA depleted samples were cultured 14 days after senescence induction.

(B) Summary of the CRISPR screen for senolytic targets in OIS and TIS.

(C) Gene-level analysis for (Left) control (IMR90 +DMSO), (Centre) oncogene-induced senescence (IMR90 ER:RAS +4OHT) and (Right) therapy-induced senescence (IMR90 + Doxo) cells infected with GECKOv2 sgRNA library and analysed via NGS of sgRNA cassette representation at day 14 compared against reference timepoint day 0. Change in sgRNA representation analysed using MaGeCK analysis pipeline. Each point represents analysis of combined effect of approximately 6 sgRNA per gene target. (n=2). Data shown without pre-filtering of sgRNAs.

(D) GO-term analysis of 574 genes with gene-level depletion of multiple sgRNAs. Significantly enriched terms include intracellular pH reduction and inta-Golgi vesicle mediated transport. Analysis performed using EnrichR

(E) Analysis of drugs that produce differential expression of 574 potential gene hit list. Significantly enriched drug expression signatures include Dasatinib, which is senolytic when used in concert with Quercitin (D+Q).

(F) Experimental design of pooled secondary shRNA screen of 574 putative CRISPR screen hits using custom shRNA libray (3,265 shRNAs, 6 per gene). Cells were collected in biological triplicate on day 0 and day 17 for each condition. To induce shRNA expression doxycycline was added at day 7 when cells were senescent.

(G) Gene-level analysis for (Left) oncogene-induced senescent (IMR90 ER:RAS +4OHT) and (Right) therapy-induced senescent (IMR90 +Doxo) cells infected with custom shRNA library against 574 gene targets. Threshold of adjusted P value shown as dotted line. (n=3). Each point represents analysis of combined effect of approximately 6 shRNA per gene target.

4.5 Secondary shRNA screen of CRISPR hits

With the primary CRISPR screen performed and preliminary analysis/filtering of the hits indicating that either internal controls were present or that hits could mimic the effect of well-known senolytic drugs, it appeared that our CRISPR screening approach was robust. CRISPR knockout is theoretically a better approach to identifying candidates as poor on-target efficacy or poor knockdown efficiency are less challenging due to specificity and knockout provided by CRISPR/Cas9 (Morgens et al., 2016). Arguments could be made however as to the applicability of this approach in a clinical setting as drugs rarely provide close to 100% target inhibition as you would see with a knockout.

To validate whether candidates could sustain their senolytic effect in a context without 100% knockout and to short list candidates for further deconvolution we elected to create a shRNA library for performing a secondary screen (Figure 4.3f). This library was generated in a tetracycline inducible shRNA vector, thereby also allowing us to perform the screen once senescence was established – something we could not do in the primary CRISPR screen. IMR90 and IMR90 ER:RAS cells were infected with a shRNA library targeting the top 549 genes (6 shRNAs per gene) that were depleted in the CRISPR screens for senolytic targets. These cells were then induced to senesce by treatment with 4-OHT or doxorubicin and were treated with doxycycline to induce shRNA expression post-senescence establishment on day 7. Genomic DNA was collected at day 0 and day 17 for reference and screening sample respectively, in triplicate for growing control and senescent cells (Figure 4.3f). shRNA cassettes were then PCR amplified, purified and subject to deep sequencing to determine shRNA read count and change in representation. Combined Fisher exact test was used to generate p values for the combined effect of 6 shRNAs for each gene and a ranking algorithm used to shortlist candidates. Several notable examples outside of the expected internal control BCL2L1 (Figure 4.3g) were detected.

For example siRNAs against ALDOA were detected in the siRNA screen for senolytic targets in OIS. Here again, ALDOA was validated using shRNAs and sgRNAs as senolytic (Figure 4.3g). COPA and COPB1, coat proteins of the COPI complex, also retested with our shRNA library adding further support to the idea that targeting COPI could have a broad specificity senolytic effect. The next step in validation of the CRISPR screen candidates would have been to deconvolute the shRNAs in this library to minimize identification of off-target false positives as was carried out for the siRNA screen. With 187 targets retesting in the secondary screen (adjusted p value = 0.01), it was clear that manual cloning of shRNAs would be prohibitively labor intensive for the scope of his project.

4.6 Summary and Discussion

Genome wide CRISPR screening has been used extensively in recent years to identify novel targets for the treatment of cancer (Wang et al., 2017b; Yamauchi et al., 2018), but also more closely examine the regulation of immune cells (Parnas et al., 2015; Shifrut et al., 2018) and stem cell pluripotency (Ihry et al., 2019; Yilmaz et al., 2018). However, the opportunity to apply this approach to one of the underlying mechanisms of ageing to gain insight into age associated pathologies and their treatment remained open. We describe here a robust CRISPR screening approach that was carried out with the aim of uncovering targets that could be used to eliminate senescent cells – one approach hypothesized to be effective at treating age-associated pathologies. To this end we identify 549 genes with potential senolytic effect in a genome-wide sgRNA library. From this only 187 were validated in secondary screens, with even fewer had a senolytic effect across multiple senescence inducers. There could be several reasons for this, one is that the effect of shRNA knockdown, whilst more applicable to a real-world drug inhibition level, may not have a comparable effect

to a CRISPR knockout. This would leave our approach to validating candidates potentially underpowered but more likely to detect candidates with a better translatability.

During senescence, oxidative phosphorylation declines and glycolysis increases (Wiley and Campisi, 2016). Blockage of glucose metabolism in a model of chemotherapy induced senescence in lymphoma, using either Bafilomycin A1, which inhibitors autophagy via vacuolar ATPase pumps, or 2DG which inhibits glycolysis, kills senescent cells (Dörr et al., 2013). Interestingly, the validation of ALDOA in both our CRISPR screen and siRNA screens, as well as enrichment for GO terms involving intracellular pH reduction would suggest that these sensitivities are not just limited to senescence in lymphoma.

DNA damage response and repair pathways were identified as enriched in our CRISPR screen hits. DNA repair remains active in senescent cells, with repair resistant regions being responsible for the sustained DDR that establishes senescence. It has been suggested that targeting these repair processes, using BET protein inhibitors that target chromatin remodelers or MDM2 inhibitors, senolysis can be induced (Jeon et al., 2017; Wakita et al., 2020). The hypothesis being that in cells that are already in a hyper-DNA damaged state that further enhancement of DNA damage response triggers the cell to override senescence processes and induce apoptosis.

The final and potentially most interesting revelation from both the genome-wide CRISPR and druggable genome siRNA screen, is that depletion of multiple genes involved in COPI complex formation elicits a senolytic effect. The COPI complex is comprised of a series of proteins, forming a cage-like structure around Golgi budding vesicles. Evidence for a role of COPI vesicle trafficking in senescence and cancer is limited with large-scale siRNA screening in cancer cell lines suggesting it is synthetic lethal with KRAS mutations in NSCLC and triple negative breast cancers (Kim et al., 2013a). As COPI vesicle trafficking is an essential part of the secretory machinery of the cell, one could posit that in highly secretory senescent cells

have an elevated requirement this machinery and that disruption could lead to proteotoxic accumulation of SASP components. Following this, in KRAS mutant tumor cells, it was found that knockdown of IL-6 prevented COPI depletion sensitivity indicating that at least in tumor cells inflammatory secretion is a risk factor (Kim et al., 2013a).

Chapter 5 – Coatomer Complex I (COPI) is essential for the survival of senescent cells

5.1 Introduction

The described siRNA and CRISPR screens for senolytic targets, proved to be robust in identifying several novel pathways that when targeted, resulted in selective elimination of senescent cells over growing/quiescent cells. This was particularly evident in the identification of several members of the COPI protein family, in different screens. Other candidates such as ALDOA also had a clear biological rationale for their effect, as alteration of glucose metabolism has been previously shown to be senolytic (Dörr et al., 2013). Whilst other gene candidates warrant their own examination, for the scope of this project COPI promised the most interesting candidate warranting further investigation.

One of the primary characteristics of senescent cells is the enhanced production and secretion of proteins that alter the tissue microenvironment – termed the SASP. The Golgi apparatus forms a nexus point for the secretory pathway of proteins from their site of translation in the ER, to their eventual secretion in the ECM (Lippincott-Schwartz et al., 2000). Golgi apparatus facilitates modification and vesicular packaging of proteins. Modifications such as phosphorylation, myristoylation, glycosylation and others that can be, in turn, be essential to protein functionality. Underscoring the importance of Golgi in the secretory pathway it's disruption results in blockage of secretion (Domozych, 1999). For the Golgi to function it must have a mechanism through which vesicles are transported and recognized at membrane interfaces either within the golgi cisternae or in transport between golgi and ER.

Coatomer complexes are a collection of structural proteins that can facilitate such transport of vesicles. They do this by forming cage-like structures around the vesicle at the point of budding. COP proteins exist in two main families; COPI, responsible for retrograde transport along the Golgi/ERGIC-ER axis (Beck et al., 2009) and COPII for anterograde transport (Dancourt and Barlowe, 2010). Whilst COPII facilitates the all-important provision of proteins to the Golgi - including large sized cargo (Saito and Katada, 2015). COPI on the other hand is limited to small cargo (Pellett et al., 2013) but has a number of diverse functions in maintenance of early secretory pathway, that is the secretory route for most proteins destined for extracellular regions (reviewed (Béthune et al., 2006a)). COPI protein involvement in this pathway is through three primary trafficking processes. The first, is retrograde trafficking between the cis-Golgi and the ER (Martínez-Menárguez et al., 1999), which facilitates protein quality control (Zerangue et al., 2001), recycles essential components of the COPII pathway (Aridor et al., 1995), retrieves ER resident proteins (Béthune et al., 2006b) and importantly maintains the ER-Golgi intermediate compartment (ERGIC) (reviewed in (Szul and Sztul, 2011)). The ERGIC forms an intermediate shuttling region for proteins moving between the ER and Golgi that facilitates protein folding and quality control (reviewed in (Appenzeller-Herzog and Hauri, 2006). Secondly, COPI is required for cycling of proteins and vesicles between cisternae, resulting in a steady-state of intra-Golgi proteins (Bonfanti et al., 1998; Matsuura-Tokita et al., 2006; Schmitz et al., 2008; Tu et al., 2008) although the exact mechanism is still a matter of debate (Glick and Luini, 2011). Lastly, COPI is essential for formation of the trans-Golgi network (TGN), formation of the early endosome and autophagy, as evidenced by the effect knockdown of COPI coat proteins (Razi et al., 2009).

COPI mediated transport begins with primarily recognition of a specific vesicle cargo. Whereas COPII cargo-recognition occurs both through indiscriminate bulk flow mechanism (Thor et al., 2009; Wieland et al., 1987) – with COPI used for retrieval of ER resident and

misfolded proteins – and through recognition of largely elusive COPII peptide motifs (Barlowe and Helenius, 2016). For COPI retrograde transport, cargo proteins typically contain a C-terminal peptide motifs K(X)KXX or K/HDEL which are in turn bound by a cargo receptor KDELR (Gomez-Navarro and Miller, 2016). The binding of KDEL receptors to their cargo is pH dependent, such that in the Golgi where pH is lower binding occurs but in the ER where pH is neutral the inverse occurs (Bräuer et al., 2019). Multiple KDELRs can be identified in mammals, each of which appear to have slightly different cargo affinities and are required for minimal assembly of COPI vesicles (Gomez-Navarro and Miller, 2016). Exceptions to the presence of the above motifs in COPI cargo can also be found however with some ER-resident proteins bound by another retrieval receptor Rer1. During COPI transport Rer1 binds polar residues in transmembrane proteins that would typically be obscured in the ER (Sato et al., 2003).

In COPI transport, once soluble cargo is bound by the respective receptor, the guanine nucleotide exchange factor (GEF) for ARF GTPase - GBF1 - is activated (García-Mata et al., 2003). This in turn results in the conversion of ARF-GDP to ARF-GTP and conformational change in ARF GTPase that embeds its myristoylated N-terminal alpha-helix into the membrane of the Golgi (Liu et al., 2009). Once ARF GTPase is activated, this leads to the recruitment and assembly of the COPI structural proteins, of which there are nine, into heptameric coat complexes (Béthune and Wieland, 2018). These structural proteins exist as two sub-complexes, the inner adaptor F-subcomplex and the outer cage B-subcomplex, both of which contact the membrane. Unlike Clathrin coat and COPII coat assembly, these subcomplexes are recruited simultaneously (Hara-Kuge et al., 1994) and undergo conformational changes to allow for polymerization into tri-heptamers. These tri-heptamers then form a curved lattice which in turn deforms the golgi membrane (Dodonova et al., 2015). The interaction of coatomer subunits such as COPG1, COPA and COPB2 with either the

cargo itself or the cargo adaptors induces such conformational changes and deformation of the membrane (Bykov et al., 2017). Moreover, interaction of COPA with COPB2 and ARCN1 can provide differing linkages of COPI tri-heptamers to change the overall vesicle size (Bykov et al., 2017; Dodonova et al., 2015; Faini et al., 2013). It remains unknown whether the above conformational changes in tri-heptamers can occur prior to their association with the membrane (see Figure 4.4).

Cryo-EM studies of COPI complexes have also highlighted additional complexity in COPI assembly in its interaction with different arrangements of ARF GTPase molecules, with β-ARF forming contact with COPB1 and ARCN1 and γ-ARF interacting with COPG1; both of which can interact with COPB2. Following membrane scission, disassembly of the COPI coat is triggered by the hydrolysis of ARF-GTP to GDP by ARFGAPs (Tanigawa et al., 1993). This process is rate-limited by ARFGAPs, as the intrinsic GTPase activity of ARF GTPase is low (Cukierman et al., 1995; Frigerio et al., 2007; Poon et al., 1999). Assembly of the COPI coat itself provides a multimeric binding site for ARFGAP2 where the triad of γ-ARF proteins is located, each of which neighbours COPB1, COPB2 & COPG1 (Dodonova et al., 2017). This structure greatly increases the activity of ARFGAP2 and has been hypothesised as a mechanism to prevent unwanted disassembly (Béthune and Wieland, 2018). The ARFGAP non-catalytic domain has also been shown to play a role in dissociation of the coatomer complex, where it is thought to physically bind ARF GTPase and COPG1 to transfer a conformational change into the COPI coat (Kliouchnikov et al., 2009; Watson et al., 2004). The final stage of COPI vesicle lifecycle is tethering, whereby complexes containing proteins such as SNAREs and Rab GTPases can localize vesicles to organelles.

Multiple intra-Golgi tethering complexes such as the COG and TRAPPII complexes associate with proteins in the COPI coat, with this tethering process though to be assisted by incomplete COPI uncoating.

The mechanism through which COPI complex maintains intra-Golgi dynamics remains a key stumbling block in understanding maturation of the Golgi. Several models have been proposed each with their own caveats (reviewed in (Glick and Luini, 2011), such as the content of COPI vesicles within the intra-Golgi - as it's thought they are incapable of large cargo trafficking and their directionality. This picture is further obfuscated by the existence of morphologically different COPI vesicles localized to different regions of the golgi as well as altered COPI isoform composition at these regions, namely COPG1 and 2 and COPZ1 and 2 (Moelleken et al., 2007). The presence of these different isoforms could explain the discordance of how COPI complexes could have bidirectionality in the intra and trans-golgi network and explain COPI vesicles could play a role in the early secretory pathway. These isoforms however only exist in higher eukaryotes and cannot explain COPI function in the intra-golgi of yeast. Whilst the mechanism of its role in maintaining Golgi trafficking is not fully understood, it has been well established now that COPI is essential to the maintain Golgi integrity and either directly or indirectly supporting the early secretory pathways in the cell.

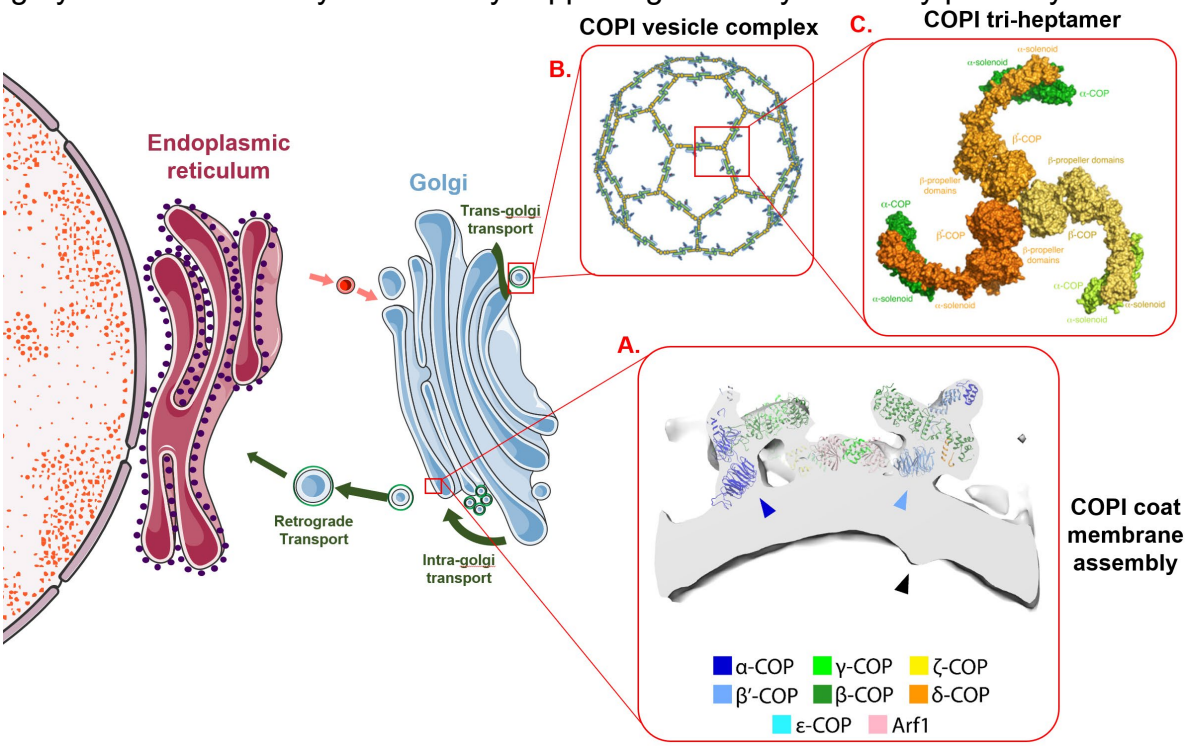

Figure 4.4 Coatomer Complex I (COPI) subunits and structure.

Summary of COPI subunits/coat structure (A) during membrane assembly (B) in the fully assembled coat complex and (C) the tri-heptamer subunits. Adapted from Dodonova et al. 2017

5.2 Detection of different COPI subunits that selectively kill senescent cells

The ability of proliferating cells to overgrow death induced by target inhibition presents an issue to estimating toxicity when comparing to growth arrested senescent cells. As discussed before cells were serum starved for senolytic experiments. However serum starvation can significantly alter autophagic flux and cell metabolism (Glick et al., 2010). This in turn may result in artefacts during identification of senolytic targets. However, COPB2 siRNAs produced no significant difference in senolytic effect whether they were cultured in high or low serum conditions (Figure 5.1a). Moreover, all four siRNAs used achieved at least 60% knockdown of COPB2 mRNA levels (Figure 5.1b).

As mentioned previously, COPI siRNAs are known to be synthetic lethal with RAS (Kim et al., 2013a). To examine whether cells that express RAS but do not undergo senescence are also sensitive to COPI depletion, our IMR90 ER:RAS cells were infected with human papillomavirus oncoprotein E6/E7 expressing vector which has been previously demonstrated in the lab to prevent the senescence growth arrest (Guerrero et al., 2019). E6 and E7 proteins inhibit p53 and phosphorylation of Rb respectively and thereby facilitate bypass of senescence growth arrest (reviewed (Hoppe-Seyler et al., 2018)). COPB2 knockdown was induced in these cells via siRNA and survival measured. Confirming previously published work, COPI depletion was toxic for RAS-expressing cells (Figure 5.1c). However, BCL2L1 siRNAs were also toxic, emphasizing therefore that a target can both be synthetic lethal with RAS and senolytic. In addition, while expression of E6/57 prevents the growth arrest caused by RAS expression, it may not resolve DDR signaling (Duensing and Münger, 2002) or $p16^{ink4a}$ expression (Munger et al., 2013), that are closely linked expression of SASP, which may be mediating susceptibility to COPI inhibition. Finally, to remove the possibility that differences in plating or separate culture conditions could be responsible for the senolytic effect, siRNAs were transfected in a fluorescently labelled co-culture of

senescent and non-senescent cells. Here, all 4 COPB2 siRNAs preferentially killed cells undergoing OIS over control IMR90s indicting further their senolytic effect (Figure 5.1d).

siRNA knockdown is useful in providing robust, rapid but transient knockdown in cells, however stable RNAi knockdown of gene expression over the course of several days requires infection of cells with shRNAs. IMR90 and IMR90 ER:RAS cells were infected with multiple inducible shRNAs against COPB2, COPA and COPG1. In each instance all multiple shRNAs produced >60% knockdown at either the RNA or protein level (Figure 5.2a - c). Next cells were induced to undergo senescence and once senescence was fully established shRNAs were induced. A senolytic effect was observed with at least 2 shRNAs targeting COPA or COPB2 in both RAS-induced and doxorubicin-induced senescence (Figure 5.2d - h). shRNAs targeting COPG1 were also able to induce senolytic effect in both settings however doxorubicin induced senescence required earlier shRNA induction (Figure 5.2i & j). Differences observed in potency between knockdown of different COPI components in different senescence systems could be due to a multitude of reasons. One possibility is that turnover of proteins between different systems is different or potentially that function of these proteins is not mutually exclusive as COPI vesicles are reported to exist in their fully assembled form briefly (Bykov et al., 2017). Another possibility is that the differing susceptibility is due to differences in underlying senescence phenotypes. These experiments together validated that targeting of the COPI complex using genetic means selectively kills senescent cells.

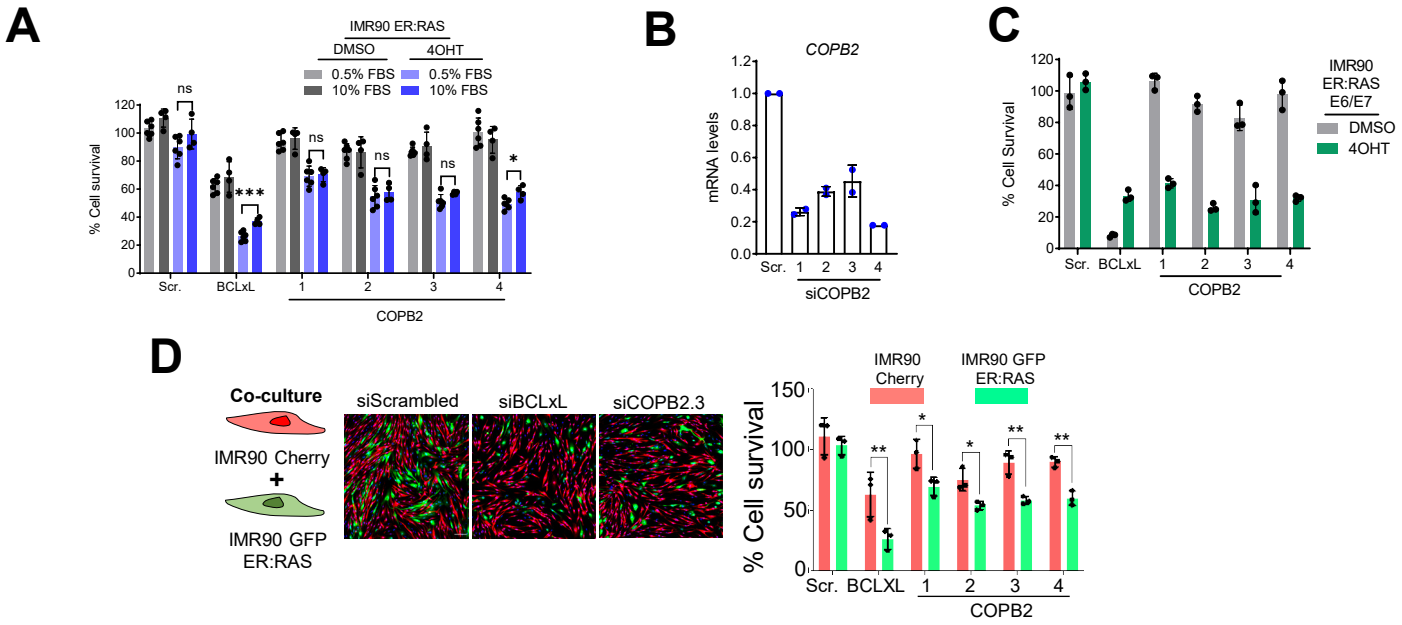

Figure 5.1 COPB2 depletion kills senescent cells intendent of culture conditions.

(A) Quantification of cell survival of senescent (4OHT) and control (DMSO) IMR90 ER:RAS cells transfected with indicated siRNAs in low serum (0.5% FBS) or high serum conditions (10% FBS). (0.5%, n=6; 10% n=4). Data represented as mean±SD. *p < 0.05 ***p < 0.001; ns, not significant. Unpaired, two-tailed, Student's t-test.

(B) Levels of COPB2 after knockdown with four independent siRNAs. mRNA levels determined by qRT-PCR and normalized to RPS14 (n=2). Data represented as mean±SD.

(C) Quantification of cell survival of 4OHT treated IMR90 ER:RAS E6/E7 cells transfected with indicated siRNAs. (n=3). Data represented as mean±SD. *p < 0.05 ***p < 0.001; ns, not significant. Unpaired, two-tailed, Student's t-test.

(D) Quantification of cell survival (right) and representative IF images (left) of the co-culture experiment of IMR90 GFP ER:RAS with IMR90 Cherry cells. Cells were transfected with the indicated siRNAs and cell numbers determined from counts of mCherry or GFP positive cells detected by IF. (n=3). Data represented as mean±SD. *p < 0.05, **p < 0.01; ns, not significant. Unpaired, two-tailed, Student's t-test. Scale bar, 100µm.

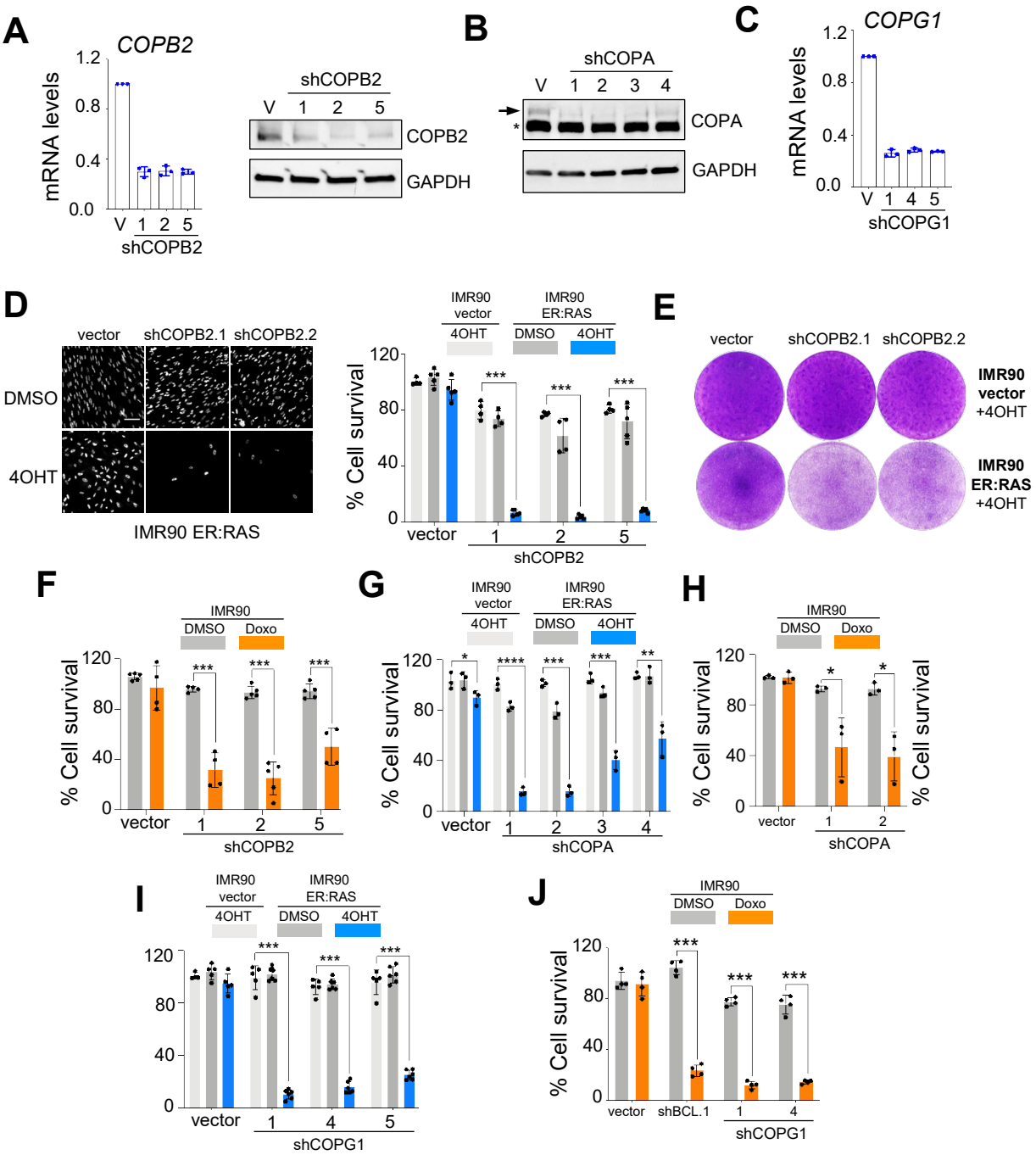

Figure 5.2 Depletion of several COPI components is senolytic.

(A) Levels of COPB2 after knockdown with three independent shRNAs. Left, qRT-PCR (n=3). Data represented as mean±SD. Right panel representative immunoblot (out of two independent experiments).

(B) Representative immunoblot (out of two independent experiments) showing the effects of four independent shRNAs targeting COPA.

(C) Levels of COPG1 after knockdown with three independent shRNAs were analysed by qRT-PCR (n=3). Data represented as mean±SD.

(E) Crystal violet staining. Doxycycline was added 7 days after senescence induction, and plates fixed and stained 9 days after. Representative image shown of three replicate experiments.

(F) Senolytic activity of COPB2 depletion in the context of doxorubicin-induced senescence in IMR90 cells (n=5). Data represented as mean±SD. ***p < 0.001; ns, not significant. Unpaired, two-tailed, Student's t-test.

(G & H) Senolytic activity of COPA depletion during (G) OIS in IMR90 ER:RAS cells (n=3) and (H) TIS in IMR90 cells (n=3). Data represented as mean±SD. *p < 0.05, **p < 0.01, ***p < 0.001; ns, not significant. Unpaired, two-tailed, Student's t-test.

(I & J) Senolytic activity of COPG1 depletion during (I) OIS in IMR90 ER:RAS cells (n=6) and (J) TIS in IMR90 cells (n=4). Data represented as mean±SD. ***p < 0.001; ns, not significant. Unpaired, two-tailed, Student's t-test.

5.3 Small molecule Inhibitors of COPI vesicle formation are senolytic.

The COPI coat proteins lack functional domains that can be targeted for inhibition by small molecule drugs. This could potentially complicate translation of these senolytic effects as without a drug, *in vivo* validation would require generation of complex genetic systems which were not feasible for the scope of this project. Fortunately, several of the enzymes that regulate COPI coat assembly on the Golgi apparatus are druggable (Figure 5.3a). To this end we screened several compounds reported to inhibit COPI vesicle formation for their senolytic effect (Figure 5.3b) (Domozych, 1999; Feng et al., 2003; Sáenz et al., 2009; Spooner et al., 2008; Zhang et al., 2007a). Two compounds, Golgicide A and Brefeldin A were able to induce potent senolytic effects in OIS with the EC_{50} in senescent cells being 11-fold and 60-fold lower respectively than their control cell counterparts (Figure 5.3c and d). Both compounds target the GTPase effector enzyme for ARF, GBF1 and are preferentially toxic towards senescent RAS cells.

Golgicide A and Brefeldin A resulted in alteration of COPI protein distribution as expected (Figure 5.4a). Both drugs were then validated in different senescence contexts, including irradiation, palbociclib treatment and treatment with either bleomycin or doxorubicin. In each context GBF1 inhibitors caused a significant senolytic effect in senescent cells (Figure 5.4b and c). Interestingly, palbociclib treatment displayed the least potency with only marginal senolytic effects at even higher concentrations of Golgicide A. One of the distinguishing phenotypes of palbociclib induced senescence is the absence of a strong pro-inflammatory phenotype, such that several groups have screened for targets that could increase it to improve its therapeutic efficacy (Ruscetti et al., 2018). Disruption of COPI, either through usage of GBF1 inhibitors or siRNAs can block secretion (Beck et al., 2009; Domozych, 1999). With most senescence phenotypes being highly secretory due to the SASP, except palbociclib-induced senescence, and the reduced COPI depletion sensitivity in the same

context, this could suggest a SASP dependency. Further supporting this hypothesis washout experiments highlighted that 24-hour incubation with GBF1 inhibitor is sufficient to elicit a senolytic effect in RAS-induced senescence (Figure 5.4d). When bleomycin-induced senescence requiring a longer 48-hour incubation (Figure 5.4e). Differences between RAS-induced senescence and chemotherapy-induced senescence could explain this, one being that RAS-induced senescence has higher levels of SASP production (Coppé et al., 2010).

To determine whether the effects of GBF1 inhibitors were cell type specific; both Golgicide A and Brefeldin A were used to treat normal human lung fibroblasts (NHLFs) and primary bronchial epithelial cells (PBECs) induced to senesce with Bleomycin. Golgicide A and Brefeldin A were senolytic in both cell types (Figure 5.4f-h). This demonstrates that COPI inhibition can target senescent cells in different cell types. PBECs were harvested from a middle-aged donor, resulting in the emergence of senescent cells in a mixed population of growing and senescent cells with relatively few passages. These cells can be detected by their high expression of $p16^{INK4a}$. This allows us to assess *in vitro,* the viability of these drugs as a senolytic for cells that had naturally become senescent during age and that are in a mixed population as they would exist *in vivo*. GBF1i, preferentially eliminated the $p16^{INK4a}$ positive cells (Figure 5.4i) suggesting that they could eliminate 'naturally' senescent cells.

Many drugs can elicit a desired effect, even at low concentrations however it is important to understand whether this is an off-target as poor understanding of a drug target mechanism can ultimately lead to poor translatability (Bunnage, 2011). Cells infected with shRNAs against GBF1, whilst not recapitulating the senolytic effect seen with the drugs, did enhance their potency (Figure 5.5a), seemingly indicating they are acting on-targeting but needing additional validation. Both Golgicide A and Brefeldin A, bind to the Sec7 domain of GFB1. A mutation derived from the canine version of GBF1, M832L, has been demonstrated to block the binding of Golgicide and Brefeldin and rescue its effect (Sáenz et al., 2009) and was used

to validate Golgicide A as a GFB1 specific inhibitor (Sáenz et al., 2009). Infection of IMR90 or IMR90 ER:RAS cells with constructs expressing this GBF1 variant rescued their senolytic effects, thereby demonstrating that their effects are on-target (Figure 5.5b-d). In should be noted that Brefeldin A is more promiscuous, binding to Sec7 domains in other proteins such as ARNO1, BIG1 (ARFGEF1) & BIG2 (ARFGEF2). Inhibition of these could also mimic some of the effects of GBF1 inhibition by targeting clathrin coat formation (Hinners and Tooze, 2003). Despite this, rescue was observed with both drugs, indicating that inhibition of COPI via usage GBF1 inhibitors is an on-target, potent and robust senolytic target.

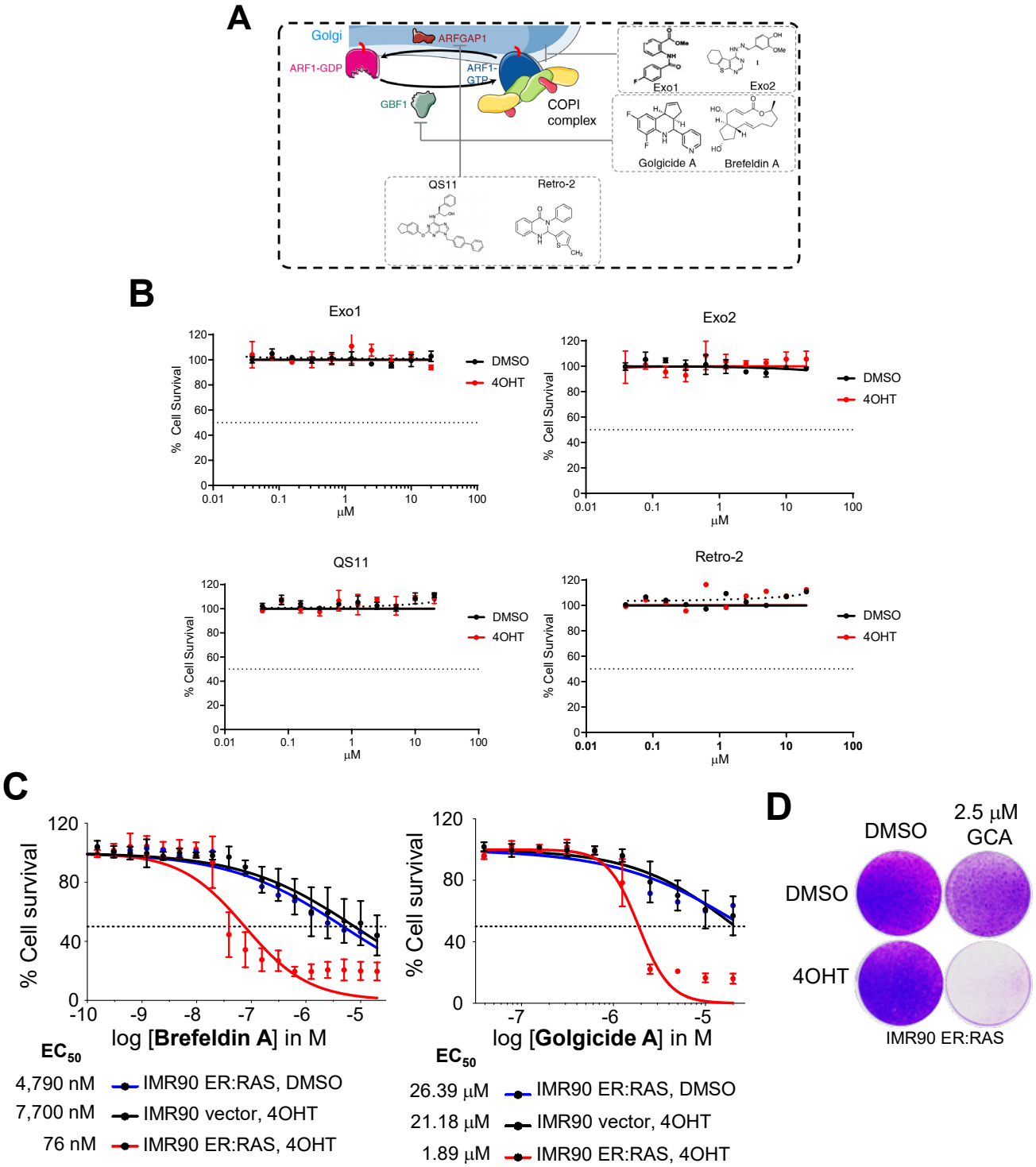

Figure 5.3 Small molecule inhibitors targeting COPI complex are senolytic

(A) Diagram of drug targetable proteins within the COPI pathway. Golgicide A and Brefeldin A target the GBF1 complex whereas QS11 and Retro-2 target ARFGAP1. The target of Exo1 and Exo2 within the pathway is unknown.

(B) Dose-response curves for senolytic effect of ARFGAP1 and COPI targeting drugs in the context of oncogene-induced senescence (n=3), (Retro-2, n=1 average of three wells of same experiment).

(C) Dose-response curves for senolytic effect of GBF1 inhibitors Brefeldin A (Left) and Golgicide A (Right) in the context of OIS (n=6). EC50, half-maximal effective concentration.

(D) Crystal violet staining of control (DMSO) or senescent (4OHT) IMR90 ER:RAS cells treated for 72 hours with either DMSO or 2.5μM of Golgicide A (GCA) 7 days after senescence induction.

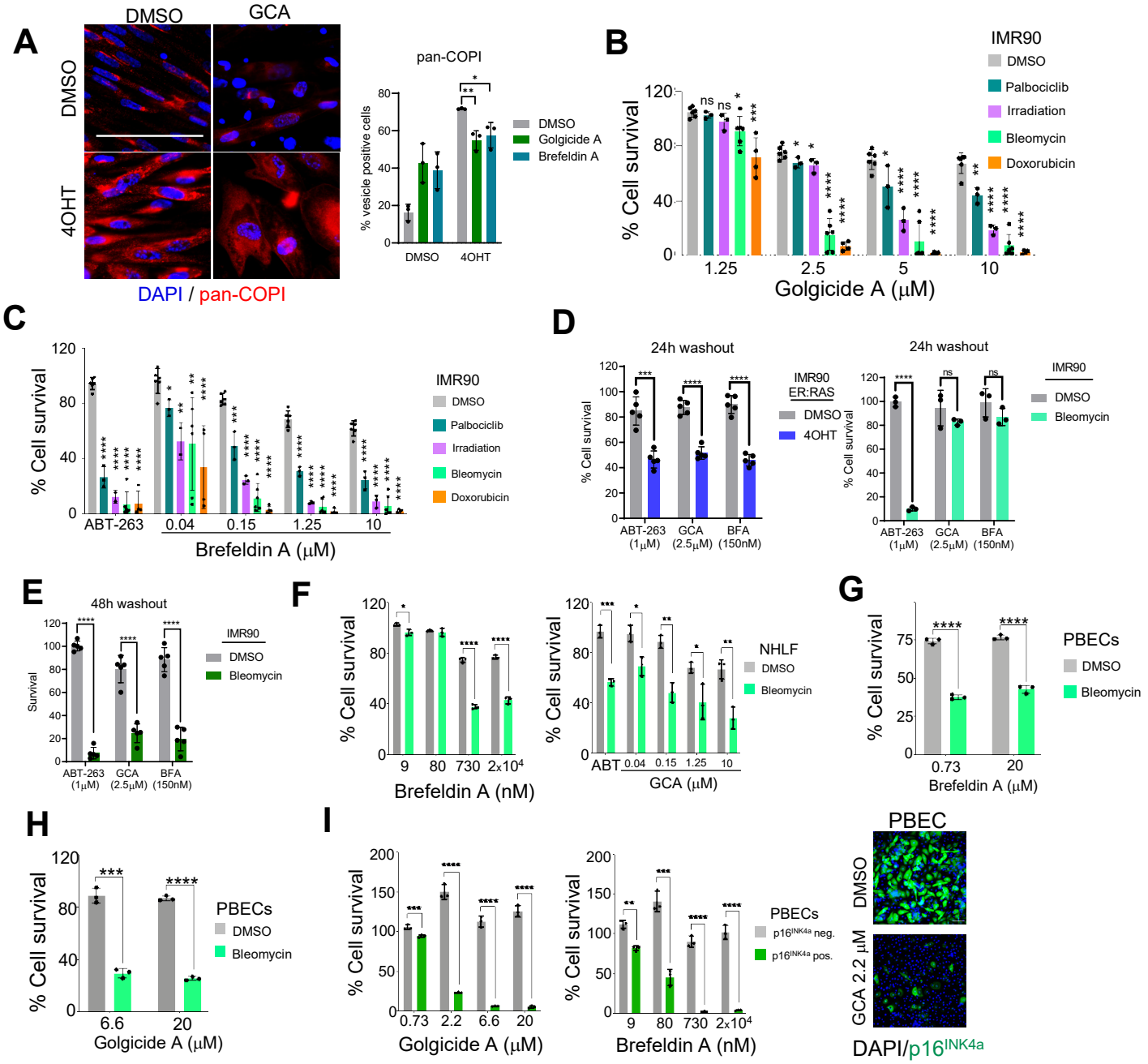

Figure 5.4 GBF1i target the COPI pathway and are senolytic

(A) Quantification of cells with punctate COPI staining (right) and representative pan-COPI IF images (left) of senescent (4OHT) and control (DMSO) IMR90 ER:RAS cells after treatment for 48 hours with 1.25μM of Golgicide A (GCA),150nM of Brefeldin A (BFA) or 1μM ABT-263 (n=3). Quantification performed by measuring the percentage of cells with >30 COPI vesicles per cell. (n=3). Data represented as mean±SD. *p < 0.05, **p < 0.01, ***p < 0.001, ****p < 0.0001; ns, not significant. Unpaired, two-tailed, Student's t-test.

(B & C) Senolytic activity of (B) Golgicide A and (C) Brefeldin A in the context of senescence induced by palbociclib, irradiation, bleomycin and Doxorubicin. (n=3 for palbociclib and irradiation treatment, n=6 for DMSO/Bleomycin and doxorubicin treatment). Data represented as mean±SD. *p < 0.05, **p < 0.01, ***p < 0.001, ****p<0.0001; ns, not significant. Unpaired, two-tailed, Student's t-test.

(D) Percentage cell survival of control (DMSO), (left) oncogene-induced senescent (IMR90 ER:RAS +4OHT, n=5) and (right) therapy-induced senescent (IMR90 +Bleomycin, n=3) 48 hours after a 24 hour washout treatment with senolytic drugs. Data represented as mean±SD. ***p < 0.001, ****p<0.0001; ns, not significant. Unpaired, two-tailed, Student's t-test. 8

(E) Percentage cell survival of control (DMSO) and therapy-induced senescent (IMR90 + Bleomycin) 24 hours after a 48 hour washout treatment with senolytic drugs. (n=5). Data represented as mean±SD. ****p<0.0001; ns, not significant. Unpaired, two-tailed, Student's t-test.

(F) Percentage cell survival of control (DMSO) or bleomycin-induced senescence in normal human lung fibroblasts (NHLF). Cells were treated for 72 hours with indicated concentrations of Brefeldin A (Left) or Golgicide A (GCA, Right), 7 days after senescence induction (n=3). Data represented as mean±SD. *p < 0.05, **p < 0.01, ***p < 0.001, ****p<0.0001; ns, not significant. Unpaired, two-tailed, Student's t-test.

(G & H) Percentage cell survival of PBECs induced to senesce with bleomycin treatment and treated for 72hours with (G) Brefeldin A or (H) Golgicide A. (n=3) Data represented as mean±SD. ***p < 0.001, ****p<0.0001; ns, not significant. Unpaired, two-tailed, Student's t-test.

(I) Representative pictures (right) of IF staining for p16INK4a in PBECs after treatment with GCA, BFA or vehicle (DMSO); p16INK4a is stained green. Scale bar, 50 μm. Quantification of p16INK4apositive and negative PBECs (right). (n=3). Data represented as mean±SD. ***p < 0.001, ****p<0.0001; ns, not significant. Unpaired, two-tailed, Student's t-test.

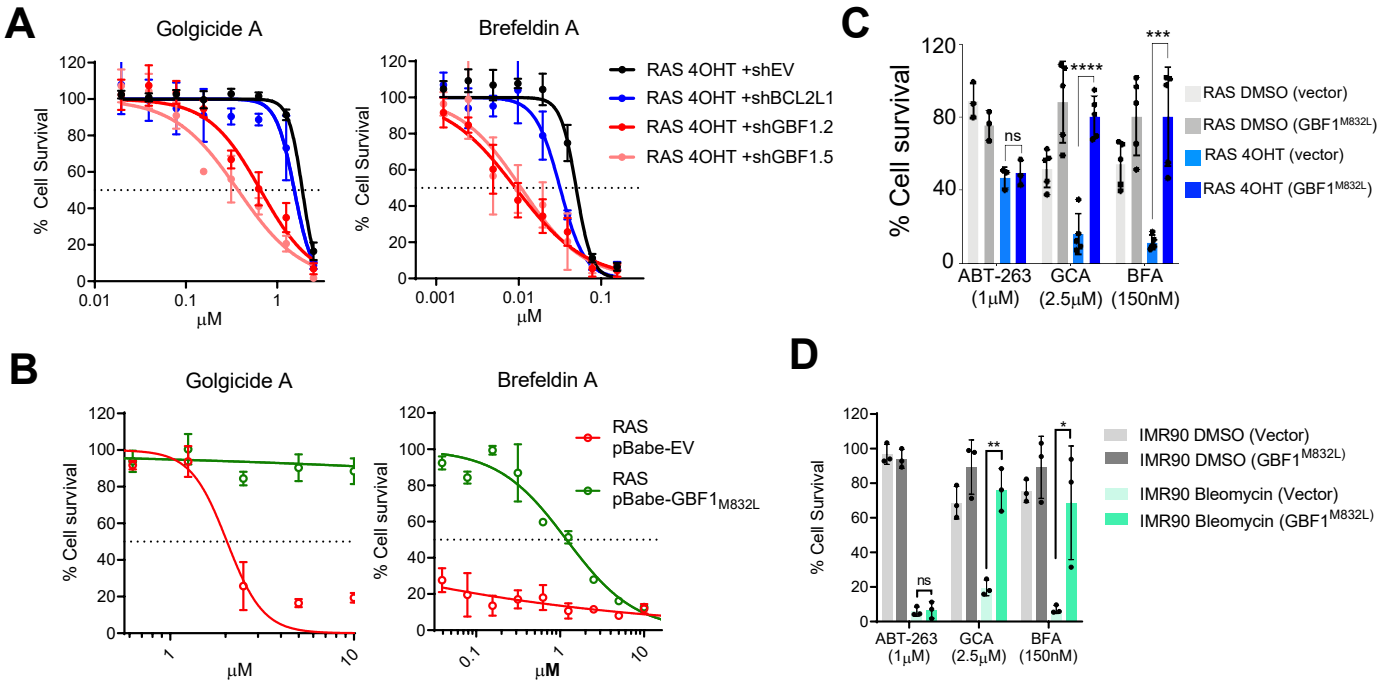

Figure 5.5 Golgicide A and Brefeldin A senolysis is dependent on GBF1

(A) Dose-response curves for senolytic effect of GBF1 inhibitors Brefeldin A (Right) and Golgicide A (Left) in the context of OIS with shRNAs against GBF1 (n=3). EC50, half-maximal effective concentration.

(B) Dose-response curves for senolytic effect of GBF1 inhibitors Golgicide A (Left) and Brefeldin A (Right) in the context of OIS with overexpression of resistant GBF1.

(C) Quantification of cell survival of control (RAS DMSO) and oncogene-induced senescent cells (RAS 4OHT) infected with the indicated vectors and treated with ABT-263, Golgicide A (GCA) or Brefeldin A (BFA) at indicated concentrations. (n=5 for GCA and BFA treated cells, n=3 for ABT-263 treated cells). Data represented as mean±SD. ***$p < 0.001$, ****$p < 0.0001$; ns, not significant. Unpaired, two-tailed, Student's t-test.

(D) Quantification of cell survival of control (IMR90 DMSO) and therapy-induced senescent cells (IMR90 Bleomycin) infected with the indicated vectors and treated with ABT-263, Golgicide A (GCA) or Brefeldin A (BFA) at indicated concentrations. (n=5 for GCA and BFA treated cells, n=3 for ABT-263 treated cells). Data represented as mean±SD. *$p < 0.05$, **$p < 0.01$; ns, not significant. Unpaired, two-tailed, Student's t-test.

5.4 The senolytic effects of COPI inhibition are caspase dependent.

Inducing cell death can occur through several different mechanisms both with benefits and drawbacks in a therapeutic context. Apoptosis is a form of programmed cell death that is organized to produce a minimally inflammatory state and reduce disruption to the surrounding tissue (Taylor et al., 2008). This is in opposition to pyroptosis and necroptosis which are pro-inflammatory (Bergsbaken et al., 2009; Weinlich et al., 2017). These forms of cell death are dependent on the activity of the caspase family of proteins (reviewed in (Shalini et al., 2015)), with different caspases being activated in different programmed cell death contexts. For example, caspase-1 is typically, through activation of the NLRP3 inflammasome, activated during pyroptosis where it processes cytokines into their mature pro-inflammatory form. Other caspases, such as caspase-3 & 7 are broadly activated across programmed cell death. If caspases were involved in the COPI dependent senolytic effect it would indicate a form of programmed cell death. To investigate this, we examined the activity of caspases in COPI disrupted cells. COPB2 knockdown was observed, via IF, to increase levels of cleaved-caspase-3 significantly in senescent cells (Figure 5.6a). Next, we investigated the kinetics of when caspases were being activated during COPB2 knockdown we imaged cells incubated with a fluorogenic substrate containing DEVD peptides that would be cleaved during activation of capase-3/7. With BCL2L1 knockdown, levels of cleaved-caspase-3/7 rapidly increased in senescent cells 24 hours after transfection peaking at around 40 hours (Figure 5.6b). This was followed by an increase in caspase activity in our control cells indicating that there is a small window of selectivity. COPB2 knockdown took longer to produce a caspase activity peak in senescent cells but increases in caspase activity in control cells were only marginally above non-targeting siRNAs (Figure 5.6c). Control cells even up to 72h post-transfection did not display a peak of caspase activity, potentially indicating greater selectivity of COPB2 siRNAs towards senescent cells. Similarly, treatment of cells with GBF1 inhibitors

resulted in significant induction of cleaved-caspase-3 activity in OIS and TIS, as detected by IF (Figure 5.6d) and using fluorogenic peptides (Figure 5.6e)

To examine whether COPI sensitivity was dependent on caspase activity we pre-treated cells with pan-caspase inhibitor QVD-VD-Oph (QVD) before transfection with siRNAs or treatment with senolytic drugs. Here, QVD treatment reduced COPB2 siRNA induced death as well as with BCL2L1 siRNA (Figure 5.6g). The reduction in cell death was relatively small however but was similar for siBCL2L1 which would directly target an apoptotic pathway that is known to be caspase dependent – indicating that this may be due to technical reasons. QVD pre-treatment resulted in a near complete rescue of the senolytic effects of ABT-263 and GBF1i.

Depletion of COPI in cancer cells has been hypothesized to induce ER stress and through the unfolded protein response (UPR) induced programmed cell death (Claerhout et al., 2012; Zhou et al., 2019). Caspase-12, activated through endoplasmic reticulum mediated release of Ca^{2+} and activation of calpain, is activated during UPR-induced apoptosis (Shalini et al., 2015). In the context of COPB2 knockdown, an inhibitor of Caspse-12, Z-ATAD-FMK (ATAD), like QVD treatment, did marginally reduce caspase-3/7 activity in senescent cells (Figure 5.6i). A reduction with both QVD and ATAD treatment was observed in cells with BCL2L1 knockdown indicating there may be broader roles of UPR in senolysis (Figure 5.5i). Likewise, inhibition of caspases was able to rescue cell death induced with GBF1i or COPB2 siRNAs with ATAD also decreasing the activity of caspase 3/7 (Figure 5.6i). These results together would indicate that senolysis from inhibition of COPI vesicle formation is caspase dependent. Further investigation would be needed however, to determine which specific caspases mediate the senolytic effects of COPI inhibition, with initial evidence suggesting a role for the ER stress regulated caspase-12.

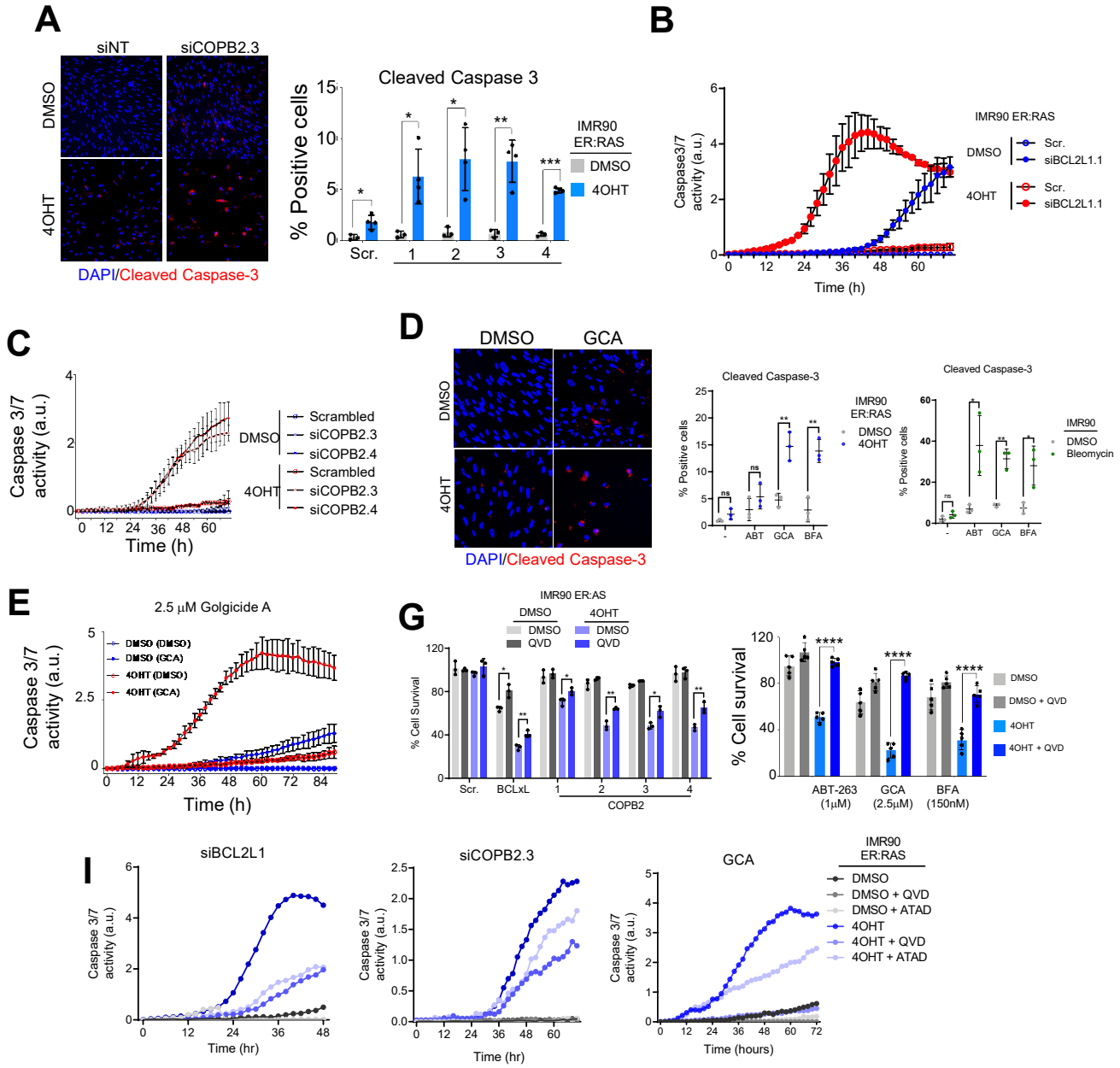

Figure 5.6. COPI sensitivity is caspase dependent

(A) Quantification of cells positive for Cleaved-caspase 3 by IF analysis (right) and representative IF images (left) of senescent (4OHT) and control (DMSO) IMR90 ER:RAS cells transfected with indicated siRNAs. (n=4). Data represented as mean±SD. *p < 0.05, **p < 0.01, ***p < 0.001; ns, not significant. Unpaired, two-tailed, Student's t-test.

(B & C) Caspase-3/7 activity in control (DMSO) or oncogene-induced senescent (4OHT) cells after transfection with the indicated siRNAs 6 days after senescence induction (n=3). Data represented as mean±SD.

(D) Quantification of cells positive for Cleaved-caspase 3 by IF analysis (right) and representative IF images (left) of senescent (4OHT) and control (DMSO) IMR90 ER:RAS cells treated with indicated drugs 7 days after senescence induction. (n=3). Data represented as mean±SD. *p < 0.05, **p < 0.01, ***p < 0.001; ns, not significant. Unpaired, two-tailed, Student's t-test.

(E) Quantification of cells positive for Cleaved-caspase 3 by IF senescent (bleomycin) and control (DMSO) IMR90 cells treated with indicated drugs 7 days after senescence induction. (n=3). Data represented as mean±SD. *p < 0.05, **p < 0.01, ***p < 0.001; ns, not significant. Unpaired, two-tailed, Student's t-test.

(F) Caspase-3/7 activity in control (DMSO) or oncogene-induced senescent (4OHT) cells after after treatment with DMSO or 2.5μM Golgicide A 7 days after senescence induction (n=3). Data represented as mean±SD.

(G) Treatment with a pan-caspase inhibitor prevents the senolytic effects of GBF1 inhibitors and COPB2 siRNAs. OIS was induced in IMR90 ER:RAS cells by adding 4OHT. 3 days after senescence induction, cells were treated with 20μM Q-VD-OPh were indicated. 7 days after senescent induction cells were treated with indicated drugs or transfected with siRNAs. Cells numbers were assessed 3 days later (GBF1i n=5, COPB2 siRNA n=3). Data represented as mean±SD. ****p < 0.0001; ns, not significant. Unpaired, two-tailed, Student's t-test.

(I) Caspase-3/7 activity in QVD or ATAD pre-treated control (DMSO) or oncogene-induced senescent (4OHT) cells after treatment with Golgicide A or transfection with the indicated siRNAs 6 days after senescence induction (n=1). Data represented as average of three wells.

5.5 COPI complex does not appear differentially regulated in senescent cells.

Evident from the screens and later retesting, was that disruption of multiple COPI complex members could, in multiple senescence contexts induce senolysis. COPI proteins perform essential processes in protein trafficking, protein quality control and maintain the Golgi structure. Therefore, one obvious answer to the question of why senescent cells are more susceptible to their depletion would be differential expression. Examining RNA-Seq and proteomics datasets performed and analyzed previously in the lab did not show that any of the COPI proteins themselves were significantly differentially expressed in senescent cells however (Figure 5.7a-c). Expression of COPB2 was additionally validated via RT-qPCR of later timepoints to investigate whether expression differences were a late senescence phenotype. Consistent with RNA-Seq results, no significant difference in expression was observed (Figure 5.7d). Additionally, we investigated whether genes regulating COPI vesicle formation, such as the ARF GTPase proteins and their respective GTPase activating proteins and effector enzymes, were differentially regulated (Figure 5.7a-c). Only ARF3, was upregulated in OIS (Figure 5.7c). However due to lack of antibodies specific to ARF3 isoforms this could not be validated by western blot. Western blot also did not show any consistent changes in the different COPI coat proteins that could explain the broad senolytic effect of COPA, COPG1 and COPB2 knockdown (Figure 5.7e). With a lack of evidence supporting expression differences being the mechanism for senescent cell sensitivity to COPI depletion, other potential mechanisms must be examined.

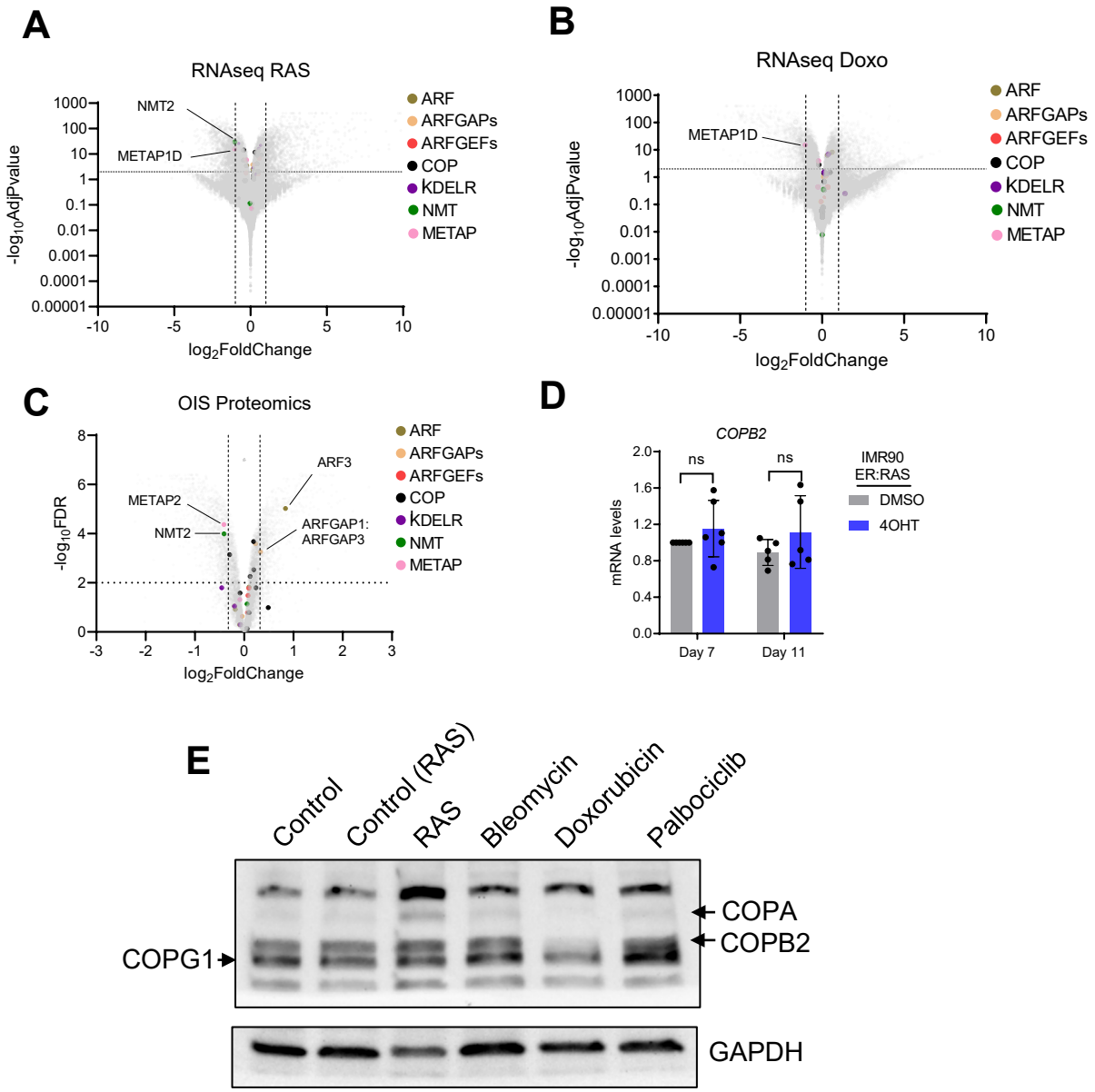

Figure 5.7 COPI proteins do not appear differentially regulated during senescence.
(A) Transcriptomic analysis of oncogene-induced senescent cells by RNA-seq. RNA extracted on day 6 from control (Quiescent IMR90 ER:RAS) and senescent (4OHT treated IMR90 ER:RAS) in triplicate and submitted for RNA-seq. COPI proteins and related pathways with significantly differentially regulated genes highlighted (LFC >< 1 & AdjPvalue < 0.01) Fold change represents change in RPKM levels (senescent / control). (see Table A15 for list of targets.)
(B) Transcriptomic analysis of therapy-induced senescent cells by RNA-seq. RNA extracted on day 6 from control (Quiescent IMR90) and senescent (Doxorubicin treated IMR90) in triplicate and submitted for RNA-seq. COPI proteins and related pathways with significantly differentially regulated genes highlighted (LFC >< 1 & AdjPvalue < 0.01). Fold change represents change in RPKM levels (senescent / quiescent). (see Table A15. for list of targets)
(C) Proteomics performed on control (Growing IMR90 ER:RAS) and senescent (4OHT IMR90 ER:RAS) 6 days after induction. Fold change represents change in LFQ levels (senescent / control).
(D) mRNA levels of COPB2 in control (DMSO) and senescent (4OHT) IMR90 ER:RAS cells 7 & 11 days after induction. (n=5). ns, not-significant; Data represented as mean±SD. (see Table A15. for list of targets)
(E) Effect of senescence induction on COPI complex expression. Oncogene induced senescent (RAS), therapy induced senescence (Bleomycin / Doxorubicin / Palbociclib) and their respective control IMR90 or IMR90 ER:RAS cells were collected at day 6 after senescence induction. Immunoblot representative of three biological replicates.

5.6 Inhibiting COPI disrupts secretory pathways of senescent cells

As discussed previously, COPI vesicles are essential to recycling of Golgi fragments between the cis and trans golgi, such that disruption of COPI through either drug inhibition of GBF1, or knockdown of COPI proteins causes destabilization of Golgi structure. This disruption of Golgi structure can also disrupt formation of the early endosome as vesicles are cycled from the trans-Golgi membrane via anterograde transport (Razi et al., 2009). To examine the effect of disrupting COPI on the senescence secretory pathway, Immunofluorescence staining for trans-golgi (TGN46), cis-golgi (GM130) and the early endosome (EEA1) were performed on cells transfected with COPB2 siRNAs. Senescent cells display higher levels of fragmentation (Figure 5.8a & b). This has been observed previously in examination of the TOR-autophagy spatial coupling compartment (TASCC) (Narita et al., 2011). The TASCC localizes to a fragmented trans-Golgi network in senescent cells where it assists in SASP production. Similar expansion of the Golgi has been observed also in other highly secretory cells such as B cells, collagen secreting fibroblasts and retinal pigment epithelial cells (Kirk et al., 2010; Ueno et al., 2010). Additionally, cells with DNA damage have been reported to have increased fragmentation of the Golgi which is associated with their survival (Farber-Katz et al., 2014), although the functional mechanism through which survival is mediated is not known. With COPB2 knockdown, as has been demonstrated by other groups (Razi et al., 2009), the trans-Golgi network and cis-golgi network lose integrity (Figure 5.8a and b). This can be visualized as a spreading of the TGN46 and GM130 IF signal, measured as an increased percentage of cells with hyper fragmented golgi or increased integrated intensity of the signal respectively. Even though there are no significant changes in COPI coat expression levels, this effect is only observed in senescent cells. Senescent cells may therefore be pre-disposed to undergo Golgi hyper-fragmentation /dispersal in response to COPI disruption, through an as yet unknown mechanism.

Senescent cells display increased numbers of early endosomal vesicles (Figure 5.8c). This could be linked with the increased levels of autophagy observed in senescent cells (Gewirtz, 2013). With COPB2 knockdown, this increase in EEA1 vesicles per cell in senescence is lost, indicating disruption of the early endosome compartment (Figure 5.8c).

Both the disruption of the trans-Golgi network, and the disruption to formation of the early endosome were observed in senescent cells treated with GBF1 inhibitors (Figure 5.8d & e). Interestingly, GBF1 inhibitors resulted also in complete dispersal of Golgi in control cells, indicating, *per se,* that the preferential toxicity to senescent cells is independent from Golgi dispersal. This raises the question, what makes senescent cells more likely to undergo cell death as a result of disruption of Golgi structure?

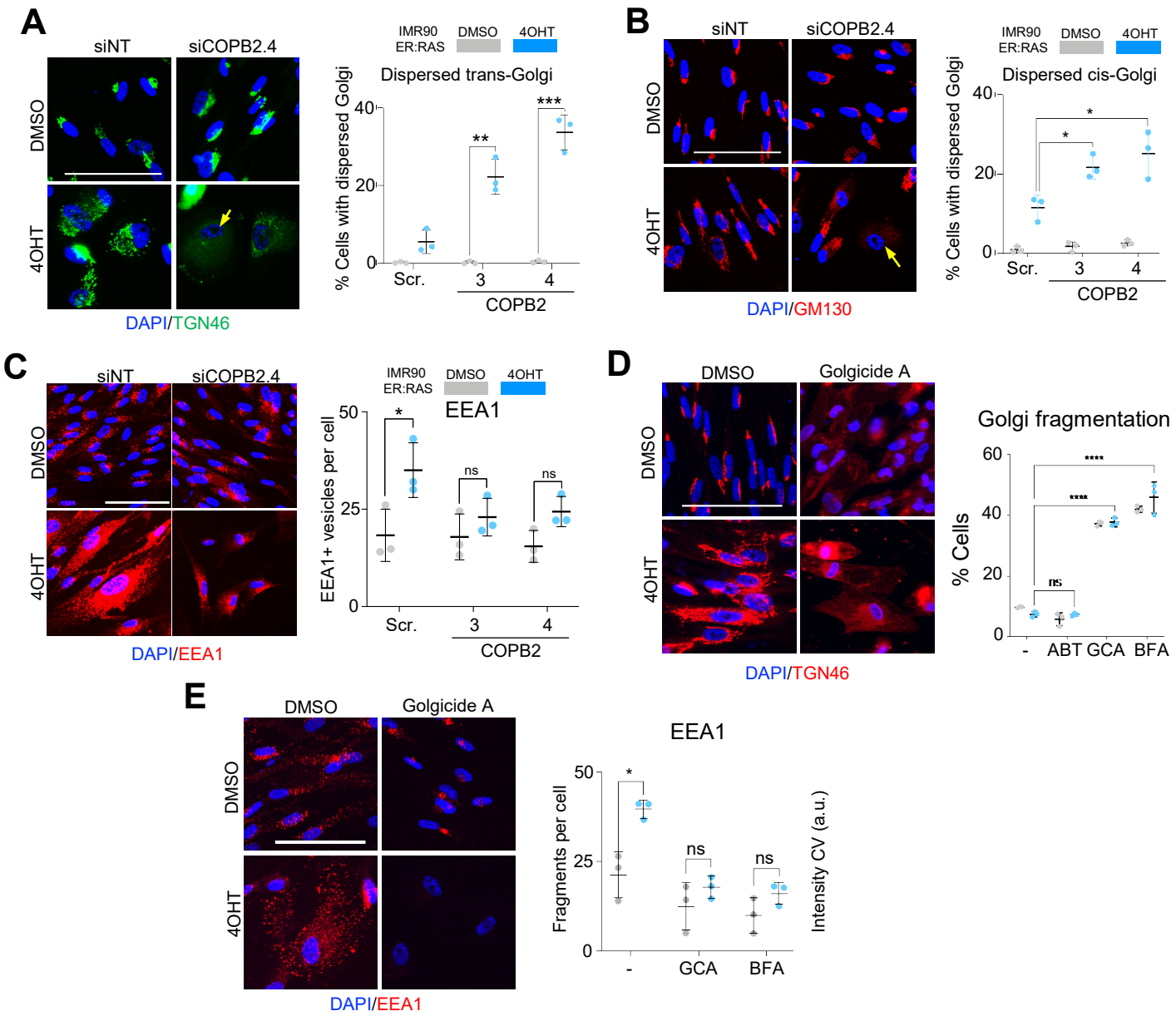

Figure 5.8. Inhibition of COPI disrupts secretory pathway of senescent cells.

(A) Quantification of cells with dispersed trans-Golgi (right) and representative TGN46 IF pictures (left) of senescent (4OHT) and control (DMSO) IMR90 ER:RAS cells after transfection with the indicated siRNAs (n=3). Quantification performed using threshold of organelle count (> 25) in 'region growing' collar using multiscale-tophat segmentation for objects 1-3 pixels in size. Data represented as mean±SD. *p < 0.05, **p < 0.01; ns, not significant. Unpaired, two-tailed, Student's t-test. Scale Bar, 100µm.
(B) Quantification of cells with dispersed cis-Golgi (right) and representative GM130 IF pictures (left) of senescent (4OHT) and control (DMSO) IMR90 ER:RAS cells after transfection with the indicated siRNAs (n=3). Quantification performed using threshold of integrated intensity (Intensity x Area) in 'region growing' collar. Data represented as mean±SD. *p < 0.05, **p < 0.01; ns, not significant. Unpaired, two-tailed, Student's t-test. Scale Bar, 100µm.
(C) Number of early endosomes per cell (right) and representative EEA1 IF pictures (left) of senescent (4OHT) and control (DMSO) IMR90 ER:RAS cells after transfection with the indicated siRNAs (n=3). Quantification performed by granule count / cell count per well. Data represented as mean±SD. *p < 0.05, **p < 0.01; ns, not significant. Unpaired, two-tailed, Student's t-test. Scale Bar, 100µm.
(D & E) (Right) Quantification of cell with fragmented trans-Golgi (D), early endosome numbers per cell (E) in senescent (4OHT) and control (DMSO) IMR90 ER:RAS cells after treatment for 48 hours with 1.25µM of Golgicide A (GCA),150nM of Brefeldin A (BFA) or 1µM ABT-263. (Left) Representative IF images of trans-golgi (F, TGN46), early endosome (G, EEA1) and IL8 (H) staining (n=3). Data represented as mean±SD. *p < 0.05, **p < 0.01, ***p < 0.001, ****p < 0.0001; ns, not significant. Unpaired, two-tailed, Student's t-test.

5.7 Inhibition of COPI blocks secretion and leads to intracellular accumulation of the SASP

Disruption of the COPI complex and the dispersal of the Golgi that follows result in inhibition of the secretory pathways of the cell, such that GBF1 inhibitors are routinely used to enhance intracellular staining of cytokines for flow cytometry (Schuerwegh et al., 2001). With senescent cells being highly secretory, we hypothesized inhibition of COPI vesicle formation could lead to a drastic increase in intracellular levels of the SASP and inhibition of secretion. Several lines of evidence led us to this hypothesis. Firstly, COPI complex inhibition results in senolysis despite senescent cells not differentially expressing COPI proteins or the enzymes that regulate them. Secondly, the preferential toxicity towards senescent cells is not dependent on Golgi dispersal, as GBF1 inhibitors equally disrupt Golgi in control cells. Finally, the degree of senolysis observed in different senescent systems would appear to correlate with the degree of SASP production in those systems. To examine this further we performed IF for two SASP factors IL-6 and IL-8 (Figure 5.9a and b), in both cases senescent cells with COPB2 knockdown showed an increase in intracellular staining. Moreover, when senescent cells were treated with GBF1 inhibitors it likewise resulted in an increase in intracellular staining (Figure 5.9c). Intracellular accumulation of these SASP factors coincided with significantly reduced levels of extracellular IL-1β when treated with GBF1 inhibition, indicating a blocking of secretion (Figure 5.9d).

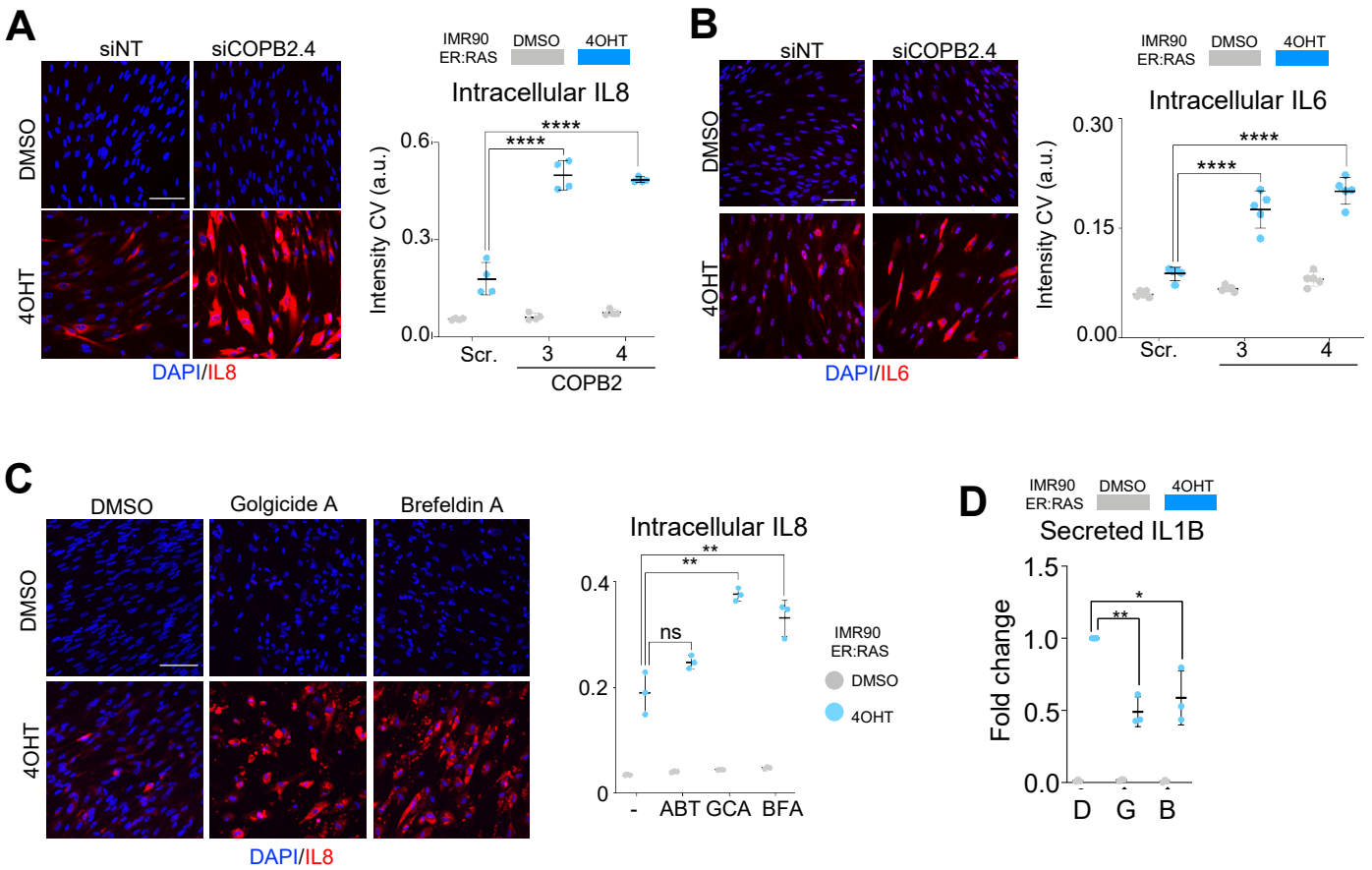

Figure 5.9. Inhibition of COPI results in intracellular accumulation of SASP in senescent cells.

(A & B) Quantification of intracellular levels of (A) IL8 or (B) IL6 (right) and representative IF pictures (left) of senescent (4OHT) and control (DMSO) IMR90 ER:RAS cells after transfection with the indicated siRNAs (n=4). Data represented as mean±SD. *p < 0.05, **p < 0.01; ns, not significant. Unpaired, two-tailed, Student's t-test. Scale Bar, 100μm
(C) (Right) Quantification of intracellular levels of IL8 in senescent (4OHT) and control (DMSO) IMR90 ER:RAS cells after treatment for 48 hours with 1.25μM of Golgicide A (GCA),150nM of Brefeldin A (BFA) or 1μM ABT-263. (Left) Representative IF images of trans-golgi (F, TGN46), early endosome (G, EEA1) and IL8 (H) staining (n=3). Data represented as mean±SD. *p < 0.05, **p < 0.01, ***p < 0.001, ****p < 0.0001; ns, not significant. Unpaired, two-tailed, Student's t-test.
(D) IL1B levels assessed by ELISA of condition media collected from control (DMSO) or oncogene-induced senescence (4OHT) cells treated with 2.5μM of Golgicide A (G) or 150nM Brefeldin A (B) for 48 hours 7 days after senescence induction (n=3). Data represented as mean±SD, *p < 0.05, **p < 0.01, ns, not significant. Unpaired, two-tailed, Student's t-test.

5.8 Inhibition of COPI induces ER stress in senescent cells

Senescent cells are already prone to activation of ER stress pathways, this is hypothesized in part due to their high requirement for protein homeostasis due to the production of the SASP (Abbadie and Pluquet, 2020; Dörr et al., 2013). SASP production requires significant expansion of the ER and Golgi machinery to facilitate synthesis, maturation and secretion of proteins. This could theoretically leave senescent cells susceptible to proteotoxic stress. We hypothesized that the inhibition of COPI could - through potentially both inhibition of secretion pathways and compromising protein quality control - trigger unfolded protein response (UPR) and therein cell death.

UPR has an extensive pathway of transducers with the PERK, ATF6 and the IRE1 pathways being its primary mediators (reviewed in (Adams et al., 2019)). These components or their downstream mediators were examined in the context of COPI disruption in senescent cells. CHOP, or C/EBP homologous protein is a transcription factor whose expression is upregulated during acute UPR where it facilitates the induction of apoptosis (Novoa et al., 2001). This apoptotic program is facilitated by the ability of CHOP to transcriptional activate or repress a host of pro or anti-apoptotic proteins such as the BCL2 family proteins, both BH3-only and multidomain. Upon COPB2 knockdown we observed a significant induction of CHOP expression (Figure 5.10a)

ATF6 is another primary transducer and transcription factor with broader roles in UPR outside of apoptosis including - proteotoxic compensation through ERAD and upregulation of protein chaperones (Adams et al., 2019). ATF6 under normal physiological conditions resides in the ER membrane with its N-terminus protruding into the cytosol and C-terminus in the ER lumen. ER stress triggers ATF6 release from its ER membrane and binding of BiP protein followed by its translocation to the golgi. Here, proteases cleave ATF6 and a fragment of ATF6 (ATF6f) localizes to the nucleus where it transcriptionally regulates ER stress-response

element containing promoters. During COPI knockdown, relocalization of ATF6 to the nucleus was observed indicating triggering of ER stress (Figure 5.10b).

Finally, IRE1 is a ER transmembrane protein that multimerizes upon induction of ER stress, either through direct association with misfolded proteins or association with another misfolded protein sensor BiP. Multimerization results in trans-autophosphorylation and eventual splicing of intronic regions in the mRNA of transcription factor XBP1. Spliced XBP1 or XBP1s then is translated and XBP1 protein translocates to the nucleus where, like ATF6, it can upregulate genes associates with ERAD and UPR-induced apoptosis, such as CHOP. Also, like ATF6 we observe COPI knockdown resulting in an increase in localization of XBP1 to nucleus (Figure 5.10c). The coinciding upregulation of CHOP along with the nuclear translocation of ATF6 and XBP1 was also identified in both OIS and TIS senescent cells treated with GBF1 inhibitors (Figure 5.11a – c). This shows that inhibition of the COPI complex triggers ER stress and the unfolded protein response specifically in senescent cells. What is not known however is if this, and the SASP accumulation observed previous are essential to the COPI inhibition induced senolysis.

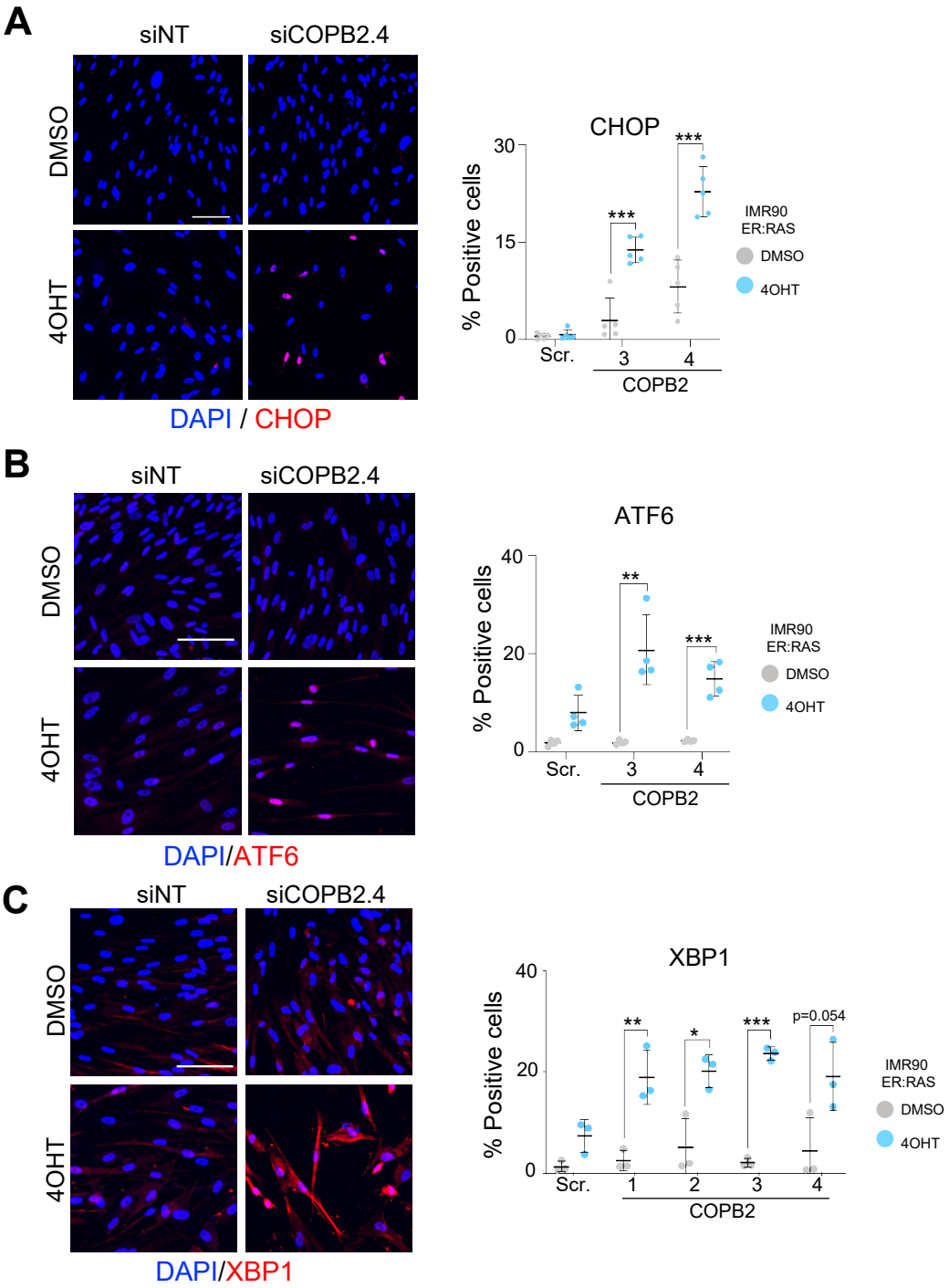

Figure 5.10. Knockdown of COPB2 triggers UPR in senescent cells

(A-C) Quantification of cells positive for CHOP (E), ATF6 (F) and XBP1 (G). 6 days after treating with 4OHT (to induce OIS) or DMSO (as control), cells were transfected with the indicated siRNAs. Cells were fixed, stained and imaged 72 hours later. Data represented as mean±SD. *p < 0.05, **p < 0.01, ns, not significant. Unpaired, two-tailed, Student's t-test. Scale Bar, 100μm.

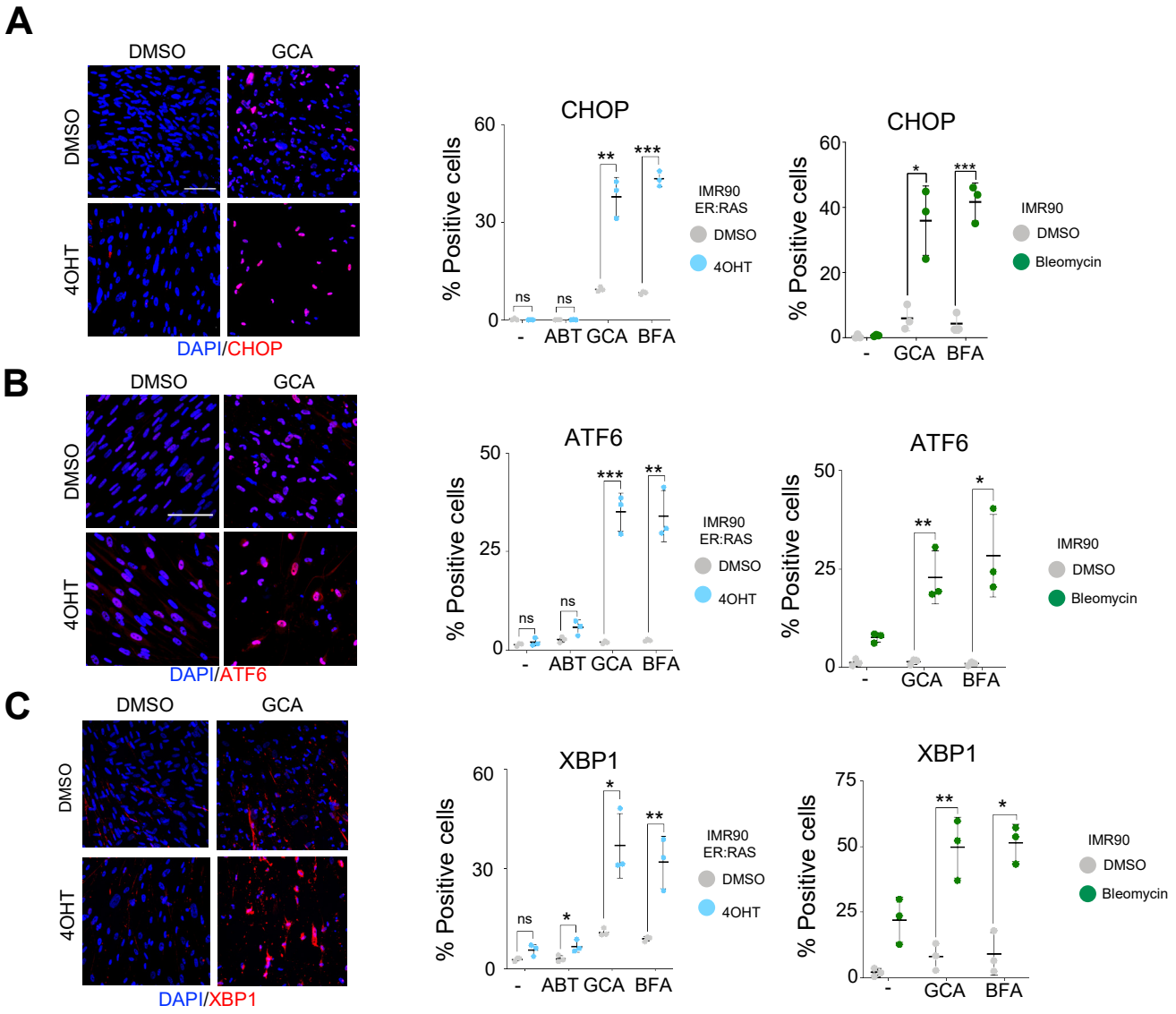

Figure 5.11. COPI inhibition induced senolysis correlates with UPR induction.
(A-C) Quantification of percentage of cells with nuclei staining positive for CHOP (A), XBP1 (B) and ATF6 (C) in control (DMSO) (centre) oncogene-induced senescent IMR90 ER:RAS or (Right) bleomycin-induced senescent IMR90 cells. Cells were treated on day 7 post-induction with 2.5μM of Golgicide A (GCA), 150nM Brefeldin A (BFA) or 1μM ABT-263 for 48 hours. (Left) Representative IF image for CHOP (A), XBP1 (B) and ATF6 (C) shown. (n=3). Data represented as mean±SD, *p < 0.05, **p < 0.01, ***p < 0.001, ns, not significant. Unpaired, two-tailed, Student's t-test.

5.9 Senolytic effect of COPI complex disruption dependent on SASP and UPR

We have shown that upon disruption of COPI vesicle formation senescent cells undergo a caspase-dependent form of programmed cell death. Moreover, this death coincides with disruption of the secretory pathways, intracellular accumulation of the SASP and triggering of ER stress and unfolded protein response. The production of the SASP could be the risk factor of senescent cells that results in their sensitivity to COPI inhibition and would coincide with the reduced senolytic effect in minimal SASP senescence systems. To provide evidence that senolysis caused by COPI inhibition is driven by the SASP and by UPR, we examined what would happen when COPI is inhibited in the context of senescence where the SASP had been suppressed. Previous work in the lab had shown that knockdown of the alternative splicing factor PTBP1, the SASP could be ameliorated but that other senescent phenotypes such as $p16^{INK4a}$/ $p21^{CIP1}$ expression, SA-β-gal activity and growth arrest would remain intact (Georgilis et al., 2018). Furthermore, we tested compounds that could be used to inhibit the SASP without affecting senescence induction, as to provide additional tools to determine the involvement of SASP in COPI inhibition sensitivity. Glucocorticoids, which had been previously identified to the suppress the SASP (Laberge et al., 2012), do so without affecting other senescence phenotypes. Treatment of senescent cells with two glucocorticoids (beclomethasone or triamcinolone) did not affect the reduction of BrdU incorporation (Figure 5.12a & b), or upregulation of $p16^{INK4a}$ or $p21^{CIP1}$ expression (Figure 5.12c) but resulted in a significant reduction in intracellular SASP components IL-6 and IL-8 (Figure 5.12d).

To test our SASP-driven hypothesis, we infected cells with shRNAs against PTBP1 and subsequently treated them with COPB2 siRNAs or GBF1 inhibitors. In both cases, the suppression PTBP1 prevented senolysis (Figure 5.13a and b). Importantly, we could not find any obvious alternative splicing targets of PTBP1 knockdown that lay within the COPI pathway, except for the non-senolytic COPZ2, indicating that this indeed was a SASP

suppression dependent rescue. Treating cells with SASP suppressing glucocorticoids was also able to rescue both COPB2 siRNAs and GBF1 inhibitor induced senolysis (Figure 5.13c & d). In addition, glucocorticoid treatment significantly reduced nuclear translocation of ATF6, indicating rescue of UPR induction (Figure 5.13e) suggesting a SASP mediated triggering of UPR.

The prevention of the senolytic effects of COPI inhibition by SASP suppressing drugs and shRNAs supports our hypothesis that the SASP was driving their sensitivity. To provide additional evidence of a UPR driven death phenotype, cells were treated with the inhibitors of UPR. KIRA6, which inhibits IRE1 splicing, was able to block death induced by GBF1 inhibitors (Figure 5.13f). Inhibitors of PERK, upstream of UPR mediator ATF4, were also similarly able to completely rescue GBF1 inhibitor induced death (Figure 5.13f). Taken together these results would suggest that sensitivity to COPI inhibition is dependent on the presence of the SASP and is partially mediated through unfolded protein response.

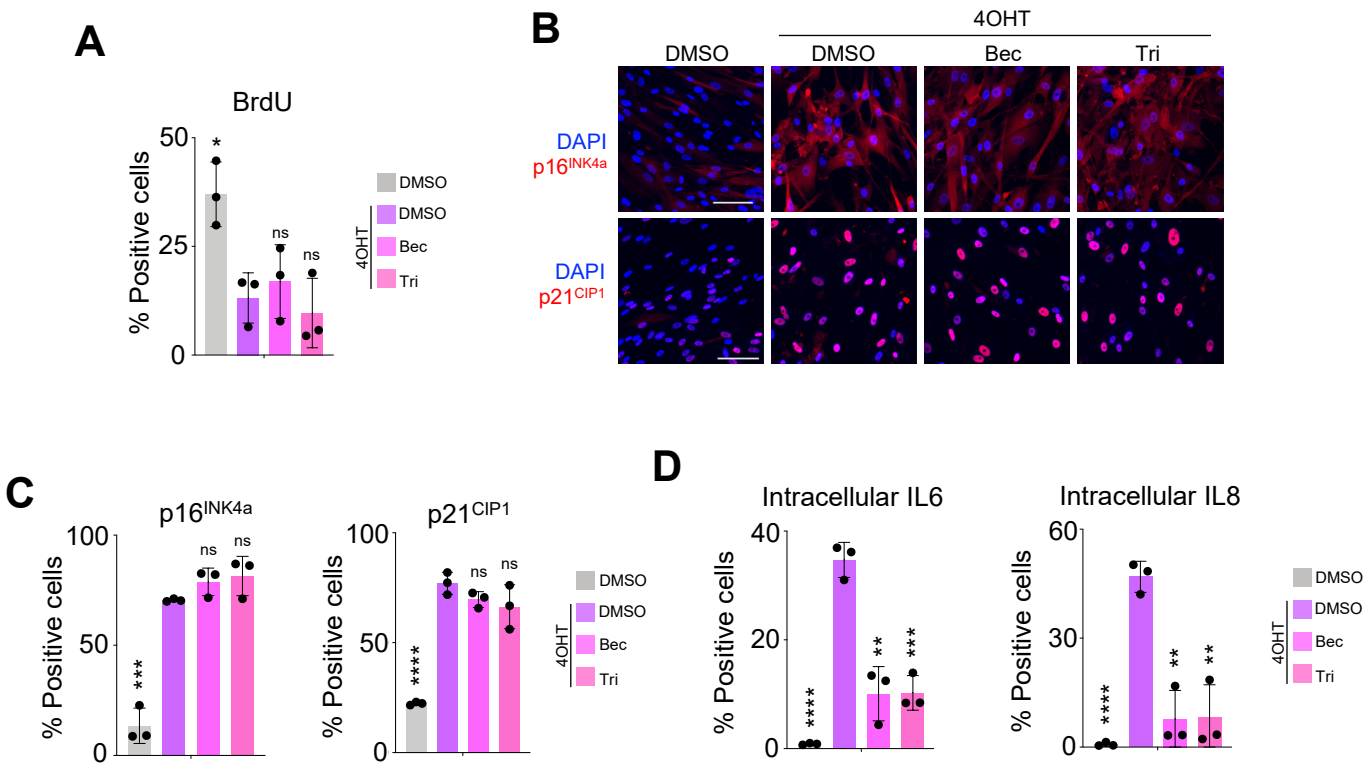

Figure 5.12. Glucocorticoids supress the SASP without bypass of senescence growth arrest.
(A) Effect of treating IMR90 ER:RAS cells, with either 10μM of Beclomethasone (from day 4 after 4OHT induction) or Triamcinolone (from day 0) on BrdU incorporation (at day 5) as measured by quantification of positive nuclei staining by IF. (n=3). Data represented as mean±SD. *p < 0.05; ns, not significant. Unpaired, two-tailed, Student's t-test.
(B) Effect of treating IMR90 ER:RAS cells, with either 10μM of Beclomethasone (from day 4 after 4OHT induction) or Triamcinolone (from day 0) on BrdU incorporation (at day 5) as measured by quantification of positive nuclei staining by IF. (n=3). Data represented as mean±SD. *p < 0.05; ns, not significant. Unpaired, two-tailed, Student's t-test.
(C) Quantification of percentage cells positive for p16INK4a (left) and p21CIP1 (right) on day 6 after senescence induction (n=3). Data represented as mean±SD. ***p < 0.001, ****p < 0.0001; ns, not significant. Unpaired, two-tailed, Student's t-test.
(D) Quantification of percentage of cells positive for IL6 (Left) and IL8 (Right) on day 10 after senescence induction (n=3) Data represented as mean±SD. **p < 0.01, ***p < 0.001, ****p < 0.0001; ns, not significant. Unpaired, two-tailed, Student's t-test.

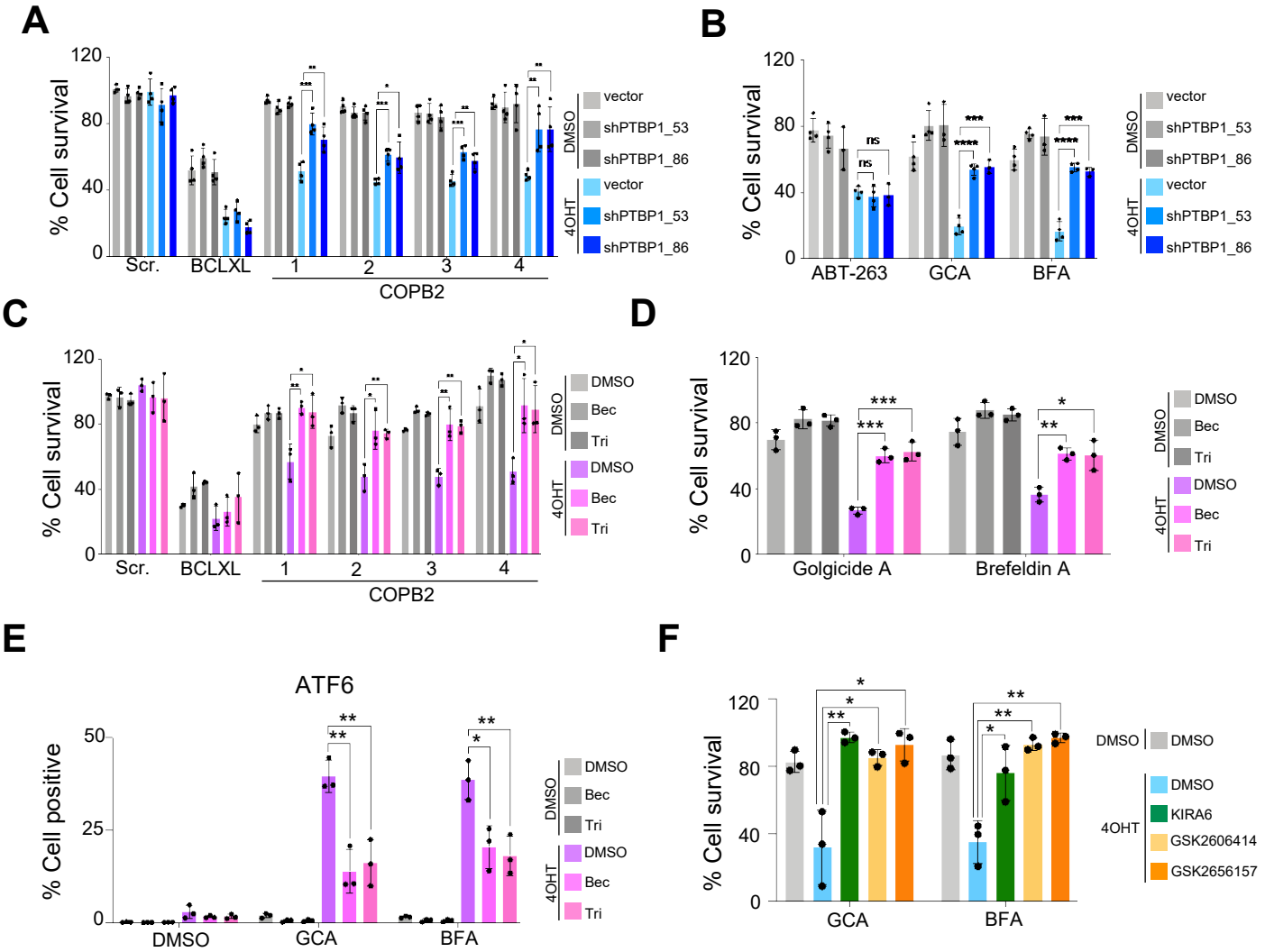

Figure 5.13 The senolytic effects caused by COPI inhibition depends on the SASP and UPR.
(A) SASP inhibition caused by knockdown of PTBP1 prevents the senolysis induced by COPB2 depletion. Quantification of cell survival of senescent (4OHT) and control (DMSO) IMR90 ER:RAS cells infected with the indicated shRNAs (n=4). Data represented as mean±SD. *p < 0.05, **p < 0.01, ***p < 0.001; ns, not significant. Unpaired, two-tailed, Student's t-test.
(B) SASP inhibition caused by knockdown of PTBP1 prevents the senolysis induced by treatment with Golgicide A (GCA) or Brefeldin A (BFA) but not ABT-263. Quantification of cell survival of senescent (4OHT) and control (DMSO) IMR90 ER:RAS cells infected with the indicated shRNAs and treated for 48 hour with either 1μM ABT-263, 1.25μM of Golgicide A (GCA) or 150nM Brefeldin A (BFA) in the context of PTBP1 knockdown. (n=4). Data represented as mean±SD. ***p < 0.001, ****p < 0.0001; ns, not significant. Unpaired, two-tailed, Student's t-test.
(C) SASP inhibition caused by treatment with 10μM of glucocorticoids (Bec, beclomethasone; Tri, triamcinolone) prevents senolysis induced COPB2 depletion. Quantification of cell survival of senescent (4OHT) and control (DMSO) IMR90 ER:RAS cells transfected with COPB2 siRNAs. Cells were treated from day 4 after senescence induction with 10μM of beclomethasone or triamcinolone (n=4). Data represented as mean±SD. ***p < 0.001, ****p < 0.0001; ns, not significant. Unpaired, two-tailed, Student's t-test.
(D) SASP inhibition caused by treatment with 10μM of glucocorticoids (Bec, beclomethasone; Tri, triamcinolone) prevents senolysis induced by treatment with Golgicide A (GCA) or Brefeldin A (BFA) but not ABT-263. Quantification of cell survival of senescent (4OHT) and control (DMSO) IMR90 ER:RAS cells treated with either 1μM ABT-263, 1.25μM of Golgicide A (GCA) or 150nM Brefeldin A (BFA) (n=3). Cells were treated from day 4 after senescence induction with 10μM of beclomethasone or triamcinolone. Data represented as mean±SD. ***p < 0.001, ****p < 0.0001; ns, not significant. Unpaired, two-tailed, Student's t-test.
(E) SASP inhibition caused by treatment with 10μM of glucocorticoids (Bec, beclomethasone; Tri, triamcinolone) prevents ATF6 induction caused by treatment with Golgicide A (GCA) or Brefeldin A (BFA). Quantification of ATF6 positive senescent (4OHT) and control (DMSO) IMR90 ER:RAS cells treated with either 1μM ABT-263, 1.25μM of Golgicide A (GCA) or 150nM Brefeldin A (BFA). IF staining performed on plates fixed 48 hours after the addition of drugs. (n=3). Data represented as mean±SD. *p < 0.05, **p < 0.01; ns, not significant. Unpaired, two-tailed, Student's t-test.
(F) Survival of control (DMSO) or OIS cells (4OHT) pre-treated with 300nM KIRA6, 1μM GSK2656157 or 1μM GSK2606414 prior to a 48 hour treatment with GCA or BFA at day 7 post-senescence induction (n=3). Data represented as mean±SD. *p < 0.05, **p < 0.01; ns, not significant. Unpaired, two-tailed, Student's t-test.

5.10 Inhibition of COPI can alleviate pro-tumourigenic and pro-fibrotic phenotypes caused by senescent cells

Senescence induced by chemotherapeutic treatment determines the outcome of anticancer therapies. A two-step strategy combining senescence-inducing anti-cancer agents (such as etoposide) followed by senolytics (such as GCA or BFA) has been proposed (Guerrero et al., 2019; Wang et al., 2019). We tested whether GBF1 inhibitors such as GCA or BFA could be used in this setting (Figure 5.14a). Treatment with GCA (Figure 5.14b & c) or BFA (Fig 5.14d & e) selectively kill cancer cells previously treated with etoposide.

Lingering senescent cells play detrimental roles in fibrosis, cancer and age-related disease (Ovadya et al., 2018). To understand whether COPI inhibition could ameliorate the negative effects played by senescent cells, we took advantage of shRNA vectors to selectively deplete the expression of COPI components in models of cancer and fibrosis. Senescent cells can enhance the proliferative potential of cancer cells to promote tumor progression (Krtolica et al., 2001). To investigate how COPI inhibition affects promotion of tumorigenesis by senescent cells, we used an experimental xenograft mouse model that monitors the effect of senescent fibroblasts on tumor growth (Georgilis et al., 2018; Herranz et al., 2015). We took advantage of HFFF2 fibroblasts expressing shRNAs targeting either COPA or COPB2 in a doxycycline dependent fashion. We co-injected squamous cell carcinoma 5PT cells with normal or senescent (irradiated) fibroblasts subcutaneously into nude mice (Figure 5.15a) and confirmed that the presence of senescent fibroblasts enhanced tumor growth (Figure 5.15b & c). Depletion of COPA or COPB2 using two independent shRNAs targeting each gene, impaired the ability of irradiated fibroblasts to promote the growth of 5PT tumor cells in this setting (Figure 5.15b & c)

To understand whether COPI inhibition could have beneficial effects beyond cancer, we resorted to a model of lung fibrosis (Triana-Martínez et al., 2019). In this model, normal or senescent (γ-irradiated) human IMR90 fibroblasts bearing inducible control or COPB2-targeting shRNAs, are transplanted into the lung of immunodeficient mice (Figure 5.15d). Mice were treated with doxycycline to induce expression of the shRNAs. 21 days after transplant we assessed expression of CDKN2A (the human gene encoding for p16INK4a) to interrogate for the presence of senescent human fibroblasts. We observed decreased expression of CDKN2A in mice transplanted with the inducible COPB2 shRNAs, suggesting that COPB2 depletion resulted in elimination of the transplanted senescent cells (Figure 5.15e). Interestingly, mice transplanted with IMR90 cells bearing COPB2 shRNAs displayed decreased expression of murine Cdkn1a (Figure 5.15f) and Col3A1 (Figure 5.15g), suggesting decreased levels of senescence and lung fibrosis. We also stained the lungs with Masson's trichome to monitor fibrosis. While lungs from mice injected with senescent fibroblast showed increased fibrosis than those injecting with normal fibroblasts, fibrosis was reduced in the lungs of mice injected with cells expressing COPB2-targeting shRNAs (Figure 5.15h & i). As an additional assessment of lung fibrosis, we measured hydroxyproline levels in the lung, confirming that COPB2 depletion resulted in reduced lung fibrosis (Figure 5.15j). The above experiments suggest that inhibiting COPI can ameliorate the effects associated with the presence of senescent cells in cancer and fibrosis.

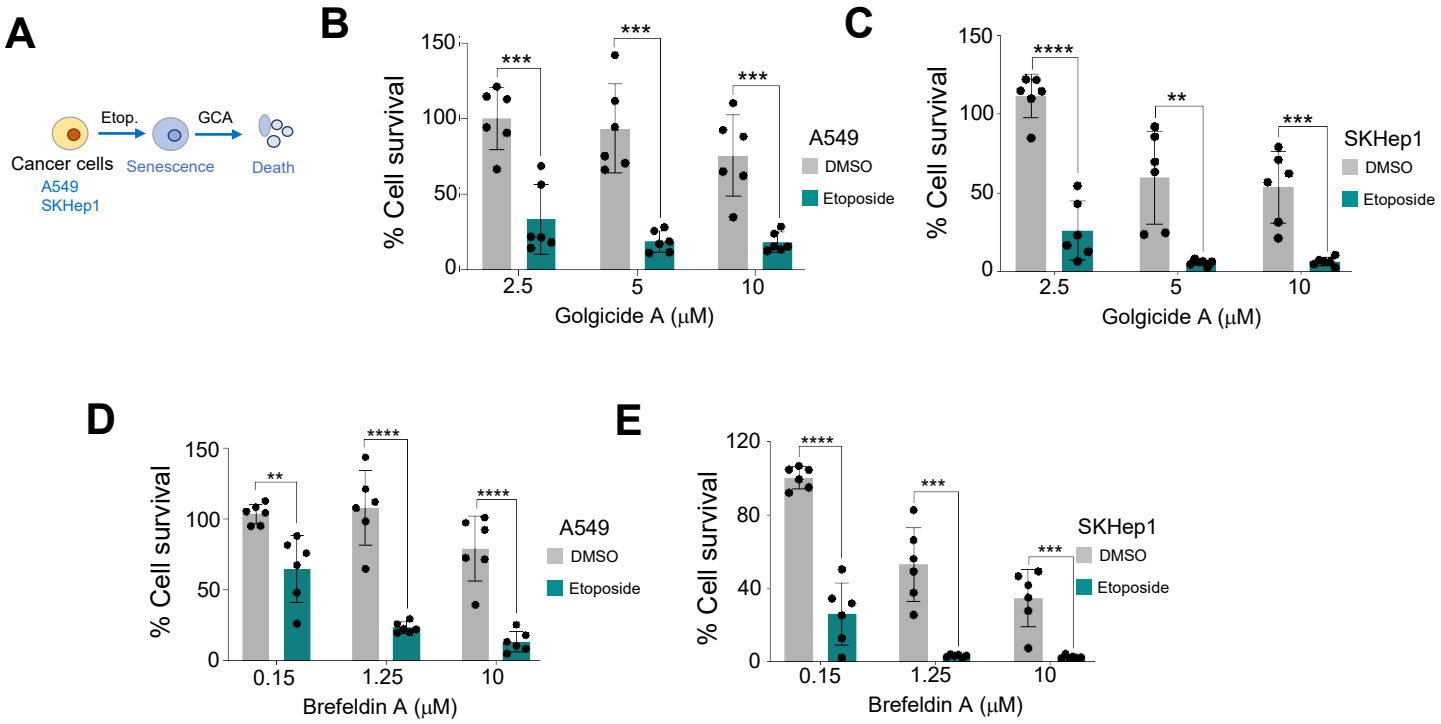

Figure 5.14. Therapeutic benefits of inhibiting the COPI pathway in cancer cells.
(A) Experimental design for sequential treatment of cancer cells with chemotherapy and Golgicide A (GCA).
(B-E) Quantification of cell survival of A549 cells (B & D) or SKHep1 cells (C & E) after treatment with Golgicide A (B & C) or Brefeldin A (D & E) at the indicated drug combinations. (n=6). Data represented as mean±SD. **p < 0.01; ***p < 0.001; ****p < 0.0001. Unpaired, two-tailed, Student's t-test.

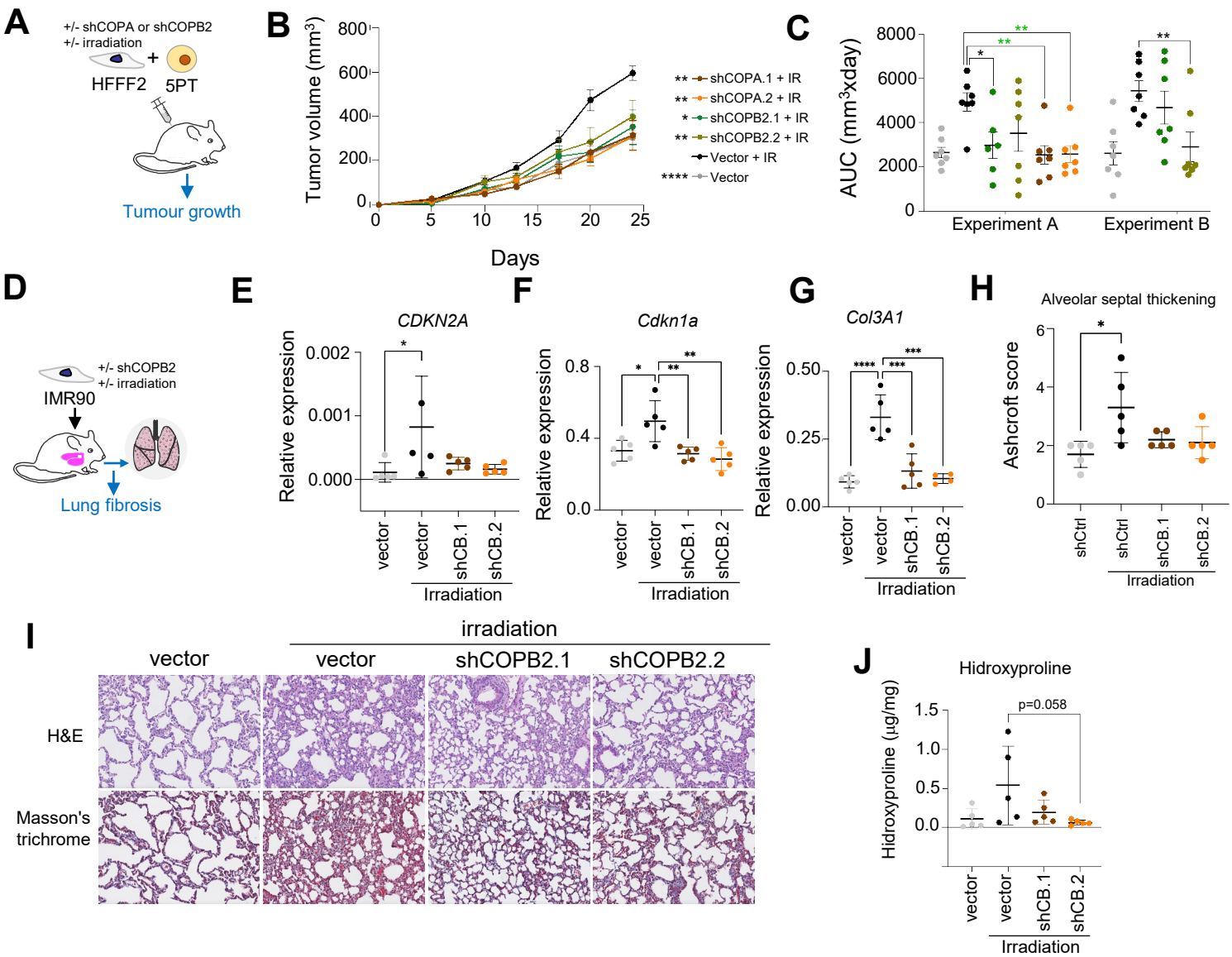

Figure 5.15. Therapeutic benefits of inhibiting the COPI pathway.

(A) Experimental design of tumor growth in NSG cancer model with 5PT squamous cancer cells co-injected with HFFF2 fibroblasts.

(B & C) Tumor growth curves showing the tumour volume monitored over time (IR=irradiation). Data represented as Mean±SEM for all mouse in each group. (n=7 per group). **p<0.01, ***p<0.001; ns, not significant. Unpaired, two-tailed, Student's t-test and ordinary two-way anova were used and refers to the area under the curve (AUC) analysis shown in (C) graph on right.

(D) Experimental design of the mouse model of lung fibrosis senescent lung fibroblast induced lung fibrosis graft model with inducible COPB2 shRNAs.

(E-H) Relative expression of the mRNAs coding for CDKN2A (E), Cdkn1a (F) and Col3a1 (G) in lung samples from the experiment described in (F). (n=5). Data represented as mean±SD. *p < 0.015; **p < 0.01; ***p < 0.001; ****p < 0.0001. Unpaired, two-tailed, Student's t-test.

(H & I) Graph showing histological scoring of fibrosis based on thickening of alveolar walls and focal areas of fibrotic masses based on H&E and Masson's Trichrome staining. Representative pictures of lung sections stained with hematoxylin and eosin (H&E, top) and Masson's trichrome (bottom) from mice of the experiment described in (F). Scale bar, 100 µm.

(J) Lung hydroxyproline content in samples from mice of the experiment described in (F). Data represented as mean±SD (n=5). Ordinary One-way ANOVA, Multiple comparison Turkey test.

(Senescent tumour growth model experiment (Figure 5.15a-c) animal handling and measurements were performed by Dr Massimiliano Mellone under Prof Gareth J Thomas (University of Southampton). Animal handling, histological and transcriptional analysis for mouse lung fibrosis model (Figure 5.15d-j) were performed by Dr Fernanda Hernández-González under Prof Manuel Serrano (IRB Barcelona))

5.11 COPI vesicle formation is *N*-myristoyltransferase (NMT) dependent and NMT inhibition is senolytic.

siRNA and CRISPR screens had identified COPI inhibition as a liability of senescent cells. Subsequently inhibitors of GBF1 were found to mimic COPI knockdown and these effects were found to be primarily dependent on the SASP and UPR pathways. The next step in validation of COPI as a senolytic target would be to test some *in vivo* models of senescence. Here however we run into an issue. The pharmacological properties of Golgicide A are unknown (Sáenz et al., 2009). Brefeldin A on the other hand has been studied extensively for its reported anti-tumor properties but further development largely abandoned due to its extremely short half-life *in vivo* (Phillips et al., 1998). Therefore, we began examining potential drugs targeting COPI vesicle formation that have better pharmacokinetic properties. ARF GTPases that regulate COPI vesicle assemble on the cytosolic side of the Golgi membrane must be anchored into this membrane. To facilitate this, ARF GTPases are modified with an N-terminal lipid chain, myristic acid, through a process of myristoylation (Kahn et al., 1988; Liu et al., 2009). This *N*-terminal modification occurs in a two-step manner, first METAP2 removes methionine on nascent amino acid chain with Methionine followed by a glycine. Amino acid chains with exposed glycine are then modified by *N*-myristoyltransferases NMT1 and NMT2 to attach myristic acid (reviewed in (Yuan et al., 2020)). Nascent protein failing to undergo N-myristoylation are degraded by an N-terminal degron system involving ZYG11B and ZER1 (Timms et al., 2019). More, recently, a global analysis of myristoylated proteins identified several ARF GTPase family members (Grocin et al., 2019).

Inhibitors of *N*-myristoyltransferases (NMTi) have already been reported to produce anti-tumorigenic effects (Beauchamp et al., 2020), in addition they are well tolerated at high doses and their pharmacokinetic properties are well understood. To test whether NMT inhibitors could also act as senolytics, we first examined whether NMT inhibitors recapitulate some of

the phenotypes observed inhibiting COPI. To validate the activity of NMT inhibitors such as IMP1088 and DDD86481 we infected IMR90 ER:RAS and IMR90 cells with N-terminal degron reporters (Timms et al., 2019) (Figure 5.16a). These reporters' function by expressing 24 N-terminal amino acids of a proteins fused to GFP, such that if a peptide is to be degraded by the proteasome it can be detected as a decrease in GFP levels. These cells also co-express DsRed as a marker. To detect inhibition of *N*-myristoylation we utilized *N*-terminal degron reporters derived from three genes - HPCA, TMEM106B and GNAO1 – all validated for their sensitivity to NMT inhibition by either drugs or knockout (Timms et al., 2019). Treating both therapy-induced senescent cells and oncogene-induced senescent cells, alongside normal cells resulted in a significant decrease in percentage of cells expressing GFP for all three degrons (Figure 5.16b – d). Interestingly, both OIS and therapy -induced senescent cells displayed lower levels of GFP, possibly indicating alteration of N-myristoylation levels in senescent cells.

To investigate this further, cells were incubated with a myristic acid analog, YnMyr, in order to metabolically label myristoylated proteins – with or without NMT inhibitor treatment. Lysates collected from these cells were either processed using the CuuC-AzTB capture method (Thinon et al., 2014) and analyzed via in-gel fluorescence or subjected to biotin pulldown and submitted TMT-mass spec proteomics. Following what was observed from the *N*-degron reporters, we observed that with NMT inhibition there is a reduction in the level of n-myristoylation (Figure 5.17a). In addition to this, ARL1 – a known *N*-myrisotylated protein – protein levels were reduced upon NMT inhibition. Cells undergoing OIS and, to a lesser extent, therapy-induced senescent cells displayed an increase in levels of *N*-myristoylation as detected by YnMyr incorporation (Figure 5.17a). The combination of lower levels of GFP with myristoylated *N*-degron reporters and higher levels of overall *N*-myristoylation with short term labelling techniques, could indicate significant alterations to turnover of *N*-myristoylated

proteins during senescence. Indeed, previous published literature suggests that senescent cells have enhanced protein turnover (Deschênes-Simard et al., 2014), potentially supporting this hypothesis.

Proteomics performed on YnMyr immunoprecipitated lysates showed that in senescent cells, both ARF1/3 and ARF4 were enriched in proteomic samples that were, conversely, depleted upon treatment with IMP1088 (Figure 5.17b & c). Suggesting they were myristoylated as has been observed by other groups (Grocin et al., 2019). This data highlights the intriguing possibility of using NMT inhibitors to directly target the COPI pathway. As it has been demonstrated by other groups, proteins failing to undergo N-myristoylation undergo proteasomal degradation (Timms et al., 2019), we hypothesized that treating cells with NMT inhibitors could result in suppression of ARF GTPase protein levels. This opens the possibility of NMT inhibitors phenocopying COPI inhibition. Indeed, immunoblotting for ARF1/3/5/6 using a pan-ARF antibody revealed that upon NMTi treatment of oncogene-induced senescent and normal cells a reduction in ARF1/3/5/6 protein levels could be observed (Figure 5.17d).

NMT inhibitors being able to directly target the COPI pathway raises the question – does treatment of senescent cells with NMTi phenocopy the Golgi disruption, SASP accumulation and ER stress phenotypes observed with inhibition of GBF1 or COPB2 knockdown?

Examining first the distribution of COPI stained vesicles in cells (Figure 5.18a) we see that there is upon addition of NMTi – as we observed with GBF1i - COPI stained vesicles become localized away from the perinuclear regions of the cell, becoming more dispersed. This likely reflects COPI proteins no longer being able to assemble on the Golgi apparatus. As with GBF1 inhibition and COPB2 knockdown, NMTi also disrupted Golgi (Figure 5.18b and c) and early endosome (Figure 5.18d). This also correlated with intracellular accumulation of the

SASP (Figure 5.18e - g) and triggering of ER stress (Figure 5.19a - c) mimicking what was observed with GBF1i and knockdown of COPB2.

We next asked whether NMTi inhibitors could act as senolytics. Cells OIS (Figure 5.20 a – c) and therapy induced senescent cells (Figure 5.20d & e) were treated with three NMTi compounds IMP1088, DDD86481 and IMP1320. In both instances, all three inhibitors displayed potent senolytic activity, with IMP1088 having an approximately 35-fold lower half-maximal effective concentration in therapy-induced senescent cells than normal cells. The senolytic effects of NMTi were prevented by KIRA6, an IRE1a inhibitor (Figure 5.20f), suggesting their dependence on UPR activation, as was the case with GBF1 inhibition.

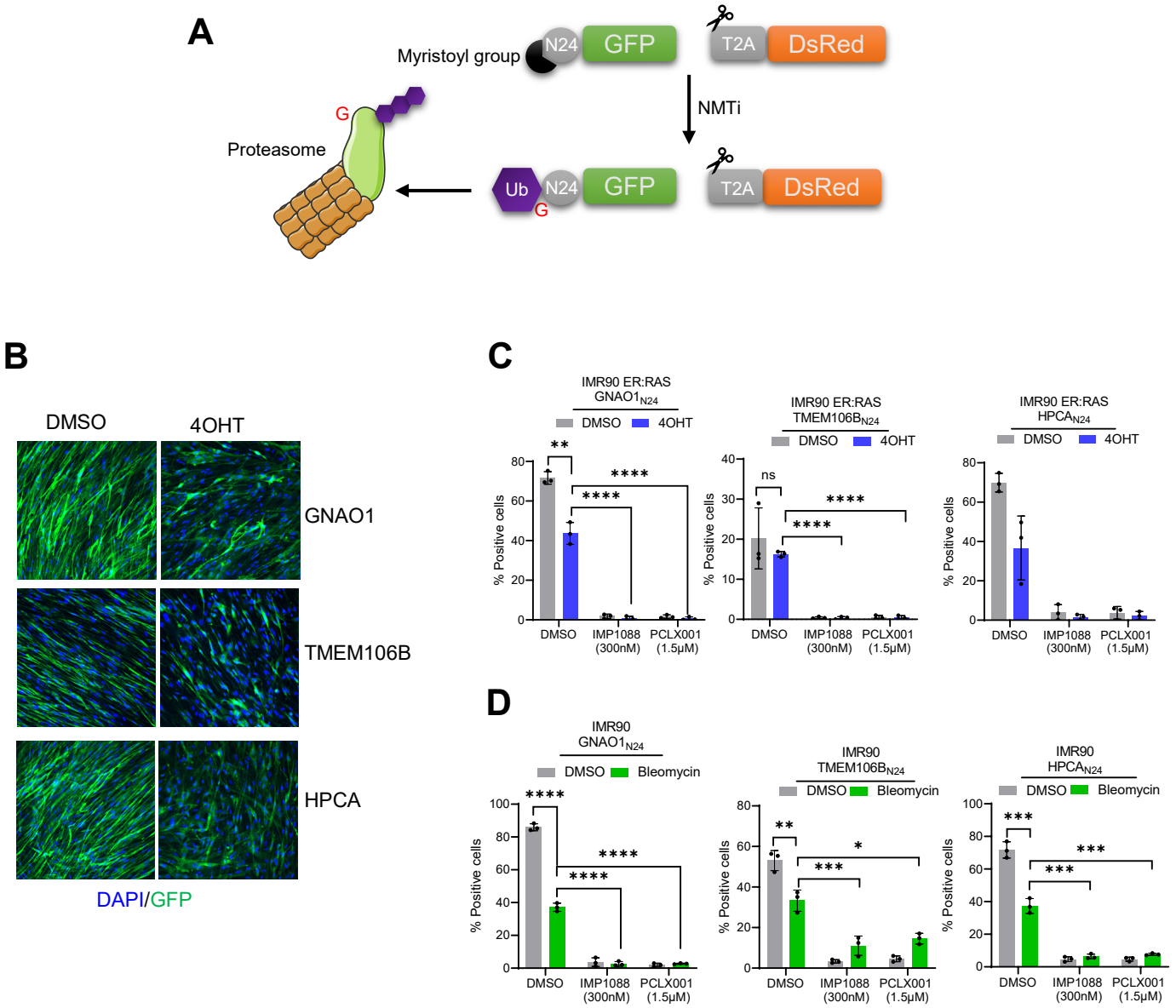

Figure 5.16. *N*-terminal myristoylation degron reporters demonstrate the effect of NMTi

(A) Overview of *N*-terminal degron reporter system.

(B) Representative IF images of GFP from control (DMSO) or senenscent (4OHT) IMR90 ER:RAS cells infected with Ub-N24 reporters for GNAO1, TMEM106B and HPCA.

(C) Quantification of percentage positive cells for GFP signal in control (DMSO) and senescent (4OHT) IMR90 ER:RAS infected with (left) GNAO1, (centre) TMEM106B and (right) HPCA Ub-N24 reporters of N-Myristoylation and treated for 3 days with NMTi. (n=3). Data represented as mean±SD. *p < 0.015; **p < 0.01; ***p < 0.001; ****p < 0.0001. Unpaired, two-tailed, Student's t-test.

(D) Quantification of percentage positive cells for GFP signal in control (DMSO) and senescent (Bleomycin) IMR90 infected with (left) GNAO1, (centre) TMEM106B and (right) HPCA Ub-N24 reporters of N-Myristoylation and treated for 3 days with NMTi. (n=3). Data represented as mean±SD. *p < 0.015; **p < 0.01; ***p < 0.001; ****p < 0.0001. Unpaired, two-tailed, Student's t-test.

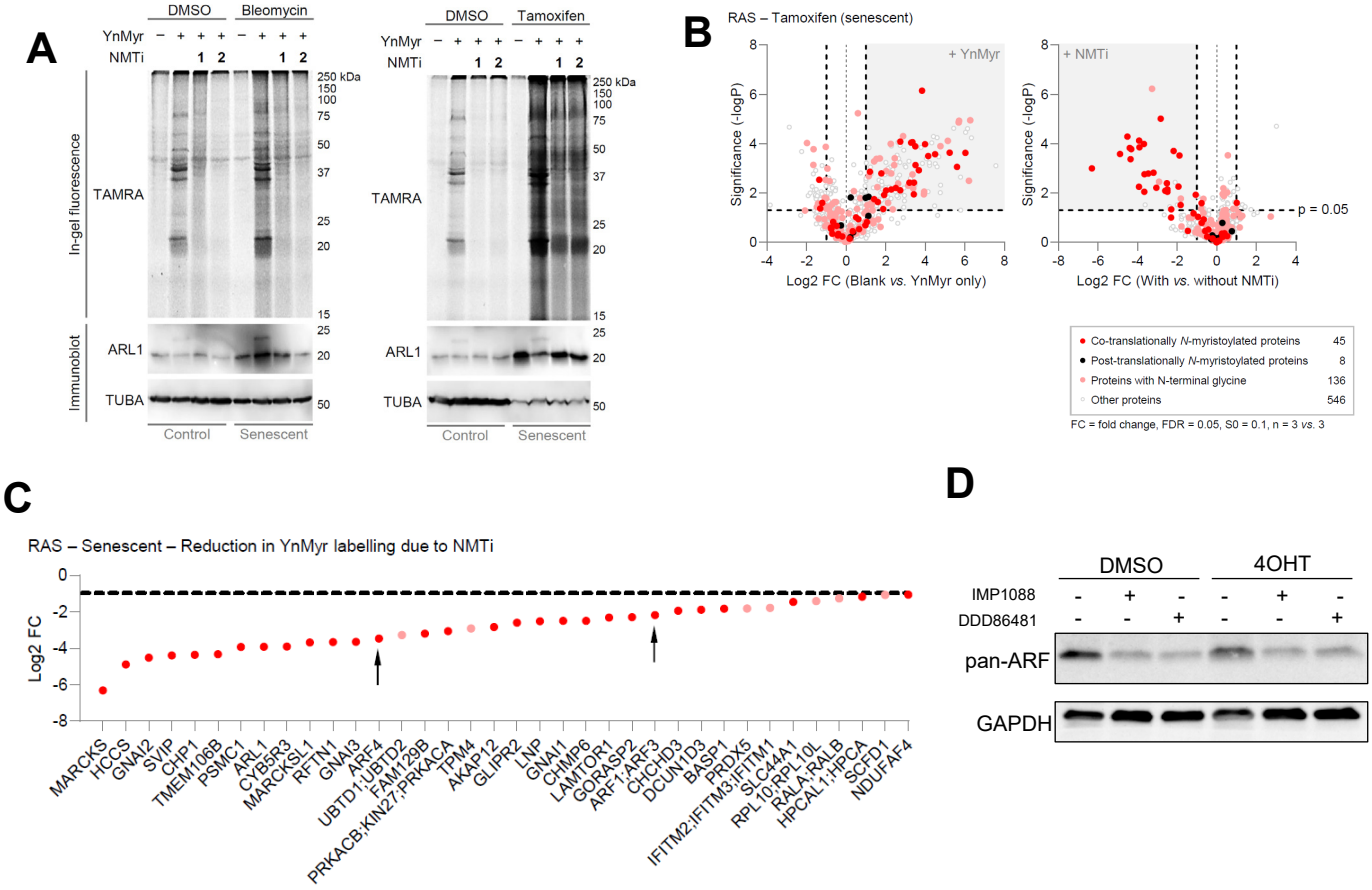

Figure 5.17. *N*-myristoylation labelling reveals that NMTi target ARF GTPases

(A) Treatment of control (DMSO), (left) therapy-induced senescent or (right) oncogene-induced senescent IMR90 and IMR90 ER:RAS cells with NMTi for 18hr decreases N-myristoylation. Whole gel fluorescence for red-fluorescent tetramethyl rhodamine (TAMRA) azide and immunoblots representative of two independent experiments. (n=2). NMTi 1. = IMP1088. NMTi 2. = DDD86481

(B) Proteomics analysis of YnMyr labelled proteins. (Left) log(fold change) of LFQ levels for 4OHT treated IMR90 ER:RAS cells incubated with and without YnMyr for 18h. (Right) log(fold change) of LFQ levels of 4OHT treated IMR90 ER:RAS cells incubated with YnMyr and YnMyr for 18h with IMP1088 (300nM). (n=3). Graph points represents mean. Protein hits filtered by adjPvalue = 0.05 and log(fold change) > 1.5.

(C) Breakdown of proteins detected via proteomics that are enriched with YnMyr treatment and become depleted with additional treatment with IMP1088 (300nM) (n=3). Threshold of log(fold change) of LFQ levels for depleted on NMTi treatment < -1

(D) Treatment with NMT inhibitors (NMTi) result in reduced levels of ARF GTPases. Control (DMSO) or senescent (4OHT) IMR90 ER:RAS cells were treated with 300nM IMP1088 or 1.5μM DDD86481 7 days after senescence induction. Protein extracts were collected 3 days later. Immunoblots of a representative experiment (out of three independent experiments) are shown.

(N-myristoylation proteomics analysis (Figure 5.17a-c) was performed by Dr Wouter Kallemeijn under Prof Edward W. Tate (Imperial College London).

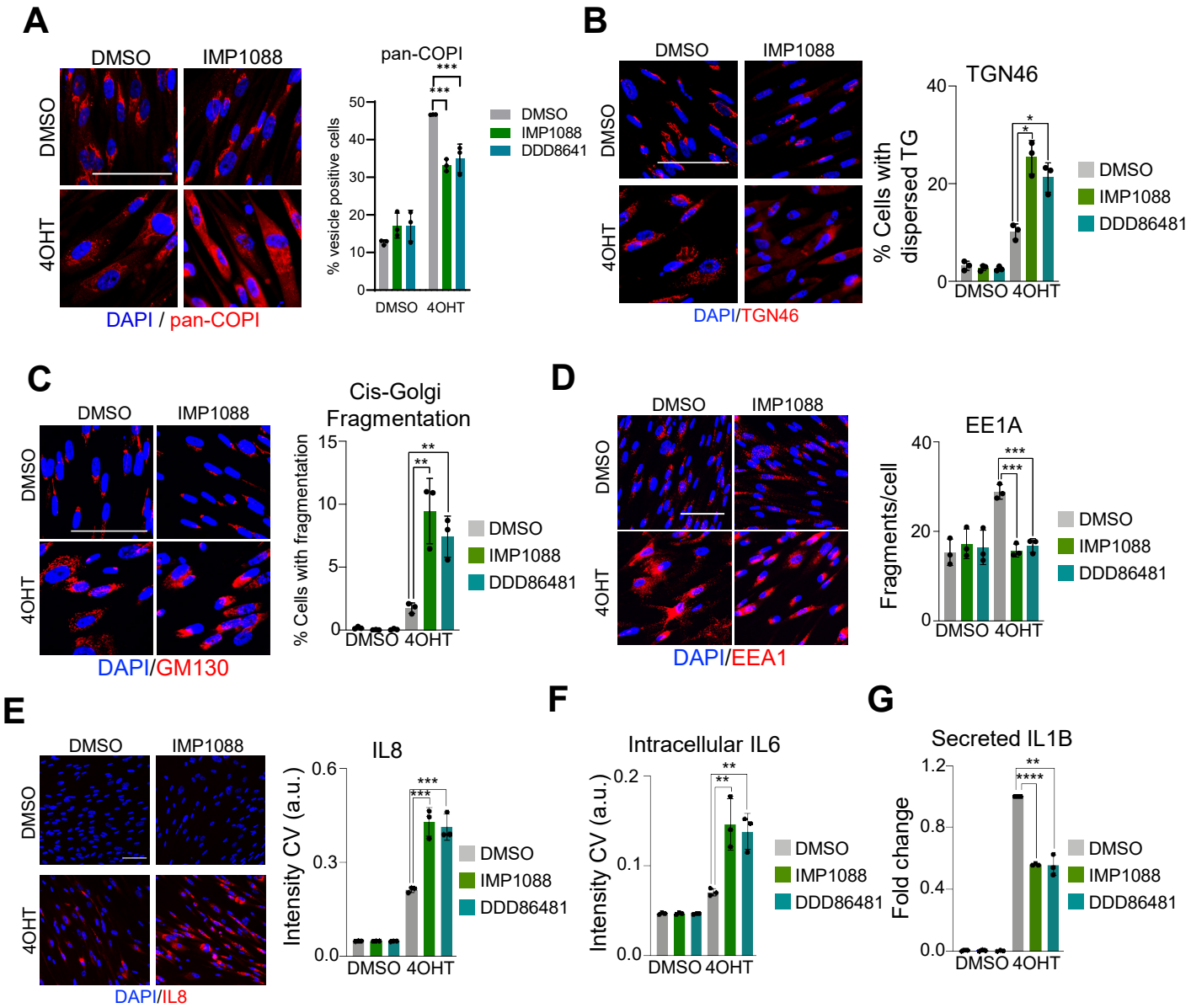

Figure 5.18. NMTi phenocopy disruption of senescence secretory pathway observed upon COPI inhibition

(A) Quantification of cells with punctate COPI staining (right) and representative pan-COPI IF images (left) of senescent (4OHT) and control (DMSO) IMR90 ER:RAS cells after treatment for 72 hours with 300nM of IMP1088 or 1.5μM of DDD8641 (n=3). Quantification performed by measuring the percentage of cells with >30 COPI vesicles per cell. (n=3). Data represented as mean±SD. ***p < 0.001, ****p < 0.0001; ns, not significant. Unpaired, two-tailed, Student's t-test.

(B-D) Quantification (right) of IF staining for Trans-Golgi dispersal (TGN46, B), cis-golgi dispersal (GM130, C) and early endosome changes (EEA1, D). IMR90 ER:RAS cells were treated with DMSO (controls) or OHT (senescence). 7 days later, cells were treated with 300nM IMP1088 or 1.5μM of DDD86481 for 3 days. (n=3). Data represented as mean±SD. *p < 0.05, **p < 0.01, ***p < 0.001; ns, not significant. Unpaired, two-tailed, Student's t-test. Representative images are shown in the left panels. Scale Bar, 100μm.

(E & F) Quantification (right) of IF staining for IL8 (E) and IL6 (F). IMR90 ER:RAS cells were treated with DMSO (controls) or 4OHT (senescence). 7 days later, cells were treated with 300nM IMP1088 or 1.5μM of DDD86481 for 3 days. (n=3). Data represented as mean±SD. *p < 0.05, **p < 0.01, ***p < 0.001; ns, not significant. Unpaired, two-tailed, Student's t-test. Representative images are shown in the left panels for IL8. Scale Bar, 100μm.

(G) IL1B levels assessed by ELISA of condition media collected from control (DMSO) or oncogene-induced senescence (4OHT) cells treated with 300nM IMP1088 or 1.5μM of DDD86481 for 3 days, 7 days after senescence induction. (n=3). Data represented as mean±SD, *p < 0.05, **p < 0.01, ns, not significant. Unpaired, two-tailed, Student's t-test.

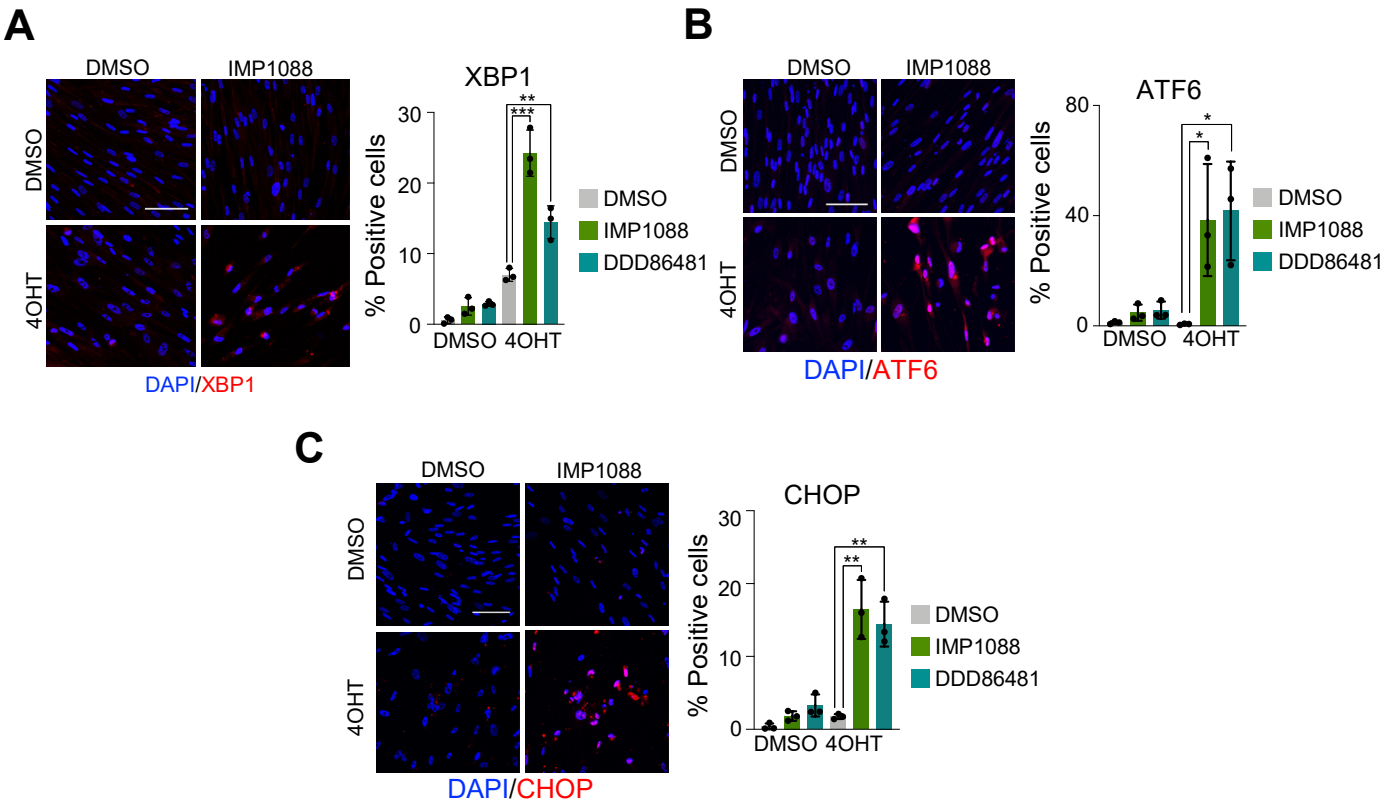

Figure 5.19. NMTi phenocopy UPR induction observed upon COPI inhibition

(A-C) Quantification (right) and representative images (left) of IF staining for XBP1 (A), ATF6 (B) and CHOP (C). IMR90 ER:RAS cells were treated with DMSO (controls) or OHT (senescence). 7 days later, cells were treated with 300nM IMP1088 or 1.5μM of DDD86481 for 5 days (n=3). Data represented as mean±SD, *p < 0.05, **p < 0.01, ns, not significant. Unpaired, two-tailed, Student's t-test. Scale Bar, 100μm.

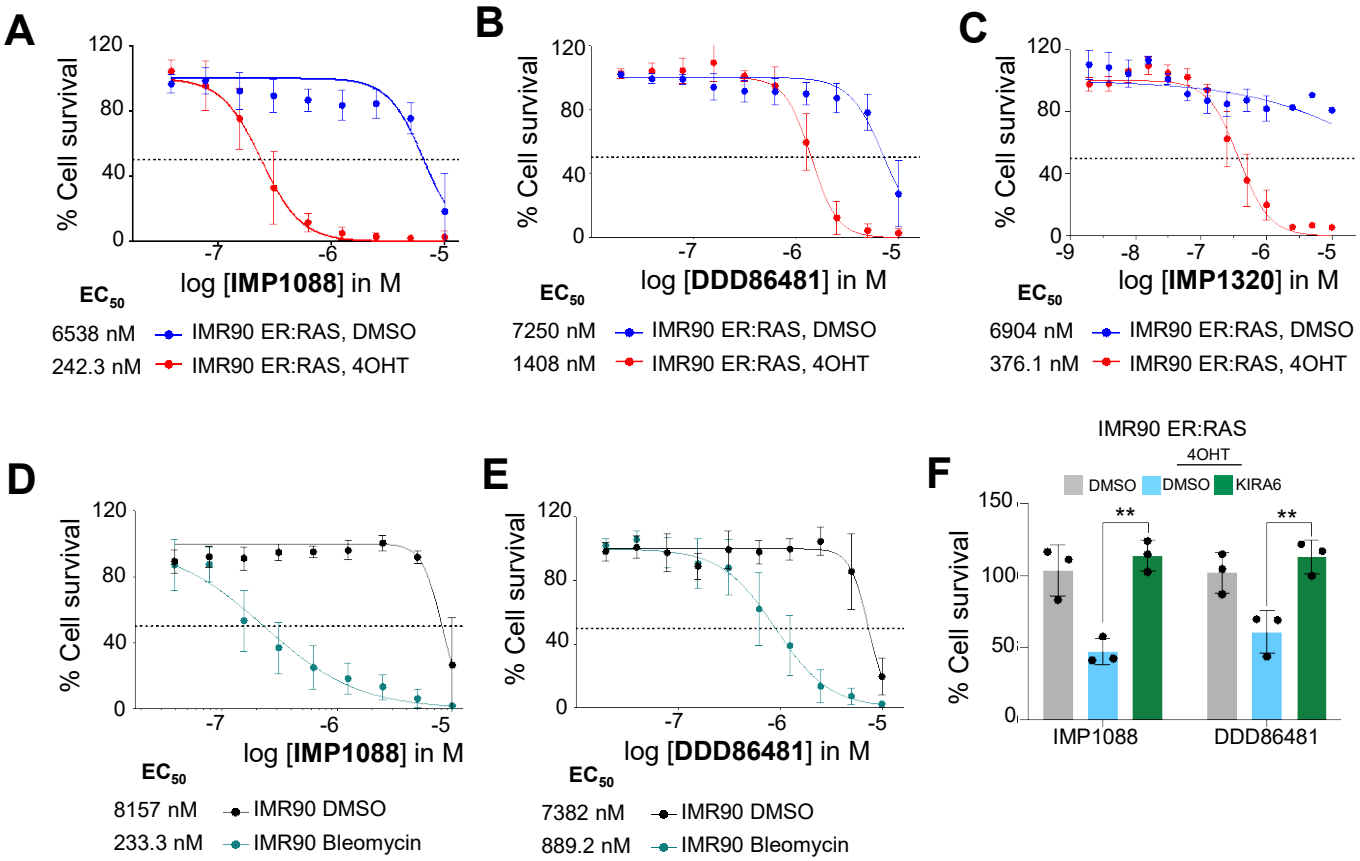

Figure 5.20. NMTi are senolytic in a UPR dependent manner

(A-C) Dose-response curves for senolytic effect of NMT inhibitors IMP1088 (A, n=8), DDD8641 (B, n=5) and IMP1320 (C, n=4). EC50, half-maximal effective concentration.

(D & E) Dose-response curves for control (DMSO) and bleomycin-induced senescent IMR90 cells treated for 7 days with NMT inhibitors, IMP1088 (H, n=6) and DDD86481 (I, n=5). Data points represented as mean±SD.

(F) Survival of control (DMSO) or OIS cells (4OHT) pre-treated with 600nM of KIRA6 from day 4 post-senescence induction and treated 5 days with NMTi. (n=3). Data represented as mean±SD, **p < 0.01, ns, not significant. Unpaired, two-tailed, Student's t-test.

5.12 Inhibition of NMTs can eliminate preneoplastic senescent cells.

NMTi display markedly superior in vivo pharmacokinetic properties to Brefeldin A (Beauchamp et al., 2020). To understand if NMTi could selectively eliminate senescent cells in the context of a tissue, we took advantage of a model of adamantinomatous craniopharyngioma, a clinically relevant pituitary pediatric tumor, in which clusters of β-catenin+ pre-neoplastic senescent cells positively influence tumorigenesis in a paracrine manner (Mario Gonzalez-Meljem et al., 2017). We have previously used *ex vivo* pituitary cultures of these model to assess other senolytic drugs (Guerrero et al., 2019, 2020). Embryonic pituitaries at 18.5 d post-coitum (18.5 dpc) were dissected and cultured ex vivo with or without the NMTi DDD86481 IMP1088 (Figure 5.21a). Treatment with DDD86481 IMP1088 induced apoptosis and eliminated the β-catenin-positive senescent cells (Figure 5.21b and c) without affecting other cell types in the pituitary, such as synaptophysin+ cells (Figure 5.21d).

To investigate whether NMT inhibitors could act as senolytics *in vivo*, we took advantage of a model of liver tumour initiation in which senescence is induced in hepatocytes by transposon-mediated transfer of oncogenic NRAS ($NRAS^{G12V}$) (Kang et al., 2011). We expressed $NRAS^{G12V}$ with gaussia luciferase reporter in livers by taking advantage of hydrodynamic tail vein injection (HDTVI) and treated a cohort with the NMTi IMP1320 (Fig 5.22a). Blood collected from mice showed a reduction in gaussian luciferase activity, indicative of either blocked secretion from construct containing cells or their elimination (Figure 5.22b). Mice treated with NMTi displayed reduced numbers of Nras-positive senescent hepatocytes as assessed by reduced NRas (Figure 5.22c), $p21^{CIP1}$ (Figure 5.22d) and SA-β-gal (Figure 5.22e) staining observed in liver sections, indicating that effects observed on gaussia luciferase blood levels was not due to simple blockage of secretion. The

above results imply that NMTi phenocopy COPI inhibition and can be used as senolytic drugs *in vivo*.

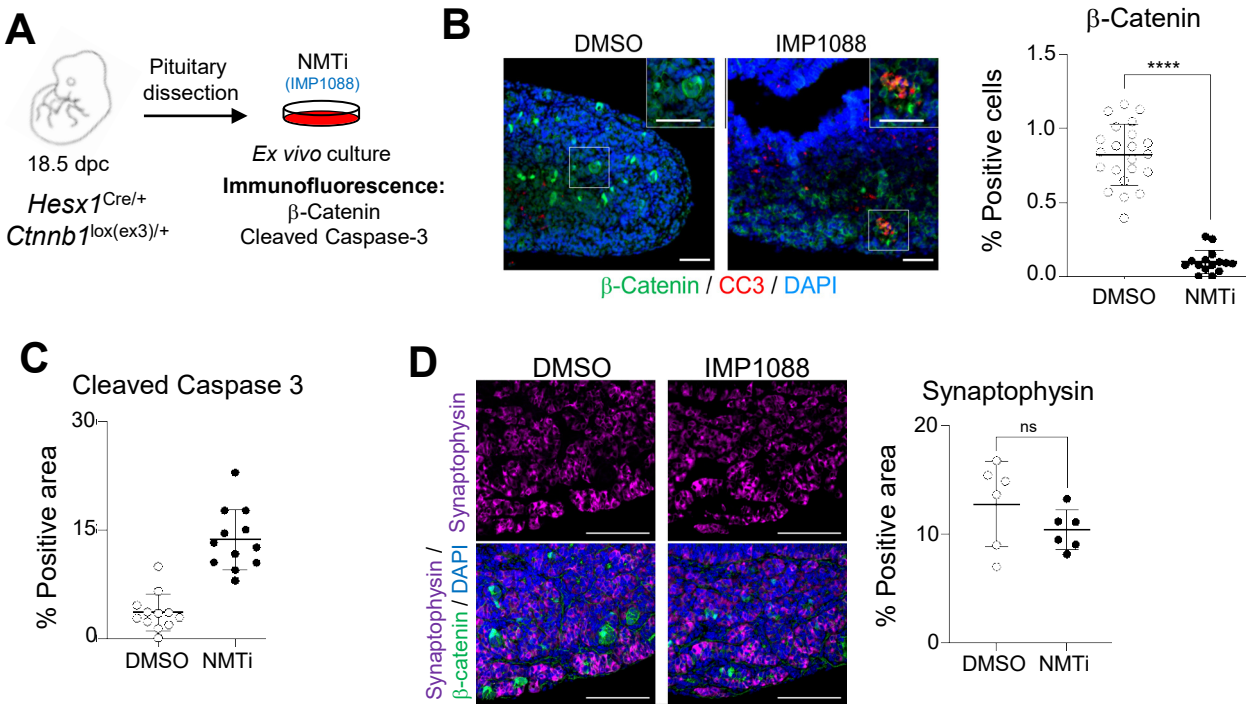

Figure 5.21. Targeting NMT eliminates senescent cells *ex vivo in a* model adamantinomatous craniopharyngioma

(A) Experimental design for the senolytic experiment in the Hesx1Cre/+;Ctnnb1lox(ex3)/+ mouse model of adamantinomatous craniopharyngioma (ACP). Tumoural pituitaries from 18.5dpc Hesx1Cre/+;Ctnnb1lox(ex3)/+ embryos were cultured in the presence of NMTi (600nM IMP1088; n=3) or vehicle (DMSO; n=5) and processed for histological analysis after 72 hr.

(B) Quantification of β-catenin accumulating cells after NMTi treatment highlights the elimination of preneoplastic senescent lesions. Immunofluorescence staining against β-catenin (green) and cleaved caspase-3 (red) shows that oncogene-induced senescent β-catenin positive cluster of cells are undergoing apoptosis. Main scale bar, 50μm - Insert scale bar, 40μm. All error bars represent mean ± SD; n represents number of pituitaries; ****p < .0001

(C) Quantification of cleaved caspase-3 positive area (% of pituitary surface) after NMTi treatment. (each group n=12) Data represented as mean ± SD; ****p < 0.0001. Unpaired, two-tailed, Student's t-test.

(D) Synaptophysin is a marker of the normal hormone-producing cells in the pituitary gland, quantification of synaptophysin positive area (purple; % of pituitary surface) after NMTi treatment highlights no significant effect of the treatment on normal cells. Left panel shows representative images. (each group n=6) Data represented as mean ± SD; ns, not significant. Unpaired, two-tailed, Student's t-test. Scale bar, 50μm.

(*Ex vivo* Adamantinomatous craniopharyngioma experiments (Figure 5.21) were performed by Romain Guiho under Prof Juan Pedro Martínez-Barbera (Great Ormond Street Institute of Child Health, UCL).

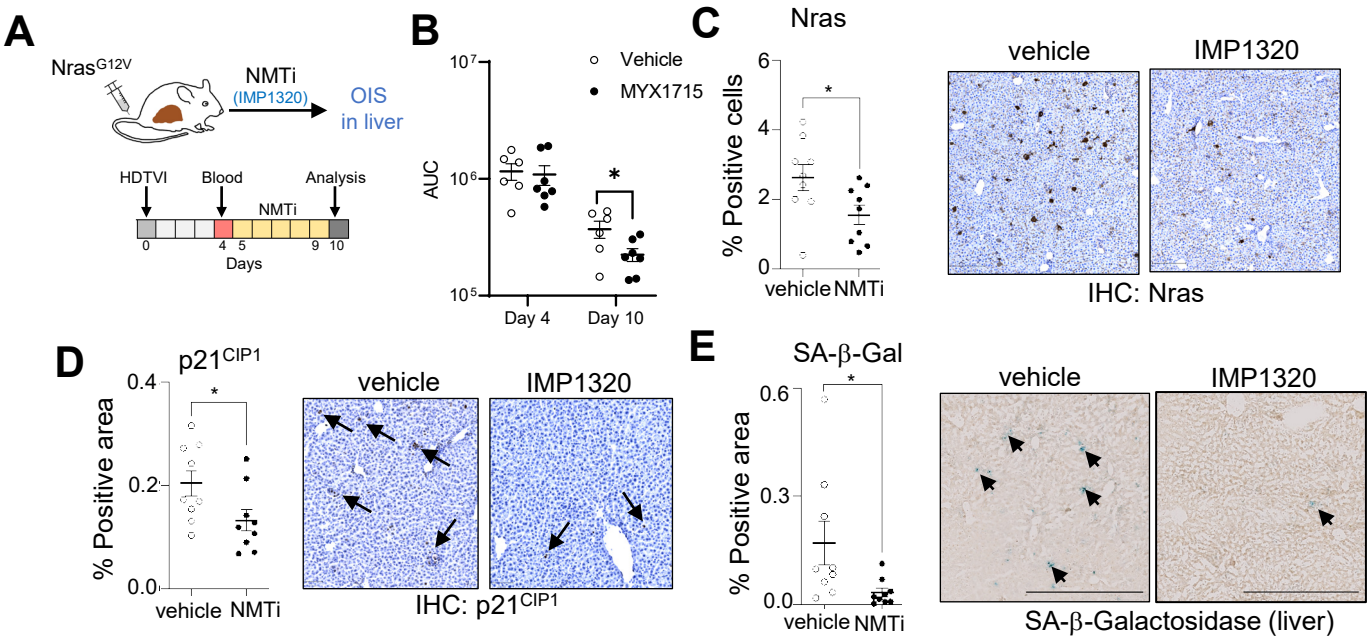

Figure 5.22 NMT inhibitors target preneoplastic senescent cells in a model of liver cancer initiation
(A) Experimental design for the oncogene-induced senescence experiment in the liver.
(B) Quantification of gaussian luciferase activity in blood of mice treated with vehicle (n=6) or IMP1320 (n=7). Samples with <500,000 AUC at day 4 were excluded from analysis due to low dynamic range. Data represented as mean±SEM. *p < 0.05. Unpaired, two-tailed, Student's t-test.
(C) (Left) Quantification of the percentage of Nras-positive cells in the liver of mice treated with vehicle (n=9) or IMP1320 (n=9). Data represented as mean±SEM. *p < 0.05. Unpaired, two-tailed, Student's t-test. (Right) Representative image of NRAS IHC staining in liver of HDTVI mice treated with either vehicle or IMP1320. Scale bar, 100µm.
(D) Quantification (left) and representative images (right) of p21CIP1 staining by IHC in liver of HDTVI mice treated with either vehicle or IMP1320. Scale bar, 50µm.
(E) Representative images (right) and quantification (left) of SA-β-galactosidase (SA-β-Gal) staining in the liver liver of mice treated with vehicle (n=9) or IMP1320 (n=9). Data represented as mean±SEM. *p < 0.05. Unpaired, two-tailed, Student's t-test. Arrows indicate examples of SA-β-galactosidase-positive cells. Scale bar, 100 µm.

5.13 Inhibition of NMTs can eliminate senescent cells in aged mice

Senescent cells accumulate during ageing and contribute to the outcome of many age-related pathologies (Baker et al., 2016). Since NMTi are able to eliminate senescent cells *in vivo*, we investigated the effect that they have in the elimination of senescent cells in old mice. To this end, we subjected 26-month old female mice to a regime of intermittent treatment with the NMTi DDD86481 (Figure 5.23a). This regime was well tolerated and to first assess whether it might result in the elimination of senescent cells, we measured levels of soluble uPAR (suPAR), recently been suggested as a biomarker of senescence (Amor et al., 2020), in blood. Consistent with those observation, we observed higher suPAR levels in blood in old mice when compared with young animals (Figure 5.23b). Interestingly, we observed that old mice treated with NMTi displayed lower levels of suPAR than their vehicle-treated counterparts (Figure 5.23b). To analyse the efficacy and impact of treatment with NMTi during ageing, we conducted RNA-Seq experiments in different organs of these mice. Gene set enrichment analysis (GSEA) of lung transcriptomes showed a downregulation of signatures for COPI and senescence in old mice treated with NMTi when compared with vehicle-treated counterparts (Figure 5.23c). Confirming the ability of NMTi to reduce senescent cell numbers, we observed reduced SA-β-galactosidase staining (Figure 5.23d) and Cdkn1a levels (Figure 5.23e) in the lungs of NMTi-treated mice. Interestingly, NMTi treatment also resulted in reduced lung fibrosis (as assessed by picrosirius red staining, Figure 5.23f), suggesting that by eliminating senescent cells, NMTi have the ability to ameliorate age-related pathologies.

To extend these results, we also analysed the liver of NMTi and vehicle-treated old mice. Transcriptome analysis and SA-β-galactosidase staining confirmed that NMTi treatment phenocopied COPI inhibition and decreased the incidence of senescence in livers (Figure 5.24a & b). Similar to what we observed in lungs, a trend towards decreased liver fibrosis was observed in mice treated with NMTi (Figure 5.24d). Interestingly, Oil Red O staining

showed reduced lipid inclusion in the liver of NMTi treated mice (Figure 5.24e). Confirming this result, we observed a reduction in liver triglyceride levels (Figure 5.24f) and GSEA of liver transcriptome also showed a downregulation of a fatty liver disease signature (Figure 5.24g), altogether suggesting that treatment with NMTi ameliorates liver steatosis. Overall, these results show that treatment with NMTi eliminates senescent cells in vivo and suggest that NMTi could be used to treat senescence-associated pathologies.

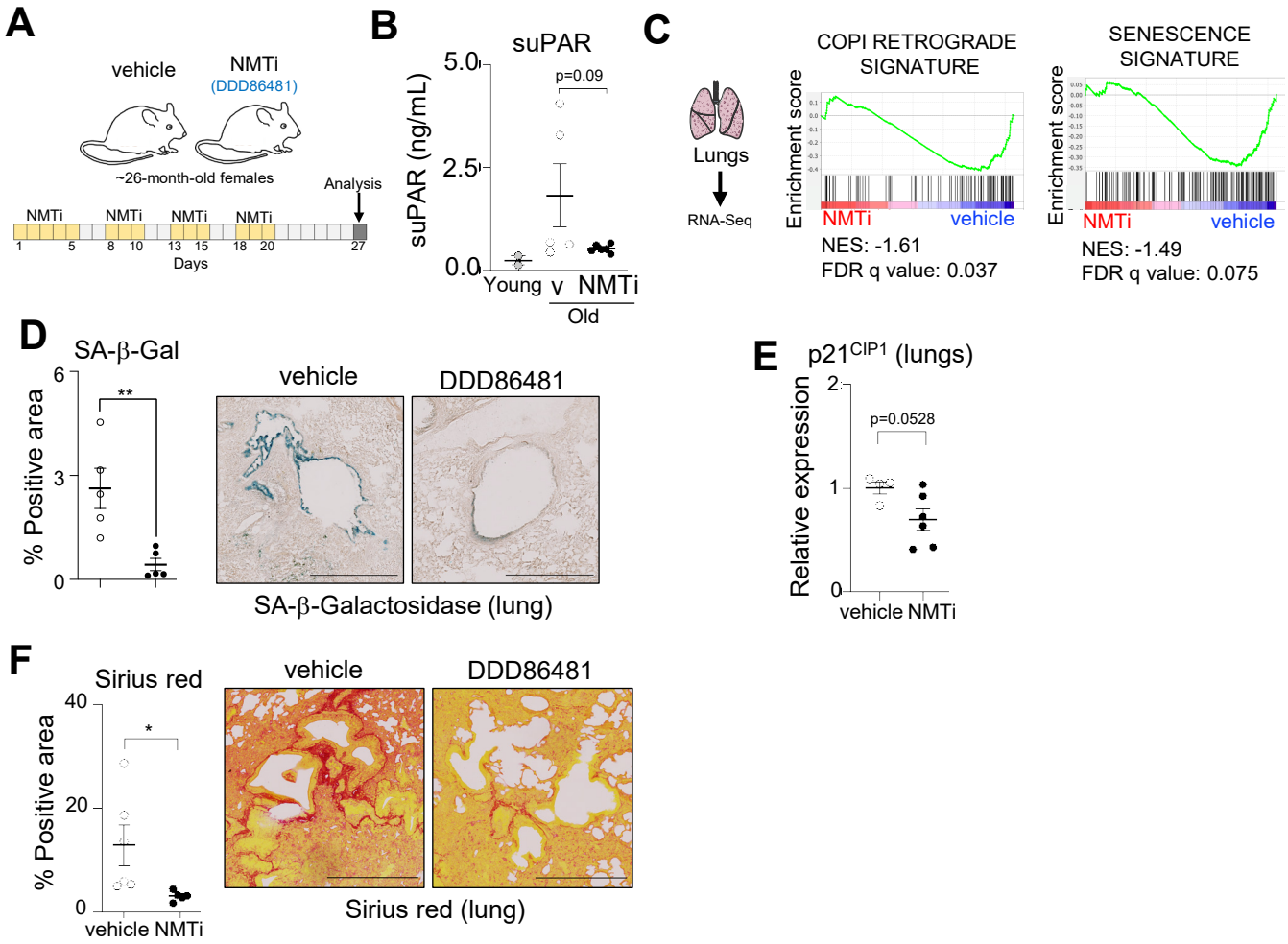

Figure 5.23 Targeting NMT reduces senescent cell burden in lungs of aged mice.
(A) Experimental design for assessing the effect of treating old female mice with the NMTi DDD86481.
(B) Soluble urokinase-type plasminogen activator receptor (suPAR) levels were assessed by ELISA of plasma collected (on day 27) from vehicle (n=5) or DDD86481 (n=6) treated old mice. Plasma of young mice (n=2) was added for reference. Data represented as mean±SEM. Unpaired, two-tailed, Student's t-test.
(C) Left, experimental design for transcriptional profiling of lungs from old mice treated with vehicle (n=4) or DDD86481 (n=6). Right, GSEA signatures COPI retrograde signalling and senescence.
(D) Percentage SA-β-gal positive area in lungs from aged mice treated with vehicle (n=6) or DDD86481(n=5). Right panel shows representative images of SA-β-gal staining in lungs. Scale bar, 100µm. Data represented as mean±SEM, **p < 0.01. Unpaired, two-tailed, Student's t-test.
(E) mRNA expression levels for p21CIP1 in lungs (vehicle n=4, NMTi n=6) of aged mice treated with NMT inhibitor. Expression measured by RT-qPCR relative to GAPDH and normalized to the average of vehicle treated group. Data represented as mean ± SEM. Unpaired, two-tailed, Student's t-test.
(F) Percentage Sirius red positive area in lungs from aged mice treated with vehicle (n=5) or DDD86481(n=5). Right panel shows representative images. Scale Bar, 100µm. Data represented as mean±SEM, *p < 0.05. Unpaired, two-tailed, Student's t-test.

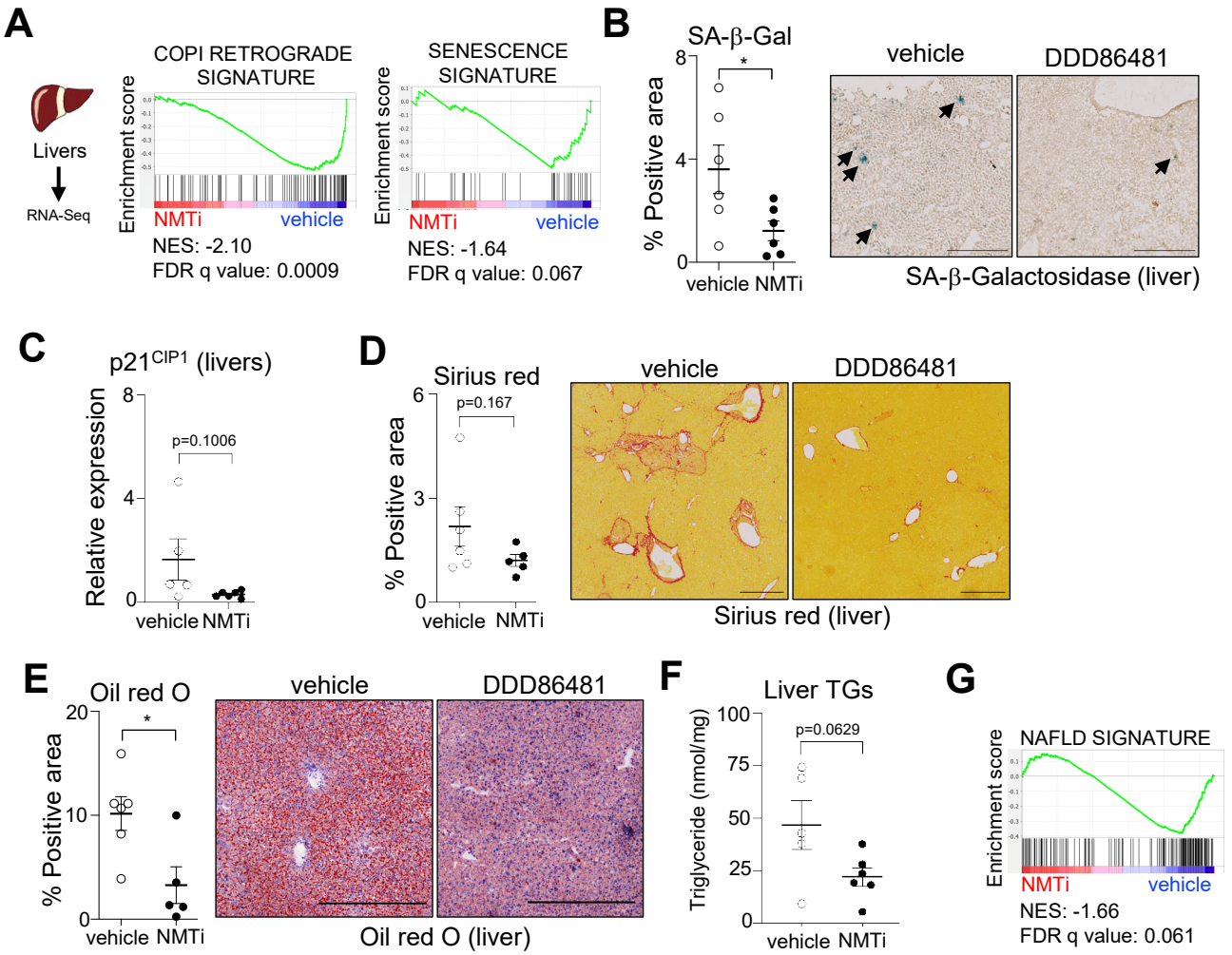

Figure 5.24 Targeting NMT reduces senescent cell burden in livers of aged mice.
(A) Left, experimental design for transcriptional profiling of livers from old mice treated with vehicle (n=4) or DDD86481 (n=6). Right, GSEA signatures COPI retrograde signalling and senescence.
(B) Left, experimental design for transcriptional profiling of livers from old mice treated with vehicle (n=4) or DDD86481 (n=6). Right, GSEA signatures COPI retrograde signalling and senescence.
(C) mRNA expression levels for p21CIP1 and livers (vehicle n=5, NMTi n=6) of aged mice treated with NMT inhibitor. Expression measured by RT-qPCR relative to GAPDH and normalized to the average of vehicle treated group. Data represented as mean ± SEM. Unpaired, two-tailed, Student's t-test.
(D) Percentage Sirius red positive area in livers from aged mice treated with vehicle (n=6) or DDD86481(n=5). Right panel shows representative images. Scale Bar, 100µm. Data represented as mean±SEM. Unpaired, two-tailed, Student's t-test.
(E) Percentage Oil red O positive area in livers from aged mice treated with vehicle (n=6) or DDD86481(n=5). Right panel shows representative images. Scale Bar, 100µm. Data represented as mean±SEM, *p < 0.05. Unpaired, two-tailed, Student's t-test.
(F) Levels of triglycerides measured in liver of aged mice treated with NMT inhibitor. (vehicle n=5, NMTi n=6). Data represented as mean±SEM. Unpaired, two-tailed, Student's t-test
(G) GSEA signature for Non-alcoholic fatty liver disease (NAFLD) is downregulated in the liver of old mice treated with NMTi. (vehicle n=4, NMTi n=6).

5.14 Summary

Unbiased genetic screenings to identify senolytic targets performed in normal, and therapy induced senescent or oncogene-induced senescent IMR90 fibroblasts, suggest that both COPI coat proteins and the enzymes that regulate their assembly into COPI vesicles are essential for senescent cell survival. Expanding upon that we have identified that targeted depletion of multiple COPI coat proteins or inhibition of ARF GTPases through direct targeting of their GTPase nucleotide exchange factors or post-translational *N*-terminal myristoylation elicits the same senolytic effect. This senolytic effect occurs largely independent of how senescence is induced, and it is observed in multiple cell types, suggesting it is a broad specificity senolytic. Following correlative evidence from both the degree of senolytic effect in different senescence modalities and kinetics of GBF1 inhibition across modalities, we hypothesized that the sensitivity of senescent cells to COPI inhibition sensitivity is dependent on the SASP and UPR. Rescue of the senolytic effects caused by COPI inhibition upon suppression of the SASP and UPR pathways, indicated dependency on both pathways. Further validation of the effects of COPI inhibition was carried out *in vivo.* To this end we have been able to show that either using genetic constructs to target the COPI coat proteins or inhibitors of NMT to target ARF GTPase myristoylation we can eliminate senescent cells in mouse models of fibrosis, tumor growth and aging.

Chapter 6. Discussion

From its early description as an *in vitro* phenomenon limiting cell growth by Hayflick (Hayflick and Moorhead, 1961), the senescence field has greatly expanded (He and Sharpless, 2017). In cancer, seminal work into understanding OIS laid the foundation to identify one of its primary functions - to provide a roadblock to aberrantly proliferating cells and thereby block tumorigenesis. However, like many functions of senescence, it is bidirectional with both favourable and detrimental outcomes on tumour progression. Many of the detrimental aspects of senescence in cancer are found to be mediated through a complex inflammatory secretome called the SASP (Kuilman and Peeper, 2009). This SASP, whilst providing essential immunosurveillance functions to supress tumour growth also can fuel tumour growth and provide pro-tumorigenic remodelling the tumour microenvironment. The discovery of the inflammatory nature of senescent cells also expanded our understanding in how this cell intrinsic process may mediate extrinsic effects resulting on widespread tissue dysfunction. As senescent cells were found to accumulate in aging tissues (Hudgins et al., 2018; Krishnamurthy et al., 2004; Wang et al., 2009) and correlate with tissue function decline, the hypothesis formed that senescent cells are a direct contributor to the reduction of healthspan observed with age (He and Sharpless, 2017). Elucidating the role of senescence in aging was complicated however by its anti-tumorigenic functions, leaving many senescent deficient mice prone to high tumour burden and reduced lifespan (Chin et al., 1999; Lim et al., 2000; Sharpless et al., 2001; Varela et al., 2005). Compounding this, targeting the extrinsic effects of senescent cells could also enhance tumorigenesis by preventing their clearance (Xue et al., 2007), further obfuscating the detrimental nature of senescence in aging. A supposition was made, if the presence of senescent cells was detrimental but the cell intrinsic program beneficial, therapeutic benefit may be had by eliminating them – essentially replacing the normal functionality of immunosurveillance.

Based on this genetic ablation systems for senescent cells were developed. These initial studies redefined our understanding on how we may target senescence. Not only was senescence found to be causative in many age-related diseases, elimination of senescent cells may be able reverse disease progression in diseases with few therapeutic options (He and Sharpless, 2017; McHugh and Gil, 2017). Whilst there are examples of normal physiological processes requiring senescent cells such as wound healing, the body of evidence now seems to point to elimination of senescent cells being beneficial. With respect to this, many groups - including our own - have attempted to identify novel ways to eliminate senescent cells *in vivo* (Fuhrmann-Stroissnigg et al., 2017; Guerrero et al., 2019; Zhu et al., 2015). Despite this there remains little knowledge outside of the anti-apoptotic BCL2 family on the mechanisms mediating senescent cell survival. This project sought to uncover pathways mediating the survival of senescent cells, with the ultimate aim to be targeting these processes *in vivo* to elicit beneficial effects in healthspan of aged mice and in cancer therapy.

6.1 RNAi and CRISPR screening provides a robust way of identifying senolytics targets

Performing high throughput non-biased screens provides great potential for the uncovering of novel cell survival pathways and has been used to great effect in uncovering genes mediating cell survival in cancer (Chen et al., 2015; Tzelepis et al., 2016; Yamauchi et al., 2018). High-throughput screening has also been used to elucidate the regulatory pathways of the senescence. Our own group has used screens to uncover novel regulators of the SASP, with siRNA screening of PTBP1 (Georgilis et al., 2018), senescence growth arrest, via shRNA screening for ARID1A (Tordella et al., 2016) and more recently the revealing of cardiac glycosides as senolytics via drug screening (Guerrero et al., 2019). Drug screening for senolytics has revealed that mediators of senescent cell survival may be modality specific. For example, both nitric oxide synthetase and SIRT2 inhibitors were found to be OIS specific whereas, cardiac glycosides and CDK1 inhibitors provide broad specificity senolytics effects

(Guerrero et al., 2019). This highlights the necessity of performing screenings in multiple senescent modalities to understand both general and specific pro-survival pathways. Baring this in mind, it was decided early in the project to perform screenings in different senescence modalities, choosing OIS and TIS models as these provide a robust and non-stochastic way of inducing senescence.

Genetic screening provides clear benefit over drug screens in elucidation of target pathways (reviewed in (Emmerich et al., 2021; Huang et al., 2020)), with off-target effects of single drugs in screens sometimes highlighting spurious candidates. Utilizing both the rapid deconvolution of an siRNA screen and the larger scale, superior knockdown efficiency of pooled CRISPR screen we opted to perform both screening approaches to search for novel senolytics pathways. BCL2L1, is one of the primary targets in the anti-apoptotic BCL2 family that is targeted by the canonical senolytic drugs ABT-263 and ABT-737. In both siRNA screens for oncogene-induced senescence and therapy-induced senescence -BCL2L1 was detectable amongst the highest scoring genes being the 5th and 7th most depleted siRNA gene pools for OIS and TIS screens out of approximately 7,000 genes. Moreover, when genome wide CRISPR screens were performed in these same systems, again sgRNAs against BCL2L1 were among the most depleted. Gene ranking placed BCL2L1 as the 22nd and 7th genes out of 19,050 genes with the highest combined level of depletion amongst its 6 sgRNAs. This was subsequently validated in secondary pooled shRNA screens with BCL2L1 being the 2nd most depleted gene in an OIS context. The detection of BCL2L1 (BCLxL) as senolytic in both our druggable genome siRNA screen and CRISPR screen, is not entirely surprising given that optimization was performed using BCL2L1 targeting siRNAs and sgRNAs. It does however demonstrate that these screening approaches and settings are robust and viable for screening for senolytics.

6.2 RNAi and CRISPR screening reveals several novel senolytic pathways.

Screening of druggable genome siRNA libraries revealed 11 gene targets out of approximately 7,000 genes targeted, as having senolytic effect in either therapy-induced or oncogene-induced senescence effect. These targets showed preferential toxicity for senescent cells with 2 or more siRNAs, reducing the likelihood that this effect was due to off-target effects of siRNAs. Some of these senolytic candidates warrant closer examination of their mechanisms and the viability as potential therapeutic targets.

GNG8 - G protein subunit γ 8, is the GTPase subunit of a G protein coupled receptor (GPCR) that we identified as a candidate senolytic target in oncogene-induced senescence. GPCR, otherwise known as seven-(pass)-transmembrane receptors are transmembrane complexes involved in a large number of ligand binding processes such as neurotransmitters and hormones (Rosenbaum et al., 2009). Relatively little is known about the function of GNG8, with global knockout mice producing deficits in cognitive function, long-term potentiation of neurons (Lee et al., 2020) and reports of it mediating phospholipase C (PLC) activation (Rünnenburger et al., 2002). Interestingly some evidence suggests PLC is involved in regulation of apoptosis in senescent vascular endothelial cells, with its knockdown elevating p53 expression (Cheng et al., 2006), opening the possibility that GNG8's effects are mediated through this access.

TREM2 and APOC2 - is a transmembrane lipid receptor that forms a complex with the TRYO tyrosine kinase complex. Mutations in TREM2 are associated with increased risk of Amyotrophic lateral sclerosis, late-onset Alzheimer's disease and Parkinson's, with patients with these mutations displaying chronic neuroinflammation and amyloid burden both of which also correlate with its increased expression (Ulland and Colonna, 2018). Typically expressed in cells of the myeloid lineage and microglia (Gratuze et al., 2018), TREM2 expression is decreased in response to pro-inflammatory cytokine signalling, contrary to observations *in vivo*. TREM2 has been demonstrated to act as a receptor for both high- and low-density

lipoproteins as well as apolipoproteins such as ApoE (Atagi et al., 2015; Wang et al., 2015b). Interestingly, not only did siRNA screening in therapy-induced senescence identify TREM2 as senolytic but also the apolipoprotein APOC2. Given the apolipoprotein binding capacity of TREM2 and evidence suggesting that TREM2 ligand binding may be a mediator of DAMP signalling to induce apoptosis (Wang et al., 2015b), the effect of lipoprotein signalling on senescent cell survival warrants further examination. Not least, because senescent cells have been shown to have altered lipid synthesis, peroxidation and homeostasis (Flor et al., 2017; Ogrodnik et al., 2017).

ALDOA – also known as fructose bisphosphate aldolase, facilitates the conversion of glyceraldehyde 3P to fructose-1,6 bisphosphate in the glycolysis pathway. Both screens in oncogene induced senescence using siRNAs and CRISPR successfully validated ALDOA as a robust senolytic target. Moreover, manual curation of the secondary shRNA screening of CRISPR screen hits suggested that ALDOA is senolytic in doxorubicin induced senescence with 3 out of 5 shRNAs showing significant levels of depletion. Senescent cells display upregulation of various enzymes in the glycolytic pathway as cells switch away from oxidative phosphorylation to glycolysis (reviewed (Wiley and Campisi, 2016)). Dorr et al. has previously identified that in a lymphoma model of therapy-induced senescence, glycolysis, among other ATP generating pathways such as fatty acid catabolism is drastically upregulated (Dörr et al., 2013). In addition, they show that by inhibiting these ATP generating pathways via inhibition of autophagy or glycolysis that senescent lymphoma cells induce a UPR response and undergo apoptosis. Given the synthetic lethal effects of inhibiting these processes in lymphoma TIS and our screens indicating siRNAs, sgRNAs and shRNAs targeting ALDOA, a key glycolytic enzyme, are senolytic – targeting energy generating processes may represent a general vulnerability of senescent cells. Concordantly, GO term analysis of CRISPR screen hits showed an enrichment in genes regulating intracellular pH reduction

processes (GO:0051452) such as acidification of lysosomes, essential for autophagy. Some of the genes in this GO term were subsequently validated with shRNAs. Moreover, bafilomycin A1, an inhibitor of vacuolar-type ATPase pumps prevents autophagy by inhibiting lysosome acidification and was found to be senolytic (Dörr et al., 2013).

Ubiquitin proteins – Senescent cells induced by ectopic oncogene expression and critically shortened telomeres display enhanced protein degradation known as senescence-associated protein degradation (SAPD) (reviewed in (Deschênes-Simard et al., 2014). Senescent cells displaying SAPD have significantly elevated levels of ubiquitination and through usage of proteasome inhibitors was shown to target proteins such as STAT3 and Heat shock proteins (Deschênes-Simard et al., 2014). SAPD appears to affect a wide range of processes in senescence such as metabolism, cell-cycle inhibition and cell migration (Deschênes-Simard et al., 2014). In our siRNA screens for senolytic targets in OIS and TIS, we identified ubiquitin proteins as senolytic targets. The suppression of UBB and UBC could disrupt SAPD and elevate its targets protein levels resulting in disruption of the senescence program. Moreover, suppression of ubiquitin proteins may hamper the ability of the senescent cell to maintain protein homeostasis, which we know from small compound library screens is specifically toxic to senescent cells with HSP90 inhibitors being potent senolytics (Fuhrmann-Stroissnigg et al., 2017). The senescent cell, probably due to production of its SASP is subject to high levels of proteotoxic stress resulting in an enhanced requirement for protein turnover, folding and secretion machinery (Abbadie and Pluquet, 2020; Deschênes-Simard et al., 2014). This leaves senescent cells potentially susceptible to inhibition of proteasomal degradation as has been observed with HSP90 inhibitors (Fuhrmann-Stroissnigg et al., 2017)and in our case depletion of ubiquitin proteins but also inhibition of autophagic processes such as is seen with inhibition of lysosomal acidification with bafilomycin A1 treatment being senolytic (Dörr et al., 2013).

Coatomer complex I – Both siRNA screens and our genome-wide CRISPR screens highlighted either multiple COPI coat proteins - eg.) COPA, COPB2, COPB1, COPG1- or proteins involved in regulation of coat formation eg.) ARF1, ARFRP1 – as senolytic targets. The numerosity of coat proteins detected as hits in the screen raises the question as to whether other COPI coat members are also essential. Further screening of COPI coat proteins for their senolytic effect using siRNAs yielded some additional targets beyond the already known COPB2 and COPG1 (Figure 6.1a), however some targets such as COPZ1/2 and COPG2 had weaker effects. This is could be due to siRNAs generating insufficient knockdown levels as most shRNA and siRNAs against COPI validated as senolytic produced a >60% decrease in mRNA levels. The senolytic nature of targeting COPI coat proteins does not appear to be dependent on the a specific COPI subcomplex either – with senolytic targets being found in both B-subcomplex (COPA*, COPB2*, COPE) and F-subcomplexes (COPB1*, ARCN1*, COPG1*/2, COPZ1/2). This follows observations in previous studies where knockdown of a single coat protein is sufficient to elicit disruption of trans-Golgi formation and autophagy in addition to be synthetic lethal with RAS mutant cancers (Kim et al., 2013a; Razi et al., 2009). Structural studies of the COPI coat structure suggest that a most of the coat proteins are found bound to one another suggesting that they are not functionally redundant (Bykov et al., 2017; Dodonova et al., 2017), with the exception of COPZ1 and its isomer COPZ2 where one is often differentially expressed in cancer over the other (Shtutman et al., 2011). Our observations of multiple COPI coat proteins being senolytic targets agree with this lack of functional redundancy and suggest that coat formation is essential for senescent cell survival. Moreover, inhibition of ARF GTPase function, either through direct siRNA knockdown or indirectly through inhibition of GBF1 of ARF resulted in senolysis also. These results support the premise that coatomer complex I formation is essential but also a druggable senolytic target.

Further examination of the COPI inhibition phenotype showed that treatment specifically induced unfolded protein response in senescent cells. UPR induction during COPI inhibition followed dispersal of the golgi and accumulation of the intracellular cytokines, similar to what has been previously observed in cancer (Kim et al., 2013a). Concordantly, suppression of the SASP phenotype, rescued senolysis suggesting COPI inhibition sensitivity was tied to the highly secretory nature of senescent cells. This observation also provides an explanation for both the reduced senolytic effect in palbociclib-induced senescence and the extended treatment window to induce senolysis in therapy-induced senescence compared with OIS as both these settings have lower levels of SASP production. The effects of SASP suppression in rescuing senolysis do not however elucidate how UPR is being induced, as in this context this may be through several mechanisms. Defects in early endosome, which is expanded in senescent cells, were observed in cells with knockdown of COPI coat proteins (Razi et al., 2009) . Early endosome maturation is essential for autophagy, and its inhibition results in accumulation of autophagosomes that are non-degradative (Razi et al., 2009). Likewise, depletion of COPI and its disruption of the early endosome coincided with an accumulation of SQSTM1/p62 as well as LAMP1 and 2 (Figure 6.1b-d), thereby indicating a decrease in functional autophagy that is not due to suppression of lysosomes. Inhibition of autophagy has been shown by others to elevate UPR and senolysis in senescent cells (Dörr et al., 2013), indeed our own CRISPR screen results suggested that inhibition of lysosome acidification – essential for autophagy - was senolytic. One possibility is that autophagy facilitates the high protein homeostasis requirements of the SASP and its inhibition results in further upregulation of UPR and induction of an autophagy-dependent form of apoptosis. Conversely, UPR also induces autophagy to support survival during proteotoxic stress (Ding et al., 2007), meaning that if inhibition of secretion leads to accumulation of unfolded proteins at the ER, the effects of COPI depletion on autophagy and on UPR related to protein

accumulation could not be disseminated. This is further compounded by the fact that COPI depletion mediated early endosome disruption is an early event in autophagic processes and therefore could not be rescued by overexpression of ATG or ULK proteins. Screening for apoptotic mediators of COPI inhibition induced senolysis showed that it is mediated through NOXA which is both activated by inhibition of autophagy as well triggering of UPR, demonstrating further the difficulty in separating these mechanisms.

Whilst the SASP may be the primary susceptibility of senescent cells, examining the effects of COPI coat knockdown on Golgi dynamics suggests that senescent cells are more likely to undergo Golgi dispersal too, thereby adding an additional layer of risk. This could be easily explained if senescent cells have differential expression of coat proteins as is seen with COPZ isomers in cancer (Shtutman et al., 2011). However, this does not appear to be the case with both transcriptomic and proteomic data showing no significant changes in expression. Examining previous data generated in the lab also suggests no alternative splicing regulation of most COPI coat proteins during senescence (Georgilis et al., 2018). How then can we explain the differential effect of coat knockdown and also NMT inhibition on the Golgi dynamics of senescent cells? One possibility is that the expanded Golgi apparatus that both we and others (Narita et al., 2011) have observed in senescent cells has a requirement for an increased level of vesicle recycling between cisternae to maintain golgi dynamics and stability. Another explanation is that the alterations in *N*-myristoylation in senescent cells could decrease the available pool of Golgi-cisternae bound ARF GTPases thereby decreasing the rate of COPI vesicle formation and making them the cell more susceptible to small perturbations in the levels of coat proteins. There is some circumstantial evidence to suggest this is the case as COPI vesicles were found more dispersed in senescent cells, however this could be due to expansion of the Golgi. This hypothesis could be examined in follow-up experiments to determine if the activity of ARF GTPases is reduced

in senescent cells and if there is a reduction of co-localization of COPI coat with Golgi markers.

Likewise, to COPI, disruption of Coatomer complex II – rather unsurprisingly given its function as the primary trafficking route of proteins into the Golgi apparatus from the ER - has been shown to induce the unfolded protein response (Xu et al., 2021), inhibit trafficking (Barlowe and Helenius, 2016; Zanetti et al., 2012) and alter Golgi dynamics (Guo and Linstedt, 2006). Despite this, siRNAs against COPII coat proteins and GTPases did not appear to elicit a senolytic effect (Figure 6.1a). This could be due to, as with non-senolytic COPI siRNAs, siRNAs not reaching a critical threshold of knockdown for Senolysis. It could also suggest a specific susceptibility of senescent cells to inhibition of COPI trafficking rather than COPII.

Inhibition of COPI, whether through COPI shRNAs or indirect targeting through treatment with NMT inhibitors resulted in elimination of senescent cells *in vivo*. The scope of this project did not allow for extensive validation of the therapeutic benefits of COPI induced senolysis *in vivo*. During aged mice, treatment with NMT inhibitors was found to reduce collagen staining in both the lung and the liver, indicating a reduction in fibrosis following previous observations on the effects of senolysis on fibrotic disease progression. It should be noted however histological analysis such as these can be biased as sectioning might not be representative. Further experiments should utilize markers of fibrosis from bulk tissue such as assays for hydroxyproline – a major component of collagen. Investigation of expression differences in the collagen genes can act as a surrogate marker of fibrosis, however transcriptomic analysis of liver and lung did not show significant changes in collagen genes. Given the relatively short window of treatment of aged mice in comparison to other senolytic studies which utilize months long treatment, we may not expect a significant resolution of fibrosis. Longer treatment regimens with NMT inhibitors could produce a more drastic effect on fibrosis in these organs and enhance their senolytic effect. NMT inhibitors also produced significant

effects on fat deposition in liver tissue, a marker of hepatic steatosis, in addition transcriptomic signatures for Non-alcoholic fatty liver disease were reduced in liver transcriptomic data. Whilst senescent cells have been shown to alter lipid metabolism and their elimination reduces age associated hepatic steatosis (Flor et al., 2017; Ogrodnik et al., 2017) – inhibition of COPI has also been shown to alter lipid metabolism (Wilfling et al., 2014) meaning that dissemination of the two may be complex. Another confounding factor in elucidating the senolytic effects of targeting COPI *in vivo* is the effects on blocking SASP secretion – which could also be mediating some beneficial effects.

6.3 *N*-Myristoylation and senescence

Another intriguing revelation found from validating the effects and targets of NMT inhibitors in senescent cells was that there appears to be significant alterations to this post-translational mark across senescence modalities. Senescent cells display higher levels of N-myristoylation when pulsed with pulsed with myristic acid analogues, however degron reporters of N-myristoylation would indicate lower levels of *N*-myristoylated proteins. These two results are seemingly incongruous, however could be explained if senescent cells despite having higher levels of turnover of *N*-myristoylated proteins. Preliminary results using longer term YnMyr pulses shows senescent cells with lower levels of myristoylated proteins (Figure 6.1g), not higher, indicating a potentially enhanced turnover of these proteins. We also did not observe consistent significant changes in expression of N-myristoyltransferases (NMT1 & 2) or upstream METAP2 across senescence modalities that could explain these results (Figure 5.6a-c and Figure 6.1h).

It should also be noted that whilst inhibition of *N*-myristoylation does phenocopy, COPI inhibition by dispersing Golgi, blocking secretion and triggering UPR, it also can affect numerous processes. Demonstrating this, multiple proteins had depletion of Myristoylation upon treatment with NMTi (Figure 5.16c). This could result in potential suppression of

proteins levels as was observed with ARF GTPases but proteins could also be aberrantly mis-localized throughout the cell potentially resulting in induction of cell death processes. NMTi levying effects on multiple pathways could explain why NMTi had a higher senolytic index than drugs such as Brefeldin A and Golgicide A. Moving forward it would not only be important to elucidate the potential senolytic effect of other myristoylated proteins but also to examine differences in the myristoylome of senescent versus non-senescent cells. Loading differences in our mass spec prevented direct comparisons with our current proteomic dataset however this could be circumvented by utilizing amino acid isotopes in SILAC-based proteomics.

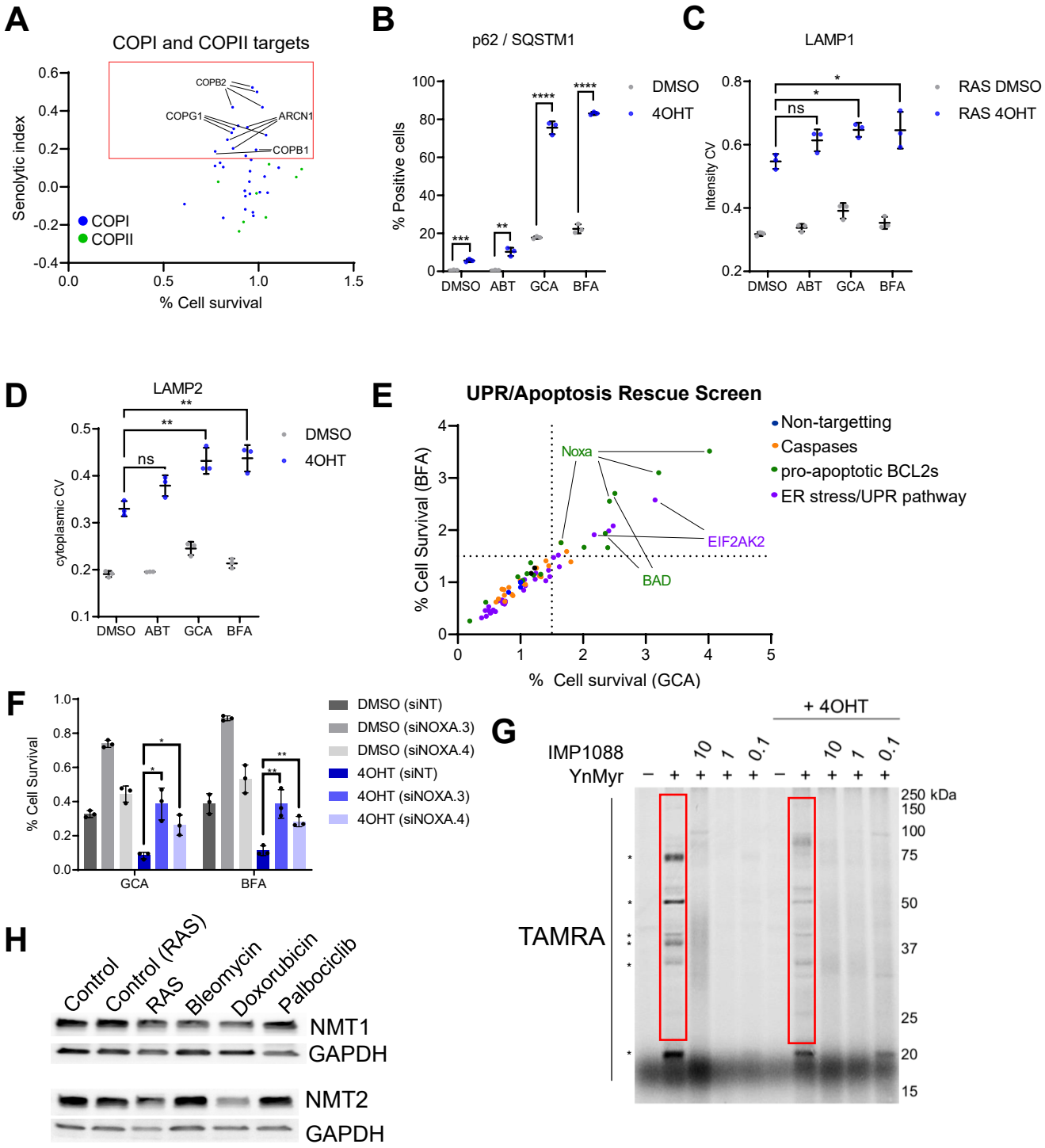

Figure 6.1 Supplemental data on mechanism of COPI liability and differential *N*-myristoylation in senescent cells

(A) Testing of COPI & II components for senolysis using siRNAs. Data represented as percentage cell survival in control cells versus the difference in cell survival between control (DMSO) and senescent (4OHT) IMR90 ER:RAS cells (senolytic index). Each point represents the mean of three replicates. (n=3)

(B-D) Quantification of IF staining for p62/SQSTM1 (B), LAMP1 (C) and LAMP2 (D). IMR90 ER:RAS cells were treated with DMSO (controls) or 4OHT (senescence). 7 days later, cells were treated with ABT-263 (1μM), GCA (2.5μM) or BFA (150nM) for 48h (n=3). Data represented as mean±SD, *p < 0.05, **p < 0.01, ns, not significant. Unpaired, two-tailed, Student's t-test. Scale Bar, 100μm.

(E) Screening for mediators of Golgicide A and Brefeldin A mediated cell death. Data represented as percentage cell survival in BFA treated versus GCA treated senescent (4OHT) IMR90 ER:RAS cells. Each point represents the mean of three replicates (n=3). Cut-off for siRNAs rescuing senolysis was >150% survival relative to scrambled siRNA.

(F) Effect of NOXA siRNAs on senolysis induced by GCA and BFA. Percentage cell survival shown for control (DMSO) or senescent (4OHT) cells transfected on day 7 with siRNAs. Replenishment of media after transfection was with GCA (2.5μM) or BFA (150nM) followed by incubation for 3 days. (n=3). Data represented as mean±SD, *p < 0.05, **p < 0.01, ns, not significant. Unpaired, two-tailed, Student's t-test. Scale Bar, 100μm.

(G) Treatment of control (DMSO) or oncogene-induced senescent (4OHT) IMR90 ER:RAS cells with NMTi for 3 days decreases N-myristoylation. Whole gel fluorescence for red-fluorescent tetramethyl rhodamine (TAMRA) azide and immunoblots represents one experiments. (n=1).

(H) Effect of senescence induction on NMT1/2 expression. Oncogene induced senescent (RAS), therapy induced senescence (Bleomycin / Doxorubicin / Palbociclib) and their respective control IMR90 or IMR90 ER:RAS cells were collected at day 6 after senescence induction. Immunoblot representative of three biological replicates.

Concluding remarks

Recent advances in the use of senescent cell reporters linked to cell death inducing receptors has provided robust evidence that the presence of senescent cells in the context of aging and numerous age-related diseases is driving tissue dysfunction. Moreover, these genetic ablation systems support the consensus theory that senescent cells in tumour stroma can enhance growth and metastases of cancer cells. Therapeutically targeting senescent cells has been demonstrated by our group and others to mediate detrimental effects in many age-related diseases and cancer (Reviewed in(He and Sharpless, 2017; McHugh and Gil, 2017)). These studies have led to surging interest in the field of senolytic therapies, with the first in-human trials being carried out recently suggesting they can elicit clinical benefit (Ellison-Hughes, 2020; Hickson et al., 2019; Justice et al., 2019). To date there are only a handful of known mechanisms mediating senescent cell survival. If the field of senolytics is to grow, it necessitates the creation of a repertoire of targetable pathways that specifically eliminate senescent cells with well understood mechanisms. Historically, building of such repertoires in cancer has utilized unbiased screening approaches and similarly loss-of-function screens have been used to uncover regulators of senescence and the SASP. Here, we have built on knowledge of how to combine these screening approaches with models of senescent cells to reveal novel senolytic targets by using siRNA and CRISPR screening. Work currently being performed in the lab suggests that a host of the targets not further investigated in this project are also robust broad specificity senolytics and pending experiments are aiming to understand their mechanisms.

From both screenings we uncovered a mechanism through which highly secretory senescent cells were dependent on an early secretory pathway for survival. Disruption of this pathway by way inhibition of COPI vesicle trafficking resulted in intracellular accumulation of SASP components and triggering of unfolded protein response. This liability of senescent cells was

also amenable to pharmacological inhibition, through targeting the enzymes that regulate COPI vesicle formation. We found that one of these pharmacological interventions – inhibition of N-myristoylation – was translatable to *in vivo* models of aging and pre-neoplastic lesions. Through the validation of targeting N-myristoylation we subsequently found that senescent cells have altered levels of myristoylation.

Experiments currently ongoing in our own lab and of those of our collaborators aim to understand if targeting COPI vesicle trafficking via *N*-myristoylation *in vivo* can ameliorate age-related decay and also to what extent does altered myristoylation facilitate this.

Table A1. Chemical compounds

Drug	Supplier	Reference
ABT-263	Selleckchem	S1001
Etoposide	Sigma-Aldrich	E1383
Palbociclib HCL	Selleckchem	S1116
Q-VD-OPh hydrate	Sigma-Aldrich	SML0063
4-hydroxytamoxifen (4OHT)	Sigma-Aldrich	H7904
Doxycycline hyclate	Sigma-Aldrich	D9891
Doxorubicin hydrochloride	Cayman chemical	15007
Triamcinolone	Selleckchem	S1933
Beclomethasone dipropionate	Selleckchem	S3078
Kira6	Selleckchem	S8658
GSK2606414	Tocris	5107
GSK2656157	Selleckchem	S7033
Golgicide A	Selleckchem	S7266
Brefeldin A	Selleckchem	S7046
IMP1088	Myricx	n/a
DDD86481	Myricx	n/a
IMP1320	Myricx	n/a
Bleomycin Sulfate	Generon	A10152
Z-VAD-FMK	R&D systems	FMK013
YnMyr	Myricx	

Table A2. Antibiotic selection markers

Antibiotic	Selection Conc.	Maintenance conc.	Selection duration
Puromycin	1µg/ml	0.5µg/ml	3 days
Blasticidin	3µg/ml	1.5µg/ml	7 days
Geneticin (G-418) /Neomycin	400µg/ml	200µg/ml	7 days
Hygromycin B	25µg/ml	12.5µg/ml	7 days

Table A3. Antibodies

Target	Company	Reference	Use	Conjugation	Dilution
BrdU	BD Biosciences	555627	IF	n/a	1/2000
$p16^{INK4a}$	CRUK	Clone JC8	IF	n/a	1/1000
α-Tubulin	MilliporeSigma	Clone DM1A	WB	n/a	1/1000
BCL2L1	CST	Clone 54H6	IF	n/a	1/200
ARL1	Proteintech	16012-1-AP	WB	n/a	1/500
GAPDH	Abcam	ab22555	WB	n/a	1/2000
IL-8	R&D systems	MAB208	IF	n/a	1/100
IL-6	R&D systems	AF-206-NA	IF	n/a	1/40, 1/200
COPA	HPA	HPA028024	WB	n/a	1/250
pan-COP	From F. Weiland	Clone 833	WB/IF	n/a	1/5000 (WB) 1/500 (IF)
FLAG	MilliporeSigma	Clone M2	WB/IF	n/a	1/1000 (WB/IF)
pan-ARF	Invitrogen	Clone 1D9	WB	n/a	1/500
COPB2	From F. Weiland	Clone 899	WB	n/a	1/10000
EEA1	BD Biosciences	Clone 14	IF	n/a	1/200
NMT1	HPA	HPA022963	WB	n/a	1/250
NMT2	HPA	HPA001303	WB	n/a	
XBP1	Abcam	ab37152	IF	n/a	1/200
ATF6	Abcam	ab37149	IF	n/a	1/500
TGN46	BioRad	AHP500G	IF	n/a	1/400
GM130	BD Biosciences	Clone 35	IF	n/a	1/500
CHOP	CST	L63F7	IF	n/a	1/1000
p21Cip1	CST	Clone 12D1	IF	n/a	1/2000
p21Cip1	Abcam	EPR18021	IHC	n/a	1/700
N-Ras	Santa Cruz	sc-31	IHC	n/a	1/100
β-catenin	Sigma	C7082	IF	n/a	1/500
β-catenin	Thermo	RB-9035-P1	IF	n/a	1/500
Synaptophysin	Leica	SYNAP-299-L	IF	n/a	1/200
Cl. Caspase 3	CST	9661	IF	n/a	1/1000
Mouse IgG	Santa Cruz	sc-2005	WB	HRP	1/2000
Rabbit IgG	Santa Cruz	sc-2004	WB	HRP	1/5000
Mouse IgG	Thermo Fisher	A11029	IF	AlexaFluor488	1/2000
Mouse IgG	Thermo Fisher	A11032	IF	AlexaFluor594	1/2000
Rabbit IgG	Thermo Fisher	A11037	IF	AlexaFluor594	1/2000
Sheep IgG	Thermo Fisher	A11016	IF	AlexaFluor594	1/2000
Sheep IgG	Thermo Fisher	A11015	IF	AlexaFluor488	1/2000

Table A4. qRT-PCR primer sequences

Target	Species	Forward primer	Reverse primer
COPG1	Human	CACCTTGAGAAGAGTGCGGTA	GGCACATTTCCGAGGGTTG
COPB2	Human	CTTCCTGTTCGAGCTGCAAAG	CACTCTAATCTGCATGTCATCCG
RPS14	Human	CTGCGAGTGCTGTCAGAGG	TCACCGCCCTACACATCAAACT
Cdkn1a	Mouse	TCCCGACTCTTGACATTGCT	TGCAGAAGGGGAAGTATGGG
Gapdh	Mouse	AACTTTGGCATTGTGGAAGG	ACACATTGGGGGTAGGAACA
Actin b	Mouse	ATGGAGGGGAATACAGCCC	TTCTTTGCAGCTCCTTCGTT
GAPDH	Human	TTCACCACCATGGAGAAGGC	CCCTTTTGGCTCCACCCT
CDKN2A	Human	GATCCAGGTGGGTAGAAGGTC	CCCCTGCAAACTTCGTCCT
Cdkn1a	Mouse	GTGGGTCTGACTCCAGCCC	CCTTCTCGTGAGACGCTTAC
Col3a1	Mouse	ACAGCAAATTCACTTACAC	CTCATTGCCTTGCGTGTTT

Table A5. siRNA sequences

Gene symbol	siRNA	siRNA Target Sequence
ARF1	1	GACCACCAUUCCCACCAUA
ARF1	3	CGGCCGAGAUCACAGACAA
COPB2	1	CAACAGCAUUGUAAAGAUA
COPB2	2	GGACACACCCAUUAUGUUA
COPB2	3	GGUCAAACAAUGUCGCUUU
COPB2	4	GGUUGUGACAGGAGCGGAU
COPG1	1	GAGGGUGGCUUUGAGUAUA
COPG1	4	GGAGGCCCGUGUAUUUAAU
TREM2	1	GGACACAUCCACCCAGUGA
TREM2	4	GGGCUGAGAGACACGUGAA
GNG8	1	CCAACAACAUGGCCAAGAU
GNG8	2	GAAGGUGUCGCAGGCAGCA
UBB	2	GUAUGCAGAUCUUCGUGAA
UBB	4	CCCAGUGACACCAUCGAAA
UBC	3	GAAGAUGGACGCACCCUGU
UBC	4	GUAAGACCAUCACUCUCGA
ALDOA	1	GGACAAAUGGCGAGACUAC
ALDOA	3	GGCGUUGUGUGCUGAAGAU
APOC2	1	AGGAAUCUCUCUCCAGUUA
APOC2	2	CAGCAGCCAUGAGCACUUA
NOXA	3	CUGGAAGUCGAGUGUGCUA
NOXA	4	GCAAGAACGCUCAACCGAG
BCL2L1	1	CCUACAAGCUUUCCCAGAA
BCL2L1	2	GGAGGCAGGCGACGAGUUU
BCL2L1	3	GAUUCAGGCUGCUUGGGAU
BCL2L1	4	GAAAGGGCCAGGAACGCUU
Scrambled	3	AUGUAUUGGCCUGUAUUAG

Table A6. TIDE PCR primers

sgRNA target	Forward primer (5'-3')	Reverse primer (5'-3')
BCL2g1	CCGGCCAACAACATGGAAAG	CTCAATCGAGGAGTGTGACGG
BCL2g2/3	AACGCTTTGTCCAGAGGAGG	ACAGGGTACGATAACCGGGA
BCL2L1g1/2/3	GGCCAGTCAGGTTTCCTCAA	CTGGTACCTGGAGGGGGAAT
BCL2L2g1/2	GGGTGTTGTAGGGGTGTCAT	CCCGTACCTCATTCCCAACAT
BCL2L2g3	CTGAGGCAGCTATGTTGGGA	GGGCTGTGAAGCAAGTTCCA

Table A7. TIDE Sequencing primer

sgRNA target	Sequencing primer (5'-3')
BCL2g1	GCTTTGTTTCATGGTACATC
BCL2g2/3	ATCCTGGATCCAGGTGTGCA
BCL2L1g1/2/3	AGATACAGAAGAAGGGCTGT
BCL2L2g1/2	TCATCCTTGCCTCTTATAGC
BCL2L2g3	CAGTCTCTCAGGGTGGGGGT

Table A8. Cloning primers

Primer ID	Sequence (5'-3')
miRE-Xho-Fw	TGAACTCGAGAAGGTATATTGCTGTTGACAGTGAGCG
miRE-EcoOligo-rev	TCTCGAATTCTAGCCCCTTGAAGTCCGAGGCAGTAGGC
5'-BmgBI-sogLUX	GATTAAGACGTGGTTTTCCTTTGAAAAACACGATGATAAT ATGGGAGTGAAGGTGCTGTT
3'sogLUX-Age1	TTTGTTACCGGTCTCATCAATCTCCCCCAGCT
Human5SnaBIGBF1	CGTACGTAGCCATGGTGGATAAGAATATTT
Human3SalIGBF1	CGGTCGACGCCTTAGTTGACCTCAGAGGTG

Table A9. shRNA sequences

Target	ID	shRNA target sequence
COPB2	1	TTAAATATCTTTACAATGCTGT
	2	TAATTGAACACTCTAATCTGCA
	5	TCAATCATCCAAAATATCTTCA
COPA	1	TTCACTTTAGAAATCTTCACAG
	2	TTGAATTTGAACTCAGTGGGAT
	3	TTATATTTTTATTAGAGACGGG
	4	TTGAAATTTAAATGTCTAAGGA
COPG1	1	TTTTCAATACAGAAGCTTGGGA
	4	TTCATTGTCATCATCCATCACA
	5	TTTTGAATGTGATCAGCTACAG
BCL2L1	1	TAGTATATCATCTTCACAAGGA

Table A10. sgRNA sequences

sgRNA ID	Gene target	Sequence (5'-3')	PAM Sequence
BCL2g1	BCL2	CACCGGGGGCCGTACAGTTCCACAA	AGG
BCL2g2	BCL2	CACCGTGGACATCTCGGCGAAGTCG	CGG
BCL2g3	BCL2	CACCGTGAAGGGCGTCAGGTGCAGC	TGG
BCL2L1g1	BCL2L1	CACCGAGTTTGAACTGCGGTACCGG	CGG
BCL2L1g2	BCL2L1	CACCGGTTTGAACTGCGGTACCGGC	GGG
BCL2L1g3	BCL2L1	CACCGGTGGCCTTTTTCTCCTTCGG	CGG
BCL2L2g1	BCL2L2	CACCGGCGCACCTTCTCTGATCTGG	CGG
BCL2L2g2	BCL2L2	CACCGAGCCCAACAACGCTTCACCC	AGG
BCL2L2g3	BCL2L2	CACCGCGGAGTTCACAGCTCTATAC	GGG
NTg1	N/A	CACCGACGGAGGCTAAGCGTCGCAA	N/A

Table A11. GECKOv2 library primers

Primer ID	Sequence (5'-3')	Barcode
NGS-Lib-Fwd-1	AATGATACGGCGACCACCGAGATCTACACTCTTTCCCTACACGACGCTCTTCCGATCTTAAGTAGAGGCTTTATATATCTTGTGGAAAGGACGAAACACC	N/A
NGS-Lib-Fwd-2	AATGATACGGCGACCACCGAGATCTACACTCTTTCCCTACACGACGCTCTTCCGATCTATCATGCTTAGCTTTATATATCTTGTGGAAAGGACGAAACACC	N/A
NGS-Lib-Fwd-3	AATGATACGGCGACCACCGAGATCTACACTCTTTCCCTACACGACGCTCTTCCGATCTGATGCACATCTGCTTTATATATCTTGTGGAAAGGACGAAACACC	N/A
NGS-Lib-Fwd-4	AATGATACGGCGACCACCGAGATCTACACTCTTTCCCTACACGACGCTCTTCCGATCTCGATTGCTCGACGCTTTATATATCTTGTGGAAAGGACGAAACACC	N/A
NGS-Lib-Fwd-5	AATGATACGGCGACCACCGAGATCTACACTCTTTCCCTACACGACGCTCTTCCGATCTTCGATAGCAATTCGCTTTATATATCTTGTGGAAAGGACGAAACACC	N/A
NGS-Lib-Fwd-6	AATGATACGGCGACCACCGAGATCTACACTCTTTCCCTACACGACGCTCTTCCGATCTATCGATAGTTGCTTGCTTTATATATCTTGTGGAAAGGACGAAACACC	N/A
NGS-Lib-Fwd-7	AATGATACGGCGACCACCGAGATCTACACTCTTTCCCTACACGACGCTCTTCCGATCTGATCGATCCAGTTAGGCTTTATATATCTTGTGGAAAGGACGAAACACC	N/A
NGS-Lib-Fwd-8	AATGATACGGCGACCACCGAGATCTACACTCTTTCCCTACACGACGCTCTTCCGATCTCGATCGATTTGAGCCTGCTTTATATATCTTGTGGAAAGGACGAAACACC	N/A
NGS-Lib-Fwd-9	AATGATACGGCGACCACCGAGATCTACACTCTTTCCCTACACGACGCTCTTCCGATCTACGATCGATACACGATCGCTTTATATATCTTGTGGAAAGGACGAAACACC	N/A
NGS-Lib-Fwd-10	AATGATACGGCGACCACCGAGATCTACACTCTTTCCCTACACGACGCTCTTCCGATCTTACGATCGATGGTCCAGAGCTTTATATATCTTGTGGAAAGGACGAAACACC	N/A
NGS-Lib-KO-Rev-1	CAAGCAGAAGACGGCATACGAGATTCGCCTTGGTGACTGGAGTTCAGACGTGTGCTCTTCCGATCTCCGACTCGGTGCCACTTTTTCAA	TCGCCTTG
NGS-Lib-KO-Rev-2	CAAGCAGAAGACGGCATACGAGATATAGCGTCGTGACTGGAGTTCAGACGTGTGCTCTTCCGATCTCCGACTCGGTGCCACTTTTTCAA	ATAGCGTC
NGS-Lib-KO-Rev-3	CAAGCAGAAGACGGCATACGAGATGAAGAAGTGTGACTGGAGTTCAGACGTGTGCTCTTCCGATCTCCGACTCGGTGCCACTTTTTCAA	GAAGAAGT
NGS-Lib-KO-Rev-4	CAAGCAGAAGACGGCATACGAGATATTCTAGGGTGACTGGAGTTCAGACGTGTGCTCTTCCGATCTCCGACTCGGTGCCACTTTTTCAA	ATTCTAGG
NGS-Lib-KO-Rev-5	CAAGCAGAAGACGGCATACGAGATCGTTACCAGTGACTGGAGTTCAGACGTGTGCTCTTCCGATCTCCGACTCGGTGCCACTTTTTCAA	CGTTACCA
NGS-Lib-KO-Rev-6	CAAGCAGAAGACGGCATACGAGATGTCTGATGGTGACTGGAGTTCAGACGTGTGCTCTTCCGATCTCCGACTCGGTGCCACTTTTTCAA	GTCTGATG
NGS-Lib-KO-Rev-7	CAAGCAGAAGACGGCATACGAGATTTACGCACGTGACTGGAGTTCAGACGTGTGCTCTTCCGATCTCCGACTCGGTGCCACTTTTTCAA	TTACGCAC
NGS-Lib-KO-Rev-8	CAAGCAGAAGACGGCATACGAGATTTGAATAGGTGACTGGAGTTCAGACGTGTGCTCTTCCGATCTCCGACTCGGTGCCACTTTTTCAA	TTGAATAG
NGS-Lib-KO-Rev-9	CAAGCAGAAGACGGCATACGAGATCCGAATCAGTGACTGGAGTTCAGACGTGTGCTCTTCCGATCTCCGACTCGGTGCCACTTTTTCAA	CCGAATCA
NGS-Lib-KO-Rev-10	CAAGCAGAAGACGGCATACGAGATATAGCCTAGTGACTGGAGTTCAGACGTGTGCTCTTCCGATCTCCGACTCGGTGCCACTTTTTCAA	ATAGCCTA
NGS-Lib-KO-Rev-11	CAAGCAGAAGACGGCATACGAGATGGCCATGAGTGACTGGAGTTCAGACGTGTGCTCTTCCGATCTCCGACTCGGTGCCACTTTTTCAA	GGCCATGA
NGS-Lib-KO-Rev-12	CAAGCAGAAGACGGCATACGAGATGGATTACAGTGACTGGAGTTCAGACGTGTGCTCTTCCGATCTCCGACTCGGTGCCACTTTTTCAA	GGATTACA
Read 1 Primer	ACACTCTTTCCCTACACGACGCTCTTCCGATCT	n/a
Read 2 Primer	GATCGGAAGAGCACACGTCTGAACTCCAGTCA	n/a

Table A12. Custom shRNA Library primers

Primer ID	Sequence (5'-3')	Barcode
P5 (Rev4long 5/18)	AATGATACGGCGACCACCGAGATCTACACTggatgtggaatgtgtgcgagg	N/A
P7 mE pC 1	CAAGCAGAAGACGGCATACGAGATaaaTAGTGAAGCCACAGATGT	aaa
P7 mE pC 2	CAAGCAGAAGACGGCATACGAGATaacTAGTGAAGCCACAGATGT	aac
P7 mE pC 3	CAAGCAGAAGACGGCATACGAGATaagTAGTGAAGCCACAGATGT	aag
P7 mE pC 4	CAAGCAGAAGACGGCATACGAGATaatTAGTGAAGCCACAGATGT	aat
P7 mE pC 5	CAAGCAGAAGACGGCATACGAGATacaTAGTGAAGCCACAGATGT	aca
P7 mE pC 6	CAAGCAGAAGACGGCATACGAGATaccTAGTGAAGCCACAGATGT	acc
P7 mE pC 7	CAAGCAGAAGACGGCATACGAGATacgTAGTGAAGCCACAGATGT	acg
P7 mE pC 8	CAAGCAGAAGACGGCATACGAGATactTAGTGAAGCCACAGATGT	act
P7 mE pC 9	CAAGCAGAAGACGGCATACGAGATagaTAGTGAAGCCACAGATGT	aga
P7 mE pC 10	CAAGCAGAAGACGGCATACGAGATagcTAGTGAAGCCACAGATGT	agc
P7 mE pC 11	CAAGCAGAAGACGGCATACGAGATaggTAGTGAAGCCACAGATGT	agg
P7 mE pC 12	CAAGCAGAAGACGGCATACGAGATagtTAGTGAAGCCACAGATGT	agt
P7 mE pC 13	CAAGCAGAAGACGGCATACGAGATataTAGTGAAGCCACAGATGT	ata
P7 mE pC 14	CAAGCAGAAGACGGCATACGAGATatcTAGTGAAGCCACAGATGT	atc
P7 mE pC 15	CAAGCAGAAGACGGCATACGAGATatgTAGTGAAGCCACAGATGT	atg
P7 mE pC 16	CAAGCAGAAGACGGCATACGAGATattTAGTGAAGCCACAGATGT	att
P7 mE pC 17	CAAGCAGAAGACGGCATACGAGATcaaTAGTGAAGCCACAGATGT	caa
P7 mE pC 18	CAAGCAGAAGACGGCATACGAGATcacTAGTGAAGCCACAGATGT	cac
P7 mE pC 19	CAAGCAGAAGACGGCATACGAGATcagTAGTGAAGCCACAGATGT	cag
P7 mE pC 20	CAAGCAGAAGACGGCATACGAGATcatTAGTGAAGCCACAGATGT	cat
P7 mE pC 21	CAAGCAGAAGACGGCATACGAGATccaTAGTGAAGCCACAGATGT	cca
P7 mE pC 22	CAAGCAGAAGACGGCATACGAGATcccTAGTGAAGCCACAGATGT	ccc
P7 mE pC 23	CAAGCAGAAGACGGCATACGAGATccgTAGTGAAGCCACAGATGT	ccg
P7 mE pC 24	CAAGCAGAAGACGGCATACGAGATcctTAGTGAAGCCACAGATGT	cct
P7 mE pC 25	CAAGCAGAAGACGGCATACGAGATcgaTAGTGAAGCCACAGATGT	cga
Sequencing Primer	TAGCCCCTTGAAGTCCGAGGCAGTAGGCA	n/a

Table A13. Sanger Sequencing Primers

Primer ID	Sequence (5'-3')	Target
miREseq	TGTTTGAATGAGGCTTCAGTAC	pRRL shRNA
sogLUXseq1	CTCAGGCAGATCAGACAGCCT	Gaussia Luciferase
sogLUXseq2	AGGCTGTCTGATCTGCCTGAG	Gaussia Luciferase
sogLUXseq3	GATCTCAGGGATGTCCACAA	Gaussia Luciferase
5'GBF1seq	ATGGTGGATAAGAATATTTAC	$GBF1^{M832L}$
5'GBF1seq2	GAAGAACCCAAGAACTATGT	$GBF1^{M832L}$
5'GBF1seq3	GCACAGCTTTGGTCCCCTAT	$GBF1^{M832L}$
5'GBF1seq4	CAGCACCGAGGCCCACTGCC	$GBF1^{M832L}$
5'GBF1seq5	GAAGCCCTCCGCCTCTACCT	$GBF1^{M832L}$
5'GBF1seq6	TGTTTGACAATCTCATCATC	$GBF1^{M832L}$
5'GBF1seq7	GAACAGGGATCGTGTGGGCT	$GBF1^{M832L}$
5'GBF1seq8	GCCCAGGCCCTTCACCCCTG	$GBF1^{M832L}$
5'GBF1seq9	ATCTGCAGCGAGCACTACTTG	$GBF1^{M832L}$
5'GBF1seq10	GCTGGAGCCTGCGTGCATGTA	$GBF1^{M832L}$
3'GBF1seq	TTAGTTGACCTCAGAGGTGGG	$GBF1^{M832L}$
3'GBF1seq2	GCTGGAGCCTGCGTGCATGTA	$GBF1^{M832L}$
3'GBF1seq3	ATCCCTCTTTGGATTTCTTCT	$GBF1^{M832L}$
3'GBF1seq4	TGTTGGCTGCATTGGTCTTCA	$GBF1^{M832L}$
3'GBF1seq5	TGGGATCCACGAAATCTTCTA	$GBF1^{M832L}$
3'GBF1seq6	TTTTGCGAAACTCCTCCAGGG	$GBF1^{M832L}$
3'GBF1seq7	CATGTTCTGGTGGCAGCCGCC	$GBF1^{M832L}$
3'GBF1seq8	TCTCATCCTTGATGAGGCCCA	$GBF1^{M832L}$
3'GBF1seq9	ATAAGGTGGTTCCATTGGGAG	$GBF1^{M832L}$
3'GBF1seq10	CTGAGAGTTCTGTTATACTGTT	$GBF1^{M832L}$
LKO1.5	GACTATCATATGCTTACCGT	U6 Promoter

Table A14. COPI vesicle formation regulators

Gene	Function
COPB1	COPI Coat
COPB2	COPI Coat
COPG1	COPI Coat
COPG2	COPI Coat
COPZ1	COPI Coat
COPZ2	COPI Coat
COPA	COPI Coat
COPE	COPI Coat
ARCN1	COPI Coat
ARF1	GTPase
ARF2	GTPase
ARF3	GTPase
ARF4/5	GTPase
ARF6	GTPase
GBF1	GTPase effector enzyme
KDELR1	cargo receptor
KDELR2	cargo receptor
KDELR3	cargo receptor
ARFGAP1	GTPase activating protein
ARFGAP2	GTPase activating protein
ARFGAP3	GTPase activating protein
METAP2	Methionine aminopeptidase
NMT1	N-myristoyltransferase
NMT2	N-myristoyltransferase

References

Abbadie, C., and Pluquet, O. (2020). Unfolded Protein Response (UPR) Controls Major Senescence Hallmarks. Trends Biochem. Sci. *45*, 371–374.

Acosta, J.C., O'Loghlen, A., Banito, A., Guijarro, M. V., Augert, A., Raguz, S., Fumagalli, M., Da Costa, M., Brown, C., Popov, N., et al. (2008). Chemokine Signaling via the CXCR2 Receptor Reinforces Senescence. Cell *133*, 1006–1018.

Acosta, J.C., Banito, A., Wuestefeld, T., Georgilis, A., Janich, P., Morton, J.P., Athineos, D., Kang, T.-W., Lasitschka, F., Andrulis, M., et al. (2013). A complex secretory program orchestrated by the inflammasome controls paracrine senescence. Nat. Cell Biol. *15*, 978–990.

Adams, C.J., Kopp, M.C., Larburu, N., Nowak, P.R., and Ali, M.M.U. (2019). Structure and molecular mechanism of ER stress signaling by the unfolded protein response signal activator IRE1. Front. Mol. Biosci. *6*, 1–12.

Agrotis, A., and Ketteler, R. (2015). A new age in functional genomics using CRISPR/Cas9 in arrayed library screening. Front. Genet. *6*, 1–15.

Aguayo-Mazzucato, C., Andle, J., Lee, T.B., Midha, A., Talemal, L., Chipashvili, V., Hollister-Lock, J., van Deursen, J., Weir, G., and Bonner-Weir, S. (2019). Acceleration of β Cell Aging Determines Diabetes and Senolysis Improves Disease Outcomes. Cell Metab. *30*, 129-142.e4.

Ahmad, T., Sundar, I.K., Lerner, C.A., Gerloff, J., Tormos, A.M., Yao, H., and Rahman, I. (2015). Impaired mitophagy leads to cigarette smoke stress-induced cellular senescence: Implications for chronic obstructive pulmonary disease. FASEB J. *29*, 2912–2929.

Aird, K.M., Zhang, G., Li, H., Tu, Z., Bitler, B.G., Garipov, A., Wu, H., Wei, Z., Wagner, S.N., Herlyn, M., et al. (2013). Suppression of Nucleotide Metabolism Underlies the Establishment and Maintenance of Oncogene-Induced Senescence. Cell Rep. *3*, 1252–1265.

Aird, K.M., Worth, A.J., Snyder, N.W., Lee, J. V., Sivanand, S., Liu, Q., Blair, I.A., Wellen, K.E., and Zhang, R. (2015). ATM Couples Replication Stress and Metabolic Reprogramming during Cellular Senescence. Cell Rep. *11*, 893–901.

Aird, K.M., Iwasaki, O., Kossenkov, A. V., Tanizawa, H., Fatkhutdinov, N., Bitler, B.G., Le, L., Alicea, G., Yang, T.L., Johnson, F.B., et al. (2016). HMGB2 orchestrates the chromatin landscape of senescence-associated secretory phenotype gene loci. J. Cell Biol. *215*, 325–334.

Allsopp, R.C., and Harley, C.B. (1995). Evidence for a critical telomere length in senescent human fibroblasts. Exp. Cell Res. *219*, 130–136.

Amor, C., Feucht, J., Leibold, J., Ho, Y.J., Zhu, C., Alonso-Curbelo, D., Mansilla-Soto, J., Boyer, J.A., Li, X., Giavridis, T., et al. (2020). Senolytic CAR T cells reverse senescence-associated pathologies. Nature *583*, 127–132.

Anderlini, P., Przepiorka, D., Lauppe, J., Seong, D., Giralt, S., Champlin, R., and Korbling, M. (1997). Collection of peripheral blood stem cells from normal donors 60 years of age or older. Br J Haematol *97*, 485–487.

Anderson, R., Lagnado, A., Maggiorani, D., Walaszczyk, A., Dookun, E., Chapman, J., Birch, J., Salmonowicz, H., Ogrodnik, M., Jurk, D., et al. (2019). Length-independent telomere damage drives post-mitotic cardiomyocyte senescence. EMBO J. *38*, 1–21.

Ansieau, S., Bastid, J., Doreau, A., Morel, A.P., Bouchet, B.P., Thomas, C., Fauvet, F., Puisieux, I., Doglioni, C., Piccinin, S., et al. (2008). Induction of EMT by Twist Proteins as a Collateral Effect of Tumor-Promoting Inactivation of Premature Senescence. Cancer Cell *14*, 79–89.

Appenzeller-Herzog, C., and Hauri, H.P. (2006). The ER-Golgi intermediate compartment (ERGIC): In search of its identity and function. J. Cell Sci. *119*, 2173–2183.

Aridor, M., Bannykh, S.I., Rowe, T., and Balch, W.E. (1995). Sequential coupling between copII and copI vesicle coats in endoplasmic reticulum to Golgi transport. J. Cell Biol. *131*, 875–893.

Asghar, U., Witkiewicz, A.K., Turner, N.C., and Knudsen, E.S. (2015). The history and future of targeting cyclin-dependent kinases in cancer therapy. Nat. Rev. Drug Discov. *14*, 130–146.

Atagi, Y., Liu, C.C., Painter, M.M., Chen, X.F., Verbeeck, C., Zheng, H., Li, X., Rademakers, R., Kang, S.S., Xu, H., et al. (2015). Apolipoprotein E is a ligand for triggering receptor expressed on myeloid cells 2 (TREM2). J. Biol. Chem. *290*, 26043–26050.

Baar, M.P., Brandt, R.M.C., Putavet, D.A., Klein, J.D.D., Derks, K.W.J., Bourgeois, B.R.M., Stryeck, S., Rijksen, Y., van Willigenburg, H., Feijtel, D.A., et al. (2017). Targeted Apoptosis of Senescent Cells Restores Tissue Homeostasis in Response to Chemotoxicity and Aging. Cell *169*, 132-147.e16.

Baker, D.J., Wijshake, T., Tchkonia, T., LeBrasseur, N.K., Childs, B.G., van de Sluis, B., Kirkland, J.L., and van Deursen, J.M. (2011). Clearance of p16Ink4a-positive senescent cells delays ageing-associated disorders. Nature *479*, 232–236.

Baker, D.J., Childs, B.G., Durik, M., Wijers, M.E., Sieben, C.J., Zhong, J., Saltness, R.A., Jeganathan, K.B., Casaclang Verzosa, G., Pezeshki, A., et al. (2016). Naturally occurring p16 Ink4a -positive cells shorten healthy lifespan. Nature *530*, 1–5.

Balestro, E., Calabrese, F., Turato, G., Lunardi, F., Bazzan, E., Marulli, G., Biondini, D., Rossi, E., Sanduzzi, A., Rea, F., et al. (2016). Immune inflammation and disease progression in idiopathic pulmonary fibrosis. PLoS One *11*, 1–11.

Banin, S., Moyal, L., Shieh, S., Taya, Y., Anderson, C.W., Chessa, L., Smorodinsky, N.I., Prives, C., Reiss, Y., Shiloh, Y., et al. (1998). Enhanced phosphorylation of p53 by ATM in response to DNA damage. Science *281*, 1674–1677.

Barlowe, C., and Helenius, A. (2016). Cargo Capture and Bulk Flow in the Early Secretory Pathway. Annu. Rev. Cell Dev. Biol. *32*, 197–222.

Barradas, M., Anderton, E., Acosta, J.C., Li, S., Banito, A., Maertens, G., Rodriguez-niedenfu, M., Banck, M., Zhou, M., Walsh, M.J., et al. (2009). Histone demethylase JMJD3 contributes to epigenetic control of INK4a / ARF by oncogenic RAS. Genes Dev. 1177–1182.

Bartkova, J., Rezaei, N., Liontos, M., Karakaidos, P., Kletsas, D., Issaeva, N., Vassiliou, L.-V.F., Kolettas, E., Niforou, K., Zoumpourlis, V.C., et al. (2006). Oncogene-induced senescence is part of the tumorigenesis barrier imposed by DNA damage checkpoints.

Nature *444*, 633–637.

Beauchamp, E., Yap, M.C., Iyer, A., Perinpanayagam, M.A., Gamma, J.M., Vincent, K.M., Lakshmanan, M., Raju, A., Tergaonkar, V., Tan, S.Y., et al. (2020). Targeting N-myristoylation for therapy of B-cell lymphomas. Nat. Commun. *11*, 1–16.

Beck, R., Ravet, M., Wieland, F.T., and Cassel, D. (2009). The COPI system: Molecular mechanisms and function. FEBS Lett. *583*, 2701–2709.

Bergsbaken, T., Fink, S.L., and Cookson, B.T. (2009). Pyroptosis: Host cell death and inflammation. Nat. Rev. Microbiol. *7*, 99–109.

Berry, D.C., Jiang, Y., Arpke, R.W., Close, E.L., Uchida, A., Reading, D., Berglund, E.D., Kyba, M., and Graff, J.M. (2016). Cellular Aging Contributes to Failure of Cold-Induced Beige Adipocyte Formation in Old Mice and Humans. Cell Metab. *25*, 1–16.

Béthune, J., and Wieland, F.T. (2018). Assembly of COPI and COPII Vesicular Coat Proteins on Membranes. Annu. Rev. Biophys. *47*, 63–83.

Béthune, J., Wieland, F., and Moelleken, J. (2006a). COPI-mediated transport. J. Membr. Biol. *211*, 65–79.

Béthune, J., Kol, M., Hoffmann, J., Reckmann, I., Brügger, B., and Wieland, F. (2006b). Coatomer, the Coat Protein of COPI Transport Vesicles, Discriminates Endoplasmic Reticulum Residents from p24 Proteins. Mol. Cell. Biol. *26*, 8011–8021.

Bhat, R., Crowe, E.P., Bitto, A., Moh, M., Katsetos, C.D., Garcia, F.U., Johnson, F.B., Trojanowski, J.Q., Sell, C., and Torres, C. (2012). Astrocyte Senescence as a Component of Alzheimer's Disease. PLoS One *7*, 1–10.

Billiau, A., Heremans, H., Vandekerckhove, F., Dijkmans, R., Sobis, H., Meulepas, E., and Carton, H. (1988). Enhancement of experimental allergic encephalomyelitis in mice by antibodies against IFN-gamma. J. Immunol. *140*, 1506 LP – 1510.

Blackledge, N.P., Rose, N.R., and Klose, R.J. (2015). Targeting Polycomb systems to regulate gene expression: modifications to a complex story. Nat Rev Mol Cell Biol *16*, 643–649.

Blasco, M., Lee, H.W., Hande, M.P., Samper, E., Lansdorp, P.M., DePinho, R. a, and Greider, C.W. (1997). Telomere shortening and tumor formation by mouse cells lacking telomerase RNA. Cell *91*, 25–34.

Blasco, M., Lee, H.W., Gottlieb, G.J., Horner, J.W., Greider, C.W., and DePinho, R.A. (1998). Essential role of mouse telomerase in highly proliferative organs. Nature *392*, 569–574.

Bonfanti, L., Mironov, A.A., Martínez-Menárguez, J.A., Martella, O., Fusella, A., Baldassarre, M., Buccione, R., Geuze, H.J., Mironov, A.A., and Luini, A. (1998). Procollagen traverses the Golgi stack without leaving the lumen of cisternae: Evidence for cisternal maturation. Cell *95*, 993–1003.

Boon, R. a, Iekushi, K., Lechner, S., Seeger, T., Fischer, A., Heydt, S., Kaluza, D., Tréguer, K., Carmona, G., Bonauer, A., et al. (2013). MicroRNA-34a regulates cardiac ageing and function. Nature *495*, 107–110.

Borghesan, M., Fafián-Labora, J., Eleftheriadou, O., Carpintero-Fernández, P., Paez-Ribes,

M., Vizcay-Barrena, G., Swisa, A., Kolodkin-Gal, D., Ximénez-Embún, P., Lowe, R., et al. (2019). Small Extracellular Vesicles Are Key Regulators of Non-cell Autonomous Intercellular Communication in Senescence via the Interferon Protein IFITM3. Cell Rep. *27*, 3956-3971.e6.

Bos, J.L. (1989). Ras Oncogenes in Human Cancer: A Review. Cancer Res. *49*, 4682–4689.

Boutros, M., Brás, L.P., and Huber, W. (2006). Analysis of cell-based RNAi screens. Genome Biol. *7*, R66.

Bracken, A.P., Kleine-Kohlbrecher, D., Dietrich, N., Pasini, D., Gargiulo, G., Beekman, C., Theilgaard-Mönch, K., Minucci, S., Porse, B.T., Marine, J.-C., et al. (2007). The Polycomb group proteins bind throughout the INK4A-ARF locus and are disassociated in senescent cells. Genes Dev. *21*, 525–530.

Bräuer, P., Parker, J.L., Gerondopoulos, A., Zimmermann, I., Seeger, M.A., Barr, F.A., and Newstead, S. (2019). Structural basis for pH-dependent retrieval of ER proteins from the Golgi by the KDEL receptor. Science (80-.). *363*, 1103–1107.

Breunig, M., Lungwitz, U., Liebl, R., and Goepferich, A. (2007). Breaking up the correlation between efficacy and toxicity for nonviral gene delivery. Proc. Natl. Acad. Sci. U. S. A. *104*, 14454–14459.

Brinkman, E.K., Chen, T., Amendola, M., and Van Steensel, B. (2014). Easy quantitative assessment of genome editing by sequence trace decomposition. Nucleic Acids Res. *42*, 1–8.

Brinkman, E.K., Chen, T., de Haas, M., Holland, H.A., Akhtar, W., and van Steensel, B. (2018). Kinetics and Fidelity of the Repair of Cas9-Induced Double-Strand DNA Breaks. Mol. Cell *70*, 801-813.e6.

Ten Broek, R.W., Grefte, S., and Von Den Hoff, J.W. (2010). Regulatory factors and cell populations involved in skeletal muscle regeneration. J. Cell. Physiol. *224*, 7–16.

Brown, J.D., Lin, C.Y., Duan, Q., Griffin, G., Federation, A.J., Paranal, R.M., Bair, S., Newton, G., Lichtman, A.H., Kung, A.L., et al. (2014). Nf-kb directs dynamic super enhancer formation in inflammation and atherogenesis. Mol. Cell *56*, 219–231.

Brunt, E.M., Kleiner, D.E., Wilson, L.A., Unalp, A., Behling, C.E., Lavine, J.E., Neuschwander-Tetri, B.A., and Network, N.C.R. (2009). Portal chronic inflammation in nonalcoholic fatty liver disease (NAFLD): A histologic marker of advanced NAFLD—Clinicopathologic correlations from the nonalcoholic steatohepatitis clinical research network. Hepatology *49*, 809–820.

Bruunsgaard, H., Skinhøj, P., Pedersen, A.N., Schroll, M., and Pedersen, B.K. (2000). Ageing, tumour necrosis factor-alpha (TNF-alpha) and atherosclerosis. Clin. Exp. Immunol. *121*, 255–260.

Bulavin, D. V, Phillips, C., Nannenga, B., Timofeev, O., Donehower, L.A., Anderson, C.W., Appella, E., and Fornace, A.J. (2004). Inactivation of the Wip1 phosphatase inhibits mammary tumorigenesis through p38 MAPK–mediated activation of the p16Ink4a-p19Arf pathway. Nat. Genet. *36*, 343–350.

Bunnage, M.E. (2011). Getting pharmaceutical R&D back on target. Nat. Chem. Biol. *7*, 335–339.

Burd, C.E., Sorrentino, J.A., Clark, K.S., Darr, D.B., Krishnamurthy, J., Deal, A.M., Bardeesy, N., Castrillon, D.H., Beach, D.H., and Sharpless, N.E. (2012). Resource Monitoring Tumorigenesis and Senescence In Vivo with a p16 INK4a -Luciferase Model. Cell *152*, 340–351.

Bykov, Y.S., Schaffer, M., Dodonova, S.O., Albert, S., Plitzko, J.M., Baumeister, W., Engel, B.D., and Briggs, J.A. (2017). The structure of the COPI coat determined within the cell. Elife *6*, 1–18.

Campaner, S., Doni, M., Hydbring, P., Verrecchia, A., Bianchi, L., Sardella, D., Schleker, T., Perna, D., Tronnersjö, S., Murga, M., et al. (2009). Cdk2 suppresses cellular senescence induced by the c-myc oncogene. Nat. Cell Biol. *12*, 54–59.

Campisi, J. (1997). Aging and cancer: The double-edged sword of replicative senescence. J. Am. Geriatr. Soc. *45*, 482–488.

Campisi, J. (2005). Senescent cells, tumor suppression, and organismal aging: Good citizens, bad neighbors. Cell *120*, 513–522.

Capell, B.C., Drake, A.M., Zhu, J., Shah, P.P., Dou, Z., Dorsey, J., Simola, D.F., Donahue, G., Sammons, M., Rai, T.S., et al. (2016). MLL1 is essential for the senescence- associated secretory phenotype. Genes Dev. *30*, 321–336.

Cawthon, R., Smith, K., O'Brien, E., Sivatchenko, A., and Kerber, R. (2003). Association between telomere length in blood and mortality in people aged 60 years or older. Lancet *361*, 393–395.

De Cecco, M., Criscione, S.W., Peckham, E.J., Hillenmeyer, S., Hamm, E.A., Manivannan, J., Peterson, A.L., Kreiling, J.A., Neretti, N., and Sedivy, J.M. (2013). Genomes of replicatively senescent cells undergo global epigenetic changes leading to gene silencing and activation of transposable elements. Aging Cell *12*, 247–256.

De Cecco, M., Ito, T., Petrashen, A.P., Elias, A.E., Skvir, N.J., Criscione, S.W., Caligiana, A., Brocculi, G., Adney, E.M., Boeke, J.D., et al. (2019). L1 drives IFN in senescent cells and promotes age-associated inflammation. Nature *566*, 73–78.

Cesare, A.J., and Reddel, R.R. (2010). Alternative lengthening of telomeres: Models, mechanisms and implications. Nat. Rev. Genet. *11*, 319–330.

Chabner, B.A., and Roberts, T.G. (2005). Chemotherapy and the war on cancer. Nat. Rev. Cancer *5*, 65–72.

Chan, H.M., Narita, M., Lowe, S.W., and Livingston, D.M. (2005). The p400 E1A-associated protein is a novel component of the p53 → p21 senescence pathway. Genes Dev. *19*, 196–201.

Chandra, T., and Kirschner, K. (2016). Chromosome organisation during ageing and senescence. Curr. Opin. Cell Biol. *40*, 161–167.

Chandra, T., Kirschner, K., Thuret, J.Y., Pope, B.D., Ryba, T., Newman, S., Ahmed, K., Samarajiwa, S.A., Salama, R., Carroll, T., et al. (2012). Independence of Repressive Histone Marks and Chromatin Compaction during Senescent Heterochromatic Layer Formation. Mol. Cell *47*, 203–214.

Chang, J., Wang, Y., Shao, L., Laberge, R.M., Demaria, M., Campisi, J., Janakiraman, K., Sharpless, N.E., Ding, S., Feng, W., et al. (2016). Clearance of senescent cells by ABT263

rejuvenates aged hematopoietic stem cells in mice. Nat Med *22*, 78–83.

Chapman, J., Fielder, E., and Passos, J.F. (2019). Mitochondrial dysfunction and cell senescence: deciphering a complex relationship. FEBS Lett. *593*, 1566–1579.

Chen, E.Y., Tan, C.M., Kou, Y., Duan, Q., Wang, Z., Meirelles, G.V., Clark, N.R., and Ma'ayan, A. (2013). Enrichr: interactive and collaborative HTML5 gene list enrichment analysis tool. BMC Bioinformatics *14*, 128.

Chen, H., Gu, X., Su, I., Bottino, R., Contreras, J.L., Tarakhovsky, A., and Kim, S.K. (2009). Polycomb protein Ezh2 regulates pancreatic β-cell Ink4a / Arf expression and regeneration in streptozotocin-induced diabetes mellitus. Genes Dev. 975–985.

Chen, Q., Fischer, A., Reagan, J.D., Yan, L.J., and Ames, B.N. (1995). Oxidative DNA damage and senescence of human diploid fibroblast cells. Proc. Natl. Acad. Sci. U. S. A. *92*, 4337–4341.

Chen, S., Sanjana, N.E., Zheng, K., Shalem, O., Lee, K., Shi, X., Scott, D.A., Song, J., Pan, J.Q., Weissleder, R., et al. (2015). Genome-wide CRISPR screen in a mouse model of tumor growth and metastasis. Cell *160*, 1246–1260.

Chen, Z., Trotman, L.C., Shaffer, D., Lin, H.-K., Dotan, Z.A., Niki, M., Koutcher, J.A., Scher, H.I., Ludwig, T., Gerald, W., et al. (2005). Crucial role of p53-dependent cellular senescence in suppression of Pten-deficient tumorigenesis. Nature *436*, 725–730.

Cheng, Y., Zhao, Q., Liu, X., Araki, S., Zhang, S., and Miao, J. (2006). Phosphatidylcholine-specific phospholipase C, p53 and ROS in the association of apoptosis and senescence in vascular endothelial cells. FEBS Lett. *580*, 4911–4915.

Chien, Y., Scuoppo, C., Wang, X., Fang, X., Balgley, B., Bolden, J.E., Premsrirut, P., Luo, W., Chicas, A., Lee, C.S., et al. (2011). Control of the senescence-associated secretory phenotype by NF-κB promotes senescence and enhances chemosensitivity. Genes Dev. *25*, 2125–2136.

Childs, B.G., Baker, D.J., Wijshake, T., Conover, C.A., Campisi, J., and van Deursen, J.M. (2016). Senescent intimal foam cells are deleterious at all stages of atherosclerosis. Science (80-.). *354*, 472 LP – 477.

Chin, L., Artandi, S.E., Shen, Q., Tam, A., Lee, S.L., Gottlieb, G.J., Greider, C.W., and DePinho, R.A. (1999). P53 Deficiency Rescues the Adverse Effects of Telomere Loss and Cooperates With Telomere Dysfunction To Accelerate Carcinogenesis. Cell *97*, 527–538.

Chinta, S.J., Lieu, C.A., Demaria, M., Laberge, R.M., Campisi, J., and Andersen, J.K. (2013). Environmental stress, ageing and glial cell senescence: A novel mechanistic link to parkinson's disease? J. Intern. Med. *273*, 429–436.

Chinta, S.J., Woods, G., Demaria, M., Rane, A., Zou, Y., McQuade, A., Rajagopalan, S., Limbad, C., Madden, D.T., Campisi, J., et al. (2018). Cellular Senescence Is Induced by the Environmental Neurotoxin Paraquat and Contributes to Neuropathology Linked to Parkinson's Disease. Cell Rep. *22*, 930–940.

Chung, P., Zhou, S., and Eslami, B. (2014). Effect of age on regulation of human osteoclast differentiation. J. Cell. Biochem. *1419*, 1–27.

Claerhout, S., Dutta, B., Bossuyt, W., Zhang, F., Nguyen-Charles, C., Dennison, J.B., Yu, Q., Yu, S., Balázsi, G., Lu, Y., et al. (2012). Abortive autophagy induces endoplasmic

reticulum stress and cell death in cancer cells. PLoS One *7*, e39400.

Collado, M., Gil, J., Efeyan, A., Guerra, C., Schuhmacher, A.J., Barradas, M., Benguría, A., Zaballos, A., Flores, J.M., Barbacid, M., et al. (2005). Tumour biology: senescence in premalignant tumours. Nature *436*, 642.

Collado, M., Blasco, M.A., and Serrano, M. (2007). Cellular Senescence in Cancer and Aging. Cell *130*, 223–233.

Colombo, M., Raposo, G., and Théry, C. (2014). Biogenesis, secretion, and intercellular interactions of exosomes and other extracellular vesicles. Annu. Rev. Cell Dev. Biol. *30*, 255–289.

Contrepois, K., Coudereau, C., Benayoun, B.A., Schuler, N., Roux, P.-F., Bischof, O., Courbeyrette, R., Carvalho, C., Thuret, J.-Y., Ma, Z., et al. (2017). Histone variant H2A.J accumulates in senescent cells and promotes inflammatory gene expression. Nat. Commun. *8*, 14995.

Coppe, J.P., Kauser, K., Campisi, J., and Beausejour, C.M. (2006). Secretion of vascular endothelial growth factor by primary human fibroblasts at senescence. J.Biol.Chem. *281*, 29568–29574.

Coppé, J.-P., Patil, C.K., Rodier, F., Sun, Y., Muñoz, D.P., Goldstein, J., Nelson, P.S., Desprez, P.-Y., and Campisi, J. (2008). Senescence-associated secretory phenotypes reveal cell-nonautonomous functions of oncogenic RAS and the p53 tumor suppressor. PLoS Biol. *6*, 2853–2868.

Coppé, J.-P., Desprez, P.-Y., Krtolica, A., and Campisi, J. (2010). The senescence-associated secretory phenotype: the dark side of tumor suppression. Annu. Rev. Pathol. *5*, 99–118.

Correia-Melo, C., Marques, F.D., Anderson, R., Hewitt, G., Hewitt, R., Cole, J., Carroll, B.M., Miwa, S., Birch, J., Merz, A., et al. (2016). Mitochondria are required for pro-ageing features of the senescent phenotype. EMBO J. *35*, 724–742.

Cosgrove, B.D., Gilbert, P.M., Porpiglia, E., Mourkioti, F., Lee, S.P., Corbel, S.Y., Llewellyn, M.E., Delp, S.L., and Blau, H.M. (2014). Rejuvenation of the muscle stem cell population restores strength to injured aged muscles. Nat. Med. *20*, 255–264.

Cruickshanks, H.A., McBryan, T., Nelson, D.M., Vanderkraats, N.D., Shah, P.P., Van Tuyn, J., Singh Rai, T., Brock, C., Donahue, G., Dunican, D.S., et al. (2013). Senescent Cells Harbour Features of the Cancer Epigenome. Nat. Cell Biol. *15*, 1495–1506.

Cukierman, E., Huber, I., Rotman, M., and Cassel, D. (1995). The ARF1 GTPase-Activating Protein: Zinc Finger Motif and Golgi Complex Localization. Science (80-.). *270*, 1999 LP – 2002.

d'Adda di Fagagna, F. (2008). Living on a break: cellular senescence as a DNA-damage response. Nat. Rev. Cancer *8*, 512–522.

Dai, J., Cai, H., Li, H., Zhuang, Y., Min, H., Wen, Y., Yang, J., Gao, Q., Shi, Y., and Yi, L. (2015). Association between telomere length and survival in patients with idiopathic pulmonary fibrosis. Respirology *20*, 947–952.

Dancourt, J., and Barlowe, C. (2010). Protein sorting receptors in the early secretory pathway. Annu. Rev. Biochem. *79*, 777–802.

Dandona, P., Aljada, A., and Bandyopadhyay, A. (2004). Inflammation: The link between insulin resistance, obesity and diabetes. Trends Immunol. *25*, 4–7.

Dankort, D., Filenova, E., Collado, M., Serrano, M., Jones, K., and McMahon, M. (2007). A new mouse model to explore the initiation, progression, and therapy of BRAFV600E-induced lung tumors. Genes Dev. *21*, 379–384.

Dankort, D., Curley, D.P., Cartlidge, R.A., Nelson, B., Karnezis, A.N., Damsky, W.E.J., You, M.J., DePinho, R.A., McMahon, M., and Bosenberg, M. (2009). Braf(V600E) cooperates with Pten loss to induce metastatic melanoma. Nat. Genet. *41*, 544–552.

Demaria, M., Ohtani, N., Youssef, S.A., Rodier, F., Toussaint, W., Mitchell, J.R., Laberge, R.M., Vijg, J., VanSteeg, H., Dollé, M.E.T., et al. (2014). An essential role for senescent cells in optimal wound healing through secretion of PDGF-AA. Dev. Cell *31*, 722–733.

Demaria, M., O'Leary, M.N., Chang, J., Shao, L., Liu, S., Alimirah, F., Koenig, K., Le, C., Mitin, N., Deal, A.M., et al. (2017). Cellular Senescence Promotes Adverse Effects of Chemotherapy and Cancer Relapse. Cancer Discov. *7*, 165–176.

Demontis, F., and Perrimon, N. (2010). FOXO/4E-BP signaling in Drosophila muscles regulates organism-wide proteostasis during aging. Cell *143*, 813–825.

Denchi, E.L., and de Lange, T. (2007). Protection of telomeres through independent control of ATM and ATR by TRF2 and POT1. Nature *448*, 1068–1071.

Denchi, E.L., Attwooll, C., Pasini, D., and Helin, K. (2005). Deregulated E2F Activity Induces Hyperplasia and Senescence-Like Features in the Mouse Pituitary Gland. Mol. Cell. Biol. *25*, 2660–2672.

Deng, Q., Liao, R., Wu, B.L., and Sun, P. (2004). High Intensity ras Signaling Induces Premature Senescence by Activating p38 Pathway in Primary Human Fibroblasts. J. Biol. Chem. *279*, 1050–1059.

Deschênes-Simard, X., Lessard, F., Gaumont-Leclerc, M.F., Bardeesy, N., and Ferbeyre, G. (2014). Cellular senescence and protein degradation: Breaking down cancer. Cell Cycle *13*, 1840–1858.

Desdín-Micó, G., Soto-Heredero, G., Aranda, J.F., Oller, J., Carrasco, E., Gabandé-Rodríguez, E., Blanco, E.M., Alfranca, A., Cussó, L., Desco, M., et al. (2020). T cells with dysfunctional mitochondria induce multimorbidity and premature senescence. Science (80-.). *368*, 1371 LP – 1376.

Dimri, G.P., Lee, X., Basile, G., Acosta, M., Scott, G., Roskelley, C., Medrano, E.E., Linskens, M., Rubelj, I., and O, P.-S. (1995). A biomarker that identifies senescent human cells in culture and in aging skin in vivo. Proc Natl Acad Sci *92*, 9363–9367.

Dinarello, C.A. (2006). Interleukin 1 and interleukin 18 as mediators of inflammation and the aging process. Am. J. Clin. Nutr. *83*, 447S-455S.

Dinarello, C.A., Donath, M.Y., and Mandrup-poulsen, T. (2010). Role of IL-1 b in type 2 diabetes. Curr. Opin. Endocrinol. Diabetes. Obes. *17*, 314–321.

Ding, W.X., Ni, H.M., Gao, W., Hou, Y.F., Melan, M.A., Chen, X., Stolz, D.B., Shao, Z.M., and Yin, X.M. (2007). Differential effects of endoplasmic reticulum stress-induced autophagy on cell survival. J. Biol. Chem. *282*, 4702–4710.

Dodonova, S.O., Diestelkoetter-Bachert, P., Von Appen, A., Hagen, W.J.H., Beck, R., Beck, M., Wieland, F., and Briggs, J.A.G. (2015). A structure of the COPI coat and the role of coat proteins in membrane vesicle assembly. Science (80-.). *349*, 195–198.

Dodonova, S.O., Aderhold, P., Kopp, J., Ganeva, I., Röhling, S., Hagen, W.J.H., Sinning, I., Wieland, F., and Briggs, J.A.G. (2017). 9Å structure of the COPI coat reveals that the Arf1 GTPase occupies two contrasting molecular environments. Elife *6*, 1–29.

Doles, J., Storer, M., Cozzuto, L., Roma, G., and Keyes, W.M. (2012). Age-associated inflammation inhibits epidermal stem cell function. Genes Dev. *26*, 2144–2153.

Domozych, D.S. (1999). Disruption of the Golgi apparatus and secretory mechanism in the desmid, Closterium acerosum, by brefeldin A. J. Exp. Bot. *50*, 1323–1330.

Dörr, J.R., Yu, Y., Milanovic, M., Beuster, G., Zasada, C., Däbritz, J.H.M., Lisec, J., Lenze, D., Gerhardt, A., Schleicher, K., et al. (2013). Synthetic lethal metabolic targeting of cellular senescence in cancer therapy. Nature *501*, 421–425.

Dou, Z., Ghosh, K., Vizioli, M.G., Zhu, J., Sen, P., Wangensteen, K.J., Simithy, J., Lan, Y., Lin, Y., Zhou, Z., et al. (2017). Cytoplasmic chromatin triggers inflammation in senescence and cancer. Nature *550*, 402–406.

Dreesen, O., Chojnowski, A., Ong, P.F., Zhao, T.Y., Common, J.E., Lunny, D., Lane, E.B., Lee, S.J., Vardy, L.A., Stewart, C.L., et al. (2013). Lamin B1 fluctuations have differential effects on cellular proliferation and senescence. J. Cell Biol. *200*, 605–617.

Duensing, S., and Münger, K. (2002). The human papillomavirus type 16 E6 and E7 oncoproteins independently induce numerical and structural chromosome instability. Cancer Res. *62*, 7075–7082.

Eggert, T., Wolter, K., Ji, J., Ma, C., Yevsa, T., Klotz, S., Medina-Echeverz, J., Longerich, T., Forgues, M., Reisinger, F., et al. (2016). Distinct Functions of Senescence-Associated Immune Responses in Liver Tumor Surveillance and Tumor Progression. Cancer Cell *30*, 533–547.

Ehses, J. a, Lacraz, G., Giroix, M.-H., Schmidlin, F., Coulaud, J., Kassis, N., Irminger, J.-C., Kergoat, M., Portha, B., Homo-Delarche, F., et al. (2009). IL-1 antagonism reduces hyperglycemia and tissue inflammation in the type 2 diabetic GK rat. Proc. Natl. Acad. Sci. U. S. A. *106*, 13998–14003.

Ellison-Hughes, G.M. (2020). First evidence that senolytics are effective at decreasing senescent cells in humans. EBioMedicine *56*, 2019–2020.

Emmerich, C.H., Gamboa, L.M., Hofmann, M.C.J., Bonin-Andresen, M., Arbach, O., Schendel, P., Gerlach, B., Hempel, K., Bespalov, A., Dirnagl, U., et al. (2021). Improving target assessment in biomedical research: the GOT-IT recommendations. Nat. Rev. Drug Discov. *20*, 64–81.

Evers, B., Jastrzebski, K., Heijmans, J.P.M., Grernrum, W., Beijersbergen, R.L., and Bernards, R. (2016). CRISPR knockout screening outperforms shRNA and CRISPRi in identifying essential genes. Nat. Biotechnol. 11–14.

Eyman, D., Damodarasamy, M., Plymate, S.R., and Reed, M.J. (2009). CCL5 secreted by senescent aged fibroblasts induces proliferation of prostate epithelial cells and expression of genes that modulate angiogenesis. J. Cell. Physiol. *220*, 376–381.

Fafián-Labora, J.A., Rodríguez-Navarro, J.A., and O'Loghlen, A. (2020). Small Extracellular Vesicles Have GST Activity and Ameliorate Senescence-Related Tissue Damage. Cell Metab. *32*, 71-86.e5.

di Fagagna, F. d'Adda, Reaper, P.M., Clay-Farrace, L., Fiegler, H., Carr, P., von Zglinicki, T., Saretzki, G., Carter, N.P., and Jackson, S.P. (2003). A DNA damage checkpoint response in telomere-initiated senescence. Nature *426*, 194–198.

Faini, M., Beck, R., Wieland, F.T., and Briggs, J.A.G. (2013). Vesicle coats: structure, function, and general principles of assembly. Trends Cell Biol. *23*, 279–288.

Farber-Katz, S.E., Dippold, H.C., Buschman, M.D., Peterman, M.C., Xing, M., Noakes, C.J., Tat, J., Ng, M.M., Rahajeng, J., Cowan, D.M., et al. (2014). DNA Damage Triggers Golgi Dispersal via DNA-PK and GOLPH3. Cell *156*, 413–427.

Farr, J.N., Fraser, D.G., Wang, H., Jaehn, K., Ogrodnik, M.B., Weivoda, M.M., Drake, M.T., Tchkonia, T., LeBrasseur, N.K., Kirkland, J.L., et al. (2016). Identification of Senescent Cells in the Bone Microenvironment. J. Bone Miner. Res. *31*, 1920–1929.

Farr, J.N., Xu, M., Weivoda, M.M., Monroe, D.G., Fraser, D.G., Onken, J.L., Negley, B.A., Sfeir, J.G., Ogrodnik, M.B., Hachfeld, C.M., et al. (2017). Targeting cellular senescence prevents age-related bone loss in mice. Nat. Med. 1–11.

Fellmann, C., Hoffmann, T., Sridhar, V., Hopfgartner, B., Muhar, M., Roth, M., Lai, D.Y., Barbosa, I.A.M., Kwon, J.S., Guan, Y., et al. (2013). An optimized microRNA backbone for effective single-copy RNAi. Cell Rep. *5*, 1704–1713.

Feng, Y., Yu, S., Lasell, T.K.R., Jadhav, A.P., Macia, E., Chardin, P., Melancon, P., Roth, M., Mitchison, T., and Kirchhausen, T. (2003). Exo1: A new chemical inhibitor of the exocytic pathway. Proc. Natl. Acad. Sci. U. S. A. *100*, 6469–6474.

Ferreira-Gonzalez, S., Lu, W.Y., Raven, A., Dwyer, B., Man, T.Y., O'Duibhir, E., Lewis, P.J.S., Campana, L., Kendall, T.J., Bird, T.G., et al. (2018). Paracrine cellular senescence exacerbates biliary injury and impairs regeneration. Nat. Commun. *9*, 1–15.

Fink, R.I., Kolterman, O.G., Griffin, J., and Olefsky, J.M. (1983). Mechanisms of Insulin Resistance in Aging. J. Clin. Invest. *71*, 1523–1535.

Finkel, T., and Holbrook, N.J. (2000). Oxidants, Oxidative Stress and Biology of Ageing. Insight Rev. Artic. *408*, 239–247.

Flaherty, K.T., LoRusso, P.M., DeMichele, A., Abramson, V.G., Courtney, R., Randolph, S.S., Shaik, M.N., Wilner, K.D., O'Dwyer, P.J., and Schwartz, G.K. (2012). Phase I, dose-escalation trial of the oral cyclin-dependent kinase 4/6 inhibitor PD 0332991, administered using a 21-day schedule in patients with advanced cancer. Clin. Cancer Res. *18*, 568–576.

Flor, A.C., Wolfgeher, D., Wu, D., and Kron, S.J. (2017). A signature of enhanced lipid metabolism, lipid peroxidation and aldehyde stress in therapy-induced senescence. Cell Death Discov. *3*, 1–12.

Franceschi, C., and Campisi, J. (2014). Chronic inflammation (Inflammaging) and its potential contribution to age-associated diseases. Journals Gerontol. - Ser. A Biol. Sci. Med. Sci. *69*, S4–S9.

Freund, A., Patil, C.K., and Campisi, J. (2011). p38MAPK is a novel DNA damage response-independent regulator of the senescence-associated secretory phenotype. EMBO

J. *30*, 1536–1548.

Freund, A., Laberge, R.M., Demaria, M., and Campisi, J. (2012). Lamin B1 loss is a senescence-associated biomarker. Mol. Biol. Cell *23*, 2066–2075.

Fried, L.P., Tangen, C.M., Walston, J., Newman, A.B., Hirsch, C., Gottdiener, J., Seeman, T., Tracy, R., Kop, W.J., Burke, G., et al. (2001). Frailty in Older Adults: Evidence for a Phenotype. J. Gerontol. Med. Sci. Am. *56*, 146–156.

Frigerio, G., Grimsey, N., Dale, M., Majoul, I., and Duden, R. (2007). Two human ARFGAPs associated with COP-I-coated vesicles. Traffic *8*, 1644–1655.

Frith, J., Jones, D., and Newton, J.L. (2009). Chronic liver disease in an ageing population. Age Ageing *38*, 11–18.

Fuhrmann-Stroissnigg, H., Ling, Y.Y., Zhao, J., McGowan, S.J., Zhu, Y., Brooks, R.W., Grassi, D., Gregg, S.Q., Stripay, J.L., Dorronsoro, A., et al. (2017). Identification of HSP90 inhibitors as a novel class of senolytics. Nat. Commun. *8*.

Fumagalli, M., Rossiello, F., Clerici, M., Barozzi, S., Cittaro, D., Kaplunov, J.M., Bucci, G., Dobreva, M., Matti, V., Beausejour, C.M., et al. (2012). Telomeric DNA damage is irreparable and causes persistent DNA-damage-response activation. Nat. Cell Biol. *14*, 355–365.

García-Cao, I., García-Cao, M., Martín-Caballero, J., Criado, L.M., Klatt, P., Flores, J.M., Weill, J.-C., Blasco, M.A., and Serrano, M. (2002). “Super p53” mice exhibit enhanced DNA damage response, are tumor resistant and age normally. EMBO J. *21*, 6225–6235.

García-Mata, R., Szul, T., Alvarez, C., and Sztul, E. (2003). ADP-Ribosylation Factor/COPI-dependent Events at the Endoplasmic Reticulum-Golgi Interface Are Regulated by the Guanine Nucleotide Exchange Factor GBF1. Mol. Biol. Cell *14*, 2250–2261.

García-Prat, L., Martínez-Vicente, M., Perdiguero, E., Ortet, L., Rodríguez-Ubreva, J., Rebollo, E., Ruiz-Bonilla, V., Gutarra, S., Ballestar, E., Serrano, A.L., et al. (2016). Autophagy maintains stemness by preventing senescence. Nature *529*, 37–42.

Geiger, H., and Van Zant, G. (2002). The aging of lympho-hematopoietic stem cells. Nat. Immunol. *3*, 329–333.

Georgilis, A., Klotz, S., Hanley, C.J., Herranz, N., Weirich, B., Morancho, B., Leote, A.C., D’Artista, L., Gallage, S., Seehawer, M., et al. (2018). PTBP1-Mediated Alternative Splicing Regulates the Inflammatory Secretome and the Pro-tumorigenic Effects of Senescent Cells. Cancer Cell *34*, 85-102.e9.

Gerland, L.M., Peyrol, S., Lallemand, C., Branche, R., Magaud, J.P., and Ffrench, M. (2003). Association of increased autophagic inclusions labeled for β-galactosidase with fibroblastic aging. Exp. Gerontol. *38*, 887–895.

Gewirtz, D.A. (2013). Autophagy and senescence: A partnership in search of definition. Autophagy *9*, 808–812.

Giannandrea, M., and Parks, W.C. (2014). Diverse functions of matrix metalloproteinases during fibrosis. Dis. Model. Mech. *7*, 193–203.

Gil, J., and Peters, G. (2006). Regulation of the INK4b-ARF-INK4a tumour suppressor locus: all for one or one for all. Nat. Rev. Mol. Cell Biol. *7*, 667–677.

Gil, J., Bernard, D., Martínez, D., and Beach, D. (2004). Polycomb CBX7 has a unifying role in cellular lifespan. Nat. Cell Biol. *6*, 67–72.

Glick, B.S., and Luini, A. (2011). Models for Golgi traffic: A critical assessment. Cold Spring Harb. Perspect. Biol. *3*, 1–16.

Glick, D., Barth, S., and Macleod, K.F. (2010). Autophagy: Cellular and molecular mechanisms. J. Pathol. *221*, 3–12.

Glück, S., Guey, B., Gulen, M.F., Wolter, K., Kang, T.-W., Schmacke, N.A., Bridgeman, A., Rehwinkel, J., Zender, L., and Ablasser, A. (2017). Innate immune sensing of cytosolic chromatin fragments through cGAS promotes senescence. Nat. Cell Biol. *19*.

Goldman, J.W., Gandhi, L., Patnaik, A., Rosen, L.S., Hilton, J.F., Papadopoulos, K.P., Tolaney, S.M., Beeram, M., Rasco, D.W., Myrand, S.P., et al. (2014). Clinical activity of LY2835219, a novel cell cycle inhibitor selective for CDK4 and CDK6, in patients with non-small cell lung cancer. J. Clin. Oncol. *32*, 8026.

Gomez-Navarro, N., and Miller, E. (2016). Protein sorting at the ER-Golgi interface. J. Cell Biol. *215*, 769–778.

González-Gualda, E., Pàez-Ribes, M., Lozano-Torres, B., Macias, D., Wilson, J.R., González-López, C., Ou, H.L., Mirón-Barroso, S., Zhang, Z., Lérida-Viso, A., et al. (2020). Galacto-conjugation of Navitoclax as an efficient strategy to increase senolytic specificity and reduce platelet toxicity. Aging Cell *19*, 1–19.

Gopinath, S.D., and Rando, T.A. (2008). Stem Cell Review Series: Aging of the skeletal muscle stem cell niche. Aging Cell *7*, 590–598.

Graja, A., and Schulz, T.J. (2015). Mechanisms of aging-related impairment of brown adipocyte development and function. Gerontology *61*, 211–217.

Gratuze, M., Leyns, C.E.G., and Holtzman, D.M. (2018). New insights into the role of TREM2 in Alzheimer's disease. Mol. Neurodegener. *13*, 1–16.

Gray-Schopfer, V.C., Cheong, S.C., Chong, H., Chow, J., Moss, T., Abdel-Malek, Z.A., Marais, R., Wynford-Thomas, D., and Bennett, D.C. (2006). Cellular senescence in naevi and immortalisation in melanoma: A role for p16? Br. J. Cancer *95*, 496–505.

Gredilla, R., Sanz, A., Lopez-Torres, M., and Barja, G. (2001). Caloric restriction decreases mitochondrial free radical generation at complex I and lowers oxidative damage to mitochondrial DNA in the rat heart. FASEB J. *15*, 1589–1591.

Greidert, C.W., Harley B., H., and Futcher, A.B. (1990). Telomeres shorten during ageing of human fibroblasts. Nature *345*, 458–460.

Grocin, A.G., Serwa, R.A., Sanfrutos, J.M., Ritzefeld, M., and Tate, E.W. (2019). Whole proteome profiling of N-myristoyltransferase activity and inhibition using sortase A. Mol. Cell. Proteomics *18*, 115–126.

Grosse, L., Wagner, N., Emelyanov, A., Molina, C., Lacas-Gervais, S., Wagner, K.D., and Bulavin, D. V. (2020). Defined p16High Senescent Cell Types Are Indispensable for Mouse Healthspan. Cell Metab. *32*, 87-99.e6.

Guerrero, A., Herranz, N., Sun, B., Wagner, V., Gallage, S., Guiho, R., Wolter, K., Pombo, J., Irvine, E.E., Innes, A.J., et al. (2019). Cardiac glycosides are broad-spectrum senolytics.

Nat. Metab. *1*, 1074–1088.

Guerrero, A., Guiho, R., Herranz, N., Uren, A., Withers, D.J., Martínez-Barbera, J.P., Tietze, L.F., and Gil, J. (2020). Galactose-modified duocarmycin prodrugs as senolytics. Aging Cell *19*, 1–13.

Gunasekaran, U., and Gannon, M. (2011). Type 2 diabetes and the aging pancreatic beta cell. Aging (Albany. NY). *3*, 565–575.

Guo, Y., and Linstedt, A.D. (2006). COPII-Golgi protein interactions regulate COPII coat assembly and Golgi size. J. Cell Biol. *174*, 53–63.

Haghnegahdar, H., Du, J., Wang, D., Strieter, R.M., Burdick, M.D., Nanney, L.B., Cardwell, N., Luan, J., Shattuck-Brandt, R., and Richmond, A. (2000). The tumorigenic and angiogenic effects of MGSA/GRO proteins in melanoma. J. Leukoc. Biol. *67*, 53–62.

Hall, B.M., Balan, V., Gleiberman, A.S., Strom, E., Krasnov, P., Virtuoso, P., Rydkina, E., Vujcic, S., Balan, K., Gitlin, I.I., et al. (2017). p16 and SAbetaGal can be induced in macrophages as part of a reversible response to physiological stimuli. Aging (Albany. NY). *9*, 1867–1884.

Hanahan, D., and Weinberg, R.A. (2011). Hallmarks of cancer: The next generation. Cell *144*, 646–674.

Hara-Kuge, S., Kuge, O., Orci, L., Amherdt, M., Ravazzola, M., Wieland, F.T., and Rothman, J.E. (1994). En bloc incorporation of coatomer subunits during the assembly of COP- coated vesicles. J. Cell Biol. *124*, 883–892.

Hardy, T., Oakley, F., Anstee, Q.M., and Day, C.P. (2016). Nonalcoholic Fatty Liver Disease: Pathogenesis and Disease Spectrum. Annu. Rev. Pathol. Mech. Dis. *11*, 451–496.

Harris, S.L., and Levine, A.J. (2005). The p53 pathway: positive and negative feedback loops. Oncogene *24*, 2899–2908.

Harrison, D.E., Strong, R., Sharp, Z.D., Nelson, J.F., Astle, C.M., Flurkey, K., Nadon, N.L., Wilkinson, J.E., Frenkel, K., Carter, C.S., et al. (2010). Rapamycin fed late in life extends lifespan in genetically heterogeneous mice. Nature *460*, 392–395.

Hayflick, L., and Moorhead, P.S. (1961). The serial cultivation of human diploid cell strains. Exp. Cell Res. *25*, 585–621.

He, S., and Sharpless, N.E. (2017). Senescence in Health and Disease. Cell *169*, 1000–1011.

Helman, A., Klochendler, A., Azazmeh, N., Gabai, Y., Horwitz, E., Anzi, S., Swisa, A., Condiotti, R., Granit, R.Z., Nevo, Y., et al. (2016). p16(Ink4a)-induced senescence of pancreatic beta cells enhances insulin secretion. Nat. Med. *22*, 412–420.

Herbig, U., Ferreira, M., Condel, L., Carey, D., and Sedivy, J.M. (2006). Cellular Senescence in Aging Primates. Science (80-.). *311*, 1257 LP – 1257.

Herranz, N., Gallage, S., Mellone, M., Wuestefeld, T., Klotz, S., Hanley, C.J., Raguz, S., Acosta, J.C., Innes, A.J., Banito, A., et al. (2015). mTOR regulates MAPKAPK2 translation to control the senescence-associated secretory phenotype. Nat. Cell Biol. *17*, 1205–1217.

Hickson, L.T.J., Langhi Prata, L.G.P., Bobart, S.A., Evans, T.K., Giorgadze, N., Hashmi,

S.K., Herrmann, S.M., Jensen, M.D., Jia, Q., Jordan, K.L., et al. (2019). Senolytics decrease senescent cells in humans: Preliminary report from a clinical trial of Dasatinib plus Quercetin in individuals with diabetic kidney disease. EBioMedicine *47*, 446–456.

Hinners, I., and Tooze, S.A. (2003). Changing directions: Clathrin-mediated transport between the Golgi and endosomes. J. Cell Sci. *116*, 763–771.

Hoare, M., Ito, Y., Kang, T.-W., Weekes, M.P., Matheson, N.J., Patten, D.A., Shetty, S., Parry, A.J., Menon, S., Salama, R., et al. (2016). NOTCH1 mediates a switch between two distinct secretomes during senescence. Nat. Cell Biol. *18*, 979–992.

Hock, H. (2012). A complex Polycomb issue: The two faces of EZH2 in cancer. Genes Dev. *26*, 751–755.

Hoppe-Seyler, K., Bossler, F., Braun, J.A., Herrmann, A.L., and Hoppe-Seyler, F. (2018). The HPV E6/E7 Oncogenes: Key Factors for Viral Carcinogenesis and Therapeutic Targets. Trends Microbiol. *26*, 158–168.

Houtkooper, R.H., Pirinen, E., and Auwerx, J. (2012). Sirtuins as regulators of metabolism and healthspan. Nat. Rev. Mol. Cell Biol. *13*, 225–238.

Hsu, P.P., and Sabatini, D.M. (2008). Cancer cell metabolism: Warburg and beyond. Cell *134*, 703–707.

Hsu, C.H., Altschuler, S.J., and Wu, L.F. (2019). Patterns of Early p21 Dynamics Determine Proliferation-Senescence Cell Fate after Chemotherapy. Cell *178*, 361-373.e12.

Huang, A., Garraway, L.A., Ashworth, A., and Weber, B. (2020). Synthetic lethality as an engine for cancer drug target discovery. Nat. Rev. Drug Discov. *19*, 23–38.

Hubackova, S., Krejcikova, K., Bartek, J., and Hodny, Z. (2012). IL1-and TGFβ-Nox4 signaling, oxidative stress and DNA damage response are shared features of replicative, oncogene-induced, and drug-induced paracrine “Bystander senescence.” Aging (Albany. NY). *4*, 932–951.

Hudgins, A.D., Tazearslan, C., Tare, A., Zhu, Y., Huffman, D., and Suh, Y. (2018). Age- and tissue-specific expression of senescence biomarkers in mice. Front. Genet. *9*, 1–6.

Hwangbo, D.S., Gersham, B., Tu, M.-P., Palmer, M., and Tatar, M. (2004). Drosophila dFOXO controls lifespan and regulates insulin signalling in brain and fat body. Nature *429*, 562–566.

Ihry, R.J., Salick, M.R., Ho, D.J., Sondey, M., Kommineni, S., Paula, S., Raymond, J., Henry, B., Frias, E., Wang, Q., et al. (2019). Genome-Scale CRISPR Screens Identify Human Pluripotency-Specific Genes. Cell Rep. *27*, 616-630.e6.

Ito, K., Hirao, A., Arai, F., Takubo, K., Matsuoka, S., Miyamoto, K., Ohmura, M., Naka, K., Hosokawa, K., Ikeda, Y., et al. (2006). Reactive oxygen species act through p38 MAPK to limit the lifespan of hematopoietic stem cells. Nat. Med. *12*, 446–451.

Iwasa, H., Han, J., and Ishikawa, F. (2003). Mitogen-activated protein kinase p38 defines the common senescence-signalling pathway. Genes to Cells *8*, 131–144.

Jacobs, J.J.L., Kieboom, K., Marino, S., DePinho, R. a, and van Lohuizen, M. (1999). The oncogene and Polycomb-group gene bmi-1 regulates cell proliferation and senescence through the ink4a locus. Nature *397*, 164–168.

James, E.L., Michalek, R.D., Pitiyage, G.N., De Castro, A.M., Vignola, K.S., Jones, J., Mohney, R.P., Karoly, E.D., Prime, S.S., and Parkinson, E.K. (2015). Senescent human fibroblasts show increased glycolysis and redox homeostasis with extracellular metabolomes that overlap with those of irreparable DNA damage, aging, and disease. J. Proteome Res. *14*, 1854–1871.

Janzen, V., Forkert, R., Fleming, H.E., Saito, Y., Waring, M.T., Dombkowski, D.M., Cheng, T., DePinho, R.A., Sharpless, N.E., and Scadden, D.T. (2006). Stem-cell ageing modified by the cyclin-dependent kinase inhibitor p16INK4a. Nature *443*, 421–426.

Jaskelioff, M., Muller, F.L., Paik, J.-H., Thomas, E., Jiang, S., Adams, A.C., Sahin, E., Kost-Alimova, M., Protopopov, A., Cadiñanos, J., et al. (2011). Telomerase reactivation reverses tissue degeneration in aged telomerase-deficient mice. Nature *469*, 102–106.

Jeck, W.R., Siebold, A.P., and Sharpless, N.E. (2012). Review: A meta-analysis of GWAS and age-associated diseases. Aging Cell *11*, 727–731.

Jeon, O.H., Kim, C., Laberge, R.-M., Demaria, M., Rathod, S., Vasserot, A.P., Chung, J.W., Kim, D.H., Poon, Y., David, N., et al. (2017). Local clearance of senescent cells attenuates the development of post-traumatic osteoarthritis and creates a pro-regenerative environment. Nat. Med. 1–9.

Jeyapalan, J.C., Ferreira, M., Sedivy, J.M., and Herbig, U. (2007). Accumulation of senescent cells in mitotic tissue of aging primates. Mech. Ageing Dev. *128*, 36–44.

Joung, J., Konermann, S., Gootenberg, J.S., Abudayyeh, O.O., Platt, R.J., Brigham, M.D., Sanjana, N.E., and Zhang, F. (2017). Genome-scale CRISPR-Cas9 knockout and transcriptional activation screening. Nat. Protoc. *12*, 828–863.

Justice, J.N., Nambiar, A.M., Tchkonia, T., LeBrasseur, N.K., Pascual, R., Hashmi, S.K., Prata, L., Masternak, M.M., Kritchevsky, S.B., Musi, N., et al. (2019). Senolytics in idiopathic pulmonary fibrosis: Results from a first-in-human, open-label, pilot study. EBioMedicine *40*, 554–563.

Kahn, R.A., Goddard, C., and Newkirk, M. (1988). Chemical and immunological characterization of the 21-kDa ADP-ribosylation factor of adenylate cyclase. J. Biol. Chem. *263*, 8282–8287.

Kamijo, T., Zindy, F., Roussel, M.F., Quelle, D.E., Downing, J.R., Ashmun, R. a, Grosveld, G., and Sherr, C.J. (1997). Tumor suppression at the mouse INK4a locus mediated by the alternative reading frame product p19ARF. Cell *91*, 649–659.

Kang, C., Xu, Q., Martin, T.D., Li, M.Z., Demaria, M., Aron, L., Lu, T., Yankner, B.A., Campisi, J., and Elledge, S.J. (2015). The DNA damage response induces inflammation and senescence by inhibiting autophagy of GATA4. Science *349*, aaa5612.

Kang, T.-W., Yevsa, T., Woller, N., Hoenicke, L., Wuestefeld, T., Dauch, D., Hohmeyer, A., Gereke, M., Rudalska, R., Potapova, A., et al. (2011). Senescence surveillance of pre-malignant hepatocytes limits liver cancer development. Nature *479*, 547–551.

Kaplon, J., Zheng, L., Meissl, K., Chaneton, B., Selivanov, V.A., Mackay, G., van der Burg, S.H., Verdegaal, E.M.E., Cascante, M., Shlomi, T., et al. (2013). A key role for mitochondrial gatekeeper pyruvate dehydrogenase in oncogene-induced senescence. Nature *498*, 109–112.

Karlseder, J., Smogorzewska, A., and de Lange, T. (2002). Senescence Induced by Altered

Telomere State, Not Telomere Loss. Science (80-.). *295*, 2446 LP – 2449.

Kiecolt-Glaser, J.K., Preacher, K.J., MacCallum, R.C., Atkinson, C., Malarkey, W.B., and Glaser, R. (2003). Chronic stress and age-related increases in the proinflammatory cytokine IL-6. Proc.Natl.Acad.Sci.U.S.A *100*, 9090–9095.

Kim, K.H., and Roberts, C.W.M. (2016). Targeting EZH2 in cancer. Nat Med *22*, 128–134.

Kim, W.Y., and Sharpless, N.E. (2006). The Regulation of INK4/ARF in Cancer and Aging. Cell *127*, 265–275.

Kim, D., Bae, S., Park, J., Kim, E., Kim, S., Yu, H.R., Hwang, J., Kim, J. Il, and Kim, J.S. (2015). Digenome-seq: Genome-wide profiling of CRISPR-Cas9 off-target effects in human cells. Nat. Methods *12*, 237–243.

Kim, H.S., Mendiratta, S., Kim, J., Pecot, C.V., Larsen, J.E., Zubovych, I., Seo, B.Y., Kim, J., Eskiocak, B., Chung, H., et al. (2013a). XSystematic identification of molecular subtype-selective vulnerabilities in non-small-cell lung cancer. Cell *155*, 552.

Kim, K.-H., Chen, C.-C., Monzon, R.I., and Lau, L.F. (2013b). Matricellular protein CCN1 promotes regression of liver fibrosis through induction of cellular senescence in hepatic myofibroblasts. Mol. Cell. Biol. *33*, 2078–2090.

Kim, N.W., Piatyszek, M.A., Prowse, K.R., Harley, C.B., West, M.D., Ho, P.L.C., Coviello, G.M., Wright, W.E., Weinrich, S.L., and Shay, J.W. (1994). Specific association of human telomerase activity with immortal cells and cancer. Science (80-.). *266*, 2011–2015.

Kirk, S.J., Cliff, J.M., Thomas, J.A., and Ward, T.H. (2010). Biogenesis of secretory organelles during B cell differentiation. J. Leukoc. Biol. *87*, 245–255.

Kirwan, J.P., Krishnan, R.K., Weaver, J. a, Del Aguila, L.F., and Evans, W.J. (2001). Human aging is associated with altered TNF-alpha production during hyperglycemia and hyperinsulinemia. Am. J. Physiol. Endocrinol. Metab. *281*, E1137-43.

Klein, M.E., Kovatcheva, M., Davis, L.E., Tap, W.D., and Koff, A. (2018). CDK4/6 Inhibitors: The Mechanism of Action May Not Be as Simple as Once Thought. Cancer Cell *34*, 9–20.

Kliouchnikov, L., Bigay, J., Mesmin, B., Parnis, A., Rawet, M., Goldfeder, N., Antonny, B., and Cassel, D. (2009). Discrete determinants in ArfGAP2/3 conferring Golgi localization and regulation by the COPI coat. Mol. Biol. Cell *20*, 859–869.

Kolde, R., Laur, S., Adler, P., and Vilo, J. (2012). Robust rank aggregation for gene list integration and meta-analysis. Bioinformatics *28*, 573–580.

Kollman, C., Howe, C.W.S., Anasetti, C., Antin, J.H., Davies, S.M., Filipovich, A.H., Hegland, J., Kamani, N., Kernan, N.A., King, R., et al. (2001). Donor characteristics as risk factors in recipients after transplantation of bone marrow from unrelated donors: the effect of donor age. Blood *98*, 2043 LP – 2051.

Konishi, A., and De Lange, T. (2008). Cell cycle control of telomere protection and NHEJ revealed by a ts mutation in the DNA-binding domain of TRF2. Genes Dev. *22*, 1221–1230.

Korkut, C., Ataman, B., Ramachandran, P., Ashley, J., Barria, R., Gherbesi, N., and Budnik, V. (2009). Trans-Synaptic Transmission of Vesicular Wnt Signals through Evi/Wntless. Cell *139*, 393–404.

Kosar, M., Bartkova, J., Hubackova, S., Hodny, Z., Lukas, J., and Bartek, J. (2011).

Senescence-associated heterochromatin foci are dispensable for cellular senescence, occur in a cell type- And insult-dependent manner, and follow expression of p16ink4a. Cell Cycle *10*, 457–468.

Kovatcheva, M., Liao, W., Klein, M.E., Robine, N., Geiger, H., Crago, A.M., Dickson, M.A., Tap, W.D., Singer, S., and Koff, A. (2017). ATRX is a regulator of therapy induced senescence in human cells. Nat. Commun. *8*.

Kreiling, J.A., Tamamori-Adachi, M., Sexton, A.N., Jeyapalan, J.C., Munoz-Najar, U., Peterson, A.L., Manivannan, J., Rogers, E.S., Pchelintsev, N.A., Adams, P.D., et al. (2011). Age-associated increase in heterochromatic marks in murine and primate tissues. Aging Cell *10*, 292–304.

Krishnamurthy, J., Torrice, C., Ramsey, M.R., Kovalev, G.I., Al-Regaiey, K., Su, L., and Sharpless, N.E. (2004). Ink4a/Arf expression is a biomarker of aging. J. Clin. Invest. *114*, 1299–1307.

Krishnamurthy, J., Ramsey, M.R., Ligon, K.L., Torrice, C., Koh, A., Bonner-Weir, S., and Sharpless, N.E. (2006). p16INK4a induces an age-dependent decline in islet regenerative potential. Nature *443*, 453–457.

Krishnan, K.J., Greaves, L.C., Reeve, A.K., and Turnbull, D. (2007). The ageing mitochondrial genome. Nucleic Acids Res. *35*, 7399–7405.

Krizhanovsky, V., Yon, M., Dickins, R.A., Hearn, S., Simon, J., Miething, C., Yee, H., Zender, L., and Lowe, S.W. (2008). Senescence of activated stellate cells limits liver fibrosis. Cell *134*, 657–667.

Krtolica, A., Parrinello, S., Lockett, S., Desprez, P.Y., and Campisi, J. (2001). Senescent fibroblasts promote epithelial cell growth and tumorigenesis: a link between cancer and aging. Proc. Natl. Acad. Sci. U. S. A. *98*, 12072–12077.

Kruiswijk, F., Labuschagne, C.F., and Vousden, K.H. (2015). P53 in Survival, Death and Metabolic Health: a Lifeguard With a Licence To Kill. Nat. Rev. Mol. Cell Biol. *16*, 393–405.

Kruse, J.P., and Gu, W. (2009). Modes of p53 Regulation. Cell *137*, 609–622.

Kudlow, B. a, Kennedy, B.K., and Monnat, R.J. (2007). Werner and Hutchinson-Gilford progeria syndromes: mechanistic basis of human progeroid diseases. Nat. Rev. Mol. Cell Biol. *8*, 394–404.

Kuhn, H.G., Dickinson-Anson, H., and Gage, F.H. (1996). Neurogenesis in the dentate gyrus of the adult rat: age-related decrease of neuronal progenitor proliferation. J Neurosci *16*, 2027–2033.

Kuilman, T., and Peeper, D.S. (2009). Senescence-messaging secretome: SMS-ing cellular stress. Nat. Rev. Cancer *9*, 81–94.

Kuilman, T., Michaloglou, C., Vredeveld, L.C.W., Douma, S., van Doorn, R., Desmet, C.J., Aarden, L.A., Mooi, W.J., and Peeper, D.S. (2008). Oncogene-Induced Senescence Relayed by an Interleukin-Dependent Inflammatory Network. Cell *133*, 1019–1031.

Kurz, D.J., Decary, S., Hong, Y., and Erusalimsky, J.D. (2000). Senescence-associated β-galactosidase reflects an increase in lysosomal mass during replicative ageing of human endothelial cells. J. Cell Sci. *113*, 3613–3622.

Kuyinu, E.L., Narayanan, G., Nair, L.S., and Laurencin, C.T. (2016). Animal models of osteoarthritis: classification, update, and measurement of outcomes. J. Orthop. Surg. Res. *11*, 19.

Kwong, J., Hong, L., Liao, R., Deng, Q., Han, J., and Sun, P. (2009). P38α and p38 mediate oncogenic ras-induced senescence through differential mechanisms. J. Biol. Chem. *284*, 11237–11246.

Laberge, R.-M., Sun, Y., Orjalo, A. V, Patil, C.K., Freund, A., Zhou, L., Curran, S.C., Davalos, A.R., Wilson-Edell, K.A., Liu, S., et al. (2015). MTOR regulates the pro-tumorigenic senescence-associated secretory phenotype by promoting IL1A translation. Nat. Cell Biol. *17*, 1049–1061.

Laberge, R.M., Zhou, L., Sarantos, M.R., Rodier, F., Freund, A., de Keizer, P.L.J., Liu, S., Demaria, M., Cong, Y.S., Kapahi, P., et al. (2012). Glucocorticoids suppress selected components of the senescence-associated secretory phenotype. Aging Cell *11*, 569–578.

Labun, K., Montague, T.G., Gagnon, J.A., Thyme, S.B., and Valen, E. (2016). CHOPCHOP v2: a web tool for the next generation of CRISPR genome engineering. Nucleic Acids Res. *44*, W272–W276.

de Lange, T. (2018). Shelterin-Mediated Telomere Protection. Annu. Rev. Genet. *52*, 223–247.

De Lange, T. (2005). Shelterin: The protein complex that shapes and safeguards human telomeres. Genes Dev. *19*, 2100–2110.

Lapasset, L., Milhavet, O., Prieur, A., Besnard, E., Babled, A., Aït-Hamou, N., Leschik, J., Pellestor, F., Ramirez, J.-M., De Vos, J., et al. (2011). Rejuvenating senescent and centenarian human cells by reprogramming through the pluripotent state. Genes Dev. *25*, 2248–2253.

Lavasani, M., Robinson, A.R., Lu, A., Song, M., Feduska, J.M., Ahani, B., Tilstra, J.S., Feldman, C.H., Robbins, P.D., Niedernhofer, L.J., et al. (2012). Muscle-derived stem/progenitor cell dysfunction limits healthspan and lifespan in a murine progeria model. Nat. Commun. *3*, 608.

Lee, B.Y., Han, J.A., Im, J.S., Morrone, A., Johung, K., Goodwin, E.C., Kleijer, W.J., DiMaio, D., and Hwang, E.S. (2006). Senescence-associated β-galactosidase is lysosomal β-galactosidase. Aging Cell *5*, 187–195.

Lee, H. ju, Choi, T.I., Kim, Y.M., Lee, S., Han, B., Bak, I.S., Moon, S.A., Yu, D.Y., Shin, K.S., Kwon, Y.K., et al. (2020). Regulation of habenular G-protein gamma 8 on learning and memory via modulation of the central acetylcholine system. Mol. Psychiatry.

Lehmann, B.D., Paine, M.S., Brooks, A.M., McCubrey, J.A., Renegar, R.H., Wang, R., and Terrian, D.M. (2008). Senescence-associated exosome release from human prostate cancer cells. Cancer Res. *68*, 7864–7871.

Lenain, C., Bauwens, S., Amiard, S., Brunori, M., Giraud-Panis, M.J., and Gilson, E. (2006). The Apollo 5′ Exonuclease Functions Together with TRF2 to Protect Telomeres from DNA Repair. Curr. Biol. *16*, 1303–1310.

Leong, W.F., Chau, J.F.L., and Li, B. (2009). p53 Deficiency leads to compensatory up-regulation of p16INK4a. Mol. Cancer Res. *7*, 354–360.

Li, H., Wang, W., Liu, X., Paulson, K.E., Yee, a S., and Zhang, X. (2010). Transcriptional factor HBP1 targets p16INK4A, upregulating its expression and consequently is involved in Ras-induced premature senescence. Oncogene *29*, 5083–5094.

Li, W., Xu, H., Xiao, T., Cong, L., Love, M.I., Zhang, F., Irizarry, R.A., Liu, J.S., Brown, M., Liu, X.S., et al. (2014). MAGeCK enables robust identification of essential genes from genome-scale CRISPR/Cas9 knockout screens. Genome Biol. 2014 1512 *15*, 819–823.

Liao, Z., Tu, J.H., Small, C.B., Schnipper, S.M., and Rosenstreich, D.L. (1993). Increased urine interleukin-1 levels in aging. Gerontology *39*, 19–27.

Libby, P. (2002). Inflammation in atherosclerosis. Nature *420*, 868–874.

Libby, P., Ridker, P.M., and Maseri, A. (2002). Inflammation and atherosclerosis. Circulation *105*, 1135–1143.

Lim, D.-S., Vogel, H., Willerford, D.M., Sands, A.T., Platt, K.A., and Hasty, P. (2000). Analysis of ku80-Mutant Mice and Cells with Deficient Levels of p53. Mol. Cell. Biol. *20*, 3772–3780.

Lin, A.W., Barradas, M., Stone, J.C., Van Aelst, L., Serrano, M., and Lowe, S.W. (1998). Premature senescence involving p53 and p16 is activated in response to constitutive MEK/MAPK mitogenic signaling. Genes Dev. *12*, 3008–3019.

Lindahl, T. (1993). Instability and decay of the primary structure of DNA. Nature *362*, 709–715.

Linton, P.J., and Dorshkind, K. (2004). Age-related changes in lymphocyte development and function. Nat. Immunol. *5*, 133–139.

Lippincott-Schwartz, J., Roberts, T.H., and Hirschberg, K. (2000). Secretory Protein Trafficking and Organelle Dynamics in Living Cells. Annu. Rev. Cell Dev. Biol. *16*, 557–589.

Liton, P.B., Challa, P., Stinnett, S., Luna, C., Epstein, D.L., and Gonzalez, P. (2005). Cellular senescence in the glaucomatous outflow pathway. Exp. Gerontol. *40*, 745–748.

Liu, D., and Hornsby, P.J. (2007). Senescent human fibroblasts increase the early growth of xenograft tumors via matrix metalloproteinase secretion. Cancer Res. *67*, 3117–3126.

Liu, J.Y., Souroullas, G.P., Diekman, B.O., Krishnamurthy, J., Hall, B.M., Sorrentino, J.A., Parker, J.S., Sessions, G.A., Gudkov, A. V., and Sharpless, N.E. (2019). Cells exhibiting strong p16 INK4a promoter activation in vivo display features of senescence. Proc. Natl. Acad. Sci. U. S. A. *116*, 2603–2611.

Liu, Y., Kahn, R.A., and Prestegard, J.H. (2009). Structure and Membrane Interaction of Myristoylated ARF1. Structure *17*, 79–87.

Loeser, R.F. (2009). Aging and osteoarthritis: the role of chondrocyte senescence and aging changes in the cartilage matrix. Osteoarthr. Cartil. *17*, 971–979.

Lomas, N.J., Watts, K.L., Akram, K.M., Forsyth, N.R., and Spiteri, M.A. (2012). Idiopathic pulmonary fibrosis: Immunohistochemical analysis provides fresh insights into lung tissue remodelling with implications for novel prognostic markers. Int. J. Clin. Exp. Pathol. *5*, 58–71.

López-Otín, C., Blasco, M.A., Partridge, L., Serrano, M., and Kroemer, G. (2013). The Hallmarks of Aging. Cell *153*, 1194–1217.

Lundblad, V., and Szostak, J.W. (1989). A mutant with a defect in telomere elongation leads to senescence in yeast. Cell *57*, 633–643.

Lunn, M.L., Nassirpour, R., Arrabit, C., Tan, J., Mcleod, I., Arias, C.M., Sawchenko, P.E., Yates, J.R., and Slesinger, P.A. (2007). A unique sorting nexin regulates trafficking of potassium channels via a PDZ domain interaction. Nat. Neurosci. *10*, 1249–1259.

Luo, X., Fu, Y., Loza, A.J., Murali, B., Leahy, K.M., Ruhland, M.K., Gang, M., Su, X., Zamani, A., Shi, Y., et al. (2016). Stromal-Initiated Changes in the Bone Promote Metastatic Niche Development. Cell Rep. *14*, 82–92.

Macip, S., Igarashi, M., Fang, L., Chen, A., Pan, Z., Lee, S.W., and Aaronson, S.A. (2002). Inhibition of p21-mediated ROS accumulation can rescue p21-induced senescence. EMBO J. *21*, 2180 LP – 2188.

de Magalhães, J.P. (2013). How ageing processes influence cancer. Nat. Rev. Cancer *13*, 357–365.

Mannava, S., Moparthy, K.C., Wheeler, L.J., Natarajan, V., Zucker, S.N., Fink, E.E., Im, M., Flanagan, S., Burhans, W.C., Zeitouni, N.C., et al. (2013). Depletion of deoxyribonucleotide pools is an endogenous source of DNA damage in cells undergoing oncogene-induced senescence. Am. J. Pathol. *182*, 142–151.

Manzella, N., Santin, Y., Maggiorani, D., Martini, H., Douin-Echinard, V., Passos, J.F., Lezoualc'h, F., Binda, C., Parini, A., and Mialet-Perez, J. (2018). Monoamine oxidase-A is a novel driver of stress-induced premature senescence through inhibition of parkin-mediated mitophagy. Aging Cell *17*.

Mario Gonzalez-Meljem, J., Haston, S., Carreno, G., Apps, J.R., Pozzi, S., Stache, C., Kaushal, G., Virasami, A., Panousopoulos, L., Neda Mousavy-Gharavy, S., et al. (2017). Stem cell senescence drives age-attenuated induction of pituitary tumours in mouse models of paediatric craniopharyngioma. Nat. Commun. *8*, 1–14.

Martínez-Menárguez, J.A., Geuze, H.J., Slot, J.W., and Klumperman, J. (1999). Vesicular tubular clusters between the ER and Golgi mediate concentration of soluble secretory proteins by exclusion from COPI-coated vesicles. Cell *98*, 81–90.

Maslov, A.Y., Barone, T.A., Plunkett, R.J., and Pruitt, S.C. (2004). Neural Stem Cell Detection, Characterization, and Age-Related Changes in the Subventricular Zone of Mice. J. Neurosci. *24*, 1726–1733.

Matheu, A., Maraver, A., Klatt, P., Flores, I., Garcia-Cao, I., Borras, C., Flores, J.M., Viña, J., Blasco, M. a, and Serrano, M. (2007). Delayed ageing through damage protection by the Arf/p53 pathway. Nature *448*, 375–379.

Matheu, A., Maraver, A., Collado, M., Garcia-Cao, I., Cañamero, M., Borras, C., Flores, J.M., Klatt, P., Viña, J., and Serrano, M. (2009). Anti-aging activity of the Ink4/Arf locus. Aging Cell *8*, 152–161.

Matsuura-Tokita, K., Takeuchi, M., Ichihara, A., Mikuriya, K., and Nakano, A. (2006). Live imaging of yeast Golgi cisternal maturation. Nature *441*, 1007–1010.

McHugh, D., and Gil, J. (2017). Senescence and aging: Causes, consequences, and therapeutic avenues. J. Cell Biol. jcb.201708092.

McMonnies, C.W. (2017). Glaucoma history and risk factors. J. Optom. *10*, 71–78.

Melk, A., Kittikowit, W., Sandhu, I., Halloran, K.M., Grimm, P., Schmidt, B.M.W., and Halloran, P.F. (2003). Cell senescence in rat kidneys in vivo increases with growth and age despite lack of telomere shortening. Kidney Int. *63*, 2134–2143.

Melk, A., Schmidt, B.M.W., Takeuchi, O., Sawitzki, B., Rayner, D.C., and Halloran, P.F. (2004). Expression of p16INK4a and other cell cycle regulator and senescence associated genes in aging human kidney. Kidney Int. *65*, 510–520.

Melov, S., Coskun, P., Patel, M., Tuinstra, R., Cottrell, B., Jun, A.S., Zastawny, T.H., Dizdaroglu, M., Goodman, S.I., Huang, T.T., et al. (1999). Mitochondrial disease in superoxide dismutase 2 mutant mice. Proc. Natl. Acad. Sci. U. S. A. *96*, 846–851.

Di Micco, R., Fumagalli, M., Cicalese, A., Piccinin, S., Gasparini, P., Luise, C., Schurra, C., Garre', M., Nuciforo, P.G., Bensimon, A., et al. (2006). Oncogene-induced senescence is a DNA damage response triggered by DNA hyper-replication. Nature *444*, 638–642.

Michalak, E.M., Burr, M.L., Bannister, A.J., and Dawson, M.A. (2019). The roles of DNA, RNA and histone methylation in ageing and cancer. Nat. Rev. Mol. Cell Biol. *20*, 573–589.

Michaloglou, C., Vredeveld, L.C.W., Soengas, M.S., Denoyelle, C., Kuilman, T., van der Horst, C.M.A.M., Majoor, D.M., Shay, J.W., Mooi, W.J., and Peeper, D.S. (2005). BRAFE600-associated senescence-like cell cycle arrest of human naevi. Nature *436*, 720–724.

Miller, J.P., and Allman, D. (2003). The decline in B lymphopoiesis in aged mice reflects loss of very early B-lineage precursors. J. Immunol. *171*, 2326–2330.

Miller, R.A., Harrison, D.E., Astle, C.M., Baur, J.A., Boyd, A.R., De Cabo, R., Fernandez, E., Flurkey, K., Javors, M.A., Nelson, J.F., et al. (2011). Rapamycin, but not resveratrol or simvastatin, extends life span of genetically heterogeneous mice. Journals Gerontol. - Ser. A Biol. Sci. Med. Sci. *66 A*, 191–201.

Min, H., Montecino-Rodriguez, E., and Dorshkind, K. (2005). Effects of aging on early B- and T-cell development. Immunol. Rev. *205*, 7–17.

Mitchell, S.J., Madrigal-Matute, J., Scheibye-Knudsen, M., Fang, E., Aon, M., Gonz??lez-Reyes, J.A., Cortassa, S., Kaushik, S., Gonzalez-Freire, M., Patel, B., et al. (2016). Effects of Sex, Strain, and Energy Intake on Hallmarks of Aging in Mice. Cell Metab. *23*, 1093–1112.

Mocchegiani, E., and Malavolta, M. (2004). NK and NKT cell functions in immunosenescence. Aging Cell *3*, 177–184.

Moelleken, J., Malsam, J., Betts, M.J., Movafeghi, A., Reckmann, I., Meissner, I., Hellwig, A., Russell, R.B., Söllner, T., Brügger, B., et al. (2007). Differential localization of coatomer complex isoforms within the Golgi apparatus. Proc. Natl. Acad. Sci. U. S. A. *104*, 4425–4430.

Moffat, J.G., Rudolph, J., and Bailey, D. (2014). Phenotypic screening in cancer drug discovery-past, present and future. Nat. Rev. Drug Discov. *13*, 588–602.

Moiseeva, O., Bourdeau, V., Roux, A., Deschênes-Simard, X., and Ferbeyre, G. (2009). Mitochondrial dysfunction contributes to oncogene-induced senescence. Mol. Cell. Biol. *29*, 4495–4507.

Molofsky, A. V, Slutsky, S.G., Joseph, N.M., He, S., Pardal, R., Krishnamurthy, J.,

Sharpless, N.E., and Morrison, S.J. (2006). Increasing p16INK4a expression decreases forebrain progenitors and neurogenesis during ageing. Nature *443*, 448–452.

Morgens, D.W., Deans, R.M., Li, A., and Bassik, M.C. (2016). Systematic comparison of CRISPR / Cas9 and RNAi screens for essential genes. Nat. Biotechnol. 1–4.

Munger, K., Gwin, T.K., and McLaughlin-Drubin, M. (2013). p16 in HPV-associated cancers. Oncotarget *4*, 1864–1865.

Muñoz-Espín, D., and Serrano, M. (2014). Cellular senescence: from physiology to pathology. Nat. Rev. Mol. Cell Biol. *15*, 482–496.

Muñoz-Espín, D., Cañamero, M., Maraver, A., Gómez-López, G., Contreras, J., Murillo-Cuesta, S., Rodríguez-Baeza, A., Varela-Nieto, I., Ruberte, J., Collado, M., et al. (2013). Programmed cell senescence during mammalian embryonic development. Cell *155*, 1104–1118.

Muñoz-Espín, D., Rovira, M., Galiana, I., Giménez, C., Lozano-Torres, B., Paez-Ribes, M., Llanos, S., Chaib, S., Muñoz-Martín, M., Ucero, A.C., et al. (2018). A versatile drug delivery system targeting senescent cells. EMBO Mol. Med. *10*, 1–18.

Myrianthopoulos, V., Evangelou, K., Vasileiou, P.V.S., Cooks, T., Vassilakopoulos, T.P., Pangalis, G.A., Kouloukoussa, M., Kittas, C., Georgakilas, A.G., and Gorgoulis, V.G. (2019). Senescence and senotherapeutics: a new field in cancer therapy. Pharmacol. Ther. *193*, 31–49.

Nalysnyk, L., Cid-Ruzafa, J., Rotella, P., and Esser, D. (2012). Incidence and prevalence of idiopathic pulmonary fibrosis: Review of the literature. Eur. Respir. Rev. *21*, 355–361.

Nandakumar, J., and Cech, T.R. (2013). Finding the end: recruitment of telomerase to telomeres. Nat. Rev. Mol. Cell Biol. *14*, 69–82.

Narita, M., Nunez, S., Heard, E., Narita, M., Lin, A.W., Hearn, S.A., Spector, D.L., Hannon, G.J., and Lowe, S.W. (2003). Rb-mediated heterochromatin formation and silencing of E2F target genes during cellular senescence. Cell *113*, 703–716.

Narita, M., Narita, M., Krizhanovsky, V., Nuñez, S., Chicas, A., Hearn, S.A., Myers, M.P., and Lowe, S.W. (2006). A Novel Role for High-Mobility Group A Proteins in Cellular Senescence and Heterochromatin Formation. Cell *126*, 503–514.

Narita, M., Young, A.R.J., Arakawa, S., Samarajiwa, S.A., Nakashima, T., Yoshida, S., Hong, S., Berry, L.S., Reichelt, S., Ferreira, M., et al. (2011). Spatial Coupling of mTOR and Autophagy Augments Secretory Phenotypes. Science (80-.). *332*, 966 LP – 970.

Niccoli, T., and Partridge, L. (2012). Ageing as a risk factor for disease. Curr. Biol. *22*, R741–R752.

North, B.J., and Sinclair, D.A. (2012). The intersection between aging and cardiovascular disease. Circ. Res. *110*, 1097–1108.

Novoa, I., Zeng, H., Harding, H.P., and Ron, D. (2001). Feedback inhibition of the unfolded protein response by GADD34-mediated dephosphorylation of eIF2α. J. Cell Biol. *153*, 1011–1021.

O'Sullivan, R.J., and Karlseder, J. (2010). Telomeres: protecting chromosomes against genome instability. Nat. Rev. Mol. Cell Biol. *11*, 171–181.

Ogrodnik, M., Miwa, S., Tchkonia, T., Tiniakos, D., Wilson, C.L., Lahat, A., Day, C.P., Burt, A., Palmer, A., Anstee, Q.M., et al. (2017). Cellular senescence drives age-dependent hepatic steatosis. Nat. Commun. *8*, 15691.

Omer, A., Barrera, M.C., Moran, J.L., Lian, X.J., Di Marco, S., Beausejour, C., and Gallouzi, I.E. (2020). G3BP1 controls the senescence-associated secretome and its impact on cancer progression. Nat. Commun. *11*, 1–15.

Omori, S., Wang, T.W., Johmura, Y., Kanai, T., Nakano, Y., Kido, T., Susaki, E.A., Nakajima, T., Shichino, S., Ueha, S., et al. (2020). Generation of a p16 Reporter Mouse and Its Use to Characterize and Target p16high Cells In Vivo. Cell Metab. *32*, 814-828.e6.

Ovadya, Y., Krizhanovsky, V., Ovadya, Y., and Krizhanovsky, V. (2018). Strategies targeting cellular senescence Find the latest version : Strategies targeting cellular senescence. J Clin Invest. *128*, 1247–1254.

Palm, W., and de Lange, T. (2008). How Shelterin Protects Mammalian Telomeres. Annu. Rev. Genet. *42*, 301–334.

Palmer, A.K., Tchkonia, T., LeBrasseur, N.K., Chini, E.N., Xu, M., and Kirkland, J.L. (2015). Cellular senescence in type 2 diabetes: A therapeutic opportunity. Diabetes *64*, 2289–2298.

Pardoll, D.M. (2012). The blockade of immune checkpoints in cancer immunotherapy. Nat. Rev. Cancer *12*, 252–264.

Parnas, O., Jovanovic, M., Eisenhaure, T.M., Herbst, R.H., Dixit, A., Ye, C.J., Przybylski, D., Platt, R.J., Tirosh, I., Sanjana, N.E., et al. (2015). A Genome-wide CRISPR Screen in Primary Immune Cells to Dissect Regulatory Networks. Cell *162*, 675–686.

Parrinello, S., Samper, E., Krtolica, A., Goldstein, J., Melov, S., and Campisi, J. (2003). Oxygen sensitivity severely limits the replicative lifespan of murine fibroblasts. Nat. Cell Biol. *5*, 741–747.

Pasmant, E., Sabbagh, A., Vidaud, M., and Bieche, I. (2011). ANRIL, a long, noncoding RNA, is an unexpected major hotspot in GWAS. FASEB J. *25*, 444–448.

Patel, P.L., Suram, A., Mirani, N., Bischof, O., and Herbig, U. (2016). Derepression of hTERT gene expression promotes escape from oncogene-induced cellular senescence. Proc. Natl. Acad. Sci. U. S. A. *113*, E5024–E5033.

Pazolli, E., Luo, X., Brehm, S., Carbery, K., Chung, J.J., Prior, J.L., Doherty, J., Demehri, S., Salavaggione, L., Piwnica-Worms, D., et al. (2009). Senescent stromal-derived osteopontin promotes preneoplastic cell growth. Cancer Res. *69*, 1230–1239.

Pearson, M., Carbone, R., Sebastiani, C., Cioce, M., Fagioli, M., Saito, S., Higashimoto, Y., Appella, E., Minucci, S., Pandolfi, P.P., et al. (2000). PML regulates p53 acetylation and premature senescence induced by oncogenic Ras. Nature *406*, 207–210.

Pellett, P.A., Dietrich, F., Bewersdorf, J., Rothman, J.E., and Lavieu, G. (2013). Inter-Golgi transport mediated by COPI-containing vesicles carrying small cargoes. Elife *2*, 1–20.

Pellicoro, A., Ramachandran, P., Iredale, J.P., and Fallowfield, J.A. (2014). Liver fibrosis and repair: immune regulation of wound healing in a solid organ. Nat. Rev. Immunol. *14*, 181–194.

Pelossof, R., Fairchild, L., Huang, C.H., Widmer, C., Sreedharan, V.T., Sinha, N., Lai, D.Y.,

Guan, Y., Premsrirut, P.K., Tschaharganeh, D.F., et al. (2017). Prediction of potent shRNAs with a sequential classification algorithm. Nat. Biotechnol. *35*, 350–353.

Pérez-Mancera, P.A., Young, A.R.J., and Narita, M. (2014). Inside and out: the activities of senescence in cancer. Nat. Rev. Cancer *14*, 547–558.

Pérez, V.I., Bokov, A., Remmen, H. Van, Mele, J., Ran, Q., Ikeno, Y., and Richardson, A. (2009). Is the oxidative stress theory of aging dead? Biochim. Biophys. Acta - Gen. Subj. *1790*, 1005–1014.

Petros, R.A., and Desimone, J.M. (2010). Strategies in the design of nanoparticles for therapeutic applications. Nat. Rev. Drug Discov. *9*, 615–627.

Phillips, L.R., Wolfe, T.L., Malspeis, L., and Supko, J.G. (1998). Analysis of brefeldin A and the prodrug breflate in plasma by gas chromatography with mass selective detection. J. Pharm. Biomed. Anal. *16*, 1301–1309.

Pickart, C.M., and Eddins, M.J. (2004). Ubiquitin: Structures, functions, mechanisms. Biochim. Biophys. Acta - Mol. Cell Res. *1695*, 55–72.

Pietras, E.M., Mirantes-Barbeito, C., Fong, S., Loeffler, D., Kovtonyuk, L. V., Zhang, S., Lakshminarasimhan, R., Chin, C.P., Techner, J.-M., Will, B., et al. (2016). Chronic interleukin-1 exposure drives haematopoietic stem cells towards precocious myeloid differentiation at the expense of self-renewal. Nat. Cell Biol. *18*, 607–618.

Pollock, P.M., and Meltzer, P.S. (2002). A genome-based strategy uncovers frequent BRAF mutations in melanoma. Cancer Cell *2*, 5–7.

Poon, I.K.H., Lucas, C.D., Rossi, A.G., and Ravichandran, K.S. (2014). Apoptotic cell clearance: basic biology and therapeutic potential. Nat. Rev. Immunol. *14*, 166–180.

Poon, P.P., Cassel, D., Spang, A., Rotman, M., Pick, E., Singer, R.A., and Johnston, G.C. (1999). Retrograde transport from the yeast Golgi is mediated by two ARF GAP proteins with overlapping function. EMBO J. *18*, 555–564.

Pott, S., and Lieb, J.D. (2015). What are super-enhancers? Nat. Genet. *47*, 8–12.

Price, J.S., Waters, J.G., Darrah, C., Pennington, C., Edwards, D.R., Donell, S.T., and Clark, I.M. (2002). The role of chondrocyte senescence in osteoarthritis. Aging Cell *1*, 57–65.

Prior, I.A., Lewis, P.D., and Mattos, C. (2012). A comprehensive survey of ras mutations in cancer. Cancer Res. *72*, 2457–2467.

Querfurth, H.W., and LaFerla, F.M. (2010). Alzheimer's Disease. N. Engl. J. Med. *362*, 329–344.

Quijano, C., Cao, L., Fergusson, M.M., Romero, H., Liu, J., Gutkind, S., Rovira, I.I., Mohney, R.P., Karoly, E.D., and Finkel, T. (2012). Oncogene-induced senescence results in marked metabolic and bioenergetic alterations. Cell Cycle *11*, 1383–1392.

Raggi, C., and Berardi, A.C. (2012). Mesenchymal stem cells, aging and regenerative medicine. Muscles. Ligaments Tendons J. *2*, 239–242.

Raisz, L.G. (1988). Local and Systemic Factors in the Pathogenesis of Osteoporosis. N. Engl. J. Med. *318*, 818–828.

Ravikumar, B., Futter, M., Jahreiss, L., Korolchuk, V.I., Lichtenberg, M., Luo, S., Massey, D.C.O., Menzies, F.M., Narayanan, U., Renna, M., et al. (2009). Mammalian macroautophagy at a glance. J. Cell Sci. *122*, 1707–1711.

Razi, M., Chan, E.Y.W., and Tooze, S.A. (2009). Early endosomes and endosomal coatomer are required for Autophagy. J. Cell Biol. *185*, 305–321.

Ressler, S., Bartkova, J., Niederegger, H., Bartek, J., Scharffetter-Kochanek, K., Jansen-Dürr, P., and Wlaschek, M. (2006). p16INK4A is a robust in vivo biomarker of cellular aging in human skin. Aging Cell *5*, 379–389.

Richardson, R.B. (2009). Ionizing radiation and aging: rejuvenating an old idea. Aging (Albany. NY). *1*, 887–902.

Rizza, S., Cardaci, S., Montagna, C., Giacomo, G. Di, De Zio, D., Bordi, M., Maiani, E., Campello, S., Borreca, A., Puca, A.A., et al. (2018). S-nitrosylation drives cell senescence and aging in mammals by controlling mitochondrial dynamics and mitophagy. Proc. Natl. Acad. Sci. U. S. A. *115*, E3388–E3397.

Rocha, L.R., Nguyen Huu, V.A., Palomino La Torre, C., Xu, Q., Jabari, M., Krawczyk, M., Weinreb, R.N., and Skowronska-Krawczyk, D. (2020). Early removal of senescent cells protects retinal ganglion cells loss in experimental ocular hypertension. Aging Cell *19*, 1–15.

Rodier, F., Coppé, J.-P., Patil, C.K., Hoeijmakers, W. a M., Muñoz, D.P., Raza, S.R., Freund, A., Campeau, E., Davalos, A.R., and Campisi, J. (2009). Persistent DNA damage signalling triggers senescence-associated inflammatory cytokine secretion. Nat. Cell Biol. *11*, 973–979.

Rodier, F., Muñoz, D.P., Teachenor, R., Chu, V., Le, O., Bhaumik, D., Coppé, J., Campeau, E., Beauséjour, C.M., Kim, S., et al. (2011). DNA-SCARS: distinct nuclear structures that sustain damage-induced senescence growth arrest and inflammatory cytokine secretion. J. Cell Sci. *124*, 68–81.

Rosenbaum, D.M., Rasmussen, S.G.F., and Kobilka, B.K. (2009). The structure and function of G-protein-coupled receptors. Nature *459*, 356–363.

Roy, A.L., Sierra, F., Howcroft, K., Singer, D.S., Sharpless, N., Hodes, R.J., Wilder, E.L., and Anderson, J.M. (2020). A Blueprint for Characterizing Senescence. Cell *183*, 1143–1146.

Rudin, C.M., Hann, C.L., Garon, E.B., Ribeiro De Oliveira, M., Bonomi, P.D., Camidge, D.R., Chu, Q., Giaccone, G., Khaira, D., Ramalingam, S.S., et al. (2012). Phase II study of single-agent navitoclax (ABT-263) and biomarker correlates in patients with relapsed small cell lung cancer. Clin. Cancer Res. *18*, 3163–3169.

Rudolph, K.L. (2000). Inhibition of Experimental Liver Cirrhosis in Mice by Telomerase Gene Delivery. Science (80-.). *287*, 1253–1258.

Rudolph, K.L., Chang, S., Lee, H.W., Blasco, M., Gottlieb, G.J., Greider, C., and DePinho, R.A. (1999). Longevity, stress response, and cancer in aging telomerase-deficient mice. Cell *96*, 701–712.

Rünnenburger, K., Breer, H., and Boekhoff, I. (2002). Selective G protein βγ-subunit compositions mediate phospholipase C activation in the vomeronasal organ. Eur. J. Cell Biol. *81*, 539–547.

Ruscetti, M., Leibold, J., Bott, M.J., Fennell, M., Kulick, A., Salgado, N.R., Chen, C.C., Ho, Y. jui, Sanchez-Rivera, F.J., Feucht, J., et al. (2018). NK cell–mediated cytotoxicity contributes to tumor control by a cytostatic drug combination. Science (80-.). *362*, 1416–1422.

Ruscetti, M., Morris IV, J.P., Mezzadra, R., Russell, J., Leibold, J., Romesser, P.B., Simon, J., Kulick, A., Ho, Y., Fennell, M., et al. (2020). Senescence-Induced Vascular Remodeling Creates Therapeutic Vulnerabilities in Pancreas Cancer. Cell *181*, 424-441.e21.

Sadaie, M., Salama, R., Carroll, T., Tomimatsu, K., Chandra, T., Young, A.R.J., Narita, M., Pérez-Mancera, P.A., Bennett, D.C., Chong, H., et al. (2013). Redistribution of the Lamin B1 genomic binding profile affects rearrangement of heterochromatic domains and SAHF formation during senescence. Genes Dev. *27*.

Sáenz, J.B., Sun, W.J., Chang, J.W., Li, J., Bursulaya, B., Gray, N.S., and Haslam, D.B. (2009). Golgicide A reveals essential roles for GBF1 in Golgi assembly and function. Nat. Chem. Biol. *5*, 157–165.

Saito, K., and Katada, T. (2015). Mechanisms for exporting large-sized cargoes from the endoplasmic reticulum. Cell. Mol. Life Sci. *72*, 3709–3720.

Salama, R., Sadaie, M., Hoare, M., and Narita, M. (2014). Cellular senescence and its effector programs. Genes Dev. *28*, 99–114.

Salminen, A., Kaarniranta, K., and Kauppinen, A. (2012). Inflammaging: Disturbed interplay between autophagy and inflammasomes. Aging (Albany. NY). *4*, 166–175.

Salvador-Barbero, B., Álvarez-Fernández, M., Zapatero-Solana, E., El Bakkali, A., Menéndez, M. del C., López-Casas, P.P., Di Domenico, T., Xie, T., VanArsdale, T., Shields, D.J., et al. (2020). CDK4/6 Inhibitors Impair Recovery from Cytotoxic Chemotherapy in Pancreatic Adenocarcinoma. Cancer Cell *37*, 340-353.e6.

Sati, S., Bonev, B., Szabo, Q., Jost, D., Bensadoun, P., Serra, F., Loubiere, V., Papadopoulos, G.L., Rivera-Mulia, J.C., Fritsch, L., et al. (2020). 4D Genome Rewiring during Oncogene-Induced and Replicative Senescence. Mol. Cell *78*, 522-538.e9.

Sato, K., Sato, M., and Nakano, A. (2003). Rer1p, a retrieval receptor for ER membrane proteins, recognizes transmembrane domains in multiple modes. Mol. Biol. Cell *14*, 3605–3616.

Schafer, M.J., White, T.A., Iijima, K., Haak, A.J., Ligresti, G., Atkinson, E.J., Oberg, A.L., Birch, J., Salmonowicz, H., Zhu, Y., et al. (2017). Cellular senescence mediates fibrotic pulmonary disease. Nat. Commun. *8*, 14532.

Schmitz, K.R., Liu, J., Li, S., Setty, T.G., Wood, C.S., Burd, C.G., and Ferguson, K.M. (2008). Golgi Localization of Glycosyltransferases Requires a Vps74p Oligomer. Dev. Cell *14*, 523–534.

Schuerwegh, A.J., Stevens, W.J., Bridts, C.H., and De Clerck, L.S. (2001). Evaluation of monensin and brefeldin a for flow cytometric determination of interleukin-1 beta, interleukin-6, and tumor necrosis factor-alpha in monocytes. Commun. Clin. Cytom. *46*, 172–176.

Schwartzenberg-Bar-Yoseph, F., Armoni, M., and Karnieli, E. (2004). The Tumor Suppressor p53 Down-Regulates Glucose Transporters GLUT1 and GLUT4 Gene Expression. Cancer Res. *64*, 2627–2633.

Selman, C., Lingard, S., Choudhury, A.I., Batterham, R.L., Claret, M., Clements, M., Ramadani, F., Okkenhaug, K., Schuster, E., Blanc, E., et al. (2008). Evidence for lifespan extension and delayed age-related biomarkers in insulin receptor substrate 1 null mice. FASEB J. *22*, 807–818.

Selman, C., Tullet, J.M.A., Wieser, D., Irvine, E., Lingard, S.J., Choudhury, A.I., Claret, M., Al-Qassab, H., Carmignac, D., Ramadani, F., et al. (2009). Ribosomal Protein S6 Kinase 1 Signaling Regulates Mammalian Life Span. Science (80-.). *326*, 140 LP – 144.

Sen, P., Lan, Y., Li, C.Y., Sidoli, S., Donahue, G., Dou, Z., Frederick, B., Chen, Q., Luense, L.J., Garcia, B.A., et al. (2019). Histone Acetyltransferase p300 Induces De Novo Super-Enhancers to Drive Cellular Senescence. Mol. Cell *73*, 684-698.e8.

Serrano, M., Lin, A.W., McCurrach, M.E., Beach, D., and Lowe, S.W. (1997). Oncogenic ras provokes premature cell senescence associated with accumulation of p53 and p16(INK4a). Cell *88*, 593–602.

Sfeir, A., and de Lange, T. (2012). Removal of Shelterin Reveals the Telomere End-Protection Problem. Science (80-.). *336*, 593–597.

Shah, P.P., Donahue, G., Otte, G.L., Capell, B.C., Nelson, D.M., Cao, K., Aggarwala, V., Cruickshanks, H.A., Rai, T.S., McBryan, T., et al. (2013). Lamin B1 depletion in senescent cells triggers large-scale changes in gene expression and the chromatin landscape. Genes Dev. *27*, 1787–1799.

Shalini, S., Dorstyn, L., Dawar, S., and Kumar, S. (2015). Old, new and emerging functions of caspases. Cell Death Differ. *22*, 526–539.

Sharpless, N.E., and Sherr, C.J. (2015). Forging a signature of in vivo senescence. Nat. Rev. Cancer *15*, 397–408.

Sharpless, N.E., Bardeesy, N., Lee, K.H., Carrasco, D., Castrillon, D.H., Aguirre, A.J., Wu, E.A., Horner, J.W., and DePinho, R.A. (2001). Loss of p16Ink4a with retention of p19Arf predisposes mice to tumorigenesis. Nature *413*, 86–91.

Shay, J.W. (2016). Role of telomeres and telomerase in aging and cancer. Cancer Discov. *6*, 584–593.

Shay, J.W., and Bacchetti, S. (1997). A survey of telomerase activity in human cancer. Eur. J. Cancer *33*, 787–791.

Shefer, G., Van de Mark, D.P., Richardson, J.B., and Yablonka-Reuveni, Z. (2006). Satellite-cell pool size does matter: Defining the myogenic potency of aging skeletal muscle. Dev. Biol. *294*, 50–66.

Shifrut, E., Carnevale, J., Tobin, V., Roth, T.L., Woo, J.M., Bui, C.T., Li, P.J., Diolaiti, M.E., Ashworth, A., and Marson, A. (2018). Genome-wide CRISPR Screens in Primary Human T Cells Reveal Key Regulators of Immune Function. Cell *175*, 1958-1971.e15.

Shimi, T., Butin-Israeli, V., Adam, S.A., Hamanaka, R.B., Goldman, A.E., Lucas, C.A., Shumaker, D.K., Kosak, S.T., Chandel, N.S., and Goldman, R.D. (2011). The role of nuclear lamin B1 in cell proliferation and senescence. Genes Dev. *25*, 2579–2593.

Shtutman, M., Baig, M., Levina, E., Hurteau, G., Lim, C.U., Broude, E., Nikiforov, M., Harkins, T.T., Carmack, C.S., Ding, Y., et al. (2011). Tumor-specific silencing of COPZ2 gene encoding coatomer protein complex subunit ζ2 renders tumor cells dependent on its

paralogous gene COPZ1. Proc. Natl. Acad. Sci. U. S. A. *108*, 12449–12454.

Slamon, D.J., Hurvitz, S.A., Applebaum, S., Glaspy, J.A., Allison, M.K., DiCarlo, B.A., Courtney, R.D., Kim, S.T., Randolph, S., and Finn, R.S. (2010). Phase I study of PD 0332991, cyclin-D kinase (CDK) 4/6 inhibitor in combination with letrozole for first-line treatment of patients with ER-positive, HER2-negative breast cancer. J. Clin. Oncol. *28*, 3060.

Smith, J.R., and Pereira-Smith, O.M. (1996). Replicative Senescence: Implications for in Vivo Aging and Tumor Suppression. Science (80-.). *273*, 63 LP – 67.

Solomon, J.M., Pasupuleti, R., Xu, L., Curtis, R., Distefano, P.S., Julie, L., Mcdonagh, T., and Huber, L.J. (2006). Inhibition of SIRT1 Catalytic Activity Increases p53 Acetylation but Does Not Alter Cell Survival following DNA Damage Inhibition of SIRT1 Catalytic Activity Increases p53 Acetylation but Does Not Alter Cell Survival following DNA Damage. Mol. Cell. Biol. *26*, 28–38.

Sone, H., and Kagawa, Y. (2005). Pancreatic beta cell senescence contributes to the pathogenesis of type 2 diabetes in high-fat diet-induced diabetic mice. Diabetologia *48*, 58–67.

Sousa-Victor, P., Gutarra, S., García-Prat, L., Rodriguez-Ubreva, J., Ortet, L., Ruiz-Bonilla, V., Jardí, M., Ballestar, E., González, S., Serrano, A.L., et al. (2014). Geriatric muscle stem cells switch reversible quiescence into senescence. Nature *506*, 316–321.

Soysal, P., Stubbs, B., Lucato, P., Luchini, C., Solmi, M., Peluso, R., Sergi, G., Isik, A.T., Manzato, E., Maggi, S., et al. (2016). Inflammation and frailty in the elderly: A systematic review and meta-analysis. Ageing Res. Rev. *31*, 1–8.

Spooner, R.A., Watson, P., Smith, D.C., Boal, F., Amessou, M., Johannes, L., Clarkson, G.J., Lord, J.M., Stephens, D.J., and Roberts, L.M. (2008). The secretion inhibitor Exo2 pertubs trafficking of Shiga toxin between endosomes and the trans-Golgi network. Biochem. J. *414*, 471–484.

Van Steensel, B., Smogorzewska, A., and De Lange, T. (1998). TRF2 protects human telomeres from end-to-end fusions. Cell *92*, 401–413.

Storer, M., Mas, A., Robert-Moreno, A., Pecoraro, M., Ortells, M.C., Di Giacomo, V., Yosef, R., Pilpel, N., Krizhanovsky, V., Sharpe, J., et al. (2013). XSenescence is a developmental mechanism that contributes to embryonic growth and patterning. Cell *155*, 1119–1130.

Sturmlechner, I., Durik, M., Sieben, C.J., Baker, D.J., and van Deursen, J.M. (2017). Cellular senescence in renal ageing and disease. Nat. Rev. Nephrol. *13*, 77–89.

Sudo, K., Ema, H., Morita, Y., and Nakauchi, H. (2000). Age-associated characteristics of murine hematopoietic stem cells. J. Exp. Med. *192*, 1273–1280.

Sun, N., Youle, R.J., and Finkel, T. (2016). The Mitochondrial Basis of Aging. Mol. Cell *61*, 654–666.

Suram, A., Kaplunov, J., Patel, P.L., Ruan, H., Cerutti, A., Boccardi, V., Fumagalli, M., Di Micco, R., Mirani, N., Gurung, R.L., et al. (2012). Oncogene-induced telomere dysfunction enforces cellular senescence in human cancer precursor lesions. EMBO J. *31*, 2839–2851.

Suzanne, M., and Steller, H. (2013). Shaping organisms with apoptosis. Cell Death Differ. *20*, 669–675.

Swanson, E.C., Manning, B., Zhang, H., and Lawrence, J.B. (2013). Higher-order unfolding of satellite heterochromatin is a consistent and early event in cell senescence. J. Cell Biol. *203*, 929–942.

Szczerba, B.M., Castro-Giner, F., Vetter, M., Krol, I., Gkountela, S., Landin, J., Scheidmann, M.C., Donato, C., Scherrer, R., Singer, J., et al. (2019). Neutrophils escort circulating tumour cells to enable cell cycle progression. Nature *566*, 553–557.

Szul, T., and Sztul, E. (2011). COPII and COPI traffic at the ER-Golgi interface. Physiology *26*, 348–364.

Tacar, O., Sriamornsak, P., and Dass, C.R. (2013). Doxorubicin: An update on anticancer molecular action, toxicity and novel drug delivery systems. J. Pharm. Pharmacol. *65*, 157–170.

Takahashi, A., Loo, T.M., Okada, R., Kamachi, F., Watanabe, Y., Wakita, M., Watanabe, S., Kawamoto, S., Miyata, K., Barber, G.N., et al. (2018). Downregulation of cytoplasmic DNases is implicated in cytoplasmic DNA accumulation and SASP in senescent cells. Nat. Commun. *9*, 1–12.

Takai, H., Smogorzewska, A., and de Lange, T. (2003). DNA Damage Foci at Dysfunctional Telomeres. Curr. Biol. *13*, 1549–1556.

Takasugi, M., Okada, R., Takahashi, A., Virya Chen, D., Watanabe, S., and Hara, E. (2017). Small extracellular vesicles secreted from senescent cells promote cancer cell proliferation through EphA2. Nat. Commun. *8*, 1–11.

Takeda, K., Smyth, M.J., Cretney, E., Hayakawa, Y., Kayagaki, N., Yagita, H., and Okumura, K. (2002). Critical role for tumor necrosis factor-related apoptosis-inducing ligand in immune surveillance against tumor development. J. Exp. Med. *195*, 161–169.

Tanigawa, G., Orci, L., Amherdt, M., Ravazzola, M., Helms, J.B., and Rothman, J.E. (1993). Hydrolysis of bound GTP by ARF protein triggers uncoating of Golgi- derived COP-coated vesicles. J. Cell Biol. *123*, 1365–1371.

Tasdemir, N., Banito, A., Roe, J.S., Alonso-Curbelo, D., Camiolo, M., Tschaharganeh, D.F., Huang, C.H., Aksoy, O., Bolden, J.E., Chen, C.C., et al. (2016). BRD4 connects enhancer remodeling to senescence immune surveillance. Cancer Discov. *6*, 613–629.

Tasselli, L., Xi, Y., Zheng, W., Tennen, R.I., Odrowaz, Z., Simeoni, F., Li, W., and Chua, K.F. (2016). SIRT6 deacetylates H3K18ac at pericentric chromatin to prevent mitotic errors and cellular senescence. Nat. Struct. Mol. Biol. *23*, 434–440.

De Tata, V. (2014). Age-related impairment of pancreatic beta-cell function: Pathophysiological and cellular mechanisms. Front. Endocrinol. (Lausanne). *5*, 1–8.

Taylor, R.C., Cullen, S.P., and Martin, S.J. (2008). Apoptosis: Controlled demolition at the cellular level. Nat. Rev. Mol. Cell Biol. *9*, 231–241.

Tchkonia, T., Morbeck, D.E., Von Zglinicki, T., Van Deursen, J., Lustgarten, J., Scrable, H., Khosla, S., Jensen, M.D., and Kirkland, J.L. (2010). Fat tissue, aging, and cellular senescence. Aging Cell *9*, 667–684.

Telgenhoff, D., and Shroot, B. (2005). Cellular senescence mechanisms in chronic wound healing. Cell Death Differ. *12*, 695–698.

Teo, Y.V., Rattanavirotkul, N., Olova, N., Salzano, A., Quintanilla, A., Tarrats, N., Kiourtis, C., Müller, M., Green, A.R., Adams, P.D., et al. (2019). Notch Signaling Mediates Secondary Senescence. Cell Rep. *27*, 997-1007.e5.

Thinon, E., Serwa, R.A., Broncel, M., Brannigan, J.A., Brassat, U., Wright, M.H., Heal, W.P., Wilkinson, A.J., Mann, D.J., and Tate, E.W. (2014). Global profiling of co- and post-translationally N-myristoylated proteomes in human cells. Nat. Commun. *5*.

Thompson, P.J., Shah, A., Ntranos, V., Van Gool, F., Atkinson, M., and Bhushan, A. (2019). Targeted Elimination of Senescent Beta Cells Prevents Type 1 Diabetes. Cell Metab. *29*, 1045-1060.e10.

Thor, F., Gautschi, M., Geiger, R., and Helenius, A. (2009). Bulk flow revisited: Transport of a soluble protein in the secretory pathway. Traffic *10*, 1819–1830.

Tilstra, J.S., Robinson, A.R., Wang, J., Gregg, S.Q., Clauson, C.L., Reay, D.P., Nasto, L.A., St Croix, C.M., Usas, A., Vo, N., et al. (2012). NF-κB inhibition delays DNA damage–induced senescence and aging in mice. J. Clin. Invest. *122*, 2601–2612.

Timms, R.T., Zhang, Z., Rhee, D.Y., Harper, J.W., Koren, I., and Elledge, S.J. (2019). A glycine-specific N-degron pathway mediates the quality control of protein N-myristoylation. Science (80-.). *365*, eaaw4912.

Tordella, L., Khan, S., Hohmeyer, A., Banito, A., Klotz, S., Raguz, S., Martin, N., Dhamarlingam, G., Carroll, T., González Meljem, J.M., et al. (2016). SWI/SNF regulates a transcriptional program that induces senescence to prevent liver cancer. Genes Dev. *30*, 2187–2198.

Triana-Martínez, F., Picallos-Rabina, P., Da Silva-Álvarez, S., Pietrocola, F., Llanos, S., Rodilla, V., Soprano, E., Pedrosa, P., Ferreirós, A., Barradas, M., et al. (2019). Identification and characterization of Cardiac Glycosides as senolytic compounds. Nat. Commun. *10*, 1–12.

Tu, L., Tai, W.C.S., Chen, L., and Banfield, D.K. (2008). Signal-Mediated Dynamic Retention of Glycosyltransferases in the Golgi. Science (80-.). *321*, 404 LP – 407.

Tu, Z., Zhuang, X., Yao, Y.-G., and Zhang, R. (2013). BRG1 Is Required for Formation of Senescence-Associated Heterochromatin Foci Induced by Oncogenic RAS or BRCA1 Loss. Mol. Cell. Biol. *33*, 1819–1829.

Turnquist, C., Horikawa, I., Foran, E., Major, E.O., Vojtesek, B., Lane, D.P., Lu, X., Harris, B.T., and Harris, C.C. (2016). P53 isoforms regulate astrocyte-mediated neuroprotection and neurodegeneration. Cell Death Differ. *23*, 1515–1528.

Tuveson, D.A., Shaw, A.T., Willis, N.A., Silver, D.P., Jackson, E.L., Chang, S., Mercer, K.L., Grochow, R., Hock, H., Crowley, D., et al. (2004). Endogenous oncogenic K-rasG12D stimulates proliferation and widespread neoplastic and developmental defects. Cancer Cell *5*, 375–387.

Tzelepis, K., Koike-Yusa, H., De Braekeleer, E., Li, Y., Metzakopian, E., Dovey, O.M., Mupo, A., Grinkevich, V., Li, M., Mazan, M., et al. (2016). A CRISPR Dropout Screen Identifies Genetic Vulnerabilities and Therapeutic Targets in Acute Myeloid Leukemia. Cell Rep. *17*, 1193–1205.

Ueno, T., Kaneko, K., Katano, H., Sato, Y., Mazitschek, R., Tanaka, K., Hattori, S., Irie, S., Sata, T., and Ogawa-Goto, K. (2010). Expansion of the trans-Golgi network following

activated collagen secretion is supported by a coiled-coil microtubule-bundling protein, p180, on the ER. Exp. Cell Res. *316*, 329–340.

Ulland, T.K., and Colonna, M. (2018). TREM2 — a key player in microglial biology and Alzheimer disease. Nat. Rev. Neurol. *14*, 667–675.

Uryga, A.K., and Bennett, M.R. (2016). Ageing induced vascular smooth muscle cell senescence in atherosclerosis. J. Physiol. *594*, 2115–2124.

Valadi, H., Ekström, K., Bossios, A., Sjöstrand, M., Lee, J.J., and Lötvall, J.O. (2007). Exosome-mediated transfer of mRNAs and microRNAs is a novel mechanism of genetic exchange between cells. Nat. Cell Biol. *9*, 654–659.

Varela, I., Cadinanos, J., Pendas, A.M., Gutierrez-Fernandez, A., Folgueras, A.R., Sanchez, L.M., Zhou, Z., Rodriguez, F.J., Stewart, C.L., Vega, J.A., et al. (2005). Accelerated ageing in mice deficient in Zmpste24 protease is linked to p53 signalling activation. Nature *437*, 564–568.

Wajapeyee, N., Serra, R.W., Zhu, X., Mahalingam, M., and Green, M.R. (2008). Oncogenic BRAF Induces Senescence and Apoptosis through Pathways Mediated by the Secreted Protein IGFBP7. Cell *132*, 363–374.

Wakita, M., Takahashi, A., Sano, O., Loo, T.M., Imai, Y., Narukawa, M., Iwata, H., Matsudaira, T., Kawamoto, S., Ohtani, N., et al. (2020). A BET family protein degrader provokes senolysis by targeting NHEJ and autophagy in senescent cells. Nat. Commun. *11*, 1–13.

Waldman, A.D., Fritz, J.M., and Lenardo, M.J. (2020). A guide to cancer immunotherapy: from T cell basic science to clinical practice. Nat. Rev. Immunol. *20*, 651–668.

Walters, H.E., Deneka-Hannemann, S., and Cox, L.S. (2016). Reversal of phenotypes of cellular senescence by pan-mTOR inhibition. Aging (Albany. NY). *8*, 231–244.

Wang, C., Jurk, D., Maddick, M., Nelson, G., Martin-ruiz, C., and Von Zglinicki, T. (2009). DNA damage response and cellular senescence in tissues of aging mice. Aging Cell *8*, 311–323.

Wang, C., Oshima, M., Sashida, G., Tomioka, T., Hasegawa, N., Mochizuki-Kashio, M., Nakajima-Takagi, Y., Kusunoki, Y., Kyoizumi, S., Imai, K., et al. (2015a). Non-lethal ionizing radiation promotes aging-like phenotypic changes of human hematopoietic stem and progenitor cells in humanized mice. PLoS One *10*, 1–14.

Wang, C., Vegna, S., Jin, H., Benedict, B., Lieftink, C., Ramirez, C., de Oliveira, R.L., Morris, B., Gadiot, J., Wang, W., et al. (2019). Inducing and exploiting vulnerabilities for the treatment of liver cancer. Nature *574*, 268–272.

Wang, L., Leite de Oliveira, R., Wang, C., Fernandes Neto, J.M., Mainardi, S., Evers, B., Lieftink, C., Morris, B., Jochems, F., Willemsen, L., et al. (2017a). High-Throughput Functional Genetic and Compound Screens Identify Targets for Senescence Induction in Cancer. Cell Rep. *21*, 773–783.

Wang, T., Yu, H., Hughes, N.W., Liu, B., Kendirli, A., Klein, K., Chen, W.W., Lander, E.S., and Sabatini, D.M. (2017b). Gene Essentiality Profiling Reveals Gene Networks and Synthetic Lethal Interactions with Oncogenic Ras. Cell *168*, 890-903.e15.

Wang, X., Spandidos, A., Wang, H., and Seed, B. (2012). PrimerBank: A PCR primer

database for quantitative gene expression analysis, 2012 update. Nucleic Acids Res. *40*, 1144–1149.

Wang, Y., Cella, M., Mallinson, K., Ulrich, J.D., Young, K.L., Robinette, M.L., Gilfillan, S., Krishnan, G.M., Sudhakar, S., Zinselmeyer, B.H., et al. (2015b). TREM2 lipid sensing sustains the microglial response in an Alzheimer's disease model. Cell *160*, 1061–1071.

Watson, P.J., Frigerio, G., Collins, B.M., Duden, R., and Owen, D.J. (2004). γ-COP Appendage Domain – Structure and Function. Traffic *5*, 79–88.

Webster, M.R., Xu, M., Kinzler, K.A., Kaur, A., Appleton, J., O'Connell, M.P., Marchbank, K., Valiga, A., Dang, V.M., Perego, M., et al. (2015). Wnt5A promotes an adaptive, senescent-like stress response, while continuing to drive invasion in melanoma cells. Pigment Cell Melanoma Res. *28*, 184–195.

Weinlich, R., Oberst, A., Beere, H.M., and Green, D.R. (2017). Necroptosis in development, inflammation and disease. Nat. Rev. Mol. Cell Biol. *18*, 127–136.

Wieland, F.T., Gleason, M.L., Serafini, T.A., and Rothman, J.E. (1987). The rate of bulk flow from the endoplasmic reticulum to the cell surface. Cell *50*, 289–300.

Wiley, C.D., and Campisi, J. (2016). From Ancient Pathways to Aging Cells - Connecting Metabolism and Cellular Senescence. Cell Metab. *23*, 1013–1021.

Wiley, C.D., Velarde, M.C., Lecot, P., Liu, S., Sarnoski, E.A., Freund, A., Shirakawa, K., Lim, H.W., Davis, S.S., Ramanathan, A., et al. (2016). Mitochondrial dysfunction induces senescence with a distinct secretory phenotype. Cell Metab. *23*, 303–314.

Wilfling, F., Thiam, A.R., Olarte, M.J., Wang, J., Beck, R., Gould, T.J., Allgeyer, E.S., Pincet, F., Bewersdorf, J., Farese, R. V., et al. (2014). Arf1/COPI machinery acts directly on lipid droplets and enables their connection to the ER for protein targeting. Elife *2014*, 1–20.

Wu, B., and Guo, W. (2015). The exocyst at a glance. J. Cell Sci. *128*, 2957–2964.

Xiao, Y.Z., Yang, M., Xiao, Y., Guo, Q., Huang, Y., Li, C.J., Cai, D., and Luo, X.H. (2020). Reducing Hypothalamic Stem Cell Senescence Protects against Aging-Associated Physiological Decline. Cell Metab. *31*, 534-548.e5.

Xie, W., Kagiampakis, I., Pan, L., Zhang, Y.W., Murphy, L., Tao, Y., Kong, X., Kang, B., Xia, L., Carvalho, F.L.F., et al. (2018). DNA Methylation Patterns Separate Senescence from Transformation Potential and Indicate Cancer Risk. Cancer Cell *33*, 309-321.e5.

Xiu, M., Kim, J., Sampson, E., Huang, C.-Y., Davis, R.J., Paulson, K.E., and Yee, A.S. (2003). The Transcriptional Repressor HBP1 Is a Target of the p38 Mitogen-Activated Protein Kinase Pathway in Cell Cycle Regulation. Mol. Cell. Biol. *23*, 8890 LP – 8901.

Xu, C., Wang, L., Fozouni, P., Evjen, G., Chandra, V., Jiang, J., Lu, C., Nicastri, M., Bretz, C., Winkler, J.D., et al. (2020). SIRT1 is downregulated by autophagy in senescence and ageing. Nat. Cell Biol. *22*, 1170–1179.

Xu, F., Du, W., Zou, Q., Wang, Y., Zhang, X., Xing, X., Li, Y., Zhang, D., Wang, H., Zhang, W., et al. (2021). COPII mitigates ER stress by promoting formation of ER whorls. Cell Res. *31*, 141–156.

Xu, M., Palmer, A.K., Ding, H., Weivoda, M.M., Pirtskhalava, T., White, T.A., Sepe, A., Johnson, K.O., Stout, M.B., Giorgadze, N., et al. (2015a). Targeting senescent cells

enhances adipogenesis and metabolic function in old age. Elife *4*, 1–19.

Xu, M., Tchkonia, T., Ding, H., Ogrodnik, M., Lubbers, E.R., Pirtskhalava, T., White, T.A., Johnson, K.O., Stout, M.B., Mezera, V., et al. (2015b). JAK inhibition alleviates the cellular senescence-associated secretory phenotype and frailty in old age. Proc. Natl. Acad. Sci. U. S. A. *112*, E6301-10.

Xu, M., Pirtskhalava, T., Farr, J.N., Weigand, B.M., Palmer, A.K., Weivoda, M.M., Inman, C.L., Ogrodnik, M.B., Hachfeld, C.M., Fraser, D.G., et al. (2018). Senolytics improve physical function and increase lifespan in old age. Nat. Med. *24*, 1246–1256.

Xu, Y., Li, N., Xiang, R., and Sun, P. (2014). Emerging roles of the p38 MAPK and PI3K/AKT/mTOR pathways in oncogene-induced senescence. Trends Biochem. Sci. *39*, 268–276.

Xue, W., Zender, L., Miething, C., Dickins, R.A., Hernando, E., Krizhanovsky, V., Cordon-Cardo, C., and Lowe, S.W. (2007). Senescence and tumour clearance is triggered by p53 restoration in murine liver carcinomas. Nature *445*, 656–660.

Yamauchi, T., Masuda, T., Canver, M.C., Seiler, M., Semba, Y., Shboul, M., Al-Raqad, M., Maeda, M., Schoonenberg, V.A.C., Cole, M.A., et al. (2018). Genome-wide CRISPR-Cas9 Screen Identifies Leukemia-Specific Dependence on a Pre-mRNA Metabolic Pathway Regulated by DCPS. Cancer Cell *33*, 386-400.e5.

Yanai, H., Shteinberg, A., Porat, Z., Budovsky, A., Braiman, A., Zeische, R., and Fraifeld, V.E. (2015). Cellular senescence-like features of lung fibroblasts derived from idiopathic pulmonary fibrosis patients. Aging (Albany. NY). *7*, 664–672.

Yilmaz, A., Peretz, M., Aharony, A., Sagi, I., and Benvenisty, N. (2018). Defining essential genes for human pluripotent stem cells by CRISPR-Cas9 screening in haploid cells. Nat. Cell Biol. *20*, 610–619.

Yosef, R., Pilpel, N., Tokarsky-Amiel, R., Biran, A., Ovadya, Y., Cohen, S., Vadai, E., Dassa, L., Shahar, E., Condiotti, R., et al. (2016). Directed elimination of senescent cells by inhibition of BCL-W and BCL-XL. Nat. Commun. *7*, 11190.

Young, A.R.J., Narita, M., Ferreira, M., Kirschner, K., Sadaie, M., Darot, J.F.J., Tavaré, S., Arakawa, S., Shimizu, S., Watt, F.M., et al. (2009). Autophagy mediates the mitotic senescence transition. Genes Dev. *23*, 798–803.

Yu, G.L., Bradley, J.D., Attardi, L.D., and Blackburn, E.H. (1990). In vivo alteration of telomere sequences and senescence caused by mutated Tetrahymena telomerase RNAs. Nature *344*, 126–132.

Yuan, M., Song, Z. han, Ying, M. dan, Zhu, H., He, Q. jun, Yang, B., and Cao, J. (2020). N-myristoylation: from cell biology to translational medicine. Acta Pharmacol. Sin. *41*, 1005–1015.

Zanetti, G., Pahuja, K.B., Studer, S., Shim, S., and Schekman, R. (2012). Erratum: COPII and the regulation of protein sorting in mammals (Nature Cell Biology (2012) 14 (20-28)). Nat. Cell Biol. *14*, 221.

Zeggini, E., Weedon, M.N., Lindgren, C.M., Frayling, T.M., Elliott, K.S., Lango, H., Timpson, N.J., Perry, J.R.B., Rayner, N.W., Freathy, R.M., et al. (2007). Replication of genome-wide association signals in UK samples reveals risk loci for type 2 diabetes. Science *316*, 1336–1341.

Zerangue, N., Malan, M.J., Fried, S.R., Dazin, P.F., Jan, Y.N., Jan, L.Y., and Schwappach, B. (2001). Analysis of endoplasmic reticulum trafficking signals by combinatorial screening in mammalian cells. Proc. Natl. Acad. Sci. U. S. A. *98*, 2431–2436.

Zhang, P., Kishimoto, Y., Grammatikakis, I., Gottimukkala, K., Cutler, R.G., Zhang, S., Abdelmohsen, K., Bohr, V.A., Misra Sen, J., Gorospe, M., et al. (2019). Senolytic therapy alleviates Aβ-associated oligodendrocyte progenitor cell senescence and cognitive deficits in an Alzheimer's disease model. Nat. Neurosci. *22*, 719–728.

Zhang, Q., Major, M.B., Takanashi, S., Camp, N.D., Nishiya, N., Peters, E.C., Ginsberg, M.H., Schultz, P.G., Moon, R.T., and Ding, S. (2007a). Small-molecule synergist of the Wnt/β-catenin signaling pathway. Proc. Natl. Acad. Sci. U. S. A. *104*, 7444–7448.

Zhang, R., Poustovoitov, M. V., Ye, X., Santos, H.A., Chen, W., Daganzo, S.M., Erzberger, J.P., Serebriiskii, I.G., Canutescu, A.A., Dunbrack, R.L., et al. (2005). Formation of macroH2A-containing senescence-associated heterochromatin foci and senescence driven by ASF1a and HIRA. Dev. Cell *8*, 19–30.

Zhang, R., Chen, W., and Adams, P.D. (2007b). Molecular Dissection of Formation of Senescence-Associated Heterochromatin Foci. Mol. Cell. Biol. *27*, 2343–2358.

Zhang, X., Kim, J., Ruthazer, R., McDevitt, M. a, Wazer, D.E., Paulson, K.E., and Yee, A.S. (2006). The HBP1 transcriptional repressor participates in RAS-induced premature senescence. Mol. Cell. Biol. *26*, 8252–8266.

Zhang, Y., Kim, M.S., Jia, B., Yan, J., Zuniga-Hertz, J.P., Han, C., and Cai, D. (2017). Hypothalamic stem cells control ageing speed partly through exosomal miRNAs. Nature *548*, 52–57.

Zhou, L., Gao, W., Wang, K., Huang, Z., Zhang, L., Zhang, Z., Zhou, J., Nice, E.C., and Huang, C. (2019). Brefeldin A inhibits colorectal cancer growth by triggering Bip/Akt-regulated autophagy. FASEB J. *33*, 5520–5534.

Zhu, J., Woods, D., Mcmahon, M., and Bishop, J.M. (1998). Senescence of human fibroblasts induced by oncogenic Raf Senescence of human fibroblasts induced by oncogenic Raf. Genes Dev. 2997–3007.

Zhu, Y., Tchkonia, T., Pirtskhalava, T., Gower, A.C., Ding, H., Giorgadze, N., Palmer, A.K., Ikeno, Y., Hubbard, G.B., Lenburg, M., et al. (2015). The Achilles' heel of senescent cells: from transcriptome to senolytic drugs. Aging Cell *14*, 644–658.

Zitvogel, L., Tesniere, A., and Kroemer, G. (2006). Cancer despite immunosurveillance: Immunoselection and immunosubversion. Nat. Rev. Immunol. *6*, 715–727.

Zoncu, R., Efeyan, A., and Sabatini, D.M. (2011). mTOR: from growth signal integration to cancer, diabetes and ageing. Nat. Rev. Mol. Cell Biol. *12*, 21–35.

Zwerschke, W., Mazurek, S., Stöckl, P., Hütter, E., Eigenbrodt, E., and Jansen-Dürr, P. (2003). Metabolic analysis of senescent human fibroblasts reveals a role for AMP in cellular senescence. Biochem. J. *376*, 403–411.